From Statistics to In-Depth Analysis: X-ray Insights into Neutron Stars

Dissertation

der Mathematisch-Naturwissenschaftlichen Fakultät
der Eberhard Karls Universität Tübingen
zur Erlangung des Grades eines
Doktors der Naturwissenschaften
(Dr. rer. nat.)

vorgelegt von
Armin Vahdat
aus Tehran/Iran

Tübingen
2024

Gedruckt mit Genehmigung der Mathematisch-Naturwissenschaftlichen Fakultät der Eberhard Karls Universität Tübingen.

Tag der mündlichen Qualifikation:	19.04.2024
Dekan:	Prof. Dr. Thilo Stehle
1. Berichterstatter:	Prof. Dr. Andrea Santangelo
2. Berichterstatter:	Prof. Dr. Klaus Werner
3. Berichterstatterin:	Dr. Bettina Posselt

From Statistics to In Depth Analysis: X-ray Insights into Neutron Stars

Armin Vahdat

Ph. D. Thesis, April 2024

In gratitude to the unseen hands and hearts that have guided my path

Zusammenfassung

Neutronensterne, die Überreste massiver Sternenexplosionen, nehmen einen einzigartigen Platz in der Astrophysik ein. Ihre extreme Dichte und ihre Magnetfelder, gepaart mit ihrer Vielfalt, machen sie zu faszinierenden Objekten der Wissenschaft.

Obwohl sie vor fast 60 Jahren entdeckt wurden, bleiben zahlreiche Fragen zur Natur von Neutronensternen unbeantwortet. Dazu gehören ihre innere Zusammensetzung, die Populationsdichte in der Galaxie, evolutionäre Pfade zwischen verschiedenen Arten von Neutronensternen sowie die Physik ihre thermischen und nichtthermischen Emissionsprozesse.

Diese Doktorarbeit, bestehend aus zwei unterschiedlichen, jedoch sich ergänzenden Projekten, zielt auf die Füllung dieser Wissenslücken ab. Das erste Projekt konzentriert sich auf die Röntgeneigenschaften der Neutronensterne und untersucht Populationsstatistiken, während das zweite Projekt eine detaillierte Erforschung der Herkunft von Röntgenemissionen eines bestimmten Neutronenstern bietet.

Die erste Studie basiert auf der bereits bekannten Korrelation der Röntgenleuchtkraft mit dem Rotationsenergieverlust der Pul-

sare. Die meisten Pulsare mit Röntgendetektionen haben eine Röntgeneffizienz von 10^{-4} bis 10^{-5}. Aufgrund der (wenigen) Detektionen von älteren Pulsaren gibt es Hinweise , dass die Röntgeneffizienz mit geringerem Rotationsenergieverlust steigt. Die faszinierende Frage ist, ob diese Clusterbildung auf die Existenz von höheren Multipolmagnetfeldkomponenten zurückzuführen ist oder ob sie aus einer Eskalation in der Leuchtkraft der Elektron-Positron- Paarheizung resultiert.

Ein mögliches Problem für unser Verständnis besteht, dass wir Untersuchungen oft auf die hellsten Pulsare konzentrieren, was uns eine voreingenommene Sicht geben könnte. Die spezielle Betrachtung von "interessanten" Pulsaren, die durch andere Methoden gefunden wurden, könnte zu einem voreingenommenen Verständnis ihrer Röntgenemissionen führen. Dieser Wandel unterstreicht die Notwendigkeit eines unvoreingenommenen Ansatzes, um wirklich zu verstehen, wie Pulsare Röntgenstrahlen aussenden, und verzerrte Interpretationen zu vermeiden.

Das erste Projekt, "Towards an X-ray inventory of nearby neutron stars, (Vahdat et al., 2022)", zielte darauf ab, unser Verständnis der Population von nahegelegenen Neutronensternen durch neue Beobachtungen mit dem *XMM-Newton*-Teleskop zu verbessern. Obwohl viele Neutronensterne in bereich beobachtet worden waren, blieben einige aufgrund von Herausforderungen in Bezug auf unsichere Entfernungen, Alter oder Positionen schwer fassbar. Um dies anzugehen, gingen wir systematisch vor und analysierten Röntgendaten aus verschiedenen Quellen, darunter *XMM-Newton*, Chandra und andere Kataloge, die mehrere Wellenlängen abdecken. Un-

sere Bemühungen führten zur Entdeckung von Röntgenpulsar- Gegenstücken, die zuvor nicht identifiziert worden waren, und bieten einen umfassenderen Überblick über der Neutronensterne innerhalb einer Entfernung von etwa 2 Kiloparsec. Dieses Projekt angewendet wurde, erweiterte die Stichprobe von nahegelegenen Röntgenemittierenden Neutronensternen und hilft zukünftigen Untersuchungen, die eine unvoreingenommene Darstellung dieser Quellen erfordern.

In unserem zweiten Projekt, "Multiwavelength Pulsations and Surface Temperature Distribution in the Middle-Aged Pulsar B1055−52, (Vahdat et al., 2024)", führten wir eine detaillierte Analyse von Beobachtungsergebnissen eines mittelalten Pulsars durch. Unter Verwendung des *XMM-Newton*-Teleskops untersuchten wir die Röntgenemission von PSR B1055−52. Unsere Untersuchungen ergaben, dass die phasenintegrierten Spektren am besten mit zwei Schwarzkörperkomponenten und einem Potenzgesetz passen.

Darüber hinaus zeigte die pulsationsphasenabhängige spektrale Analyse von B1055 Veränderungen in den thermischen Emissionsparametern während des Rotationszyklus des Pulsars. Diese zeigt die Uneiheitlichkeit der Temperaturoberflächenverteilung an. Die Anwendung verschiedener statistischer Analysetechniken, und der Untersuchung von Pulsprofilen bei verschiedenen Wellenlängen, ermöglichte Vergleiche mit anderen isolierten Pulsaren und Diskussionen über Temperatur- und Magnetfeldverteilungen, die Geometrie des Pulsars sowie die Mechanismen, die die zugrunde liegenden Heizprozesse antreiben.

Abstract

Neutron stars, the remnants of massive stellar explosions, hold a unique place in astrophysics. Their extreme densities and magnetic fields, coupled with their diversity, make them captivating objects for study.

Despite being discovered almost 60 years ago, numerous questions about the nature of neutron stars remain unanswered. These include their inner composition, population density across the galaxy, evolutionary paths between different types of neutron stars, as well as the physics of their thermal and non-thermal emission processes.

This Ph.D. thesis aims to address these gaps in knowledge through the presentation of two distinct yet complementary projects. The first project focuses on X-ray properties, delving into population statistics, while the second project offers a detailed exploration of the distribution of different emission components over pulse phase and their origin from a specific neutron star.

The correlation between the spin down-energy loss and X-ray luminosity in pulsars has been a focal point in numerous studies. This so-called X-ray efficiency appears to converge within the range

of 10^{-4} to 10^{-5} at elevated spin down-energy loss values. Due to the (few) detections of older pulsars, there are indications that the X-ray efficiency increases with lower rotational energy loss. The intriguing question persists regarding whether this clustering is attributed to the existence of higher multipole magnetic field components, or if it stems from an escalation in electron-positron pair heating luminosity.

One challenge is that we often focus on the brightest pulsars, which might give us a biased view. Looking specifically at "interesting" pulsars found through other methods might lead to a biased understanding of their X-ray emissions.

The first project, "Towards an X-ray inventory of nearby neutron stars, (Vahdat et al., 2022)", aimed to enhance our understanding of the population of nearby neutron stars by conducting a survey using the *XMM-Newton* telescope. Although many neutron stars had been observed in X-rays, some remained elusive due to challenges related to uncertain distances, ages, or locations. To address this, we took a systematic approach, analyzing X-ray data from various sources, including *XMM-Newton*, Chandra, and other catalogs covering multiple wavelengths. Our efforts resulted in the discovery of X-ray sources that were previously unidentified, offering a more comprehensive overview of these celestial objects within a distance of about 2 kiloparsecs. This project expanded the sample of nearby X-ray-emitting neutron stars, providing essential input for future investigations that require an unbiased repre-

sentation of these sources.

In our second project, "Multiwavelength Pulsations and Surface Temperature Distribution in the Middle-Aged Pulsar B1055−52, (Vahdat et al., 2024)", we conducted a detailed analysis of an isolated, middle-aged pulsar. Observations from the *XMM-Newton* telescope, we carefully examined the X-ray emission of PSR B1055−52. Our investigations found that the phase-averaged spectra is best fitted with two blackbody components and a power law.

Furthermore, the phase-resolved spectral analysis of B1055 revealed variations in the thermal emission parameters throughout the pulsar's rotational cycle. This discovery suggests the non-uniformity of the blackbody components, especially the hotter one. Applying different statistical analysis techniques and multiwavelength pulse profile analysis allowed for comparisons with other isolated pulsars and facilitated discussions on temperature and magnetic field distributions, as well as the mechanisms driving the underlying heating processes. Additionally, the observation of a second hot spot confirmed the orthogonal geometry indicated by the radio observation.

Preface

This thesis comprises four distinct chapters, each serving a specific purpose within the context of my research.

In the **first chapter**, I present the introduction, setting the stage for the thesis while offering an insight into the rationale behind the chosen title.

Chapter 2 is dedicated to instrumentation, setups, techniques, formulas, and methodology that I employed in the subsequent chapters. Here, I aim to introduce the observatories and facilities integral to my research, providing formal guidelines for spectral, timing, and statistical analysis – elements that were crucial in the pursuit of my research objectives. Certain specific data reduction and analysis details are deliberately excluded from this chapter; they will be introduced later in the subsequent chapters, as they are closely tied to the specifics of the individual projects.

In **Chapter 3**, I summarize the aims of Vahdat et al. (2022) and Vahdat et al. (2024), along with the analyses conducted in these publications, without delving too deeply into the specifics of data

reduction and methodology.

Vahdat et al. (2022) has been published in Astronomy & Astrophysics and was a collaborative effort involving Bettina Posselt, George Pavlov, and Andrea Santangelo. This study delves into our extensive four-year XMM-Newton Fulfil survey, during which we significantly expanded the number of X-ray investigated pulsars.

Vahdat et al. (2024) has also be published in the Astrophysical Journal and was a collaborative venture with Bettina Posselt, George Pavlov, Peter Weltevrede, Simon Johnston, and Andrea Santangelo. This project delves into a multifaceted approach aimed at unraveling the physical properties and geometry of a unique pulsar known as B1055.

In **Chapter 4**, I will present the main findings of these two publications, as well as discuss and interpret these results and explore potential future studies.

Contents

List of Figures

List of Tables

1 Introduction to Astrophysics of Pulsars

> *It does not matter where I am. The sky is always mine. Windows, ideas, air, love, earth, all mine.*
>
> **— Sohrab Sepehri**
>
> (The Foot Steps Of Water, 1964)

1.1 A Historical Odyssey

The history of neutron stars (NSs) is a fascinating narrative, blending theoretical postulations with unexpected discoveries. This scientific exploration, spanning several decades, transforms our understanding of these enigmatic celestial entities. In 1934 Walter Baade and Fritz Zwicky made a groundbreaking proposition where they suggested that supernova explosions might give rise to compact stars primarily composed of neutrons. This idea was a response to the question of where the immense energy in supernova explosions comes from. Baade and Zwicky's theory imagined stars or star remnants with the density

of atomic nuclei, a crucial concept in astrophysics (Baade and Zwicky, 1934).

For over three decades, the theoretical notion of NSs persisted, but tangible proof remained elusive. It wasn't until 1967 that this story began to take a concrete form when Jocelyn Bell and her mentor, Antony Hewish, inadvertently stumbled upon a celestial marvel. Their quest to study interplanetary scintillation led to the serendipitous discovery of pulsars. Initially, these signals were mistaken for terrestrial radio interference, but their celestial origin soon became undeniable. The first pulsar, CP1919, with a pulse period of 1.337 seconds, took center stage, and the term 'pulsar' was coined in recognition of the characteristic pulse-like emissions (Hewish et al., 1979).

The pulsar's discovery sparked a lot of theoretical conjecture, setting off an intense wave of scientific speculation. Three primary categories of theories emerged: the pulsations could emanate from radial oscillations within the star, result from the orbital dynamics of binary star systems, or stem from the fast rotation of an unidentified cosmic object (Hewish et al., 1979; Thorne and Ipser, 1968; Saslaw et al., 1968; Gold, 1968). As more pulsars were uncovered, it became clear that some of these theories could not explain all the observed properties.

The pivotal moment came when it was revealed that pulsars were slowing down, indicated by lengthening of their spin periods. This discovery discredited the theories based on binary systems. The prevailing explanation was that pulsars were rapidly rotating NSs with misaligned magnetic fields, which explained their observed

characteristics (Gold, 1968). Further evidence of NSs and pulsars came through careful observations in radio and X-ray frequencies. The launch of the first X-ray satellite, Uhuru, in 1970 marked a turning point, leading to the discovery of X-ray binary pulsars (Pacini, 1968). These observations affirmed that pulsars were indeed fast-spinning NSs with powerful magnetic fields. The radio waves from these pulsars resembled the sweeping beam of a lighthouse (Gold, 1968; Pacini, 1968). The discovery of pulsars within supernova remnants, the leftovers from stellar explosions further cemented the link between pulsars and NSs, with famous examples like the Crab pulsar and Vela pulsar (Staelin and Reifenstein III, 1968; Large et al., 1968).

1.2 The Birth of Neutron Stars: Progenitors and Formation Processes

Stars originate within relatively dense conglomerates of cold interstellar gas and dust known as 'molecular clouds', which are prevalent in most galaxies, including our own Milky Way. These frigid regions create favorable conditions for molecular formation, such as H_2 and CO_2, leading to the clumping of gas into higher densities. As density reaches a critical threshold, gravitational instability takes hold, causing denser portions of the cloud to collapse under their own gravitational forces. Consequently, protostars form in these dense regions, gradually heating up and ultimately evolving into the progenitor stars over a span of time (Woosley et al., 2002).

One crucial obstacle to the formation of stars is angular momentum. When a gas cloud collapses to give rise to stars, it can convert its angular momentum into rotational motion, both individually and as components of larger assemblies, orbiting a common center of mass. These stars acquire energy through interactions with other stars within dense stellar environments, making it more challenging for individual stars to form. This phenomenon accounts for the prevalence of binary or triple star systems among the majority of stars in galaxies. These newly formed stars attain a state of hydrostatic equilibrium, wherein the gravitational force is counterbalanced by thermal gas pressure originating from hydrogen nuclear fusion. They also tend to maintain thermal equilibrium, as their energy output remains constant, matching the energy loss at their surfaces. When these stars eventually deplete their nuclear fuel, they are no longer capable of withstanding gravitational collapse. However, if the star possesses sufficient mass, the contracting core can become hot enough to initiate helium burning, leading to the production of various heavier elements.

As atomic nuclei become heavier, the star can extract progressively less energy from nuclear fusion. This process comes to a near standstill with the production of iron. In essence, fusion reactions up to iron can serve as a source of heat, generating pressure to support the star against its own gravitational pull. Conversely, nuclear reactions that yield elements heavier than iron actually withdraw heat from the star. As a result, at this stage, the pressure diminishes, rendering the star unstable (Pons et al., 1999; Woosley et al., 2002). Subsequent events depend on the mass of these stars.

Stars similar in mass to our Sun, up to approximately 8 solar masses ($M_\odot$), shed their outer layers until the stellar core is exposed. This remnant, an Earth-sized star, is referred to as a white dwarf (WD). White dwarfs typically possess a mass of around 1 $M_\odot$, primarily composed of carbon and oxygen and maintain stability through electron degeneracy pressure that balances gravity.

Stars with masses between approximately 9 $M_\odot$ and 25 $M_\odot$ experience a supernova explosion and evolve into a NS, an extremely dense objects about 10 kilometers in radius, supported by the pressure of a degenerate neutron gas. Stars exceeding about 25 $M_\odot$, directly form black holes (BH) (Heger et al., 2003; Vahdat et al., 2019).

NSs are extremely compact, with their minimum radius being approximately 1.5 times their Schwarzschild radius:

$$R_{\text{min}} = 1.5 \times \left(\frac{2GM}{c^2} \right) \tag{1.1}$$

where G is the gravitational constant, c is the speed of light, and M is the NS mass. A maximum radius can be obtained assuming that the rotating star is stable against centrifugal forces:

$$R_{\text{max}} = \sqrt{\frac{1.57P}{c}} \tag{1.2}$$

Where P is the spin period. The NS is able to contrast the gravitational collapse thanks to the pressure granted by degenerate neutrons. The stellar structure of the NS can be described by an equation of state, establishing a connection between the density and pressure of the star. This relationship can then be translated into an observationally-related mass-radius equation of state.

Given the extreme physical properties of NSs, testing the equation of state in Earth laboratories is prohibitive. Indeed, for a typical NS with a mass of 1.4 $M_\odot$ and a radius of about 10 km, the *average* density is $\sim 6.7 \times 10^{14}$ g cm^{-3} , about the same order of magnitude of the density of an atomic nucleus. Therefore NSs have long been recognized as excellent testing grounds for investigating cold and dense baryonic matter. These extreme conditions offer a unique opportunity to explore thermodynamic realms not easily achievable in conventional terrestrial laboratories (Fortin et al., 2020). Observational constraints can be derived by simultaneously measuring the radii and masses of NSs (Lattimer and Prakash, 2001; Guillot and Rutledge, 2014), along with statistics on maximum NS masses or radius estimates (Raaijmakers et al., 2021), and observations from NS merger events (Raaijmakers et al., 2021).

A description of the different kinds of equation of state proposed so far by theoretical physicists is beyond the goals of this thesis. Briefly, in most of them a NS with a very short interval of radii (10 km - 13 km) is expected to be found in the mass range from 0.5 $M_\odot$ to 2.5 $M_\odot$ (Lyne and Graham-Smith, 2012). The bulk of the NS population is known to have a mass around 1.4 $M_\odot$ (see review by Özel and Freire 2016, and references therein), corresponding to radii in the interval of 10.5 km and 11.5 km.

The maximum mass allowed to a system supported by the pressure of degenerate electrons is well known as the Chandrasekhar limit. The same value for a system supported by the pressure of degenerate neutrons is however unknown, as a consequence of our ignorance about the equation of state. A possible value, the so-

called 'Tolman-Oppenheimer-Volkov' limit, is of about 2.5 $M_\odot$ (Lattimer and Prakash, 2001). However, none of the NSs with a precise mass measurement reach such a value, although few candidates are known (Freire et al., 2008; Demorest et al., 2010) close to 2.2 $M_\odot$, especially among the class of recycled NSs.

1.3 Thermal evolution of Neutron stars

A NS is composed of distinct regions: the outer crust, inner crust, outer core, and inner core (Fig 1.1). The outer crust, forming the star's envelope, comprises ions and electrons. At high densities, the electrons act as a relativistic gas, while ions create a solid or liquid Coulomb system (Yakovlev, 2021). As density increases, electron capture processes favor neutron-rich nuclei. Neutron dripping from nuclei starts at the outer crust's base, forming a neutron gas. The inner crust consists of electrons, free neutrons, and neutron-rich atomic nuclei. As density increases, the fraction of free neutrons rises, and nuclei may lose their spherical shape (see review by Lattimer and Prakash 2001 and reference therein).

At approximately half the nuclear saturation density, where the binding energy per nucleon peaks, nuclei disappear, transforming matter into a homogeneous mixture of neutrons, protons, and electrons. The inner crust is approximately one kilometer thick. Below the inner crust lies the stellar core, with matter composed of degenerate neutrons, protons, electrons, and possibly muons. These constituents interact through nuclear forces, forming a strongly

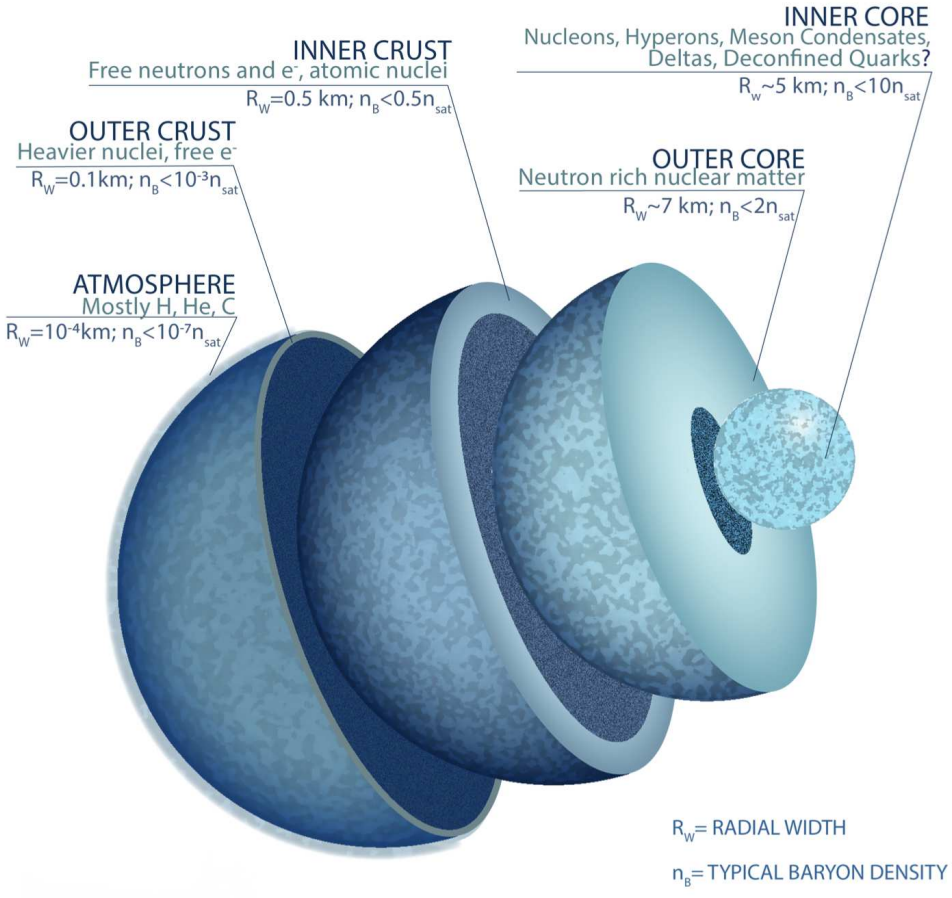

Figure 1.1: Structure and composition of a NS. Credit Muse collaboration.

non-ideal liquid. The exact composition of inner core is unknown and may even include hyperons or quark matter.

Exploring the thermal evolution of NSs presents a significant motivation, as it offers the potential to gain insights into the composition of matter within the stellar interior when observations are systematically compared with theoretical frameworks. Tsuruta and Cameron (1966) laid the groundwork for the theory of NS cooling, and subsequent studies in the 1990s by Pethick (1992) and Yakovlev et al. (1999) further developed this field.

Detecting thermal radiation proves to be a challenging task due to various factors. Young pulsars, with ages around t $\sim$ 1000 yrs, exhibit strong non-thermal emission caused by active processes in

their magnetospheres (see Section 1.4 and Fig. 1.3), obscuring the thermal radiation.

Older pulsars ($t \gtrsim 10^6$) may have hot polar spots, complicating the extraction of thermal radiation from the rest of the colder stellar surface (Pavlov et al., 2002; Yakovlev, 2021). Consequently, reliable detection of thermal radiation has been achieved only from a few isolated middle-aged NSs ($t \sim 10^4$-10^6 yrs), where it constitutes a substantial portion of the total radiation.

Figure 1.2 displays the average surface temperatures of a few well-studied young and middle-aged NSs (obtained from BB fits of X-ray spectra), including Pulsar B1055, the primary focus of the second project in this study.

The thermal component is typically described by either a blackbody spectrum or a NS atmosphere model (see Section 2.4.2 for more details), with or without a magnetic field (Pavlov et al., 1995; Heinke et al., 2006; Mori and Ho, 2007; Ho et al., 2008).

To align observations with theory, the NS's effective temperatures $T_{\rm s}$ and ages t are crucial. Due to the compact nature of NSs, the effects of general relativity must be considered (Shapiro et al., 1983). For a NS with the mass M, radius R and effective temperature of $T_{\rm s}$, the thermal photon luminosity in the local reference frame of the star is defined as follows:

$$L_\gamma = 4\pi R^2 \sigma T_{\rm s}^4 \tag{1.3}$$

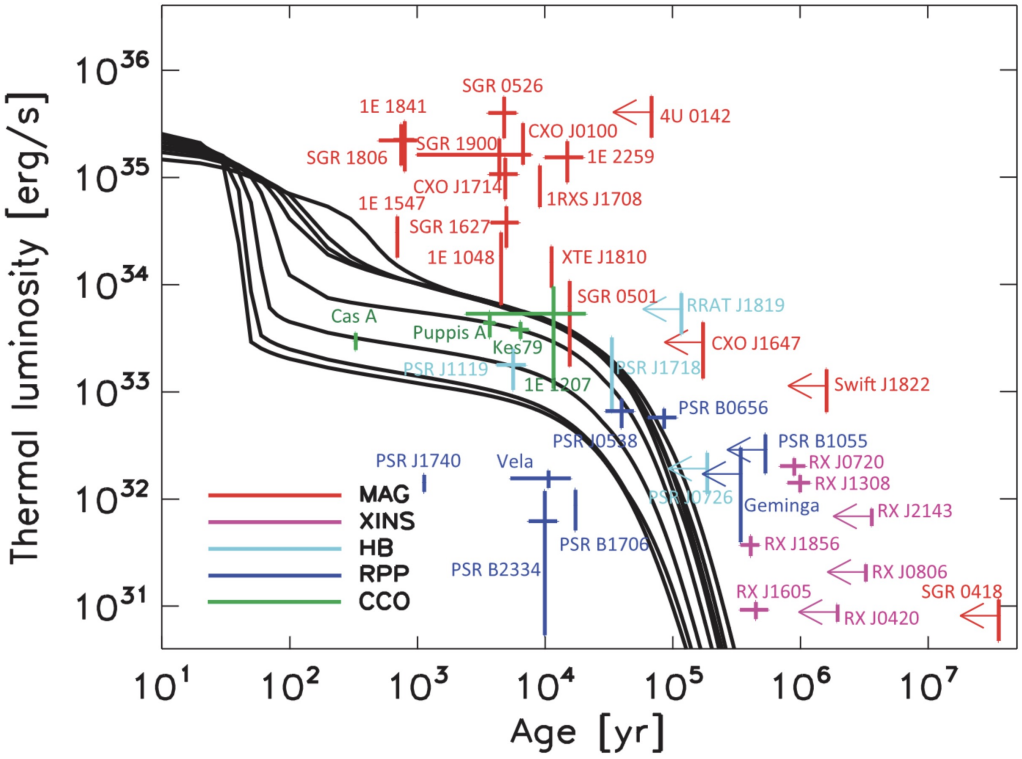

Figure 1.2: Thermal luminosity and upper limits for numerous isolated NSs for B=0 NS models. The theoretical cooling curve of a NS with light-element envelopes and varying masses (from 1.1 up to 1.76 $M_\odot$) is illustrated by the solid black lines. From Viganò et al. (2013).

where σ is the Stefan-Boltzmann constant. The apparent (redshifted) effective temperature $T_{\rm s}^{\infty}$ and luminosity L_γ^{∞} as observed by a distant observer are then given by:

$$T_{\rm s}^{\infty} = T_{\rm s}\sqrt{1 - r_g/R} \quad \text{and} \quad L_\gamma^{\infty} = L_\gamma\,(1 - r_g/R), \tag{1.4}$$

where $r_g = 2GM/c^2 \approx 2.95\,M/M_\odot$ km is the Schwarzschild radius.

Cooling theories allow one to compute cooling curves (Such as the one in figure 1.2), $T_{\rm s}^{\infty}(t)$ (or $L_\gamma^{\infty}(t)$), for comparison with observations. Based on the current models and observational constrains, three distinct cooling stages can be identified:

- **Thermal relaxation state**: Between the first 10-100 years, both the core and the crust of the NS cool separately. The surface temperature reflects the crust's thermal state (Sales et al., 2020). the crust and the core remain thermally decoupled until the cooling wave of the core reaches the crust, manifesting as a steep decay in the surface temperature (around 100 years, as shown in Fig 1.2).

- **Neutrino-dominated stage**: From about 100 to 10^5 years, neutrino emission from the stellar interior, mainly the core, dominates the cooling process. Meanwhile, the surface temperature adjusts to the internal temperature. The temperature decay rate from the thermal relaxation stage to the neutrino cooling stage depends on the type of neutrino emission, such as direct Urca, modified Urca, or nucleon-nucleon (NN) bremsstrahlung (Yakovlev and Pethick, 2004; Lin et al., 2020).

- **Photon cooling stage**: After about 10^5 years, neutrino cooling significantly decreases, and the star cools via photon emission from the surface. The evolution of the internal temperature is influenced by radiation from the stellar surface, making it sensitive to properties of the outer star regions.

1.4 Pulsar Magnetosphere

In a rudimentary approximation, we can model a pulsar as a sphere with perfect electrical conductivity, which possesses a magnetic dipole moment oriented along its rotational axis. As it spins with

an angular frequency Ω, the magnetic field B, which is constant throughout the sphere, induces an electric field $E+(v\times B)$ (Deutsch, 1955).

The pioneering work by Goldreich and Julian (1969) marked a significant advancement in our understanding of pulsar magnetospheres. They revealed that a rotating NS cannot exist in a vacuum due to its intense magnetic fields, which generate substantial electric fields at the stellar surface. These fields, exceeding gravitational forces, are capable of extracting charges from the NS, thereby forming a co-rotating magnetosphere. This magnetosphere extends to the light-cylinder radius (R_{LC}):

$$R_{\rm LC} = \frac{c}{\Omega} \sim 5 \times 10^9 \ P \ {\rm cm} \tag{1.5}$$

where c is the speed of light and P is the star's spin period. In the force-free magnetosphere, the alignment with the star's rotation is characterized by the condition:

$$E + \frac{(\Omega \times r)}{c} \times B = 0 \tag{1.6}$$

The charge density in the magnetosphere, defined by Goldreich and Julian (1969), is expressed as:

$$\rho_{\rm GJ} = -\frac{1}{4\pi} \nabla \cdot \left(\frac{1}{\alpha} (\Omega_0 - \omega) \times B \right) \tag{1.7}$$

where α represents the conductivity of the plasma within the magnetosphere, Ω_0 is the angular velocity of the corotating plasma in the magnetosphere and ω is the angular velocity of a particular charged particle within the magnetosphere.

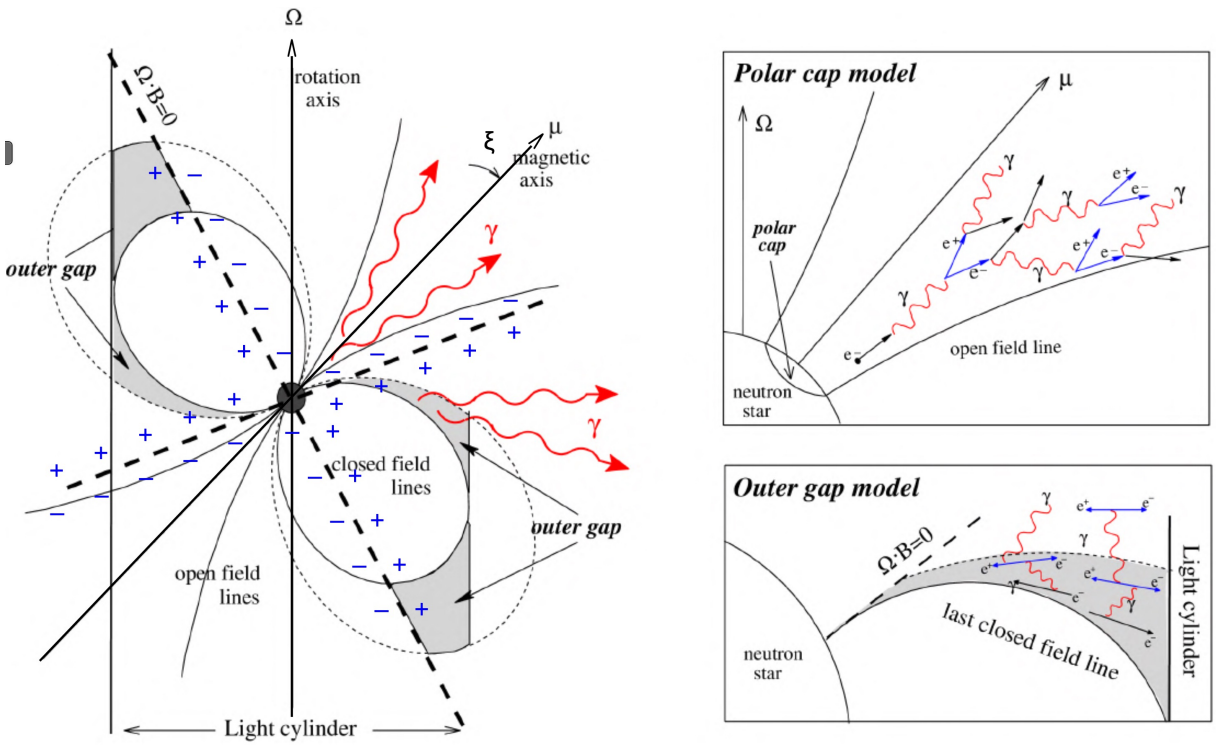

Figure 1.3: Left: A schematic of the pulsar magnetosphere, illustrating the light cylinder and the null charge surface where $\Omega \cdot B = 0$, leading to charge separation. The diagram also shows the misalignment between the pulsar's spin axis and its magnetic axis, indicated by ξ (same as α in the rest of the thesis). Right: Illustration of two particle acceleration mechanisms in pulsars. The polar cap model (above) shows particles being accelerated above the magnetic polar caps, while the outer gap model (below) demonstrates radiation production in the outer magnetosphere, between the null charge surface and the light cylinder, along the last closed magnetic field line. From Lopez et al. (2009).

Considering the magnetosphere's influence, the energy losses then can be approximated as:

$$E = \frac{B_p^2 R_{\rm NS}^4 \Omega^4}{4c^3}(1 + \sin^2 \xi) \tag{1.8}$$

where B_P and $R_{\rm NS}$ denote the magnetic field strength of the star at the pole and its radius, respectively. The term $\sin^2 \xi$ accounts for the angle between the magnetic axis of the NS and the rotation axis of the magnetosphere.

The pulsar magnetosphere's structure and behavior can be further understood through the polar cap and outer gap models. The

polar cap model focuses on particle acceleration above the magnetic poles along open magnetic field lines, leading to high-energy emissions through a cascade process (Fig. 1.3).

The radius of the polar cap ($R_{\rm PC}$) containing these open field lines is given by the formula:

$$R_{\rm PC} \approx R_{\rm NS} \sin\theta_{\rm PC} \approx R_{\rm NS}\sqrt{\frac{\Omega R_{\rm NS}}{c}} = (2\pi R_{\rm NS}^3/cP)^{1/2} \tag{1.9}$$

where $\theta_{\rm PC}$ is the polar cap angle determined by

$$\theta_{\rm PC} = \sin^{-1}\left(\sqrt{\frac{\Omega R}{c}}\right) \tag{1.10}$$

The outer gap model, on the other hand, is significant for γ-ray emissions. Unlike polar cap models, where strong magnetic fields enable one-photon pair production to have a significant impact on the cascade, the outer gap region has weaker magnetic fields (Fig. 1.3). In this scenario, curvature photons primarily engage in photon-photon pair production with thermal X-rays from the polar caps, such as seen in pulsars like Vela or Geminga. Additionally, non-thermal X-rays produced by the outer gap cascade, as observed in the Crab, also play a role in these interactions.

Additionally, the magnetosphere comprises two main regions: the closed field line region and the open field line region. The closed field line region, or the 'dead-zone', contains charges confined within the field lines, leading to no emissions. In contrast, the open field line region allows for plasma escape, necessitating a continuous

replenishment of magnetospheric charges. This dynamic is crucial for sustaining the pulsar's emissions.

Electrons moving along the open magnetic field lines are accelerated to relativistic velocities, producing high-energy photons primarily via curvature radiation. These photons subsequently initiate electron-positron pair production, leading to a cascade that contributes significantly to the pulsar's multiwavelength emission profile.

Beyond the polar cap and outer gap models, a deeper comprehension of the pulsar magnetosphere now relies on understanding current sheets and the Y-point models (Contopoulos et al., 2014).

The equatorial current sheet, a narrow yet intense layer of charged particles, divides the regions of closed and open magnetic field lines. Within this sheet, opposite currents induce magnetic reconnection, causing field lines to break and release energy, potentially boosting particles to high energies (Contopoulos, 2016).

The Y-point, located where the closed and open field lines meet the current sheet, acts as a crucial junction. Its position and properties heavily influence particle trajectories and acceleration regions (Fig. 1.4). Recent research suggests the Y-point might not be a single point but rather a "Y-region" with complex topology, further highlighting the dynamic nature of the magnetosphere (Contopoulos et al., 2024).

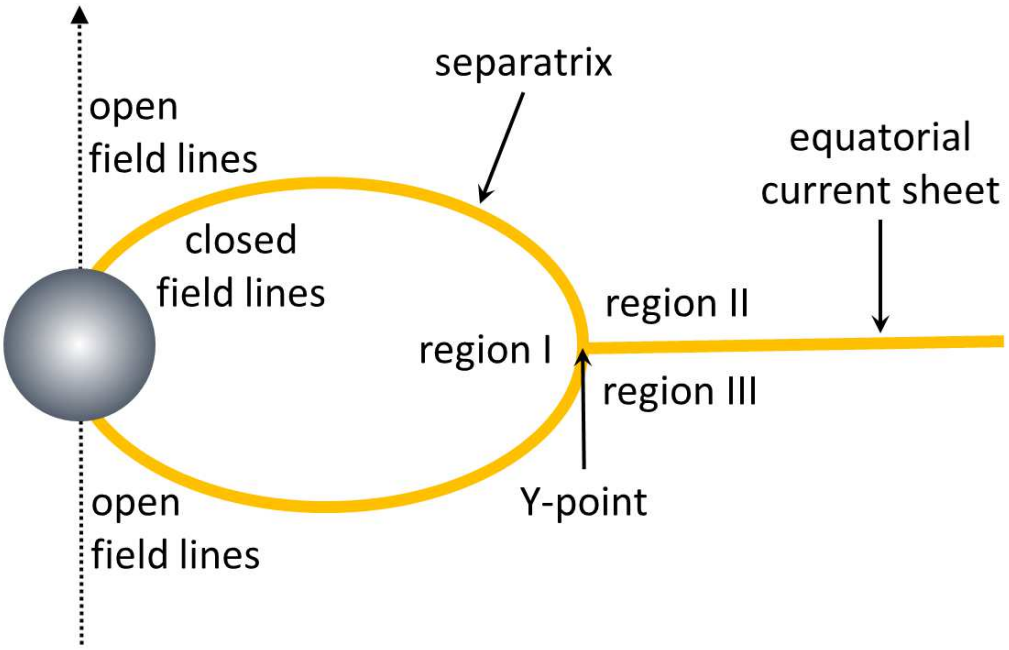

Figure 1.4: Diagram illustrating open and closed magnetic field regions I, II, and III within the magnetosphere. These regions are divided by electric current sheets and converge at the Y-point junction. From Contopoulos et al. (2024).

1.5 The spin of pulsars and spin-down evolution

The key observational parameters of pulsars include the rotational frequency (ν) and its corresponding period (P=1/ν). In some cases, the spin-down or the the spin-up rate $\dot{\nu}$, represented by the first time derivative of ν, and the derivation of the second frequency derivative, $\ddot{\nu}$are also measured. For a pulsar with angular velocity $\Omega = \frac{2\pi}{P}$, decreasing at a rate of $\dot{\Omega} = -2\pi P^{-2}\dot{P}$, the loss of rotational energy, $\dot{E}_{\rm rot}$, occurs at a rate of:

$$\dot{E}_{\rm rot} = I\Omega\dot{\Omega} = -\frac{4\pi^2 I\dot{P}}{P^3} \tag{1.11}$$

where I is the stellar moment of inertia. For practical calculations, I is approximated to be around 10^{45} g cm^2 based on canonical NS parameters. The provided equation pertains to the specific

scenario of a braking index set at a value of 3, and it is expressed as follows:

$$n = \frac{\nu\ddot{\nu}}{(\dot{\nu})^2} \tag{1.12}$$

The braking index can be determined by obtaining the second derivative of the spin frequency. The spin-down luminosity ($L_{\rm sd}$), which represents the rate of rotational kinetic energy loss, is directly related to the rate of loss given by $\dot{E}_{\rm rot}$ and can be estimated as:

$$L_{\rm sd} \approx 3.95 \times 10^{31} I_{45} \dot{P}_{15} P^{-3} \,{\rm erg\,s^{-1}} \tag{1.13}$$

To estimate the pulsar's magnetic field, one can equate the rotational energy loss rate to that of a classical magnetic dipole radiation of a rotating magnetic dipole. This estimate, introduced by Ostriker and Gunn (Ostriker and Gunn, 1969), involves the magnetic field strength at the pole of the NS ($B_{\rm p}$) and is given by:

$$B_p \approx 3.2 \times 10^{19} \sqrt{P\dot{P}}\,{\rm G} \tag{1.14}$$

For I_{45} = 1 and $R_{\rm NS}$ = 10 km, assuming an orthogonal rotator (alignment angle $\alpha = 90°$).

Furthermore the characteristic age τ_c of a pulsar, inferred from its rotational period and rate of deceleration (Manchester and Lyne, 1977) is defined as:

$$\tau_c = \frac{P}{(n-1)\dot{P}}\left[1 - \left(\frac{P_0}{P}\right)^{n-1}\right] \approx \frac{P}{(n-1)\dot{P}} \tag{1.15}$$

This age is derived under the assumption that the initial rotation period P_0 of the NS was much shorter than its current period P. For pulsars where the magnetic dipole braking is the dominant mechanism, n is typically taken as 3, simplifying the equation to:

$$\tau_c = \frac{P}{2\dot{P}} \tag{1.16}$$

This approximation provides a convenient method to estimate the pulsar's age. However, in a plasma-filled magnetosphere which is a more realistic scenario, the braking index, assumes a modified definition that accounts for plasma effects on the pulsar's spin-down. Unlike in vacuum, the presence of plasma introduces additional torques that alter the spin-down rate (Philippov et al., 2014) and provide a revised expression for the braking index (Ekşi et al., 2016) which indicates a range for n such that $3 < n < 3.25$, and does not diverge as it would in a vacuum for small alignment angles. Another illustration of variability in n occurs, for instance, when n takes the value of 5 in the context of magnetic quadrupole-driven radiation. Furthermore, recent measurements indicate significant deviations of n from 3 (Lower et al., 2021).

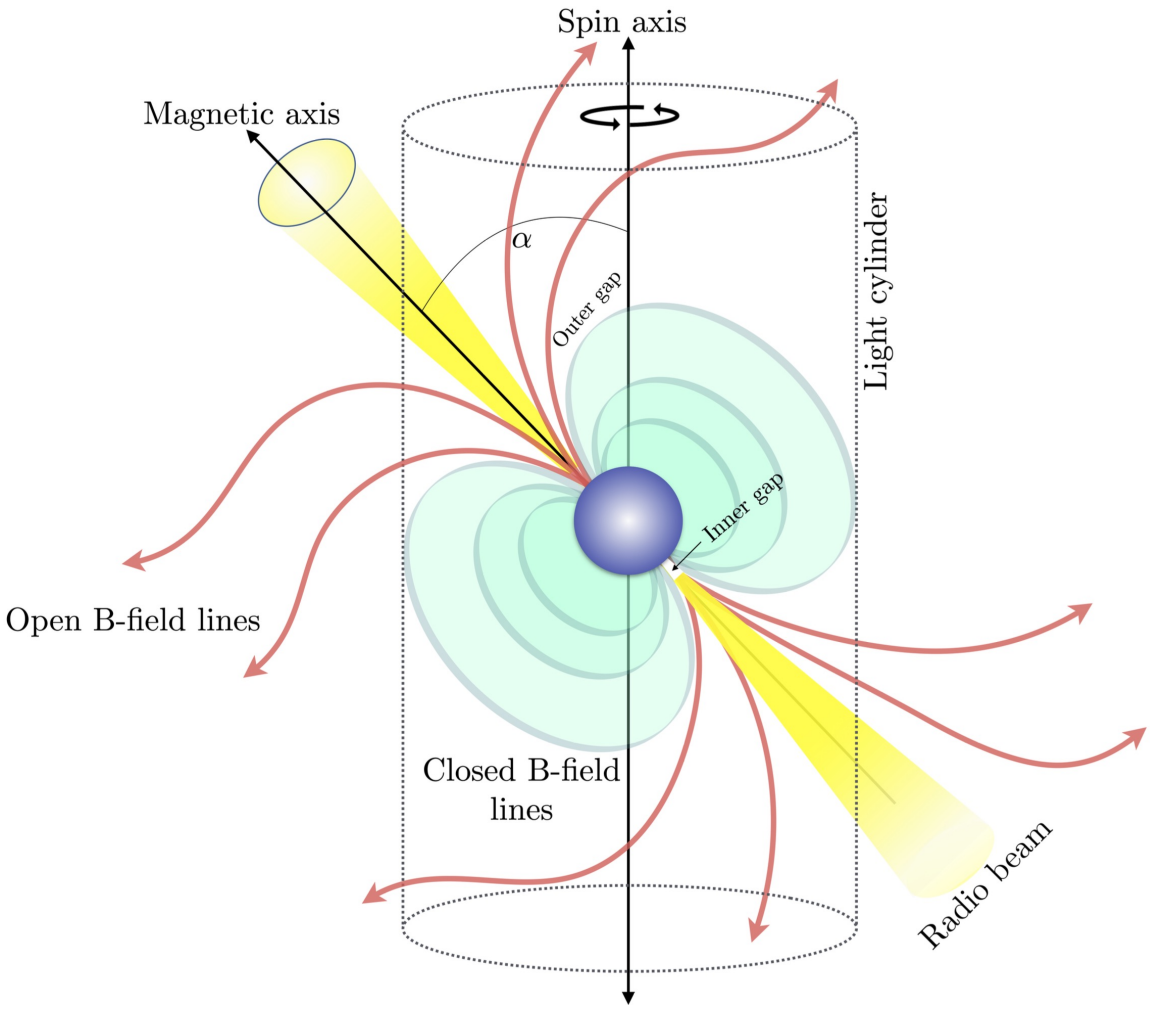

Figure 1.5: Schematic view of the traditional magnetic dipole model of a pulsar. Electrons and positrons generated in the 'gap' regions of the magnetosphere follow open magnetic field lines, emitting coherent radio radiation, as well as X-rays and γ-rays in high-energy pulsars. When the magnetic axis is misaligned with the rotation axis, a lighthouse effect occurs, producing observable radiation pulses as the NS rotates. The light cylinder is a critical feature, separating closed magnetic field lines inside from open ones outside, with curvature radiation being the main emission mechanism. The alignment angle, α, quantifies the spin axis's orientation relative to the magnetic axis. Figure adapted from Lorimer and Kramer (2005)

.

1.6 Classification of neutron stars

NSs exhibit remarkable diversity in their characteristics and behaviors. They can be categorized into distinct classes based on their primary sources of energy, spin-down luminosity, magnetic field strength, and age. Based on their main source of energy, they are crudely classified into three subclasses:

1. **Accretion-powered neutron stars**:

   Accretion-powered pulsars are found in binary systems where a companion star transfers material onto the spinning NS. The gravitational potential energy released during this accretion process predominantly fuels the observed emission. This category encompasses systems where the NS is actively accreting matter, resulting in high-energy radiation (Bildsten et al., 1997).

2. **Rotation-powered neutron stars**:

   Rotation-powered pulsars, in contrast, derive their energy from the loss of rotational kinetic energy. This loss powers the creation and acceleration of electron-positron (e+e-) pairs within the strong magnetic field surrounding the NS. The resulting electromagnetic radiation constitutes the primary source of emission for these pulsars (Michel, 1991).

3. **Magnetically-powered neutron stars**:

   Magnetically-powered pulsars harness the energy from their extremely high magnetic fields. This energy is released through

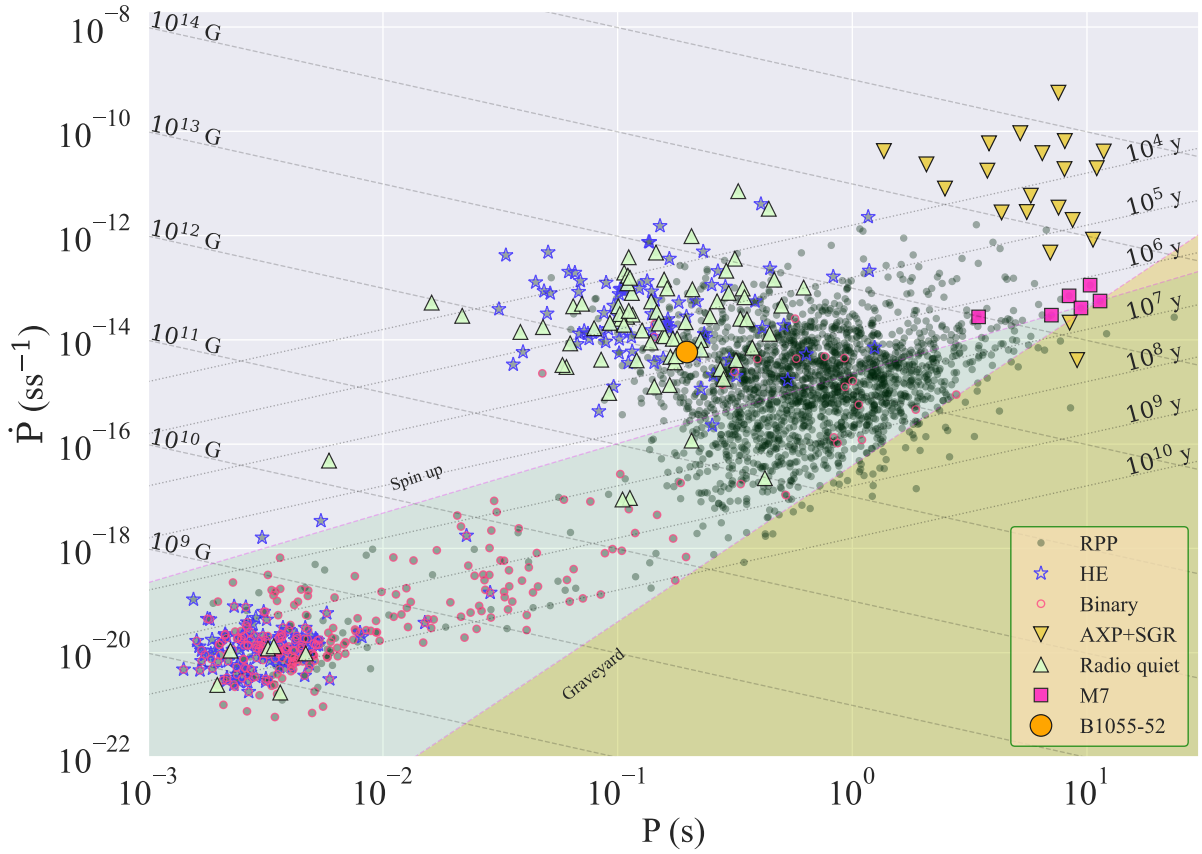

Figure 1.6: The period-period derivative diagram for different types of pulsars is based on data from the ATNF pulsar catalog (v1.70, Manchester et al. 2005). The lines of constant age and magnetic field (assuming magnetic dipole braking) are displayed with dashed lines. RPPs are Rotation-Powered Pulsars. HE refers to pulsars with pulsed emission from radio to infrared or higher energies. Binaries are pulsars with one or more stellar companion(s). AXP+SGR refers to Anomalous X-ray Pulsars and Soft γ-ray Repeaters with detected pulsations. M7 refers to the Magnificent Seven, isolated NS with pulsed thermal X-ray emission but no detectable radio emission. PSR B1055-52 is displayed with orange circle.

processes like crustal heating and cracking, leading to powerful bursts and 'quiescent' emission in the hard X-ray band and hot surfaces (thermal emission) (Duncan and Thompson, 1992).

Furthermore, the P-Pdot diagram, where observational parameters such as P, $\dot{P}$, τ and B_s are plotted for all pulsars, serves as a common representation of the NS population. As of the most recent data available, there are 3389 known pulsars (Fig 1.6, Manch-

ester et al. 2005). Some of the important subclasses of pulsars in the P-Pdot diagram are listed below

A. Ordinary Pulsars:

Ordinary pulsars constitute the central region of the P-Pdot diagram. These pulsars typically exhibit spin periods ranging from 100 milliseconds to a few seconds, with characteristic ages spanning from approximately 1,000 years to 1 billion years. Young and energetic ordinary pulsars often emit radio and gamma-ray radiation and are frequently associated with supernova remnants. As they age, their spin gradually decreases, causing them to move towards the lower-right end of the P-Pdot diagram. Eventually, their spin-down luminosity becomes insufficient to sustain radiative mechanisms, resulting in the cessation of emission. The 'death line' approximates the region in the P-Pdot diagram where this phenomenon occurs, although it is highly uncertain and influenced by various factors beyond just dipole magnetic emissions (Bhattacharya and van den Heuvel, 1991). Moreover, the recent discovery of ultralong period pulsars, such as PSR J0901-4046 (P = 75.9 s, Caleb et al. 2022), and GLEAM-X J162759.5-523504.3 (P = 1091 s, Hurley-Walker et al. 2022), which are likely positioned below the death line, necessitates a reassessment of the death line.

B. Millisecond Pulsars:

Millisecond pulsars, or MSPs, constitute a distinct subtype of pulsars that emerges from binary systems. These pulsars un-

dergo a process known as recycling, where angular momentum is transferred to them as they accrete matter from an expanding companion star (Alpar et al., 1982). This rejuvenation allows MSPs to achieve extremely short spin periods, often around a few milliseconds. Notably, MSPs tend to exhibit lower magnetic fields compared to ordinary pulsars. Their remarkable rotational stability makes them natural precision clocks and invaluable for timing experiments. Furthermore, pulsar Timing Arrays (PTAs) serve a crucial role in gravitational wave (GW) experiments, specifically targeting the nanohertz frequency range (Foster III, 1990). These arrays involve the meticulous monitoring of numerous millisecond pulsars, characterized by their rapid spin periods. Through the detection of dynamic perturbations in space-time, PTAs become unique instruments capable of identifying GW radiation (Manchester et al., 2013). Unlike other methods such as resonant bars and laser interferometers, pulsar timing extends the observational window to previously inaccessible frequencies which allows for the exploration of phenomena like supermassive black hole binaries and stochastic backgrounds from cosmic strings (Verbiest et al., 2022).

C. Magnetars:

Magnetars, positioned in the upper-right region of the P-Pdot diagram, represent a unique class of NSs. This category includes Anomalous X-ray pulsars (AXPs) and Soft Gamma Repeaters (SGRs), believed to be different manifestations of the

same object. Magnetars possess comparatively long rotation periods (1-12 seconds) and exhibit large spin-down rates due to their extraordinarily high magnetic fields, reaching up to 10^{15} Gauss (Camilo et al., 2006). While they are typically radio-quiet, they emit strong pulsed X-rays. Magnetars are known for their dramatic X-ray outbursts, often accompanied by large glitches (sudden and brief increases or decrease in their ν). These outbursts are attributed to the untwirling of twisted magnetic field lines, and some evidence suggests a possible connection between magnetars and high-magnetic-field young radio pulsars (Mereghetti et al., 2015). The origin of the magnetic field in magnetars remains a subject of intense scientific inquiry, with two prevailing hypotheses offering insights into their formation. One hypothesis, known as the fossil field scenario, suggests that the powerful magnetic fields of magnetars originate during the collapse of massive progenitors. In this model, magnetic flux conservation during the collapse results in the generation of a nominally large magnetic field in the NS, enough to account for the observed strength in magnetars. In this scenario, magnetars naturally emerge from the high-field tail of the progenitor distribution, with population synthesis calculations supporting its viability (Mereghetti et al., 2015).

Alternatively, the protoneutron star dynamo hypothesis proposes that the magnetic field amplification occurs within the protoneutron star through dynamo action driven by convec-

tion or differential rotation. Over a span of approximately ten seconds, these processes lead to a significant increase in magnetic field strength. Interestingly, shear-driven dynamos operating efficiently under stratification provide a mechanism for enhanced magnetic field growth. Both dynamo scenarios involve intricate processes such as Tayler and magnetorotational instabilities, as well as r-mode instabilities, contributing to the amplification of the magnetic field (Mereghetti et al., 2015; Kaspi and Beloborodov, 2017).

D. **Rotating Radio Transients (RRATs)**: Rotating radio transients (RRATs) represent a group of pulsars that exhibit sporadic emission. Discovered in 2006, RRATs display characteristics consistent with rotating NSs. Their radio pulses exhibit wide variability in intensity, ranging from less than one pulse to hundreds per hour. The nature of RRATs within the pulsar population remains uncertain. They may represent pulsars with highly variable emission, where only the strongest pulses are detectable from Earth (Keane and McLaughlin, 2011). Alternatively, some RRATs may be linked to magnetars, given their variable emission characteristics and their position in the P-Pdot diagram, indicating high magnetic fields. Further investigation is required to disentangle the complexity of RRATs, which may consist of multiple populations, including highly variable pulsars and highly magnetized NSs with intrinsically variable emission (Bhattacharyya et al., 2018).

E. Magnificent Seven: A subgroup of isolated NSs, collectively known as the 'Magnificent Seven', has garnered attention due to their distinctive properties. These NSs were discovered through ROSAT and are characterized by their thermal X-ray spectra, as well as broad X-ray absorption features that likely correspond to proton- or ion-cyclotron lines, indicating extraordinarily strong magnetic fields on the order of 10^{15} Gauss. The Magnificent Seven exhibit similar properties, including pulse emissions with periods ranging from 3.4 to 11.4 seconds (Haberl, 2007). Recently, there has also been a report regarding significant hard X-ray emissions from two of the Magnificent seven, RX J1856.6-3754 and RX J0420.0-5022 (Dessert et al., 2020).

F. Central compact objects (CCO's): Central Compact Objects (CCOs) represent a distinct subset of NSs localized in close proximity to the central regions of supernova remnants (SNRs). Their characteristic soft X-ray spectra, comprising two blackbody components with temperatures ranging from ≈ 0.1 to 0.4 keV, deviate from the expectations for young NSs, displaying elevated luminosities in the range of $10^{32} - 10^{34}$ erg s^{-1} (Viganò and Pons, 2012). Distinctive features of CCOs include the absence of typical magnetar-like activity, except for the intriguing case of 1E 161348−5055. Long-term observational campaigns have provided insight into three CCOs: RX J0822−4300 in SNR Puppis A with a spin period (P) of 112 ms, CXOU J185238.6+004020 in Kes 79 with P of 105 ms, and 1E 1207.4−5209 in PKS 1209−51/52 with P of 424 ms. The inferred magnetic dipole fields (B_p) for

these CCOs fall within the range of $10^{10} - 10^{11}$ G, notably lower than the 10^{12} G dipole fields observed in young radio pulsars (Viganò and Pons, 2012; De Luca, 2017). These findings challenge conventional models of NS evolution and magnetic field amplification. Despite their NS classification, CCOs manifest unique characteristics. Unlike pulsars, CCOs do not exhibit non-thermal radio emission, and the conspicuous absence of a pulsar wind nebula raises questions about the underlying mechanisms governing these objects (De Luca, 2017).

1.7 Main Properties of pulsars across the electromagnetic spectrum

1.7.1 Radio

The primary method for detecting pulsars involves identifying highly regular radio pulses, a characteristic observed in approximately 95% of known pulsars. As outlined in the previous section, young pulsars subjected only to dipolar braking, undergo a spin-down process. This progression takes them toward a densely populated area in the P-Pdot space, commonly referred to as the 'pulsar island', depicted as a large central cluster in Figure 1.6. The typical pulsar is assumed to continue on its trajectory toward the pulsar graveyard, a region characterized by longer periods and a lack of pulsations due to an extensive voltage gap.

Pulsars exhibit significant variability in their radio profiles from pulse to pulse. However, by aggregating numerous pulses (ranging from hundreds to a few thousand), a highly stable integrated

pulse profile emerges at a specific frequency, unique to each pulsar. These profiles usually span 2-5% of a complete rotation, although some range from as little as 0.2% to as much as 100%.

The radio spectrum typically adheres to a power-law distribution with a spectral index ranging from -4 to 0.

Pulsar broadband emissions are instrumental in investigating the interstellar medium (ISM). The dispersion of radio waves by free electrons in the ISM causes a frequency-dependent delay (Δt) in signal arrival times (with the speed of v_1 and v_2) which can be estimated as follows:

$$\Delta t = \frac{e^2}{2\pi\, c\, m_e}[\frac{1}{v_1^2} - \frac{1}{v_2^2}] \int_0^d n_e\, dl \tag{1.17}$$

Where e, m_e and n_e are the charge of an electron, mass of an electron and electron number density respectively. The first part is a constant typically referred as the dispersion constant:

$$\mathcal{D} = \frac{e^2}{2\pi\, c\, m_e} \sim 4.1488056 \times 10^3\, \mathrm{MHz^2 pc^{-1} cm^3 s} \tag{1.18}$$

The integral term involves integrating the product of electron number density, n_e, and the infinitesimal length (dl) along the entire path (d) of the radio waves through the ISM referred as dispersion measure DM:

$$\mathcal{DM} = \int_0^d n_e\, dl \tag{1.19}$$

Conversely, knowing this average electron content can help estimate pulsar distances. Comprehensive models of the Milky Way's electron content often rely on pulsar DM and distance data. The most common models are: Taylor and Cordes (1993) ,Cordes and Lazio (2002) and Yao et al. (2017).

The accuracy of these models improves continually with new pulsar discoveries and more precise DM and parallax-based measurements. The typical uncertainty in DM-based pulsar distance estimations, around 20%, primarily arises from the model's assumptions about electron distribution rather than from the measurement errors in DM. This is because DM calculations are based on well-determined values of Δt.

1.7.2 X-rays

The accretion process, with a typical accretion rate of $\dot{M} \approx 10^{-7} - 10^{-10} M_{\odot}$, yr^{-1} onto a NS is one of the most energetic and efficient X-ray processes in the universe. It plays a crucial role in the emission of X-rays in X-ray binaries, transforming gravitational energy into kinetic energy. Similarly, magnetars experience unpredictable outbursts, during which the constant X-ray luminosity undergoes a substantial surge, reaching an output of approximately $\sim 10^{35} - 10^{36}$ erg s^{-1} (and up to $\sim 10^{41} - 10^{42}$ erg s^{-1} for ultraluminous X–ray sources). While Vahdat et al. (2022) includes a few millisecond X-ray pulsars with companions, none of the sources of our interest show hints of on-going accretion or bursts and the primary focus of this thesis is the X-ray analysis of rotation-powered pul-

sars. Although chapters 3 and 4 will delve deeper into the X-ray phenomenology of these pulsars, below i provide a brief overview of the characteristics of X-ray spectral components of isolated NSs:

I) Thermal Emission:

Thermal emission arises from the bulk surface of cooling NSs, as well as NS atmosphere, typically with surface temperatures around 10^6 K ($\sim$ 100 eV). The thermal spectrum, typically described with a BB, may exhibit low-amplitude intensity variations across the optical to soft X-ray spectrum, correlating with the spin period (Pavlov et al., 1994). Soft thermal X-ray emission is also produced from relativistic particles bombarding the polar caps of NSs and heating them, originating from the pulsar magnetosphere (Zavlin et al., 1996).

II) Non-Thermal Pulsed Emission:

This emission results from charged relativistic particles accelerated within the pulsar magnetosphere. Typically a power-law distribution in the X-ray broad band spectra can be described with a slope of $\Gamma \sim$ 1-3 and is observable across the optical to γ-ray bands (Michel, 1991; Pavlov et al., 1995). The X-ray luminosity of rotation-powered pulsars, has an efficiency (the correlation between the spin down-energy loss and X-ray luminosity) estimated between 10^{-5} and 10^{-3} (see also Kargaltsev et al. 2012; Vahdat et al. 2022).

III) Non-Thermal Non-Pulsed Emission:

Originating from pulsar-driven synchrotron nebulae, this emission involves charged particles emitting synchrotron radiation along magnetic field lines (Michel, 1991; Zhang and Jiang, 2006). It spans from radio to hard X-ray energies and includes emissions from the interaction between the pulsar wind and the interstellar medium, as well as shock waves from the interaction between the pulsar wind and companion star outflows (Zhang and Jiang, 2006).

.

While the simplified models presented above provide a framework for understanding X-ray emissions of NS, the reality is often more complex. As NSs evolve over time, their emissions and temperature distribution undergo notable changes. Count statistics poses challenges in distinguishing between thermal and nonthermal emissions, adding a layer of ambiguity to our observations. For instance, in middle-aged pulsars, a third, thermal-like spectral component is sometimes observed. This can be approximated by a blackbody with kT $\sim 0.1 - 0.3$ keV and a radius smaller than the star's actual radius. The prominence of these spectral components varies with pulsar age: young energetic pulsars ($\tau \lesssim 5$ kyr) mainly exhibit nonthermal magnetospheric emission; middle-aged pulsars (10 kyr $\lesssim \tau \lesssim$ 50 kyr) display all three components; while older ms pulsars ($\tau \gtrsim 1$ Myr) contain both polar cap thermal and nonthermal components.

The interstellar medium (ISM) plays a crucial role in shaping the observed X-ray spectrum by absorbing and scattering X-ray pho-

tons along the line of sight with varying cross sections. This absorption primarily occurs through interactions with electrons bound in the ISM, a process dominated by the photoelectric effect. While the absorption is more pronounced for lower X-ray energies, it also affects higher energies to a lesser extent. The degree of absorption, simplified as N_H, depends on the phases of the ISM, with warm and cold phases exhibiting different behaviors (Wilms et al., 2000). He et al. (2013) demonstrated a correlation between DM and NH:

$$N_H = 0.30 + 0.13 \times \mathrm{DM} \tag{1.20}$$

Here, N_H is measured in units of 10^{20} cm^{-2} and DM in pc cm^{-3}. The correlation between DM and N_H serves as a valuable tool in pulsar observations, enabling the estimation of one quantity based on the other.

1.7.3 γ-RAYS

γ-ray pulsars, based on their unique properties, are categorized into two groups. The first group includes ms pulsars, characterized by their relatively weaker magnetic fields ($\sim 10^9$ G) and shorter rotational periods. These pulsars have gained speed due to the process of accretion. In contrast, the second group consists of younger pulsars, notable for their stronger magnetic fields ($\sim 10^{12}$ G) and longer rotation periods (typically around 100 milliseconds). Pioneering discoveries in the 1970s, such as the Crab and Vela pulsars identified by SAS-2 and COS-B respectively, marked the early

recognition of γ-ray sources. The 1990s saw further advancements with the Compton γ-ray Observatory, which increased the known number of high-energy pulsars to ten, including Geminga, a pulsar not observable in radio frequencies (Cerutti 2019, and references therein) .

Pulsars emit gamma rays, which account for about 1-10% of their total energy output (Abdo et al., 2010). This indicates their significant efficiency as particle accelerators. The emission pattern of γ-ray pulsars is distinctive. They display a hard power-law spectrum at lower energy levels and an exponential cutoff at higher energies, typically around a few GeV (Caraveo, 2014). These pulsars generally show two distinct peaks in their light curves, and sometimes, emissions are observed between these peaks, known as 'bridge emission'. Interestingly, these γ-ray peaks often do not align with radio pulses, implying that different regions of the pulsar's magnetosphere are involved in generating these emissions (Hirotani, 2013).

1.7.4 Infrared, optical and ultraviolet bands

In the optical band, pulsars, demonstrate comparably fainter emission. Initially identified by Nather et al. (1969) and Cocke et al. (1973), the Crab pulsar remains the most luminous example in this wavelength (Fig. 1.7). Recent technological advancements have facilitated the discovery of optical counterparts for several pulsars. Optical light curves, when analyzed alongside those from X-ray and γ-ray bands, are crucial in mapping the emission regions within

the pulsar's surface and magnetosphere. Moreover, optical spectroscopy aids in constraining cooling models for pulsars, especially for those older than 1M years, by capturing a major portion of their thermal emission. Additionally, the high angular resolution of optical observations is valuable for determining pulsar distances through measurements of proper motion and parallax (see review by Mignani 2011).

In the ultraviolet (UV) and near-infrared (IR) spectra, young pulsars exhibit non-thermal emissions, likely of synchrotron origin, emanating from their magnetospheres. These emissions generally follow a power-law spectrum. However, variances in spectral indices across these bands have been observed in some cases, such as the Crab pulsar, but not in others like the Vela pulsar. Middle-aged pulsars display a secondary emission component in the optical/UV range, which is typically associated with thermal emissions from the NS's surface, characterized by a Rayleigh–Jeans spectrum. It's noteworthy that even within the proximity of wavelengths in the optical and UV bands, pulsar light curves exhibit notable differences. For instance, the Crab pulsar's light curve features, like the width and separation of its main peaks, vary between the optical and UV bands. This variation is potentially linked to the differences in the power-law slope between these two bands (Percival et al., 1993; Shibanov et al., 2003; Bühler and Blandford, 2014).

X-ray observations of pulsars are more sensitive to thermal emissions from their hotter polar regions and less so to emissions from cooler surface areas. These lower-temperature emissions are more detectable in the optical-UV range. For MSPs, measuring surface

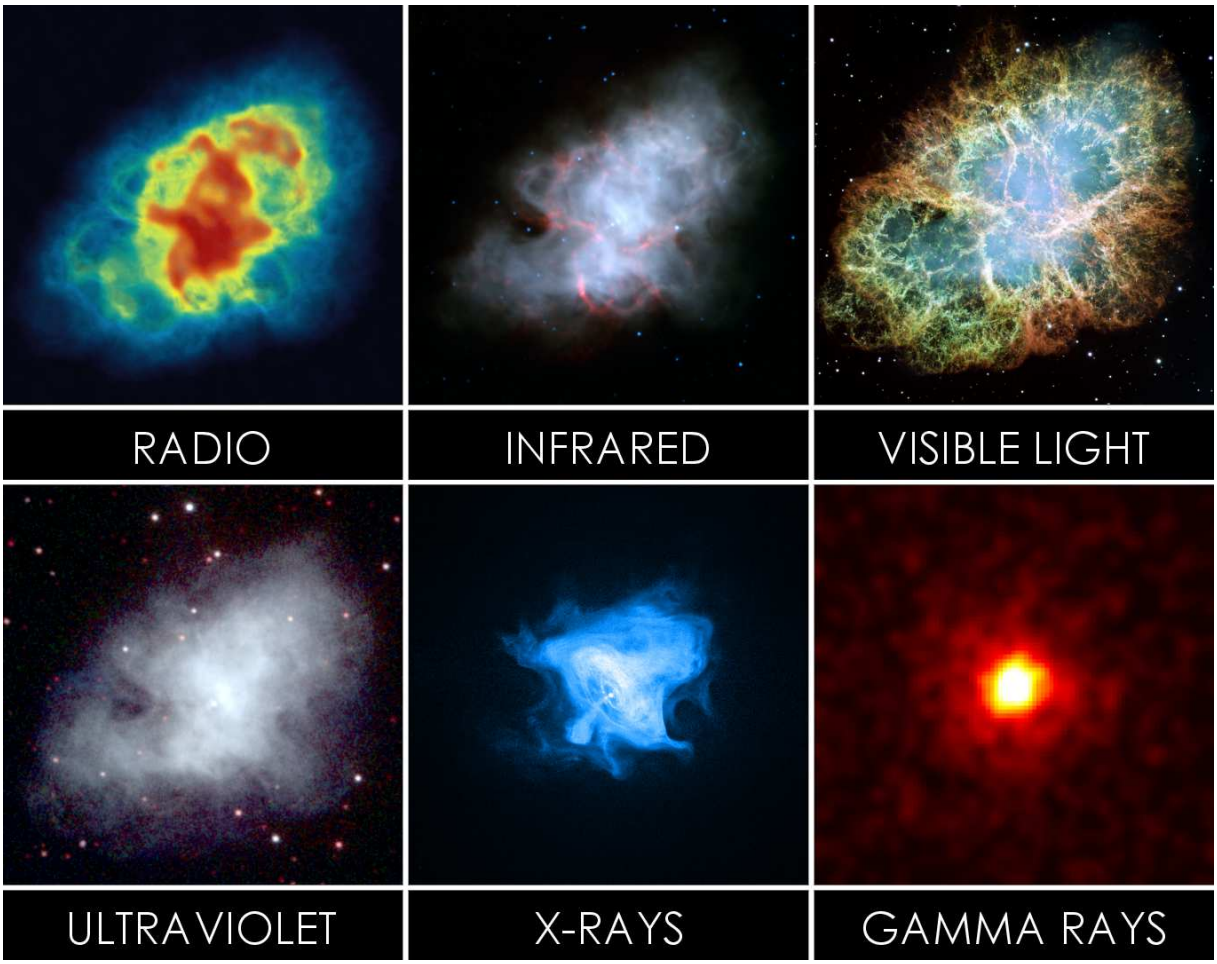

Figure 1.7: Crab Nebula in Multiple Wavelengths. The pulsar lies at the centre of the Nebula. This image combines data from six different telescopes: the Very Large Array (radio) ; Spitzer Space Telescope (infrared) ; Hubble Space Telescope (visible); Swift Observatory (ultraviolet); Chandra X-ray Observatory (X-ray) and Fermi (Gamma rays).

temperatures is vital for constraining NS heating models and understanding internal physical processes. The optical-UV range also plays a key role in detecting the magnetospheric component of these emissions, thus shedding light on the properties of relativistic particles in MSP magnetospheres (Mignani, 2011).

2 Instrumentation, spectral and timing analysis

> ***Robert:*** *When I came to you with those calculations, we thought we might start a chain reaction that might destroy the entire world.*
> ***Albert:*** *I remember it well. What of it?*
> ***Robert:*** *I believe we did.*
>
> **— Oppenheimer (2023)**

2.1 XMM-Newton and EPIC instrument

iming for excellence in X-ray astronomy, the *XMM-Newton* observatory, launched by the European Space Agency in December 1999, stands as a premier astronomical facility. Originally designed for a decade of service, the satellite continues to function beyond its initial lifespan, contributing significantly to our understanding of the high-energy universe including NS and BH phenomena.

XMM-Newton operates in a highly elliptical 48-hour orbit, which distances it from the Earth's radiation belts for extended periods,

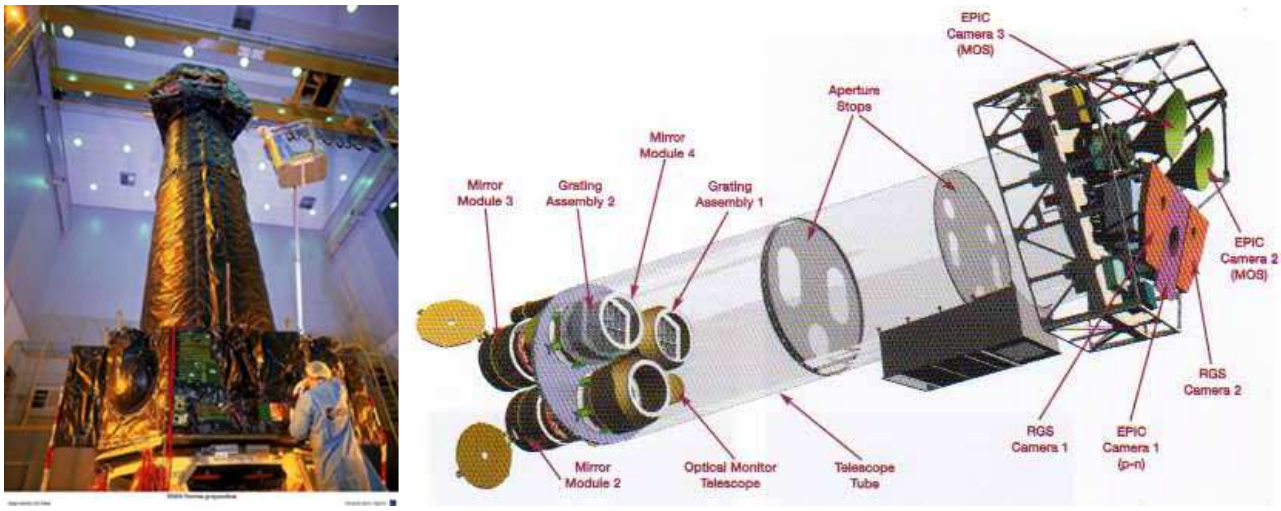

Figure 2.1: Right: Schematic of the *XMM-Newton* spacecraft with EPIC PN, EPIC MOS1/2 and RGS cameras, optical monitor and the grating assemblies. Left: *XMM-Newton* during the integration phase at ESA. (Credit: ESA)

allowing for uninterrupted observations. The orbit stretches from 7,000 to 114,000 kilometers above Earth, positioning it to capture phenomena unobscured by the radiation belts for about 40 hours per orbit.

The observatory's main instrument, the European Photon Imaging Camera (EPIC), is crucial for capturing high-resolution X-ray images in $0-15.0$ keV. It consists of three X-ray charge-coupled device (CCD) cameras: two MOS (Metal Oxide Semiconductor) arrays (Turner et al., 2001) and one pn CCD array (Strüder et al., 2001). The EPIC is known for its ability to conduct sensitive imaging observations over a $30'$ field of view, with a spectral resolution $(E/\Delta E)$ ranging approximately from 20 to 50 and an angular resolution of $6''$ Full Width at Half Maximum (FWHM). The pn CCDs, back-illuminated to enhance soft energy response, have a pixel size of about $150\ \mu m^2$, facilitating detailed spatial and temporal mapping of X-ray sources (refer to Table 2.1 for additional information).

The EPIC is equipped with versatile readout modes to adapt to various observational requirements. For the EPIC-pn camera (with a pixel size of $\sim 4.1''$), the operational modes include:

- The **Full Frame** mode captures a complete image of 376 x 384 pixels at intervals of approximately 73.5 ms.
- The **Extended Full Frame** mode provides a 376 x 384-pixel image at longer intervals of about 199.1 ms.
- The **Partial Window** mode is available, utilizing either the larger window mode or the smaller one, each reading out half the CCD array to yield a 198 x 384-pixel image roughly every 47.7 ms. In the '**Small Window**' mode, a segment of the CCD produces a 63 x 64-pixel image at a rate of 5.7 ms.
- In the **Timing** mode, spatial data is preserved solely along the column (RAWX) axis delivering data every 0.03 milliseconds for high temporal resolution. For the pn detector, the entire width of CCD4 is utilized.
- For exceptionally bright sources, **Burst** mode is utilized, offering extremely high temporal resolution with images captured every 7 microseconds.

EPIC's MOS cameras (with a pixel size of $\sim 1.1''$) operate in similar readout modes:

- The Full Frame mode here reads out the entire field of view, resulting in a 600 x 600-pixel image every 2.6 seconds.

- The **Partial Window** mode limits the readout to a 300 x 300 pixel area of the CCD, yielding images every 0.9 seconds or opting for the '**Small Window**' mode for a 100 x 100-pixel image every 0.3 seconds.

- In **Timing** mode one-dimensional array is read at high speed, producing data every 1.75 ms. For the MOS detector, only approximately 100 columns around the boresight are active. Given the perpendicular orientation of the two MOS cameras, this mode allows for effective coverage of the sky without overlaps.

The EPIC instrument is not immune to the ageing process. Subtle degradations, primarily caused by radiation exposure, affect its performance, particularly at lower energies. While its core range (0.15-15 keV) remains robust, quantum efficiency below 0.3 keV has gradually declined, increasing background noise and making faint signal detection challenging. Calibration uncertainties also rise at these energies.

In addition to EPIC, the Reflection Grating Spectrometer (RGS) comprises assemblies of reflection gratings that capture about 58% of the light deflected by the telescope mirrors. The RGS extends *XMM-Newton*'s capabilities into high-resolution spectroscopy, with a resolving power ranging from 150 to 800, across an energy spectrum from 0.35 to 2.5 keV. It provides detailed spectral data crucial for understanding the physical conditions of cosmic phenomena.

The Optical/UV Monitor Telescope (OM) enables concurrent observations in the optical and UV spectra, with a 17′ field of view. The OM's micro-channel plate intensified CCD camera offers high-

Table 2.1: Key characteristics of XMM-Newton as outlined in the XMM-Newton Users' Handbook

Instruments	**EPIC-MOS**	**EPIC-PN**	**RGS**	**OM**
Bandpass	0.15–12 keV	0.15–15 keV	0.35–2.5 keV(1)	180–600 nm
Field of view (FOV)	$\sim 30'$	$\sim 30'$	$\sim 5'$	17'
PSF (FWHM/HEW)	5"/14"	6"/15"	N/A	1"4–2"0
Pixel size	40 μm ($\sim 1.1''$)	150 μm ($\sim 4.1''$)	81 μm (9×10^{-3} Å)	$0.4765''$
Timing resolution(2)	1.5 ms	0.03 ms	0.6 s	0.5 s
Spectral resolution(3)	~ 70 eV	~ 80 eV	0.04/0.025 Å(4)	350(5)
Effective area (cm^2 @ 1 keV)	922	1227	185	N/A

(1) Extended energy range
(2) In full frame mode
(3) @ 6 keV
(4) 1st/2nd order
(5) Between the 3000–5000 Å .

resolution imagery and photometry in visible and ultraviolet light, thus broadening the scope of multiwavelength studies possible with *XMM-Newton*. Unfortunately, the OM is not sensitive enough for our pulsar study.

2.2 Chandra X-ray Observatory and ACIS instrument

The Chandra X-ray Observatory, initially known as the Advanced X-ray Astrophysics Facility and later renamed in tribute to the distinguished physicist Subrahmanyan Chandrasekhar, was deployed by NASA into space on July 23, 1999. This observatory is in a high-eccentricity orbit that grants it approximately 55 hours per orbit for uninterrupted observations, a feature that enables the detailed study of cosmic phenomena.

Chandra is equipped with a set of four precision-formed mirrors arranged in a nested Wolter-I configuration. These mirrors

Table 2.2: The core specifications of Chandra's scientific instruments sourced directly from the Chandra proposers' observatory guide.

	ACIS-S	**ACIS-I**	**HRC-S**	**HRC-I**
Field of view (FOV)	$8.3' \times 50.6'$	$16.9' \times 16.9'$	$6' \times 9'$	$30' \times 30'$
Bandpass (keV)	0.2–10.0		0.08–10.0	
PSF (FWHM)[a]	$\sim 0.492''$		$\sim 0.4''$	
Pixel size	$\sim 0.492''$		$\sim 0.132''$	
Time resolution	TE[b]: 0.2–10.0 s; CC: ~ 2.85 ms		16 μs	
Spectral resolution (E/ΔE)	FI[c]: 20–50; BI: 9–35		~ 1	
Effective area (cm^2 @ 1 keV)	FI: 340; BI: 340		N/A	227

[a] PSF: point spread function; FWHM: full width half maximum
[b] TE: Timed Exposure Mode; CC: Continuous Clocking Mode
[c] FI: front-illuminated CCDs; BI: back-illuminated CCDs

are designed to capture X-rays with minimal diffraction, focusing them onto two primary detectors: the Advanced CCD Imaging Spectrometer (ACIS, Garmire et al. 2003), and the High-Resolution Camera (HRC, Murray et al. 2000). These detectors work in conjunction with two sets of transmission gratings, the High-Energy Transmission Grating (HETG) and the Low-Energy Transmission Grating (LETG), to provide high-resolution spectroscopy.

ACIS is an intricate instrument consisting of charge-coupled device (CCD) chips that yield high-resolution images and spectra across an energy range of 0.2 to 10.0 keV. It contains an array of ten 1024 x 1024 pixel CCDs, with certain chips optimized for imaging (ACIS-I) and others for spectroscopic readout (ACIS-S). The ACIS-S is particularly noted for its placement at the focal point, optimizing its sensitivity to softer X-ray bands, while the ACIS-I offers a broader field of view.

The current quantum efficiency (QE) of the low-energy ACIS is lower compared to its initial launch. This decline is believed to be

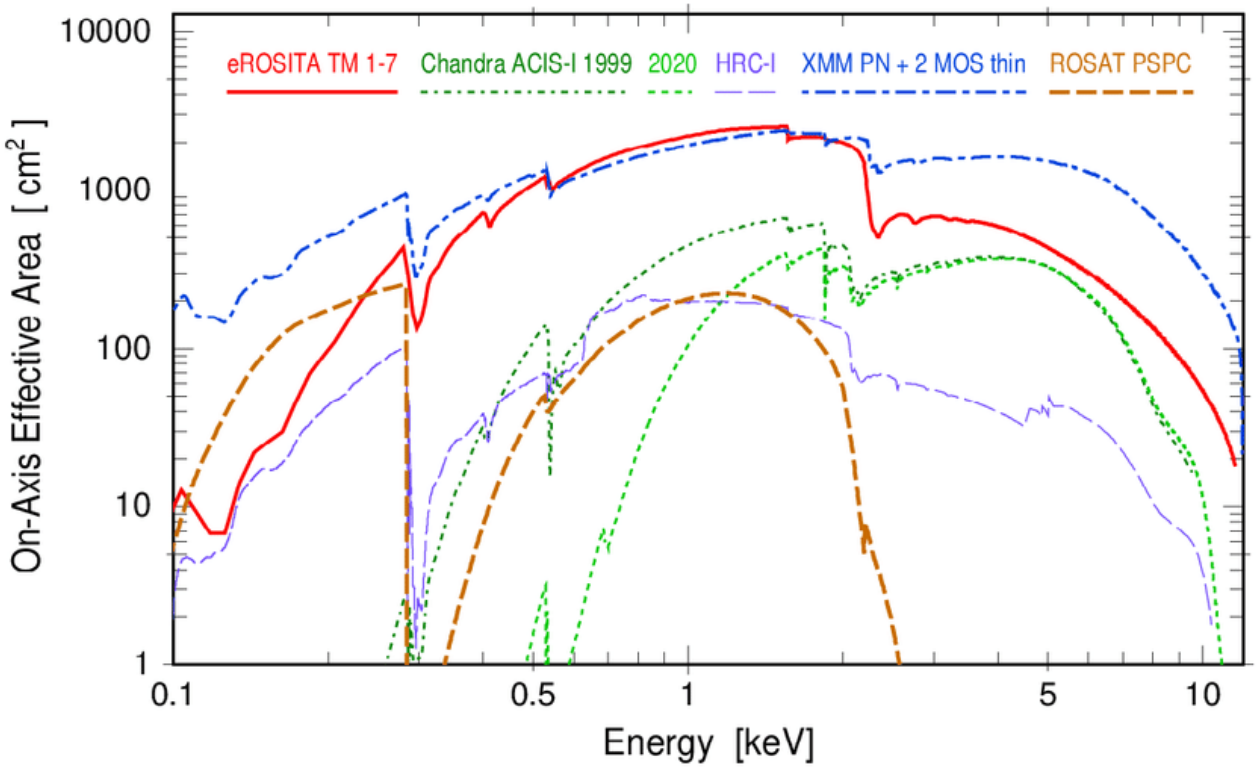

Figure 2.2: On-axis effective areas as a function of energy for eROSITA (in red), Chandra ACIS-I (dark green for 1999, and light green for 2020), Chandra HRC-I (in purple), *XMM-Newton* (in blue), and ROSAT (in brown). (Credit: ESA)

caused by the accumulation of certain materials on the ACIS detectors or optical blocking filters. As these contaminants deepen over time, the QE for low-energy detection decreases accordingly (Townsley et al., 2002). To address this issue, a correction for contamination is applied during the creation of ACIS response files.

The HRC, incorporating two cesium iodide-coated microchannel plate detectors, is prized for its superb spatial resolution, with the HRC-I designed for wide-field imaging and the HRC-S functioning as a readout for the LETG. The HRC-S also boasts the fastest timing resolution among Chandra's detectors, capable of capturing data with microsecond-scale precision.

2.3 X-ray Spectral analysis

X-ray spectra portray the variation of emitted energy as observed. By modeling this variation using either physical or phenomenological models, we can gain insight into the physical processes occurring in the observed sources that produce this emission. An X-ray spectrometer measures event counts C in each channel (I, unique to each telescope/instrument). The link between the observed spectrum $C(I)$ and the actual source spectrum $S(E)$ (where E is energy) can be expressed by:

$$C(I) = \int S(E)R(I,E)A(E)dE \tag{2.1}$$

In this equation, $A(E)$ represents the instrument's effective area, and $R(I,E)$ denotes the normalised instrumental response (indicating the likelihood of a photon with energy E being recorded in channel I. To fit data with physical models, the forward-folding technique is commonly used where a hypothetical model spectrum (like a power law or blackbody for the NS) is assumed, based on the physical characteristics of the source and convolved with the instrument's response (e.g., Ducci and Malacaria 2023 and references therein). This yields counts in the instrument's energy space, not the actual photon flux emitted by the source.

The modeled spectrum is then compared to the actual observed spectrum using a statistical method (e.g., Buchner and Boorman 2023 and references therein), adjusting the model parameters iteratively for the best fit, indicated by the lowest statistic value. If the best-fit model is not satisfactory, the initial model needs reeval-

uation. The presence of background noise and other physical constraints affecting the detector's response complicate spectral analysis, making direct inversion of the instrumental response impractical, hence the preference for forward-folding.

Spectral analysis must also consider background contributions, which could be cosmic X-ray background (CXB) or particle-induced, also known as 'non-X-ray background' (NXB). Events, which denote the detection of individual X-ray photons by the instrument's detector are considered valid if they meet specific criteria. Good Time Intervals (GTIs) are established by filtering observations to exclude high energy-background periods, resulting in cleaned event list specific to the instrument.

For imaging detectors such as EPIC-pn/MOS, signal-to-noise optimization is crucial. Assuming a point-spread function, software tools like `eregionanalyse` assist in determining the optimal centroid and size for source extraction regions (circle or ellipse).

Various software packages are designed to simplify X-ray spectral analysis. These tools handle instrumental responses, offer diverse spectral models, and provide statistical modeling, analysis and visualization capabilities.

One widely used software for spectral analysis is XSPEC (Arnaud, 1996). Primarily used for interactive tasks, it also supports scripting through interfaces in programming languages like Python and TCL. For the X-ray spectral analysis presented in Chapters 3 and 4 of this work, I utilized the Python interface of XSPEC (v12.12.0), known as PyXspec (v2.1.0).

2.4 The considered XSPEC X-ray spectral models

2.4.1 Blackbody

Blackbody radiation is the most simple thermal emission model. The spectral distribution (intensity at different wavelengths) of a black body's emission typically depends primarily on its temperature, rather than its material composition or shape. The black body model serves as an initial approximation, offering a foundational understanding of thermal emission. However, its simplicity may limit its ability to provide a comprehensive understanding of complex phenomena, such as those observed in NSs.

In NSs that are relatively young and exhibit temperatures in the order of approximately 10^7 Kelvin, the radiation predominantly falls within the X-ray region of the electromagnetic spectrum. The power intensity of emitted radiation can be mathematically represented by the equation:

$$I(E,T) = \frac{2E^3}{h^2c^2(\exp(\frac{E}{kT}) - 1)} \tag{2.2}$$

In this expression, h denotes Planck's constant. The majority of NS thermal spectra are modeled with a blackbody description due to its simplicity and minimal assumptions, despite the challenge it presents in constraining more complex models. For example, blackbody emission is independent of the magnetic field and assumes isotropic emission. The presence of a magnetized crust or atmosphere significantly alters the thermal emission's spectral profile (see section 2.4.2).

In XSPEC (and PyXspec), the Blackbody spectrum (toggled with `bbody` keyword) is described by the equation:

$$A(E) = \frac{K_1 \times 8.0525 E^2 dE}{(kT)^4 [\exp(\frac{E}{kT}) - 1]} \tag{2.3}$$

Where the spectral radiance, A(E), is directly proportional to the scaling factor ($K_1 = L_{39}/D_{10}^2$, where L_{39} and D_{10} is the source luminosity and distance) and square of the energy (E) and inversely proportional to the fourth power of the temperature (kT).

In my analysis in Chapter 3 and 4, I used a slight modified version of blackbody named `bbodyrad` defined as follows:

$$A(E) = \frac{K_2 \times 1.0344 \times 10^{-3} E^2 dE}{\exp(\frac{E}{kT}) - 1} \tag{2.4}$$

where the normalization K_2 (= R_{km}^2/D_{10}^2) is adjusted to correspond with the emitting surface's area.

2.4.2 NS Atmosphere

The widely held view is that NSs are surrounded by a thin atmospheric layer, with its thickness ranging from a few millimeters to few centimeters and its density lying between 0.1 to 10. g/cm^3 (see review by Potekhin 2014 and references therein). It's theorized that a hydrogen-rich atmosphere might form over a NS, though if the hydrogen is in sufficient quantity (due to accretion or fall back material) to create a thick atmosphere remains a matter of debate. In scenarios where less than 10^{16} g of hydrogen is present, it's plausible that a dense atmosphere might not develop. In scenarios where

hydrogen burn-off due to diffusion occurs or if thermonuclear reactions consume all accreted matter, a helium-dominated atmosphere could exist (e.g., Mori and Ho 2007).

Initial investigations into atmospheric spectra did not account for the ionization of heavier elements and assumed a spectral shape that was less rigid compared to a blackbody spectrum. This approach results in an underestimation of the star's temperature by a factor of 2-3 and an overestimation of its radius when fitting observed spectra (Bogdanov et al., 2006).

Numerous researchers have developed atmospheric models for NS, building on the seminal work by Shibanov et al. (1992) (see also Pavlov et al. 1994). These models, which are calculated under the assumption of a plane-parallel geometry, vary based on the chosen strength and distribution of the magnetic field, as well as the chemical composition and the ionization degree of the medium. Differences arise due to the impact of these factors on the binding energies of atoms, molecules, and other forms of bound matter, which in turn can significantly influence the abundances of such bound states, contributing to the opacity (Pavlov et al., 1995; Zavlin and Pavlov, 2002).

Recent models that account for partially ionized atmospheres have advanced our understanding, replacing earlier fully ionized models (Ho and Lai, 2003). Some of these models have been integrated into the XSPEC in three models, NSA, NSMAXG and NSATMOS.

The NSA model (Zavlin et al., 1996; Pavlov et al., 1995) which assumes a fully ionized hydrogen atmosphere, calculates X-ray spectra (ranging from 0.05 to 10.0 keV) emitted from a NS's hydrogen

atmosphere. This model offers three variations: one without magnetization (magnetic field strength $B < 10^8 - 10^9$ G) with a uniform temperature between $logT_{\text{eff}} = 5.0 - 7.0$ and two with magnetization, one with $B = 10^{12}$ G and another with $B = 10^{13}$ G, both having a temperature between $logT_{\text{eff}} = 5.5 - 6.8$. The models consider the NS atmosphere in both radiative and hydrostatic equilibrium, with negligible heat sources above the atmospheric layer.

The NSATMOS model also assuming a complete ionization performs interpolations on a set of NS atmospheric calculations provided by George Rybicki and Ramesh Narayan, producing a spectrum that characterizes an NS atmosphere. The grid of models spans a broad spectrum of gravitational forces and temperatures while including the effects of electron conduction and self-irradiation by photons around the star. This model works under the assumption that the influence of magnetic fields is minimal ($B < 10^9$ G), and it assumes an atmosphere composed exclusively of hydrogen (Heinke et al., 2006).

The NSMAXG model which assumes a partial ionization (Mori and Ho, 2007; Ho et al., 2008) computes spectra from NS atmospheres, generating a final spectrum reliant on several parameters (Table 3.2). The spectra, resulting from both fully ionized, strongly magnetized hydrogen or mid-Z element plasma, are derived from the recent equations of state and opacity values, and are calculated by solving the radiative transfer equations for two polarization modes in a magnetized medium. The models are in equilibrium, both radiatively and hydrostatically. They are sensitive to the

effective surface temperature $logT_{\text{eff}}$, the magnetic field's strength B and orientation θ_B. When θ_B is set to zero, α aligns with θ_k, simplifying the calculation since opacities become dependent solely on α and the radiation's propagation geometry relies on θ_k. This holds true particularly for emissions from smaller areas like the magnetic polar caps because these regions have negligible magnetic variation.

It's important to note that all these models are specifically for phase-averaged spectra. However, common issues with such fits include potential underestimation of NS radii due to assumptions about solid surfaces and the spectral models used for them.

2.4.3 Power-law

The nonthermal part of NS spectrum (in the absence of PWN) emanates from relativistic particles that are accelerated by the pulsar's intense magnetic field, which rotate in unison with the star as detailed in section 1.7.2.

In XSPEC (and PyXspec), the spectral flux density, A(E), for a power law (toggled with powerlaw `or power`) is quantified as:

$$A(E) = KE^{-\alpha} \tag{2.5}$$

where α symbolizes the dimensionless photon power law index, and K signifies the normalization constant in units of $(10^{-6}$ photons /keV/cm^2/s at 1 keV).

When discussing NSs, it's crucial to consider the relativistic effects that are significant in the presence of intense gravitational fields. There are few relativistic phenomena to account for in any model of these objects. Initially, there's the gravitational redshift, where the photon's energy as detected is less than what it would be in the NS's own frame of reference. Additionally, the curvature caused by gravity allows for the visibility of over half the star's surface from a distant point.

With higher spin rates, NS emission models must also integrate the effects of beaming and kinematic Doppler-shift. Regarding the gravitational redshift, photons of energy E emitted from the surface of a NS with radius R will be observed with an energy E_∞ by a distant observer. This relationship is expressed as:

$$E_\infty = E\sqrt{1 - \frac{r_g}{R}} \tag{2.6}$$

where r_g, the gravitational radius, is given by:

$$r_g = \frac{2GM}{c^2} \tag{2.7}$$

2.5 Timing Analysis and Epoch Folding

Pulsars at all wavelengths are observed through their characteristic periodic emission profiles, whose shape can vary from a very simple sinusoid to very complicated combinations of sharp and broad components. The method of timing analysis is key to investigating the temporal patterns in observational data. This fundamental technique is important in tracing the frequency variations

of pulsars, which in turn facilitates an understanding of the pulsar's physical properties.

The pulsed signal from a pulsar is often much weaker than the surrounding noise and DC component in the data. As a result, researchers use Fourier analysis to look for any repeating patterns in the signal. This method has led to the identification of more potential pulsar signals, many of which are interference from earthly sources or satellites.

Subsequently, our focus will center on X-ray pulse signals. For accurate pulse timing analysis and bypass Doppler delays induced by the motion of the observatory, the observational time series of the light curve (also referred as event times) has to be corrected to the frame of the solar system's barycenter.

The process of constructing a frequency timeline for pulsating NSs typically initiates upon identifying a suspected or known period, often through techniques like Epoch Folding (Leahy et al., 1983). Contrary to the assumption of periodic binning, which involves segmenting data into time intervals, Epoch Folding involves compressing and overlaying a light curve, which spans a time interval T_{obs}, based on the anticipated periodicity.

When examining a pulsed profile p_i, divided into $N_{\rm bin}$ uniform bins, the preferred statistical measure is the Epoch Folding chi-squared statistic, as indicated by Leahy et al. (1983); Leahy (1987):

$$\chi = \sum_{i=1}^{N_{\rm bin}} \left(\frac{p_i - \bar{p}}{\sigma_i} \right)^2 \tag{2.8}$$

Here, $\bar{p}$ symbolizes the mean profile, while σ_i is the standard deviation in each bin. Typically, the uncertainties σ_i are inferred from the statistical errors in the individual flux readings. Assuming these follow either a Poisson or normal distribution and that the central limit theorem is applicable, the phase-folded count readings p_i will conform to a normal distribution and σ_i is derived from the standard deviation of the X_j via error propagation:

In comparisons of pulse profiles at different periods, it is usual to assume identical σ_i, derived from the standard deviation of the flux measurement via error propagation:

$$\sigma_i \equiv \sigma = \mathrm{std}(X_j)\sqrt{\left(\frac{N_{\mathrm{samples}}}{N_{\mathrm{bin}}}\right)} \tag{2.9}$$

Provided the normal distribution assumption is valid, χ will follow a $\chi^2_{N_{\mathrm{bin}}-1}$ distribution when the time series contains only noise. This simplifies the process of assessing the likelihood of rejecting the null hypothesis.

2.5.1 Z^2_n and H Statistics

Buccheri et al. (1983) presented a now widely used alternative statistic in X- and γ-ray studies, denoted as Z^2_n. This statistic is particularly effective for detecting pulsed signals that can be approximated using a limited set of sinusoidal harmonics. The Z^2_n statistic is defined when observing N photons with a pulse phase of ϕ_i for each photon ($i = 1..N$), as shown below:

$$Z_n^2 = \frac{2}{N} \sum_{k=1}^{n} \left[\left(\sum_{j=1}^{N} \cos k\phi_j \right)^2 + \left(\sum_{j=1}^{N} \sin k\phi_j \right)^2 \right] \tag{2.10}$$

This equation quantifies the extent to which a series of n sinusoidal harmonics represents the distribution of pulse phases. For a single harmonic, the statistic Z_1^2 is also referred as the Rayleigh test (Mardia, 1975).

By analyzing different trial pulse periods and calculating Z_n^2 for each, one can identify periods that yield the highest statistic values, i.e., the strongest signal. The Z_n^2 statistic conforms to a χ_{2n}^2 distribution when analyzing noise powers, aiding in setting detection thresholds and calculating the probability of rejecting the null hypothesis based on a Z_n^2 value.

Moreover, one can utilize a single test to determine if a signal is best represented by a sum of harmonics and the optimal number of harmonics required. This is encapsulated in the H test (de Jager et al., 1989), essentially a comparison of various Z_n^2 values, normalized for direct comparison:

$$H = \max(\mathrm{Z_n^2} - 4\mathrm{n} + 4), , n = 1 - 20 \tag{2.11}$$

With the peak value typically indicated as n.

2.6 Decomposing Periodic Signals Using Fourier Series

In the preceding section, we discussed the technique of epoch folding as a method for examining the pulse profile properties of pulsars. Given the necessity of visualizing pulse profiles for analysis, epoch folding serves this purpose. However, this method introduces inherent uncertainties associated with the binning process. To mitigate these issues, the Fourier decomposition of periodic signals offers a more precise alternative. This method leverages Fourier harmonics to decompose nearly periodic signals, such as those from pulsars, into their constituent components. By analyzing these components, we can gain deeper insights into the signal's structure and behavior without the limitations imposed by binning. The following formulas, are detailed comprehensively in Hare et al. (2021). We include them here as they form the foundation of the pulse profile analysis conducted in Vahdat et al. (2024), which is based on Fourier decomposition.

A signal that is almost periodic $\mathcal{F}(\phi)$ (with a period that may change slowly), normalized so that $\int_0^1 \mathcal{F}(\phi), d\phi = 1$, can be expressed as a combination of Fourier harmonics:

$$\mathcal{F}(\phi) = 1+\sum_{k=1}^{K}(a_k \cos 2\pi k\phi+b_k \sin 2\pi k\phi) = 1+\sum_{k=1}^{K} s_k \cos 2\pi(k\phi-\psi_k) \tag{2.12}$$

where ϕ is the pulse phase defined as follows:

$$\phi = \phi(t) = \phi_0 + f(t - t_0) + \dot{f}(t - t_0)^2/2 + \dots \tag{2.13}$$

f and $\dot{f}$ are the frequency and frequency derivative, t_0 is the reference time. Furthermore:

$$a_k = s_k \cos 2\pi\psi_k \quad \text{and} \quad b_k = s_k \sin 2\pi\psi_k \tag{2.14}$$

are the Fourier coefficients for the k-th harmonic, defining the amplitude s_k, the power s_k^2, and the phase ψ_k of the harmonic:

$$s_k^2 = a_k^2 + b_k^2, \qquad \tan 2\pi\psi_k = b_k/a_k, . \tag{2.15}$$

If the frequency consists of a series of stochastic (for example, Poisson-distributed) discrete events (such as photon detections), numbered as $i = 1, 2, \ldots, N$, with event phases $\phi_i = \phi(t_i)$, then the expected values and variances of the Fourier coefficients are determined as follows:

$$\begin{aligned} a_k &= 2\langle \cos 2\pi k\phi \rangle = \frac{2}{N}\sum_{i=1}^{N} \cos 2\pi k\phi_i, \\ b_k &= 2\langle \sin 2\pi k\phi \rangle = \frac{2}{N}\sum_{i=1}^{N} \sin 2\pi k\phi_i. \end{aligned} \tag{2.16}$$

and

$$\sigma_{a_k}^2 = \frac{4}{N}\big(\langle \cos^2 2\pi k\phi \rangle \langle \cos 2\pi k\phi \rangle^2\big) = \frac{1}{N}\big(2 + a_{2k} - a_k^2\big), \tag{2.17}$$

$$\sigma_{b_k}^2 = \frac{4}{N}\big(\langle \sin^2 2\pi k\phi \rangle \langle \sin 2\pi k\phi \rangle^2\big) = \frac{1}{N}\big(2 - a_{2k} - b_k^2\big) \tag{2.18}$$

The profile normalization can be changed if needed. For instance, if we want the area under the pulse profile to be equal to the number of events, we can multiply $\mathcal{F}(\phi)$ by the bin-averaged count.

2.7 Pulsed Fraction of a pulsar

Having established the methodology of Fourier decomposition for analyzing pulsar light curves, we now turn our attention to the concept of pulsed fractions. This is a crucial aspect in understanding the variability and periodicity of pulsar signals, as it provides a quantitative measure of the signal's oscillatory component.

The pulsed fraction is conceptualized as the proportion of the light curve's pulsating part to its total area and is expressed as:

$$p_{\text{area}} = 1 - \mathcal{F}_{\text{min}} \,, \tag{2.19}$$

where $\mathcal{F}_{\text{min}}$ represents the lowest value of $\mathcal{F}(\phi)$. Another way to define pulsed fraction is:

$$p_{\text{amp}} = \frac{\mathcal{F}_{\text{max}} - \mathcal{F}_{\text{min}}}{\mathcal{F}_{\text{max}} + \mathcal{F}_{\text{min}}} \tag{2.20}$$

This is sometimes referred to as the 'peak-to-peak' or 'max-to-min' pulsed fraction.

Hare et al. (2021) prefer to term it 'modulation amplitude', hence denoted as p_{amp} in here and following chapters.

Both the area pulsed fraction and the modulation amplitude are susceptible to significant uncertainties, particularly due to the imprecise measurement of $\mathcal{F}_{\text{min}}$ (and to some extent $\mathcal{F}_{\text{max}}$), especially when $\mathcal{F}_{\text{min}}$ approaches zero. To prevent this issue, pulsations can

be characterized by the root mean square (rms) of the signal $\mathcal{F}(\phi)$, termed 'rms pulsed fraction' (though technically, it's not a pulsed fraction per se):

$$p_{\rm rms} = \left\{ \int_0^1 [\mathcal{F}(\phi) - 1]^2 d\phi \right\}^{1/2} = \left(\frac{1}{2} \sum_{k=1}^{K} s_n^2 \right)^{1/2} = \frac{\mathcal{S}_n}{\sqrt{2}} = \left(\frac{Z_n^2}{N} \right)^{1/2} \tag{2.21}$$

where s_k^2 and the Z_K^2 statistic are computed using the optimal signal frequency and frequency derivative (that is, $Z_K^2 = Z_{K,\rm max}^2$). Consequently, the signal rms can be easily calculated from Z_n^2 as shown in Equation (2.21). The calculation of $p_{\rm rms}$ doesn't rely on measuring $\mathcal{F}_{\rm min}$, making it more practical and less error-prone compared to $p_{\rm area}$ and $p_{\rm amp}$, especially when the number of harmonics is manageable.

The calculated pulsed fraction derived from the timing of events detected within the source aperture typically have a lower value compared to its intrinsic counterpart due to the inclusion of background signals. To adjust for this background interference, we compensate by multiplying the recorded pulsed fractions by the ratio N/N_s, where N represents the total count (source + background) within the source aperture, $N_s = N - N_b$ denotes the source count, and N_b signifies the background count adjusted for the area of the source aperture.

3 Summary of the original publications

> *The sky calls to us. If we do not destroy ourselves, we will one day venture to the stars. There was a time the stars seemed an impenetrable mystery. Today we have begun to understand them. In our personal lives also, we journey from ignorance to knowledge. Our individual growth reflects the advancement of the species. The exploration of the cosmos is a voyage of self discovery.*
>
> **— Carl Sagan**
> (Cosmos, 1980)

In this chapter, we outline the objectives of (Vahdat et al., 2022) and (Vahdat et al., 2024), along with the analyses conducted in both. These analyses are detailed in the appendix. Readers are encouraged to consult these publications for further information on data reduction, multiwavelength observations (including light curves, spectra, timing, etc.), and the methodologies employed. The primary findings will be presented and discussed in Chapter 4.

3.1 Toward an X-ray inventory of nearby neutron stars, (Vahdat et al., 2022)

3.1.1 Aim of the publication

Since the first X-ray pulsar was detected by the Uhuru satellite in the early 1970s, various types of NSs emitting X-rays have been identified. Over the past twenty years, extensive observations using *XMM-Newton* and Chandra satellites have not only enhanced our understanding of isolated and binary NSs (by refining the equation of state and studying pulsar geometry), but have also provided insights into the NS environment, such as the mechanisms accelerating pulsar wind nebulae and intrabinary shocks. Certain NS characteristics are exclusively investigated through X-ray analysis. For example, the correlation between spin-down energy loss, $\dot{E}$, and X-ray luminosity, L_x, has been extensively studied by researchers (Becker and Truemper, 1997; Possenti et al., 2002; Li et al., 2008; Kargaltsev et al., 2008). The X-ray efficiency of pulsars tends to range between 10^{-4} and 10^{-5} at higher $\dot{E}$ values (Fig. 3.1). The debate persists regarding whether the change of efficiency as noted above is due to the presence of higher multipole magnetic field components (Kisaka and Tanaka, 2017) or the result of increased electron-positron pair heating luminosity (Harding and Muslimov, 2011). Since studies typically focus on the brightest or most exceptional pulsars, there may be a bias in our understanding. To address this, we initiated an *XMM-Newton* Fulfil survey (led by B. Posselt, PropID 082303).

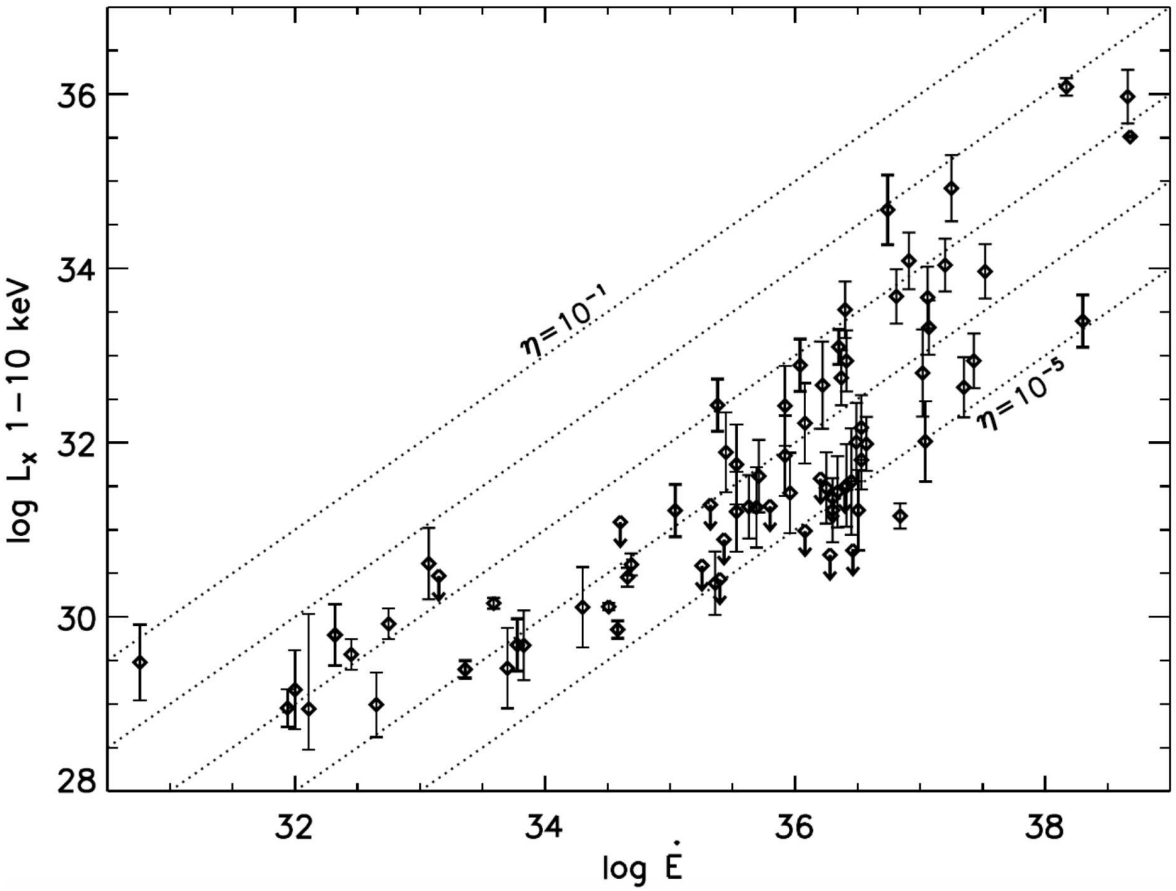

Figure 3.1: Non-thermal X-ray pulsar luminosities L_X, in 1.0-10.0 keV and upper limits vs. the pulsar spin-down power, $\dot{E}$, for ordinary and recycled pulsars (Posselt et al., 2012). It's noteworthy that there appears to be a higher X-ray efficiency at lower $\dot{E}$, although there is a scarcity of objects in that range. Serendipitous searches in archival *XMM-Newton* and *Chandra* data (such as the one by Prinz and Becker 2015) usually find unconstrained large upper limits on L_X for pulsars with $\dot{E} < 10^{35}$ erg s^{-1} because the objects covered by chance are typically a few kpc away.

3.1.2 Source selection and strategy in Vahdat et al. (2022)

For source selection, we utilized the ATNF catalog (v1.57, Manchester et al. 2005) to identify nearby NSs within approximately 2 kiloparsecs (kpc) that lacked X-ray coverage in archived *XMM-Newton* and Chandra observations. A $13'$ search radius was applied for *XMM-Newton* and a $10'$ radius for Chandra to account for the respective field of views of the instruments. We selected a 2 kpc distance cut-off because beyond this, absorption effects hinder the detection of thermal emission-dominated NSs, like the Magnificent Seven (Haberl et al., 2004). Distance estimates were derived from ATNF using dispersion measure (DM) from radio timing observations and the YMW+17 electron density model (Yao et al., 2017), with some estimates differing from those based on the NE2001 model (Cordes and Lazio, 2002). These distances were included in our analysis. By considering the pulsar's spin-down power ($\dot{E}$), distance (D), and average hydrogen column density (N_{H}) as estimated from DM according to formula 1.20, we assumed a preliminary X-ray efficiency of 10^{-4} to estimate expected absorbed X-ray fluxes, prioritizing pulsars with higher likelihood of detection in short exposure times. In 2018 and 2019, we observed 14 pulsars using the *XMM-Newton* EPIC instrument, with exposures ranging from 5 to 20 ks (PI: Bettina Posselt, Program ID: 082303) employing Thin and Medium filters. These sources, which are the main part of the Vahdat et al. (2022), are displayed in Table 3.1, along with the exposure times and selected observational characteristics.

Table 3.1: Properties of the ordinary and millisecond pulsars that are investigated with *XMM-Newton* in this study (Vahdat et al., 2022).

Pulsar	ObsID	$t_{\rm PN}$ (ks)	$t_{\rm M1}$ (ks)	$t_{\rm M2}$ (ks)	$b_{\rm PN}$ (c/s)	$b_{\rm M1}$ (c/s)	$b_{\rm M2}$ (c/s)	P (ms)	D_1 (kpc)	D_2 (kpc)	log $\dot{E}$ ($ergs\,s^{-1}$)	$N_{\rm H,21}$
J0711−6830	0823030601	11.9 (6.1)	13.8 (9.8)	13.8 (9.2)	2.5 (TN)	0.35 (M)	0.35 (M)	5	0.11	0.86	33.6	0.6
J0745−5353	0823031401	18.9 (13.5)	20.8 (18.4)	20.8 (16.1)	0.4 (TN)	0.2 (TN)	0.2 (TN)	215	0.57	0.25	34.0	3.8
J0942−5552	0823031301	18.7 (13.5)	20.6 (20.2)	20.6 (20.2)	0.5 (TN)	0.35 (TN)	0.35 (TN)	664	0.30	3.8	33.5	5.6
J0945−4833	0823031101	17.7 (11.2)	19.6 (17.5)	19.6 (17.2)	0.5 (TN)	0.2 (TN)	0.25 (TN)	331	0.35	1.51	33.7	3.0
J0954−5430	0823030401	14.7 (4.7)	16.6 (6.9)	16.6 (6.0)	2.0 (M)	0.35 (M)	0.35 (M)	473	0.43	3.96	34.2	6.2
J0957−5432	0823031001	15.7 (5.6)	17.6 (17.2)	17.6 (17.3)	0.8 (M)	0.35 (M)	0.35 (M)	203	0.45	4.33	34.0	7.0
J1000−5149	0823030301	7.0 (5.8)	8.9 (6.2)	8.9 (8.7)	0.4 (TN)	0.35 (M)	0.35 (M)	255	0.13	1.93	33.4	2.2
J1003−4747	0823030201	14.7 (9.3)	16.6 (16.4)	16.6 (16.3)	1.0 (TN)	0.35 (M)	0.35 (M)	307	0.37	2.94	34.5	3.0
J1017−7156 ^{B}	0823030701	10 (5.3)	11.9 (10.7)	11.9 (10.0)	0.6 (TN)	0.2 (M)	0.25 (M)	2	0.26	2.98	33.8	2.9
J1125−5825 ^{B}	0823031601	18.7 (5.7)	20.6 (16.9)	20.6 (16.9)	0.7 (TN)	0.35 (M)	0.35 (M)	3	1.74	2.62	34.9	3.9
J1543−5149 ^{B}	0823030901	6.5 (5.3)	8.4 (8.3)	8.4 (8.2)	0.4 (TN)	0.35 (TN)	0.35 (TN)	2	1.15	2.42	34.9	1.6
J1725−0732	0823031501	15.1 (12.3)	17.0 (16.7)	17.0 (16.7)	0.4 (TN)	0.35 (M)	0.35 (M)	240	0.20	1.90	33.1	1.8
J1740−3015	0823030101	4.7 (1.7)	6.6 (6.0)	6.6 (5.7)	1.0 (TN)	0.35 (M)	0.35 (M)	607	0.40	2.94	34.9	4.7
J1755−0903	0823030501	4.7 (3.9)	6.6 (6.5)	6.6 (6.5)	0.4 (TN)	0.35 (M)	0.35 (M)	191	0.23	1.79	33.6	2.0

The first column lists the pulsar names along with their *XMM-Newton* observation IDs. Pulsars in binary systems are denoted with a superscript 'B'. The second column displays the total and GTI-filtered exposure times for EPIC-pn and EPIC-MOS detectors, with values given in parentheses. The third column lists the GTI filter for the background light curve and the corresponding filters for each EPIC detector: 'TN' for thin filter, 'TK' for thick filter, and 'M' for medium filter. The last column presents source properties: 'P' represents the spin period in seconds, 'D_1' indicates the best estimate of pulsar distance in kpc based on the ATNF pulsar catalog using the YMW+17 dispersion measure (DM)-based distance as default, log $\dot{E}$ denotes the common logarithm of the spin-down energy loss rate in ergs per second, and $N_{\rm H}$ represents the hydrogen column density in units of 10^{21} cm^{-2} estimated from the DM .

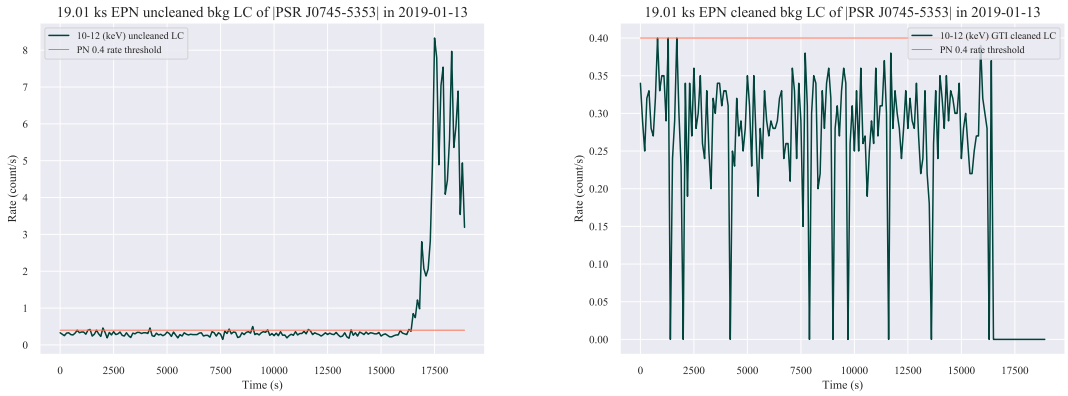

Figure 3.2: Example background light curves for one of our survey sources, PSR 0745−5353. Left: Raw (unfiltered) background light curve. Right: Corrected (filtered) background light curve accounting for various factors influencing detection efficiency (e.g., vignetting, bad pixels, PSF variation, quantum efficiency) and stability (e.g., dead time, GTIs) within the exposure.

To optimize our source detection method, we analyzed detection likelihoods of known X-ray-detected pulsars in 4XMM-DR10. Energy bands 0.3-2.0 keV and 1.0-4.5 keV showed the highest number of detections based on maximum likelihood distributions. Additional energy ranges of 0.3-1.2 keV, 0.3-1.5 keV, and 0.3-4.5 keV were included for analysis, which provided the highest detection significance (in some point sources) defined as:

$$S = \frac{N_{\rm s}}{\hat{\sigma}(N_{\rm s})} = \frac{N_{\rm T} - \alpha N_{\rm bgr}}{\sqrt{N_{\rm T} + \alpha^2 N_{\rm bgr}}} \tag{3.1}$$

where S represents detection significance, $N_{\rm s}$ is the background-subtracted source counts, $N_{\rm T}$ and $N_{\rm bgr}$ are total counts within source and background regions, and α is the ratio of source to background region.

3.1.3 Data analyses and flux estimation in the study

All data were processed using the *XMM-Newton* Science Analysis Software (SAS, V18.0.0), employing standard procedures. We ap-

plied a FLAG==0 filter to remove CCD gaps and bad pixels. Additionally, we conducted good time interval (GTI) screening to eliminate flares caused by energetic protons. Due to the presence of numerous background flares during our short observations, standard background flare screening would have significantly reduced exposure time. Consequently, we allowed a higher background contribution in some cases to maximize potential photon counts from our targets. The complete list of GTI rates used for observations is presented in Table 3.1.

We evaluated various GTI filters derived from 100-second binned light curves of events with energies above 10 keV. For each GTI-filtered event file, we generated images and exposure maps across five energy bands. We then utilized the SAS tool 'eregionanalyse' to optimize the aperture, maximizing the source-to-background count ratio. The optimal extraction radii ranged from 10″ to 15″. We centered 'eregionanalyse' on positions up to 3σ from the radio pulsar position, incorporating proper motion corrections when available. Only one source, PSR J0745−5353, had a high proper motion that its position needed to be corrected. We obtained background-subtracted source count rates and 3σ statistical upper limits for each X-ray NS candidate covered by individual EPIC instruments.

For combined EPIC count rates and significance, we employed the 'emldetect' task, conducting simultaneous maximum likelihood (ML) point spread function (PSF) fits to the source count distributions of EPIC-pn and EPIC-MOS events. The resulting values and upper limit values are provided in Table 4.1. 'Emldetect' also yielded the statistical positional error for X-ray sources in our sur-

vey, which, when combined with a systematic error of $1.5''$, provided the total positional uncertainties for identifying multiwavelength sources near X-ray NS candidates. For sources with a combined net count number above 100 in the EPIC instrument, we performed spectral fits. Only PSR J1831−0952 met this criterion.

Due to insufficient counts for meaningful spectral fits, we assumed two different spectral models to convert count rates to fluxes: a power-law (PL) with a photon index of 1.7 and a blackbody (BB) with $kT = 300$ eV. We utilized PIMMS v4.11 for this conversion and estimated the hydrogen column density ($N_{\rm H}$). We chose the input energy ranges of 0.3-2.0 keV and 1.0-4.5 keV for BB and PL models to convert EPIC-pn count rates to absorbed and unabsorbed fluxes. Lastly, we used DM-based distances to convert unabsorbed fluxes and upper limits to X-ray luminosities $L_{1-10\,\rm keV} = 4\pi D^2 F^{\rm unabs}$.

3.2 Multiwavelength Pulsations and Surface Temperature Distribution in the Middle-Aged Pulsar B1055-52, (Vahdat et al., 2024)

3.2.1 Aim of the publication

Radiation from rotation powered pulsars includes both nonthermal and thermal components. The nonthermal component comes from relativistic particles in the pulsar's magnetosphere, while the thermal component originates from the NS's surface. Studying these emissions across different wavelengths helps understand particle acceleration, magnetosphere properties, NS surfaces, and their thermal evolution. By comparing multiband spectra and pulse pro-

files with X-ray data we can measure surface temperatures, probe temperature variations, estimate NS sizes, and analyze magnetospheric emission characteristics. As pulsars age, their thermal and nonthermal components evolve differently. In younger pulsars, magnetospheric emission dominates, masking the thermal emission from the NS surface.

However, as pulsars age, the magnetospheric emission weakens, revealing the thermal emission in the X-ray range. This thermal emission consists of both a cold component, originating from the NS's residual heat, and a hot component, likely heated by particles from the pulsar magnetosphere. In older pulsars, the NS becomes too cool to emit X-rays, and only the hot thermal component is observable in soft X-rays, along with faint magnetospheric emission. Studying middle-aged pulsars, around 0.1 to 1 million years old, allows researchers to comprehensively investigate the electromagnetic radiation from NSs, providing valuable insights into NS physics and evolution. Notable middle-aged NSs include PSRs B0656+14, J0633+1746, and B1055−52, known as the 'Three Musketeers' which exhibit similarities in their properties such as X-ray emissions and spin-down characteristics (Becker and Truemper, 1997).

B1055−52 was initially studied by *XMM-Newton* in 2000, where a phase-resolved spectral analysis was conducted (De Luca et al., 2005). Subsequent observations with Chandra in 2012 revealed significant spectral changes, including a notable >30% decrease in flux compared to the 2000 *XMM-Newton* observation (Posselt et al., 2012). These changes, too large to attribute to cross-calibration issues,

suggest long-term spectral variability, a phenomenon uncommon in middle-aged NSs (Posselt et al., 2023). Therefore, in 2020, we conducted another observation of B1055 using *XMM-Newton*, employing a better-suited instrument mode than the 2000 observations to more accurately measure the magnetospheric spectral component and correlate it with the radio and gamma-ray pulse profiles. Additionally, we coordinated simultaneous radio observations of the source using the Parks and MeerKAT Radio Telescopes. The objective of Vahdat et al. (2024) was to analyze the multiwavelength data from B1055, aiming to understand the temperature distribution and investigate both thermal and non-thermal emission characteristics. Furthermore, we sought to search for phase-dependent absorption features in the new data, since such features have been discovered in some other middle-aged pulsars.

3.2.2 Data analyses conducted in the study

We analyzed X-ray data obtained from four separate observations conducted with the *XMM-Newton* telescope over a span of 20 years. Simultaneously, we conducted radio observations from the Parks and Meerkat telescopes, taken alongside the *XMM-Newton* data in 2019, as well as γ-ray data from the Fermi-Lat instrument (Fig. 3.3). Our analysis of the X-ray data primarily focused on three aspects: Phase-integrated Spectral Analysis, Phase-resolved Spectral Analysis, and timing Analysis. Initially, we compared two 2019 observations (101N and 201N) to ensure consistency in terms of source and background count ratios, distribution, and spectral fit

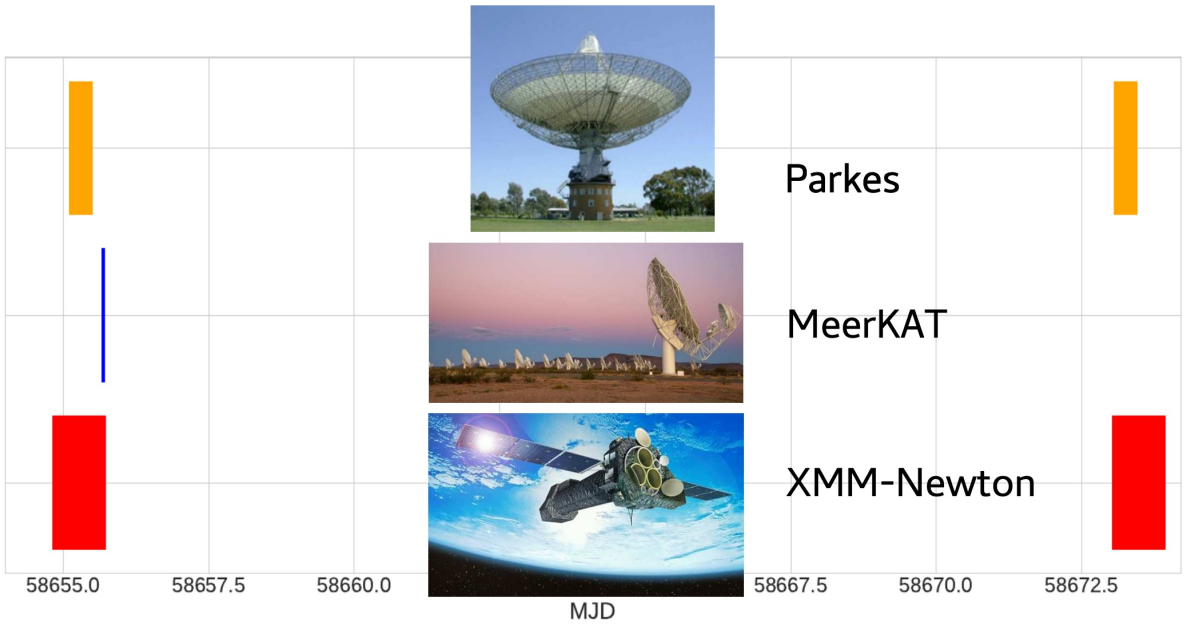

Figure 3.3: Simultaneous multiwavelength observation of PSR B1055

parameters within an energy range of 0.3-8 keV. We utilized PyXspec, python interface with XSPEC, for X-ray spectral fitting, employing the Tübingen-Boulder model through its XSPEC implementation. Our analysis included fitting the high-energy portion (2.3-8 keV) of the spectra with an absorbed power-law model. Subsequently, we performed broad-band spectral fitting (0.3-8 keV) using a three-component model consisting of two blackbody models and a power-law model. Upon establishing consistency, we compared the combined 2019 data with that of 2000, noting differences in count statistic and background noise levels, particularly at high energies. Finally, we conducted a comprehensive analysis by combining 12 spectra and performing a 2BB+PL fit, yielding best-fit parameters. Additionally, we evaluated various NS atmosphere models available in XSPEC, specifically applicable to magnetic fields of approximately 10^{12} G. However, fitting with single-component and two-component atmosphere models resulted in

Table 3.2: NSMAXG XSPEC fit results of PSR B1055-52 combined with PL or BB components

Switch	Element	$B(10^{12}$ G)	Θ_B	θ_m	$\log g$ (cm/s^2)	$\log T_{eff}$	Γ	χ^2/dof
1100	H	0.1	0	N/A	2.4	5.5	5.7	2.84
1200	H	1.0	0	N/A	0.4 - 2.5	5.58	1.8	1/0.9
1260	H	4.0	0	N/A	2.4	5.7	1.8	1.2/1
1300	H	10.0	0	N/A	0.4 - 2.5	5.7	1.8	1.6/1
1211	H	1.26	0	N/A	1.6	5.7	1.8	1.3/1
12006	C	1.0	0	N/A	2.4	5.8 - 6.9	6	1.3
12008	O	1.0	0	N/A	2.4	6.9	6	1.5
12010	Ne	1.0	0	N/A	2.4	6.9	6.1	1.9
123100	H	1.0 - 1.82	0-90	0	1.6	5.5	1.7	3
123190	H	1.0 - 1.82	0-90	90	1.6	5.5	2.1	2
130100	H	5.5 - 10.0	0-90	0	1.6	5.6	1.7	4.5

significant systematic residuals at higher energies, while two-component and three-component models exhibited similar issues at lower energies.

Table 3.2 presents the fitting results for the NSMAXG atmospheric model applied to PSR B1055 using XSPEC. The model's performance with carbon, oxygen, and neon elements, as well as with hydrogen atmospheres at high inclinations, was suboptimal, yielding poor fits. Acceptable fits were primarily achieved with hydrogen atmospheres featuring moderate to high magnetic fields and low inclination angles. These fits were conducted using both single-component and multi-component atmospheric models, incorporating PL or BB components as additional parameters.

When fitting with single-component models, and combinations of two-component atmospheres, the results showed significant systematic discrepancies at higher energies, with a reduced chi-squared value $\chi^2_v \gtrsim 8$. Similarly, combinations of two-component and three-component models that included an added PL or BB failed to produce satisfactory fits due to pronounced systematic residuals at lower energies, specifically below 1.5 keV.

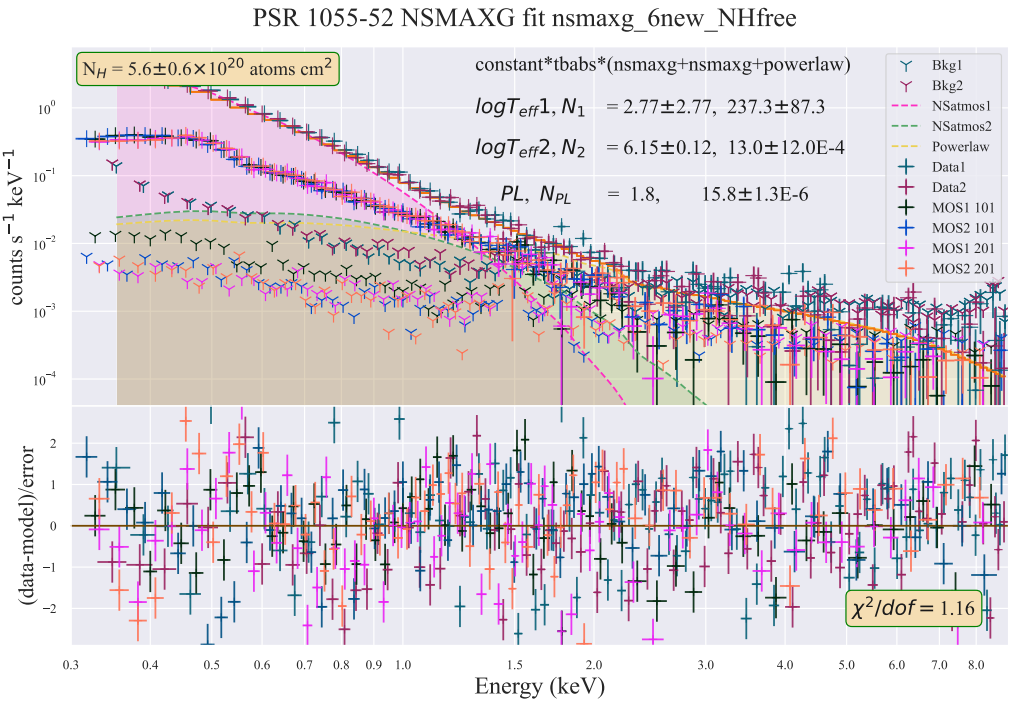

Figure 3.4: Phase-integrated spectral fitting results for PSR B1055, using the 2019 *XMM-Newton* dataset. The fitting was performed over the 0.3-8 keV energy range, incorporating six spectra within a two-component NSMAXG model with an additional PL, set with a Switch parameter of 1200.

In our timing analysis, we employed the Z_n^2 statistic (Buccheri et al., 1983) to investigate X-ray pulsations near the expected radio frequency. To ensure robust signal extraction with high signal-to-noise ratios (S/N) and significant $Z^2_{n,\mathrm{max}}$ values, we optimized GTI screenings, energy regions, and extraction apertures.

Before searching for ν and $\dot{\nu}$ in the X-ray data, we adjusted the event times of 101N and 201N by subtracting $(t_1 + T_{\mathrm{span2}} + t_2)/2$ (where T_{span2} is the times elapsed between the first and last detected events for 201N) to minimize correlation between ν and $\dot{\nu}$, setting the reference time to MJD 58664.376681.

Conducting the Z_n^2 test separately for each dataset at fixed $\dot{\nu} = -1.478\times10^{-13}$ Hz/s, we utilized the stingray Python package (Huppenkothen et al., 2019). For 101N (201N), we extracted 44113 (41984)

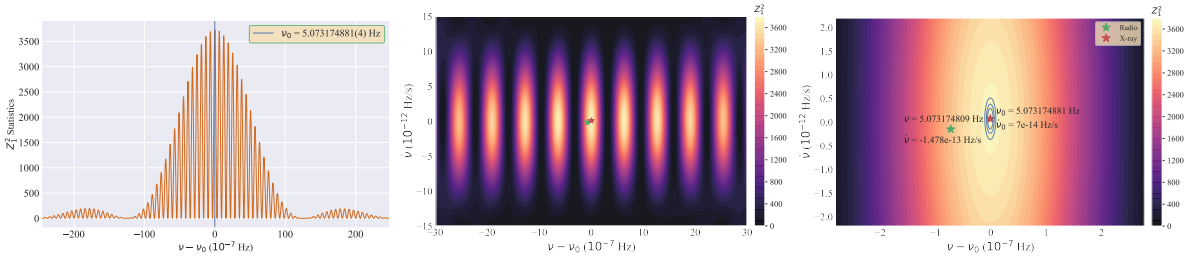

Figure 3.5: Left: Z_1^2 statistics with a fixed $\dot{\nu}$=7e-14 Hz/s obtained for $0.3-7$ keV events extracted from EPIC-pn source region. Middle and right: Maps of $Z_1^2(\nu,\dot{\nu})$ in the vicinity of pulsar's expected (green star) frequency and its derivative from Parkes radio timing solution for the energy range $0.3-7$ keV. The red star indicates the location of the highest $Z_1^2(\nu,\dot{\nu})$ value ($Z^2_{1,\max}=3739$). The 1,2 and 3σ statistical error contours for $Z_1^2(\nu,\dot{\nu})$ are displayed with blue ellipses. From Vahdat et al. (2024)

events from GTI-filtered $0.3-7$ keV data using a $30''$ radius extraction region. The H-test (de Jager et al., 1989) indicated a maximum at three harmonics ($n=3$) for each dataset, yielding $Z^2_{1,\max}$ = 1925 (1802) and $Z^2_{3,\max}$ = 2123 (2029) at frequencies $\nu = 5.07317468(13)$ Hz ($5.07317498(14)$ Hz).

Combining the two EPIC-pn datasets, we obtained $Z^2_{1,\max}$ = 3739 ($Z^2_{3,\max}$ = 4155) at $\nu(Z^2_{1\max}) = 5.073174881(4)$ Hz and $\dot{\nu}(Z^2_{1,\max}) = +7\times10^{-14}$ Hz s^{-1}. This is consistent with the expectation that the sum of the squared individual data sets, $Z^2_{1,\max,\,\mathrm{obs1}}$+$Z^2_{1,\max,\,\mathrm{obs2}}$, should be approximately equal to the squared coherence of the combined data, $Z^2_{1,\max,\,\mathrm{combined}}$, suggesting good phase connection between the datasets.

These results suggest good phase connection between datasets.

Despite the lower accuracy of the X-ray timing solution compared to radio, we utilized it to maximize signal strength. For phase-resolved spectroscopy, we divided the data into 5 equal-sized phase bins and extracted spectra from each bin using the same extraction radius, filtering, and binning criteria as the phase-integrated analysis. Ensuring each bin contained a minimum of 15,000 counts,

we confirmed adequate spectral constraints. Employing the best-fit 2BB+PL model from the phase-integrated analysis, as starting point we conducted spectral fits with fixed parameters for the absorbing hydrogen column ($N_{\rm H} = 2 \times 10^{20}$ cm^{-2}) and photon index ($\Gamma = 1.8$). Figure 3.6 presents each spectrum along with its corresponding best-fit model parameters and χ^2_v values. All bins yielded satisfactory fits, effectively constraining the parameters of the three spectral components across all phases. However, in the fourth bin (ϕ=0.6–0.8), the statistical analysis using the `ftest` suggested that including the Hot BB component was not necessary.

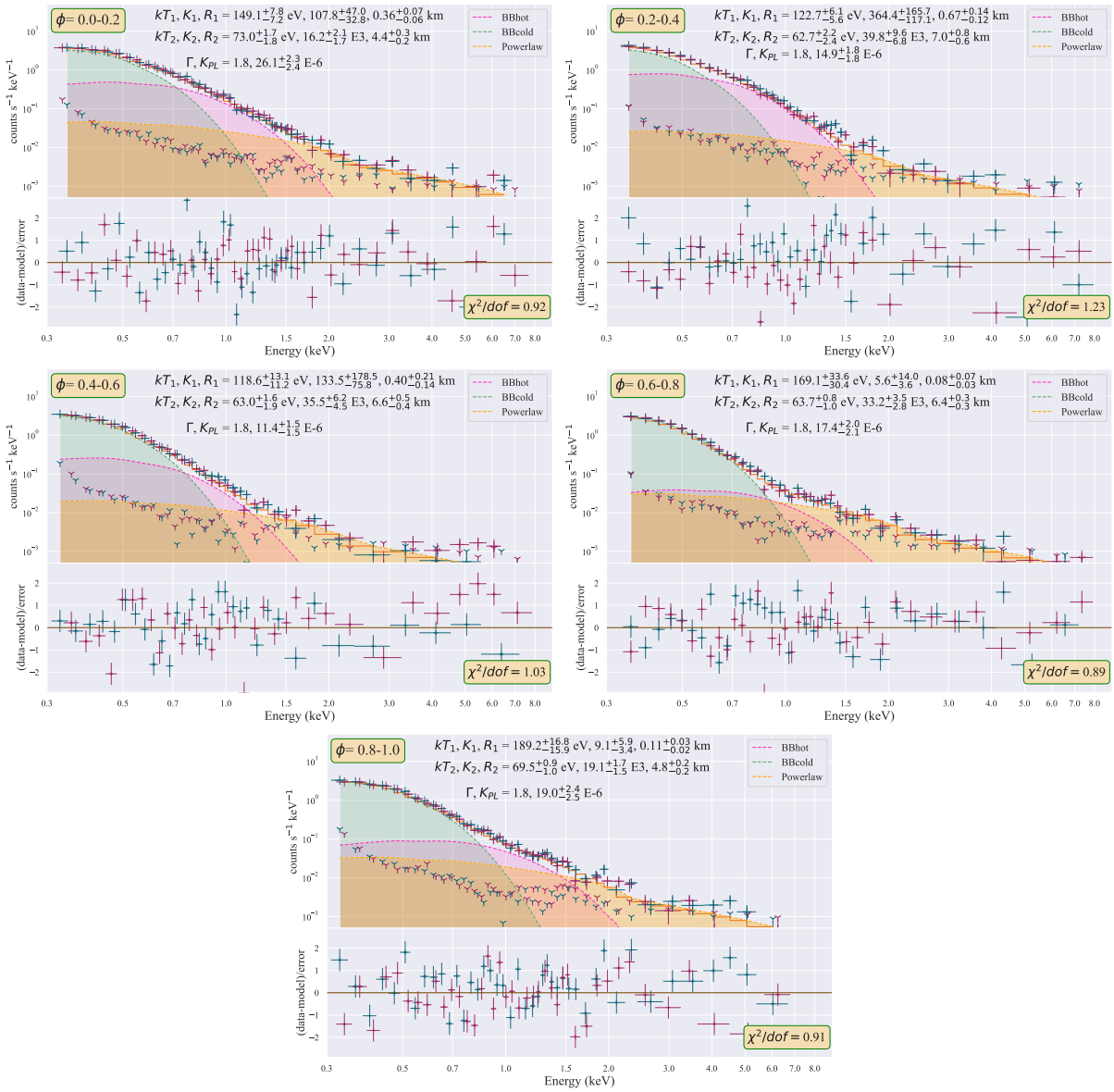

Figure 3.6: Fits to phase-resolved spectra for 5 equal-sized phase bins of the 2019 EPIC-pn data. Hot BB, cold BB, and PL components are displayed with red, green, and yellow colors. The fit parameters with a margin of 1σ error are shown at the top of each panel.

4 Results & Discussion

> *Life is like riding a bicycle. To keep your balance you must keep moving.*
>
> **— Albert Einstein**
> (Letter to his son Eduard, 1930)

This chapter is dedicated to presenting the main findings of (Vahdat et al., 2022) and (Vahdat et al., 2024), as well as discussing and interpreting these results. Additionally, each section includes a segment titled 'Additional Notes and Outlook', where I will delve into additional findings and ideas that were not included in the papers but are important or beneficial for the further development of the studies conducted therein.

4.1 Toward an X-ray inventory of nearby neutron stars, (Vahdat et al., 2022)

4.1.1 Detected pulsars from the survey

Among the five X-ray energy bands specified in Vahdat et al. (2022), the 0.3—2.0 keV band exhibited the highest overall detection significance in the EPIC instru-

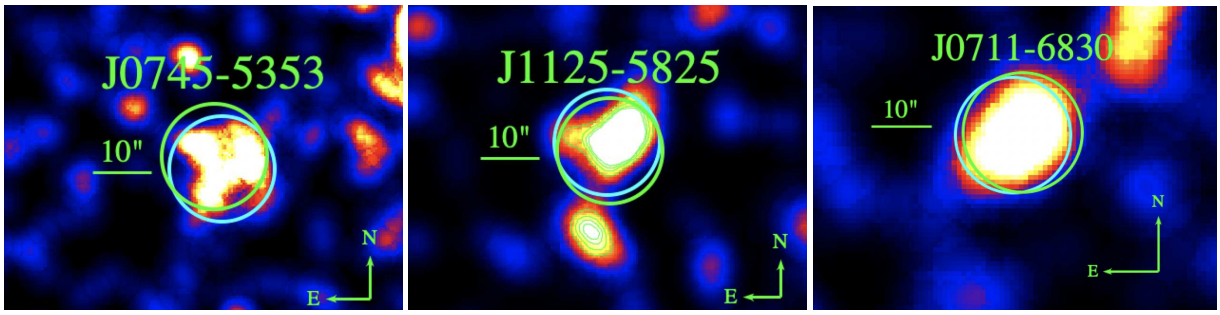

Figure 4.1: X-ray counterpart candidates in 0.3-2.0 keV as observed with the EPIC-pn and EPIC-MOS2 (PSR J0711-6830). The green circles are centered at the radio timing position of the pulsars, the cyan circles are centered at the position where the X-ray source has the highest significance. The images have pixel scales of 0.4″, and are smoothed with Gaussian length scales σ =3.4″ (for PSR J1125−5825), and σ =2.4″ (for PSRs J0745−5353 and J0711−6830). The angular separations between X-ray and radio positions are given in Table 4.1.

ments for our survey sources. Thus, we present results for this band, acknowledging a exposure loss of up to 65% due to background flaring events, which exceeded our expectations.

In our program, we identified three X-ray point sources with at least 3.5σ significance, closely aligned with the radio positions of pulsars J0711−6830, J0745−5353, and J1125−5825, warranting further investigation for possible associations. The relevant exposure times, distances, and source properties are detailed in Table 3.1, while Table 4.1 provides angular separations (between radio and X-ray positions) and X-ray source significance. Corresponding EPIC images are displayed in Figure 4.1. Observational properties of the identified sources are listed below:

PSR J0711−6830: The candidate X-ray counterpart is positioned $1.7''$ from the radio location of the pulsar. Despite a lack of counts in the narrower soft energy band, inclusion of higher energies led to detection. However, irregular count distribution in EPIC-MOS2, noise-like appearance in EPIC-pn, and absence in EPIC-MOS1 raised doubts about the validity of this detection.

PSR J0942−5552: The most significant X-ray location according to `eregionanalyse` is $9.7''$ from the radio pulsar position (not shown in Figure 4.1), casting uncertainty on a match due to non-detection in EPIC-MOS1/MOS2 and considerable angular separation. Additionally, a nearby extended X-ray source, with an angular separation of $\approx 25''$ from the radio pulsar, is unlikely to be associated.

PSR J0745−5353: This pulsar, initially identified in the second Molonglo pulsar survey (Manchester et al., 1978). Analyzing EPIC-pn data revealed a 30% exposure time loss during GTI-screening. The X-ray source, located $1.54''$ from the radio pulsar position, emerged as a promising counterpart candidate. Detailed statistics and flux calculations are provided in Table 3.1, along with information on nearby astronomical sources.

PSR J1125−5825: The pulsar was first discovered in the High Time Resolution Universe Pulsar survey I (Keith et al., 2010). It has a helium-core white dwarf (WD) companion with a mass of 0.33 $M_\odot$ (Hui et al., 2018). The recycled pulsar is located at 1.7 kpc (YMW+17 model) and has a surface dipole field of $B_{surf} = 4.4 \times 10^8$ G with a $\log \dot{E} = 35$ and characteristic age of 0.8 Gyr. We had a clean exposure time of 5.7 ks in EPIC-pn and 17 ks in EPIC-MOS1/MOS2 after background filtering. The X-ray source position has an angular separation of $0.6''$ from the radio position.

For this X-ray source, there are 2 Gaia sources $1.3''$ and $3.8''$away with the second one having a 2MASS and WISE counterpart. We were not able to exclude any of them as an optical counterpart of the X-ray source based on their astrometric or spectral features.

Table 4.1: Properties of the selected ordinary and millisecond pulsars that are investigated in this survey (from Vahdat et al. 2024).

Pulsar	ObsID	Δ_{X-R}	PN$_{0.3-2\,keV}$			MOS1$_{0.3-2\,keV}$			MOS2$_{0.3-2\,keV}$			Combined EPIC		
			N_s	S	UL[1]	N_s	S	UL[1]	N_s	S	UL[1]	N_s	S	ML
		(arcsec)	(counts)	(σ)	(c/s)	(counts)	(σ)	(c/s)	(counts)	(σ)	(c/s)	(counts)	(σ)	
J0711−6830	0823030601	1.7	23.5±13.0	1.8	0.0080	−−	−−	0.0005	11.3±4.7	2.4	0.0018	54.8±15.7	3.5[1]	14.9
J0745−5353	0823031401	1.5	27.2±7.6	3.6	−−	6.2±4.0	1.6	0.0006	8.1±4.3	1.9	0.0007	39.6±9.2	4.3[2]	16.2
J0942−5552	0823031301	9.7	31.7±10.3	3.1	−−	−−	−−	0.0004	−−	−−	0.0006	−−	−−	−−
J0945−4833	0823031101	2.3	14.8±7.2	2.2	0.0021	3.3±5.1	−−	0.0007	−−	−−	0.0004	−−	−−	−−
J0954−5430	0823030401	1.2	4.4±4.2	1.1	0.0021	1.7±3.2	−−	0.0009	2.5±2.9	−−	0.0012	−−	−−	−−
J0957−5432	0823031001	8.5	9.0±5.8	1.6	0.0024	8.3±5.6	1.5	0.0008	−−	−−	0.0003	−−	−−	−−
J1000−5149	0823030301	2.7	−−	−−	0.0007	−−	−−	0.0005	−−	−−	0.0010	−−	−−	−−
J1003−4747	0823030201	2.1	10.5±8.4	1.3	0.0019	3.4±3.8	−−	0.0005	−−	−−	0.0002	−−	−−	−−
J1017−7156	0823030701	5.3	1.6±3.9	−−	0.0015	−−	−−	0.0002	−−	−−	0.0003	−−	−−	
J1125−5825	0823031601	0.6	18.8±6.7	2.8	0.0038	17.4±6.3	2.8	0.0012	10.3±5.2	2.0	0.0009	47.4±10.2	4.7[2]	20.9
J1543−5149	0823030901	1.2	4.0±4.0	1.0	0.0018	3.8±3.6	1.2	0.0011	−−	−−	0.0007	−−	−−	−−
J1725−0732	0823031501	4.4	3.3±3.8	−−	0.0006	1.6±2.7	−−	0.0004	−−	−−	0.0003	−−	−−	−−
J1740−3015	0823030101	7.8	6.4±3.5	1.8	0.0064	−−	−−	0.0008	−−	−−	0.0008	−−	−−	−−
J1755−0903	0823030501	0.3	6.2±4.1	1.5	0.0031	−−	−−	0.0006	−−	−−	0.0009	−−	−−	−−

The Δ_{X-R} column displays angular separation in arcseconds between the pulsar's radio timing position and the centroid of the nearest X-ray source. Background-subtracted counts N_s at the optimized X-ray source position and their corresponding significance S according to Equation (1) are listed for each detector, as well as the maximum likelihood for the detections considering all EPIC instruments together. The 3σ upper limits (UL) for individual instruments are Bayesian upper limits according to Kraft et al. (1991). The ML values are given in 0.3-2.0 keV for PSRs J0745−5353 and J1125−5825 and in 0.3-4.5 keV for PSR J0711−6830.

4.1.2 New archival X-ray counterpart of pulsars

While analyzing archival X-ray source catalogs to refine our detection energy range, we uncovered potential pulsar counterparts that have not been previously reported. To identify them, we cross-referenced the radio positions of pulsars from the latest ATNF catalog (Manchester et al., 2005) with the *XMM-Newton* (4XMM DR10, Webb et al. 2020) and *Chandra* (CSC v2) catalogs, selecting those within search radii of $10''$ and $5''$ respectively. Initially, we identified 340 X-ray sources, which we narrowed down to 101 candidates assuming a pulsar distance limit of 2 kpc. After excluding pulsars with known X-ray counterparts in databases like SIMBAD and ADS, we identified three potential new X-ray counterparts for nearby pulsars in the 4XMM-DR10 catalog.

Additionally, we conducted a search for significant detections of pulsars previously only listed with upper limits in X-ray surveys by Prinz and Becker (2015) and Lee et al. (2018). This effort yielded 5 additional sources in the *XMM-Newton* catalog within a $10''$ search radius of radio pulsar positions. We found no unpublished X-ray emitting pulsar candidates in CSC v2. To ensure consistency, we applied the same analyses to archival sources as to our survey pulsars, enabling direct comparisons in terms of energy bands and fluxes. The total positional uncertainty of archival sources was obtained from the 4XMM-DR10 catalog, using the POSERR at the 3σ confidence level. Notably, two archival sources had distances exceeding 2 kpc based on the *YMW+17* model, yet we retained them

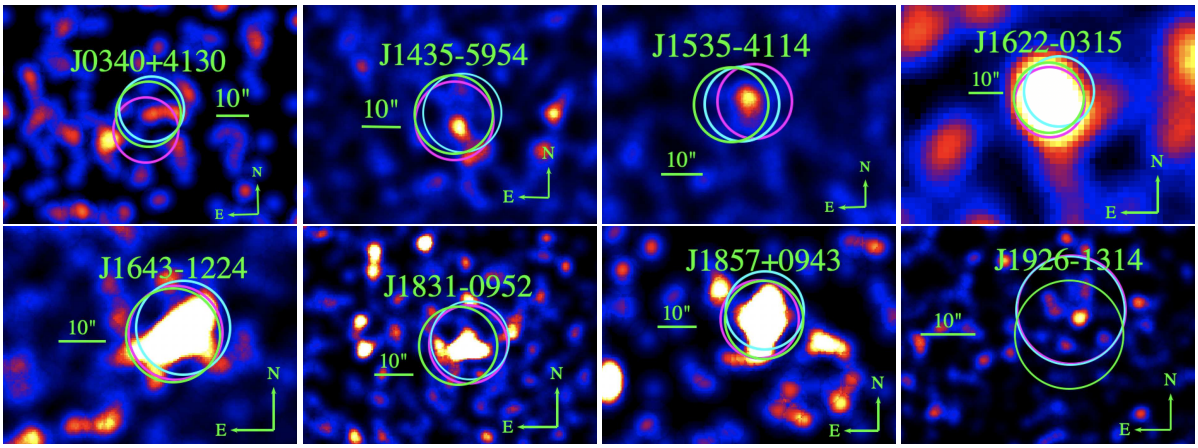

Figure 4.2: X-ray counterpart candidates in 0.3-2.0 keV as seen with the EPIC-pn (except for J1831 and J1535 which are displayed in EPIC-MOS1). The green circles are centered at the radio timing position of the pulsars whereas the blue circles are centered at the X-ray source with the highest significance. The Magenta circles show the 4XMM-DR10 positions close to these pulsars. The images have pixel scales of 0.4″, and are smoothed with Gaussian length scales σ =2.2″ (except PSRs J1535−4115 and J1926−1314 with σ =1.4″). The angular separations between X-ray and radio positions are given in Table 4.2 (from Vahdat et al. 2022).

due to their intriguing X-ray characteristics that are summarized in Vahdat et al. (2022).

4.1.3 Potential alternatives to explain the X-ray sources

We utilized the 3σ positional uncertainty radius to examine nearby optical or infrared sources that could account for or contribute to the observed X-ray emission. Our search incorporated data from various catalogs including *Gaia*-EDR3, 2MASS, WISE, NOMAD, and the TESS Input Catalog.

To explore alternative counterparts, we hypothetically attributed all X-ray flux to an optical/NIR source, analyzing resulting X-ray/optical/NIR flux ratios, color-color, and color-magnitude diagrams, alongside proper motions and known distances when available. We classified optical/NIR sources based on established schemes by Maccacaro et al. (1988), Covey et al. (2007) and Bailer-Jones et al. (2019).

Table 4.2: Properties of ordinary and ms-pulsars with possible counterparts in 4XMM-DR10 catalog for which we could not find a respective note in the literature or previously marked as upper-limit (From Vahdat et al. 2022).

Pulsar	ObsID	Δ_{X-R}	θ	IAU name	ML	PN$_{0.3-2\,keV}$		MOS1$_{0.3-2\,keV}$		MOS2$_{0.3-2\,keV}$	
						N_s	S	N_s	S	N_s	S
		(arcsec)	(arcmin)			(counts)	(σ)	(counts)	(σ)	(counts)	(σ)
J0340+4130	0605470101	4.74	7.8	4XMM J034023.3+413040	12.0	11.4±5.4	2.1	13.9±5.6	2.5	13.6±4.3	3.1
J1435−5954	0692050101	2.59	16.9	4XMM J143500.1-595452	11.3	66.8±17.9	3.7	−−	−−	−−	−−
J1622−0315	0784770401	0.84	1.7	4XMM J162259.6-031538	63.5	33.9±7.8	4.3	24.1±6.8	3.5	20.1±6.9	2.9
J1535−4114	0652610201	5.6	4.3	4XMM J153516.5-411402	12.7	72.5±16.5	4.4	21.0±9.8	2.1	19.8±8.5	2.3
J1643−1224	0742520101	1.5	1.1	4XMM J164338.0-122458	112.7	66.8±11.3	5.9	24.4±6.4	3.8	22.3±6.3	3.5
J1831−0952	0822330101	2.2	2.3	4XMM J183134.1-095201	96.9	−−	−−	28.9±9.6	3.0	29.0±9.7	3.0
J1857+0943	0742520201	1.3	1.2	4XMM J185736.4+094317	38.3	27.9±6.8	4.1	7.1±4.5	1.6	13.8±4.7	2.9
J1926−1314	0742620101	5.5	1.1	4XMM J192653.7-131358	6.9	59.6±16.7	3.5	13.5±8.2	1.6	27.6±9.6	2.8

Δ_{X-R} column displays angular separation in $''$ between the pulsar's radio timing position and the centroid of the nearest X-ray source according to 4XMM-DR10. θ is the EPIC-pn off-axis angle. ML is the reported 4XMM-DR10 maximum likelihood in the energy band 0.2-12.0 keV. Background-corrected counts N_s at the optimized X-ray source position and their corresponding significance are displayed for EPIC-pn and EPIC-MOS1/MOS2. PSR J1831−0952 has a $\sim 6\sigma$ significance in 0.3-4.5 keV with Epic-MOS cameras. The off-axis angle is given for Epic-MOS1.

Visual magnitudes (m_V) were derived from *Gaia*-EDR3 passbands and colors using Landolt standard stars observed with *Gaia*.

Interpreting X-ray to optical flux ratios, we employed Maccacaro et al. (1988)'s classification scheme to assess the likelihood of optical sources being, for example, AGNs or main sequence stars. Objects like galaxies and AGNs may not conform to *Gaia* photometry conversion relations. Astrometric properties from *Gaia*-EDR3, including distances and proper motions, were also utilized to verify stellar origins.

In the absence of 2MASS counterparts, Gaia colors were converted to SDSS colors for classification following Covey et al. Additionally, Jones et al.'s empirical classification of *Gaia*-DR2 objects was considered, aiding in the categorization of potential multiwavelength counterparts.

Table 4.3: *Gaia*-EDR3 sources that fall within 3σ positional uncertainty radius of the X-ray sources.

Gaia-EDR3	Associated PSR	μ_α	μ_δ	D	$T_{\rm eff}$	V	$\log(f_{\rm x}/f_{\rm v})$	Macc88	CV07	BJ19	Excluded	
		(mas/y)	(mas/y)	(kpc)	(K)	(mag)			(Spectral type)		(S)	(GXY)
237123598225544064	J0340+4130 (4.64″)	-0.5±0.4	-2.6±0.4	2.0±1.1	4154±182	20.6±0.7	-0.5	AGN	−−	S, QSR	Y	Y
5339616527672093056	J1125−5825 (1.27″)	-4.8±0.1	1.1±0.1	4.0±2.0	−−	18.7±0.4	-0.85	M, AGN, GXY	M1, M5, M2	S, QSR	N	Y
5339616527704864768	J1125−5825 (3.85″)	-6.8±0.1	1.0±0.1	1.7±0.1	5488±393	16.4±0.3	-1.7	M, K, GXY	G8	S, GXY	N	Y
5878785517750906240	J1435−5954 (4.35″)	-9.5±0.1	-2.4±0.1	2.2±1.1	6635±180	19.1±0.4	-1.3	M, GXY	M6, M7, M8	S, GXY	N	Y
5878785517754291968	J1435−5954 (6.83″)	-6.5±0.2	-2.6±0.1	2.3±1.1	5456±212	19.9±0.5	-0.9	M, AGN, GXY	M5, M6, K7	S, GXY, QSR	N	Y
4358428942492430336	J1622−0315 (0.89″)	-13.2±0.3	2.3±0.2	2.7±1.9	6108±254	19.6±0.4	-0.7	M, GXY, AGN	− − −	S	Y	Y
4310888159960965632	J1857+0943 (2.71″)	-1.9±0.6	-4.1±0.6	1.5±0.8	−−	21.5±0.5	-0.2	AGN	− − −	S, GXY, QSR	Y	Y
4186460380401976448	J1926−1314 (0.96″)	−−	−−	−−	−−	18.2±0.5	-2.1	M,K	−−	S, QSR	N	Y
4186460380401976576	J1926−1314 (1.96″)	5.6±0.9	-4.9±0.5	4.2±2.3	−−	14.7±0.4	-1.8	M,K	−−	S, QSR	N	Y
4186460380410768640	J1926−1314 (2.97″)	2.4±0.1	-5.4±0.1	1.5±0.1	5861±123	18.4±0.5	-3.5	B-F,G,K	M3, M4, F-8	S, GXY	N	Y

The respective pulsars are listed in the second column, followed by the angular distance to the *Gaia*-EDR3 source in parentheses. The next columns show the proper motions, distances and effective temperatures obtained from TESS Input Catalog - v8.0 (Stassun et al., 2019). The V-band magnitude (Vega) was estimated from the *Gaia* magnitudes using Johnson-Cousins relationships of Landolt standard stars that were observed with *Gaia* according to Evans et al. (2018). $\log(f_{\rm x}/f_{\rm v})$ is the X-ray to optical flux ratio. The Macc88, CV07 and BJ19 columns represent classifications according to Maccacaro et al. (1988) Covey et al. (2007) and Bailer-Jones et al. (2019) respectively. S, GXY, QSR and AGN represents star, Galaxy, Quasar and active galactic nucleus, respectively.

Finally, we considered point source (stars) and extended source (e.g., galaxies) classifications provided by the TESS input catalog. Within the 3σ uncertainty regions of six X-ray candidates (including five archival sources), we identified ten potential optical/NIR counterparts (Table 4.3).

4.1.4 X-ray efficiency of pulsars

Assuming the X-ray fluxes solely originate from the pulsars and considering the proximity of our distance estimates to reality, we illustrate in Figure 4.3 the relationship between X-ray luminosity (L_X) and spin-down luminosity ($\dot{E}$) for both thermal and non-thermal emission, encompassing both survey and archival sources.

Many sources in our sample exhibit an efficiency (η) around 10^{-4}. Notably, only three pulsars from our archival X-ray observations

have firm flux estimates derived from parallax distances, highlighted in yellow in Figure 4.3, with consistent estimates for the majority except for J0711−6830.

The solitary millisecond pulsar J0711−6830 displays an X-ray efficiency significantly lower than typical values, although this is subject to uncertainty due to distance ambiguity. Without a parallax measurement, the discrepancy between DM-based distance estimates (D_2 and D_1) leads to an uncertainty factor of 8. Assuming a distance of 0.86 kpc based on the *NE2001* model, the source's luminosity falls within the typical range for X-ray efficiency.

Another noteworthy case is the middle-aged pulsar J1926−1314, exhibiting an X-ray efficiency of $\eta_{\rm X} \sim 10^{-1.5}$, with minimal variation using the *NE2001*-based distance.

This source, known to possess a notably stronger dipole magnetic field than typical middle-aged pulsars, hints at potential magnetothermal heating if the X-ray source indeed represents the pulsar counterpart, and if the DM-distances are accurate.

Figure 4.3 showcases relatively consistent X-ray efficiency values across different spectra and energy bands. This stability arises from the conversion of a fixed count number in the same energy band to fluxes for both spectral models, limiting flux variation. Enhanced accuracy in future X-ray efficiency determinations can be achieved with improved distance estimates and resolution of thermal versus non-thermal components through follow-up observations, as demonstrated by PSR J1831−0952.

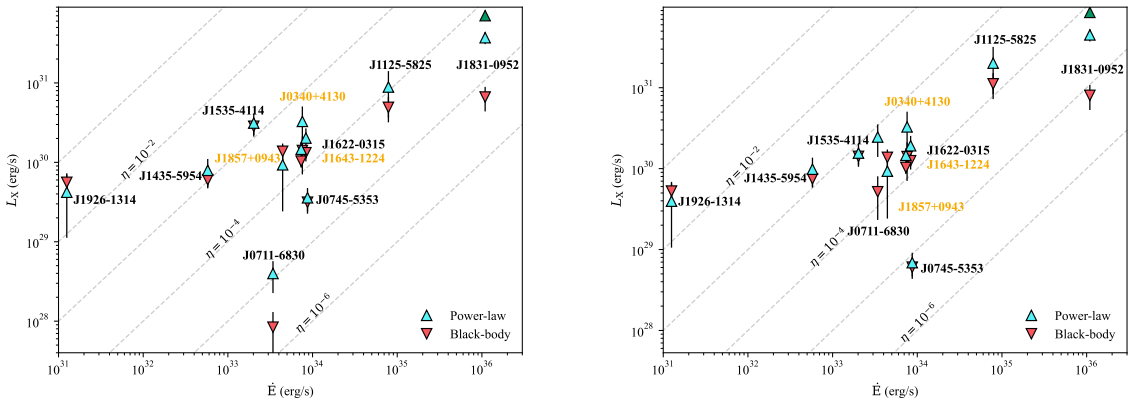

Figure 4.3: X-ray luminosity of ordinary and millisecond pulsars investigated in this study vs. their spin-down powers $\dot{E}$ calculated with *YMW+17* based distances (left) and *NE2001* based distances (right). Sources with parallax measurements are displayed with yellow. The up-pointing triangles display the 1–10 keV non-thermal luminosities obtained via the PL assumption (with $\Gamma = 1.7$) for the underlying spectra, and the down-pointing triangles shows the 0.3–2.0 keV thermal luminosities obtained via BB assumption (with kT = 300 eV). Spectrum-derived PL flux for J1831−0952 is shown with green triangle. $\dot{E}$ values are corrected for the Shklovskii effect where relevant (From Vahdat et al. 2022).

4.1.5 Additional notes

Our initial Fulfil survey, aimed at obtaining X-ray coverage of a less biased pulsar sample, observed 14 NSs (out of 17 proposed) between 2018 and 2019. Among these 14 targets, 8 have 'clean' EPIC observations (without strong background flares) for 50% of the approved times. Among these, four had detection rates above 3σ, while the other four have constrained limits down to flux values of 4×10^{-14} erg/s/cm^2. For the next cycle of *XMM-Newton* Proposal, we refined our survey strategy and proposed more sources to be observed. These improvements included accounting for distance uncertainties by comparing different estimates (parallax distances and various models based on radio dispersion measure, DM). We only proposed targets with either parallax measurements, small distance deviations (less than a factor of 2) for different DM models, or detectability for the largest listed distance. With this refined

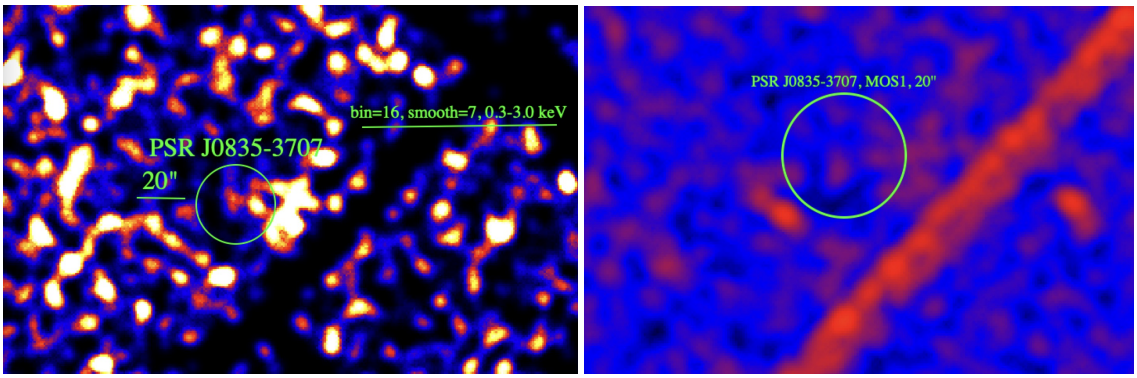

Figure 4.4: X-ray count distribution of PSR J0835-3707 in 0.3-3.0 keV as observed with the EPIC-pn (left) and EPIC-MOS1 (right)

strategy, we secured several observation opportunities in AO21, AO22 and AO23 cycles (PI: Armin Vahdat). Some of these observations have already been conducted, providing us with new data not included in Vahdat et al. (2022), which will be discussed below.

PSR J0835-3707

PSR J0835-3707 is a middle-aged pulsar ($\tau_c \approx 8.8 \times 10^5$ yr) with a P and $\dot{P}$ of 0.54 s and 9.78 $10^{-15} ss^{-1}$, respectively. The source was discovered by the Parkes multi-beam pulsar survey (Manchester et al., 2001), and its DM-based distance estimates (YMW+17) place the source at 0.55 kpc.

In December 2021, the pulsar was observed for about 20 ks with *XMM-Newton* EPIC cameras, unaffected significantly by background flares. Notably, EPIC-MOS1 achieved a detection significance of 2.6σ (see Fig. 4.4). Upper limits (3σ) for X-ray emission from the pulsar, as measured by individual EPIC instruments, are summarized in Table 4.4.

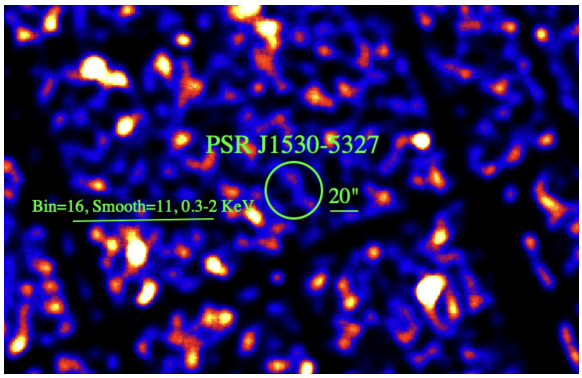

Figure 4.5: X-ray count distribution of PSR J1530-5327 in 0.3-2.0 keV as observed with the EPIC-pn

PSR J1530-5327

PSR J1530-5327 is a middle-aged pulsar ($\tau_c \approx 9.5 \times 10^5$ yr) with a P of 0.28 s and a $\dot{P}$ of 4.68 $\times 10^{-15}$ s s^{-1}(Parthasarathy et al., 2019). Based on DM measurements (YMW+17), the pulsar is situated at 1.12 kpc. In March 2022, *XMM-Newton* EPIC cameras observed the pulsar for approximately 15 ks. While the EPIC-pn camera experienced a slight reduction in observing time due to background flares, affecting about 20% of the approved time, the EPIC-MOS cameras remained unaffected. Unfortunately, no X-ray emission was detected within the EPIC cameras (see Fig. 4.5). Upper limits (3σ) for X-ray emission from the pulsar, as determined by individual EPIC instruments, are provided in Table 4.4.

PSR J1918+1541

PSR J1918+1541 is the third and the last middle-aged pulsar in the current list with a $\tau_c \approx 2.3 \times 10^6$ yr and with a P and $\dot{P}$ of 0.37 s and 2.54×10^{-15} s s^{-1}, respectively (Camilo et al., 2006). The source has DM-based distance estimates (YMW+17) of 0.73 kpc. In April 2023, the pulsar was observed for about 16 ks with *XMM-Newton*

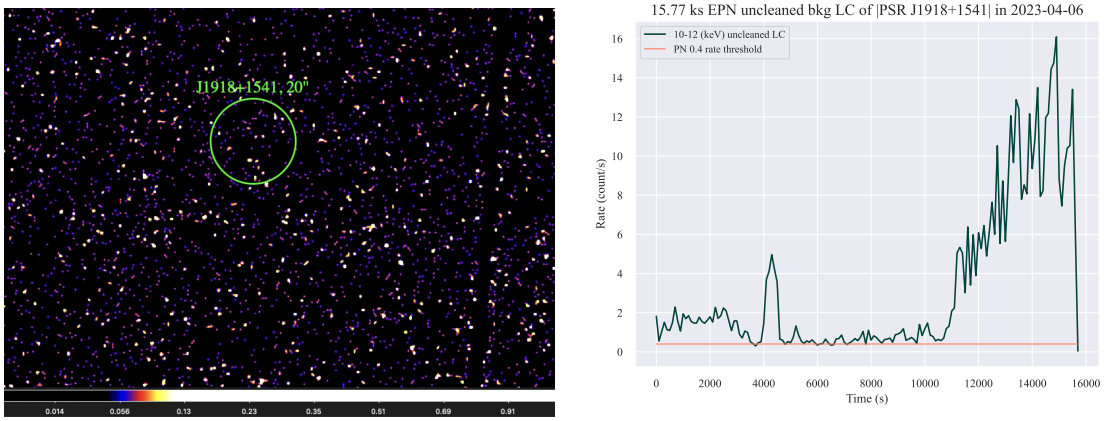

Figure 4.6: X-ray count distribution of PSR J1918+1541 in 0.3-2.0 keV as observed with the EPIC-pn (left) and background light curve of observation (right) highlighting the background flare.

Table 4.4: Properties of the selected middle-aged pulsars that are investigated in the new AO21 and A022.

Pulsar	ObsID	$\Delta_{\mathrm{X-R}}$	PN$_{0.3-2\,\mathrm{keV}}$			MOS1$_{0.3-2\,\mathrm{keV}}$			MOS2$_{0.3-2\,\mathrm{keV}}$			Combined	EPIC
			N_s	S	UL[1]	N_s	S	UL[1]	N_s	S	UL[1]	N_s	S
		(arcsec)	(counts)	(σ)	(c/s)	(counts)	(σ)	(c/s)	(counts)	(σ)	(c/s)	(counts)	(σ)
$J1530-5327$	0884180301	2.3	$--$	$--$	0.0011	$--$	$--$	0.0006	$--$	$--$	0.0004	$--$	$--$
$J0835-3707$	0884180401	1.9	13.6±10.1	1.3	0.0017	17.4±6.5	2.6	$--$	$--$	$--$	0.0005	32.6±9.2	3.0
$J1918+1541$	0901590201	4.3	$--$	$--$	0.0034	13.7±7.2	1.8	$--$	$--$	$--$	0.0007	$--$	$--$

The $\Delta_{\mathrm{X-R}}$ column displays angular separation in arcseconds between the pulsar's radio timing position and the centroid of the nearest X-ray source. Background-subtracted counts N_s at the optimized X-ray source position and their corresponding significance S according to Equation (1) are listed for each detector, as well as the ML for the detections considering all EPIC instruments together. The 3σ upper limits (UL) for individual instruments are Bayesian upper limits according to Kraft et al. (1991).

EPIC cameras. Regrettably, the EPIC instrument encountered a significant background flare, impacting around 40% of the allocated observation time (see Fig 4.6, right). Despite the extensive observation period, the pulsar did not exhibit any significant detection in any of the instruments (refer to Fig 4.6, left). The upper limits (3σ) for X-ray emission from the pulsar, as measured by individual EPIC instruments, are summarized in Table 4.4.

In summary, we conducted an investigation into the X-ray emissions of three middle-aged pulsars as part of our ongoing Fulfil survey. Regrettably, none of the pulsars exhibited a detection sig-

nificance above 3.5σ. However, PSR J0835-3707 displayed a significance of 2.6σ in Epic-MOS1, with a combined detection significance of 3σ. The absence of detections in these pulsars could be attributed to several factors. Firstly, the distance of the source may be incorrect. Nonetheless, according to our survey methodology, the pulsars should have been detected even if the distance based on dispersion measure (DM) is accurate, assuming the assumed X-ray efficiency for the pulsars is correct. Since parallax measurements are unavailable for any of the pulsars, it is plausible that the true source distance differs significantly from the DM-based distance measurements, necessitating further exposure. Additionally, two out of three of our observations were impacted by background flaring, which may have contributed to the lack of detection. Finally, our general assumption regarding the X-ray efficiency rate of 10^{-4} may be inaccurate. As demonstrated in Vahdat et al. (2022), certain pulsars, such as PSR J0711−6830 and PSR J1831−0952, exhibit a lower X-ray efficiency rate of 10^{-5}, which could also be the case for these pulsars.

4.2 Multiwavelength Pulsations and Surface Temperature Distribution in the Middle-Aged Pulsar B1055-52, (Vahdat et al., 2024)

4.2.1 Timing properties

We examined the harmonic behavior of the X-ray pulse profile using Fourier coefficients and generated a phase-folded light curve in the $0.3 - 7$ keV range with the timing solution obtained previ-

ously. The phase-folded light curve and contributions from each harmonic are depicted in Figure 4.7. Different energy bands may require varying numbers of harmonics. To compare, we used a chi-square test to assess the agreement between the sum of 3 harmonics and the 20-bin histogram of the folded light curve.

The results from the two descriptions of the pulse profile align well, indicating that binning may not be necessary for examining smooth pulsations. Using Fourier analysis can help avoid additional uncertainties associated with the binning process.

In Figure 4.8, we plotted the normalized X-ray pulse profile $\mathcal{F}(\phi)$ in the $0.3 - 7$ keV range alongside the Parkes radio profile at 2.4 GHz, and the Fermi-LAT γ-ray light curve from 50 MeV to 300 GeV. Figure 4.9 illustrates the pulse profiles and their 3σ uncertainties in four energy bands, along with Parkes radio and Fermi-LAT γ-ray light curves.

To estimate the intrinsic uncertainty in the alignment of the radio and X-ray profiles, we calculated the maximum phase shift, $\Delta\phi_{\rm max}$, between the X-ray and Parkes radio timing solutions. We found $\Delta\phi_{\rm max}$ to be 0.12, considering the midpoint of each observation as the reference times for the respective solutions, and 0.13, considering the beginning of observation 1 and the end of observation 2 as the reference times.

The pulsated fraction (PF) is a crucial property of a folded light curve, depending primarily on the phases and amplitudes of Fourier harmonics and their energy dependence. We estimated PFs for three different definitions: amplitude PF ($p_{\rm amp}$), area PF ($p_{\rm area}$), and root-mean-square PF ($p{\rm rms}$). The energy dependence of the PFs

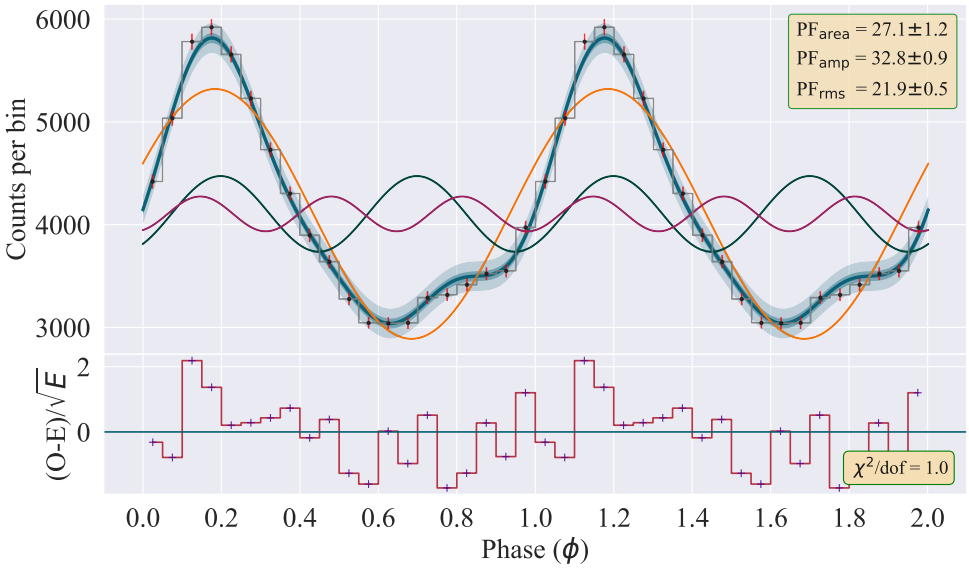

Figure 4.7: The $0.3 - 7$ keV phase-folded light curve (X-ray pulse profile) plotted as a histogram with 20 phase bins and as the sum of 3 harmonics, $(N/20)\mathcal{F}(\phi)$, where $\mathcal{F}(\phi)$ is the normalized pulse profile and $N = 86097$ is the total number of events in the chosen energy range. The $\pm 3\sigma$ uncertainty of the X-ray pulse profile is shown with transparent blue color. The orange, green, and red sine waves correspond to the first, second, and third harmonics, respectively. Area, amplitude and rms pulse fractions in percents, with their 1σ uncertainties, are displayed at the top right corner.

is displayed in Figure 4.10. Both amplitude and area PFs increase with photon energy, saturating at around $\sim$ 70%–75% above 1 keV, with a slight decrease towards 5 keV. Similarly, $p_{\rm rms}$ rises with energy from 0.15 to about 1.2 keV, then declines at higher energies. Although the pulse profiles in Figure 4.9 do not explicitly cover all discussed energy ranges, the analysis considers a broader band to comprehensively explore the pulsar's emission behavior.

We also explored the pulsation behavior using two approaches to represent the 2D phase-energy space of the X-ray events. First, following Arumugasamy et al. (2018), we calculated deviations of counts, $N_{i,j}$, in each phase-energy bin from the phase-averaged value. These deviations were then used to create a significance map, restricted to the $0.15 - 7.0$ keV energy range. Second, we employed a normalization method by Tiengo et al. (2013), dividing counts in

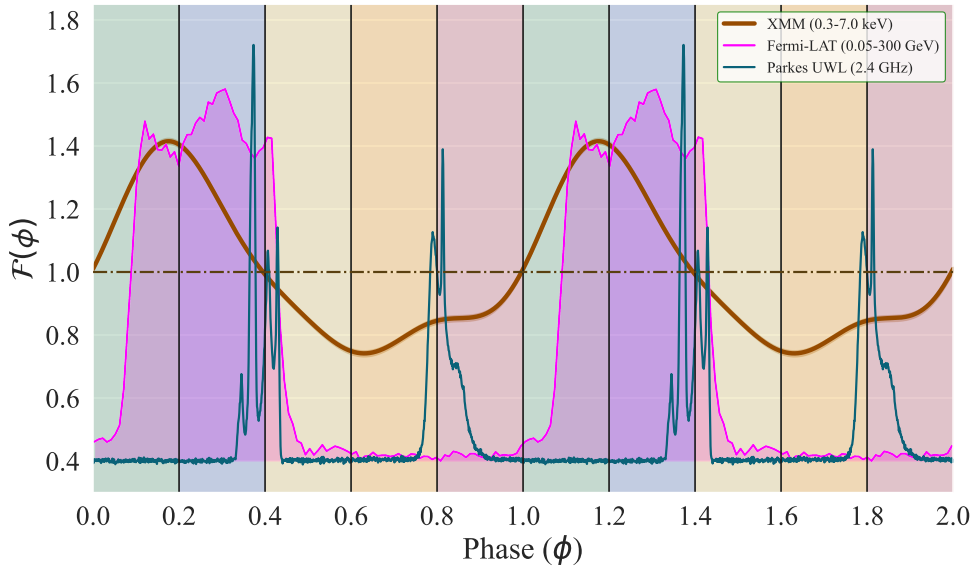

Figure 4.8: Normalized X-ray pulse profile, $\mathcal{F}(\phi)$, in $0.3-7$ keV. Phase bins are displayed with different transparent colors. The Parkes radio light curve (at 2.4 GHz) and Fermi-LAT γ-ray light curve (0.05–300 GeV) are over-plotted with blue and magenta colors, respectively.

phase-energy bins by phase-averaged counts in each energy bin and energy-averaged counts in each phase bin.

The resulting normalized phase-energy map is shown in Figure 4.11 (right). Upon examination, we categorized the counts into four distinct energy regions. In the first region ($0.15-0.3$ keV), we observed minimal pulsation between phases $\phi = 0.1-0.4$, followed by a faint peak between phases $\phi = 0.7-0.9$. The second region ($0.3-0.5$ keV) displayed minimal to negligible pulsation across all phases, contrasting with the continuous pulsation observed in the soft to mid X-ray range in the phase-energy deviation map and the pulse profile.

In the fourth region ($0.5-1.5$ keV), a pronounced pulsation maximum was evident between phases $\phi = 0.1-0.4$, along with a pulse minimum between phases $\phi = 0.6-1.0$, consistent with the pulse profile. The count distribution in the last region ($2.0-5.0$ keV) appeared dispersed in both panels, making it challenging to de-

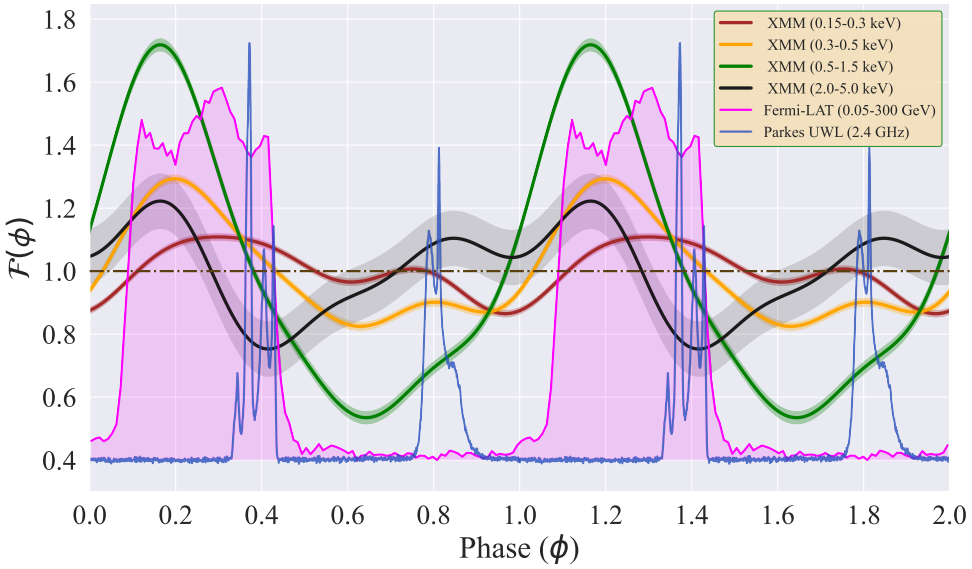

Figure 4.9: Normalized pulse profiles, $\mathcal{F}(\phi)$, are displayed for four energy bands. The X-ray pulse profiles' 1σ uncertainties is depicted with transparent colors. The Parkes radio light curve (at 2.4 GHz) and Fermi-LAT γ-ray light curve (0.05–300 GeV) are over-plotted with blue and magenta colors, respectively.

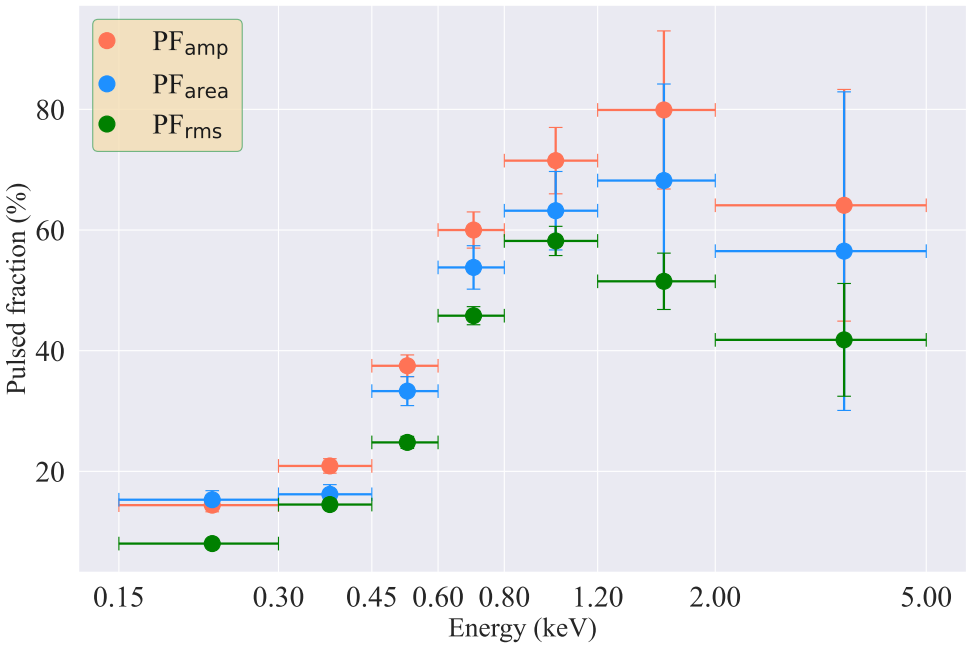

Figure 4.10: Energy dependence of three background-corrected pulse fractions plotted with 90% confidence level errors for the energy bands between 0.15 and 5.0 keV. The orange, blue and green dots correspond to amplitude, area and root-mean-square pulse fractions.

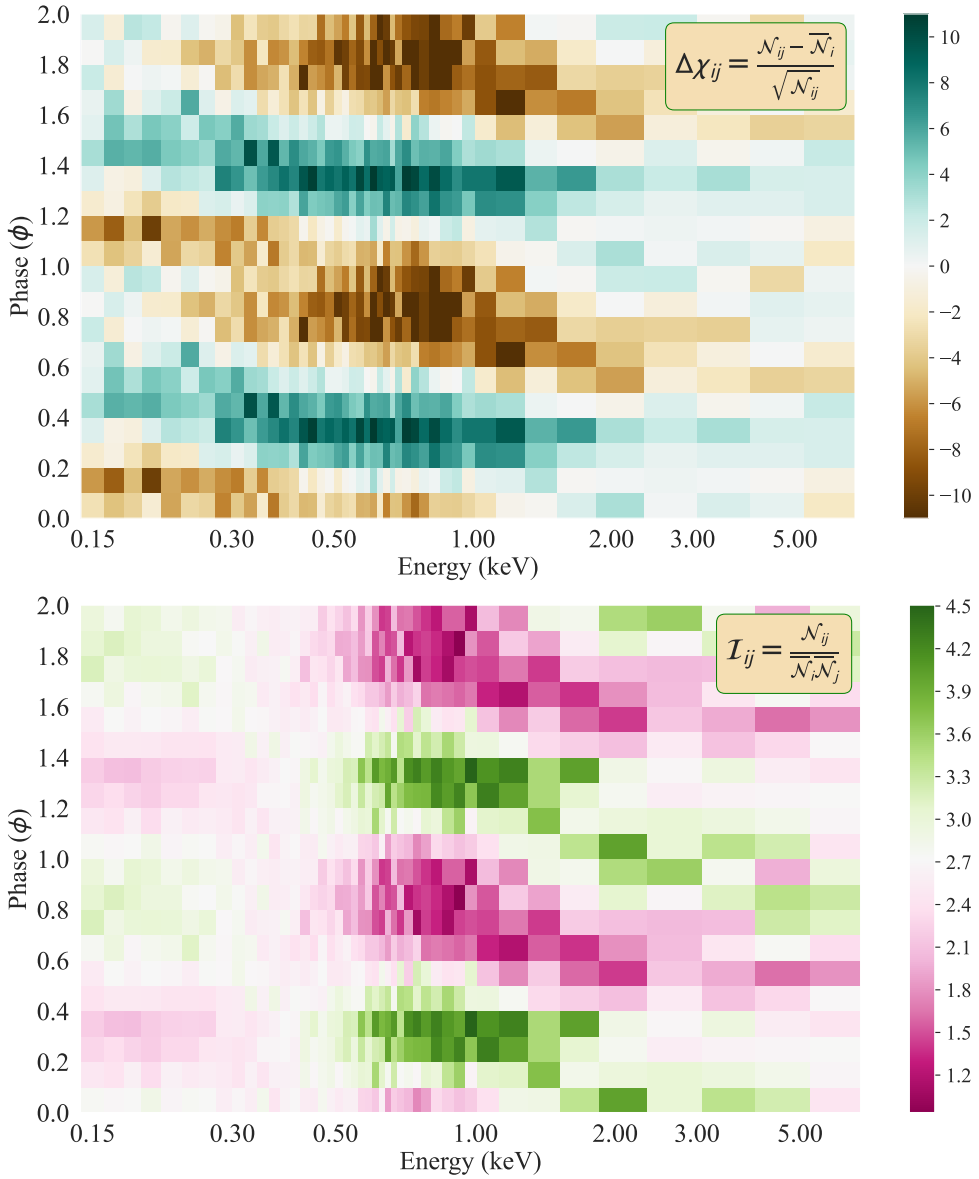

Figure 4.11: Different representations of the EPIC-pn X-ray events of B1055in phase-energy space. The upper panel shows a phase-energy map where only the normalization is applied, while the lower panel shows deviations from the phase-averaged values in each phase-energy bin.

termine the emission pattern, although a pulsation minimum and maximum were observed between $2.0 - 3.0$ keV.

4.2.2 The phase-resolved thermal X-ray spectra

We analyzed the pulsation behavior using phase-resolved spectral analysis, deviating from the commonly used two-temperature blackbody (BB) model for middle-aged pulsars. Instead, we found sig-

nificant phase variations in both the hot and cold BB temperatures, indicating non-uniform temperature distributions on the NS surface.

Similar phase variations in BB temperatures were previously observed for PSR B0656+14 (Arumugasamy et al., 2018). Our analysis of B1055's phase-resolved spectra revealed temperature variations in the hot spot BB ('$S1$'), where the temperature decreased from the peak of the $0.5 - 1.5$ keV light curve to its minimum near the descending part, then increased to a maximum at the ascending part. This temperature fluctuation was partially offset by a normalization variation, resulting in a smaller flux increase than otherwise expected.

The cold BB component showed comparable behavior to the hot BB component, with temperature and radius variations out of phase. These findings contradict the assumption of uniform temperature distribution in the BB components.

Furthermore, the phase-energy maps indicated the presence of a secondary spot ('$S2$'), suggesting the existence of at least one additional thermal component. The presence of $S2$ is also evident in the light curves, particularly in the $0.3 - 0.5$ keV range, coinciding with the radio inter-pulse.

The observed high pulsed fraction (PF) in the $0.8 - 1.2$ keV range for B1055 suggests the presence of hot spots. However, existing models for internal heating and magnetic field configurations do not fully explain the observed PFs. The contribution of atmospheric effects and a toroidal magnetic field component may provide a more comprehensive explanation for the observed behavior. Further in-

vestigations are needed to fully understand the thermal emission properties of B1055.

4.2.3 Heating mechanism in B1055

Hot spots on NS can form through two main mechanisms. Firstly, anisotropic internal heating, driven by heat transfer from the NS interiors to its surface layers, especially in the presence of a nonuniform magnetic field, can create temperature variations. However, existing models fail to fully match observed data for pulsars like B1055. Additionally, if a toroidal magnetic field component exists alongside the dipolar field, it can lead to distinct temperature and size differences in the hot spots, altering the overall thermal distribution.

Another mechanism, external heating, involves relativistic particles from the pulsar's magnetosphere heating its polar caps. This mechanism can explain the thermal X-ray emission from hot spots in older pulsars and may contribute to the X-ray emission of middle-aged pulsars like B1055. Estimates of B1055's hot spot luminosity align with predictions from the polar cap (PC) heating models.

Further complexities arise when considering off-centered dipole magnetic fields, affecting internal and external heating differently. Recent studies have explored these configurations and their impact on temperature patterns, light curves, and spectra in middle-aged pulsars (Igoshev et al., 2021).

In summary, both internal and external heating mechanisms can contribute to hot spot formation on B1055's surface. Detailed at-

mosphere modeling, including beamed emissions, is necessary for a comprehensive understanding, but is beyond the scope of this study and warrants future research.

4.2.4 Nonthermal emission and multiwavelength pulse profile of B1055

The phase shifts seen in multiwavelength pulse profiles, like those observed in B1055 (refer to Figures 4.8 and 4.9), indicate distinct emission mechanisms operating at different locations and heights. Thermal X-ray emission originates directly from the NS surface (Posselt et al., 2023), while radio emission likely arises from higher altitudes above the magnetic poles (Weltevrede and Wright, 2009).

Regarding nonthermal X-ray emission, our spectral analyses reveal a dominant nonthermal component at energies above $\sim$ 2.0 keV. Although its phase-integrated photon index is notably higher than that seen in the GeV gamma-ray range (Posselt et al., 2023), variations in the X-ray photon index across phases are not statistically significant in our observations. The 2.0-5.0 keV light curve displays a prominent peak, aligned with the γ-ray pulse profile, suggesting a potential connection between the locations of nonthermal X-ray emission and γ-ray emission.

Furthermore, our data hints at a secondary peak in the 2.0-5.0 keV light curve near the radio interpulse. This secondary peak is likely due to thermal emission from another hot component rather than nonthermal emission. Unfortunately, the limited number of detected nonthermal X-ray photons prevents a more detailed investigation of this connection.

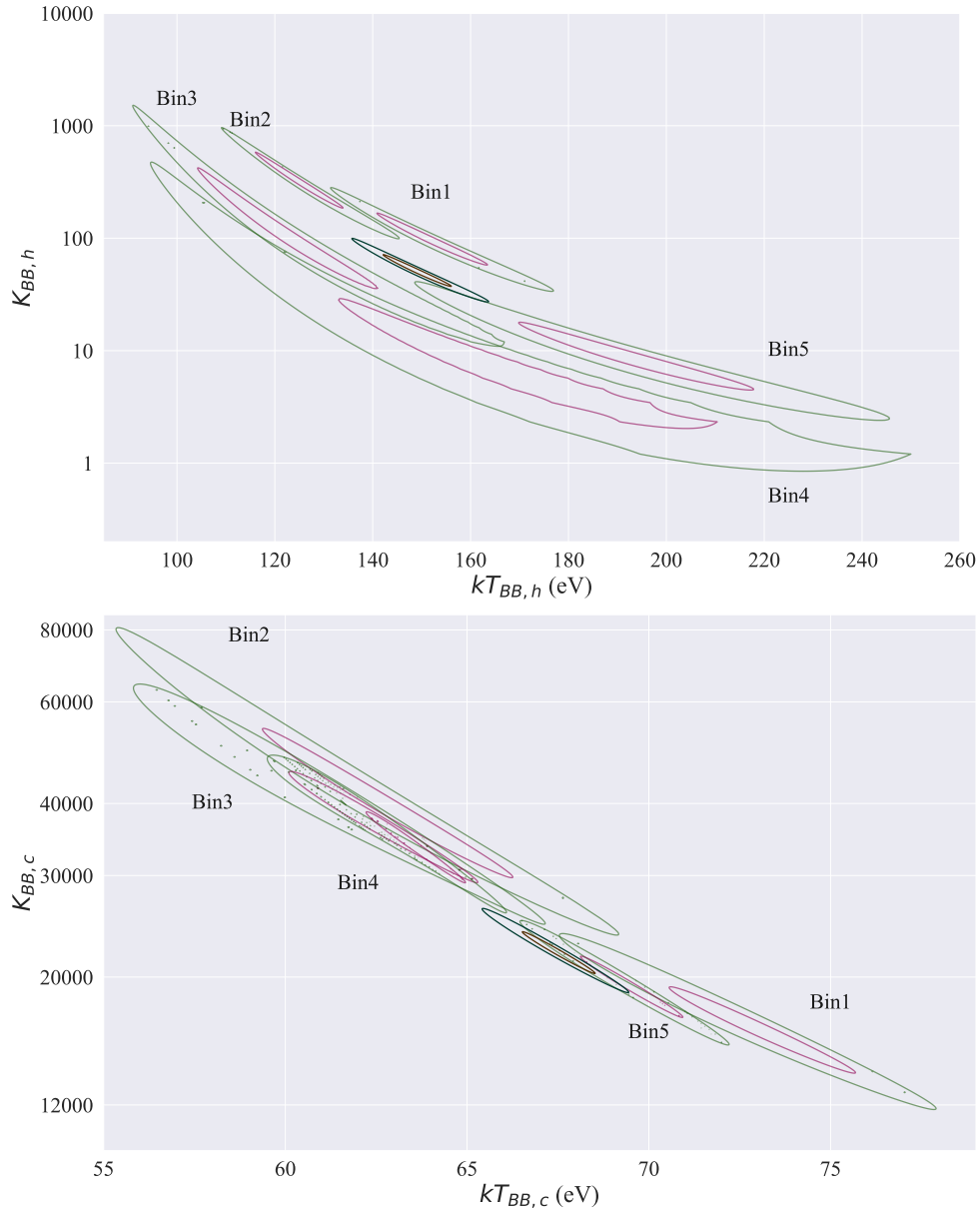

Figure 4.12: Variations of hot BB (top) and cold BB (bottom) with phase in the temperature-normalization plane. Red and green contours correspond to confidences levels of 68.3% and and 99% respectively. Additionally, we depict the confidence contours of phase-integrated spectra using brown (68.3%) and black (99%) colors. Errors are estimated for two parameters of interest. Small dots in some contour plots are small contours themselves representing local minima, indicating a complicated shape of the χ^2 surface.

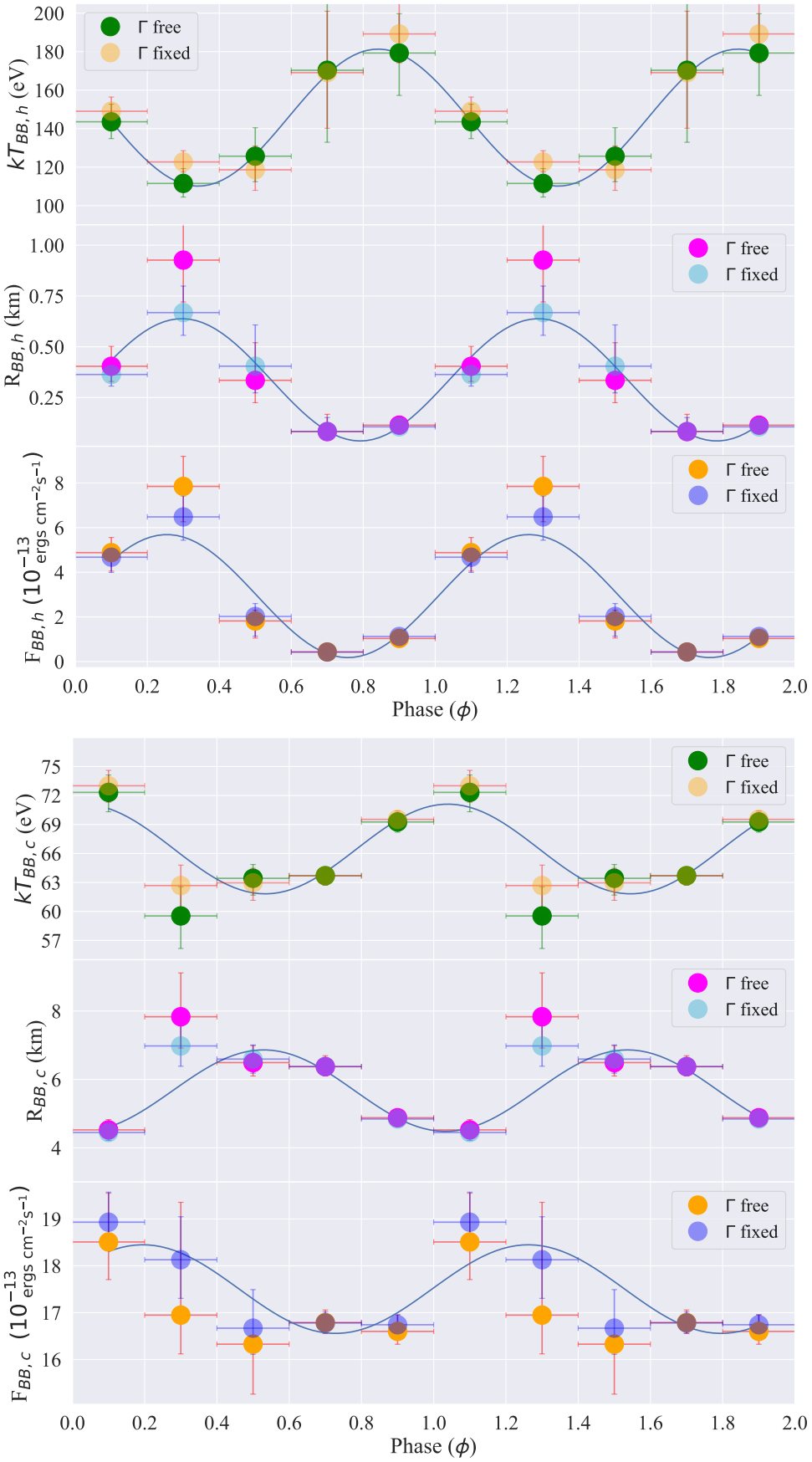

Figure 4.13: Phase dependencies of the temperatures (top), radii of equivalent emitting sphere (middle), and unabsorbed fluxes in $0.3 - 8.0$ keV band (bottom) for hot BB and cold BB components. The vertical error bars show 1σ uncertainties of the fitting parameters. Blue lines represent sine function fits to the data for visualization purposes.

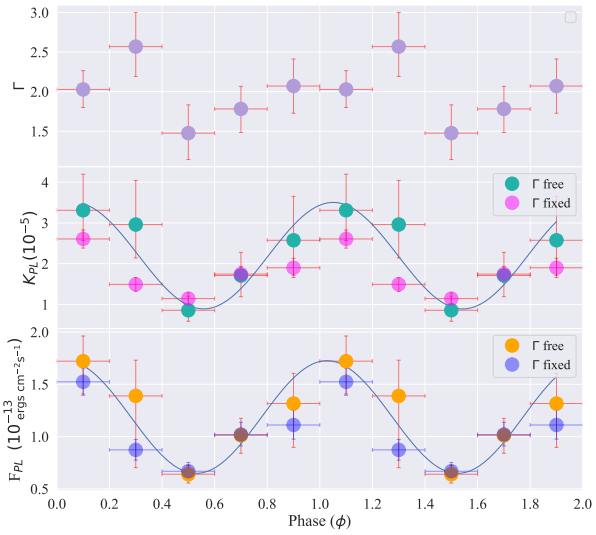

Figure 4.14: Phase dependence of the photon index Γ (top), normalization $K_{\rm PL}$ (middle), and unabsorbed fluxes in $0.3 - 8.0$ keV band (bottom) for the PL component. The vertical error bars show 1σ uncertainties of the fitting parameters. Blue lines represent sine function fits to the data for visualization purposes.

Analysis of the radio and γ-ray light curves offers additional insights into pulsar geometry. B1055 is often interpreted as a nearly-orthogonal rotator based on the separation between its radio interpulse and main pulse. However, existing emission models struggle to fully explain both the γ-ray and radio light curves of B1055. Despite this, recent efforts have attempted to refine these models, albeit without conclusive results for B1055 specifically (Pierbattista et al., 2015).

In our X-ray observations, we observe the primary peak from hot spot S1 at $\phi \approx 0.3-0.4$, along with a secondary thermal X-ray peak possibly linked to another hot spot (S2), trailing the main peak by $\Delta\phi \approx 0.5$. Additionally, S2 manifests as a hump near the radio interpulse phase at $\phi \approx 0.8$ in the 0.3—0.5 keV pulse profile. The time delays observed between the X-ray and radio pulses are consistent with with the two-pole interpretation, supporting the idea of B1055 as an orthogonal rotator. Additionally, the spatial arrange-

ment of emission sites on the NS surface, inferred from polarization angle analysis, further supports this interpretation (Weltevrede and Wright, 2009).

Overall, the observed X-ray and multiwavelength pulse profiles offer valuable insights into the complex interplay of emission mechanisms and pulsar geometry. Further studies and refined models are needed to fully understand these phenomena, particularly in pulsars exhibiting unusual light curves like B1055.

4.2.5 Additional notes and outlook

A future step, as emphasized in our paper, involves modeling the source with light-element atmospheric models and/or a condensed surface. The currently existing atmosphere models, such as NSMAXG (Mori and Ho, 2007; Ho et al., 2008), employ various geometries and assume different surface magnetic fields. However, they cannot adequately fit both the low and high energy spectra. Hence, a more customized atmosphere model is necessary, one that takes into account the geometry and other properties of B1055. Furthermore, all existing atmosphere models are for phase-averaged spectra. To comprehend and constrain temperature variations, phase-dependent modeling is required.

An additional avenue for research could involve conducting detailed magnetothermal simulations to better comprehend the thermal evolution of NS and the phase-resolved temperature nonuniformities observed. Igoshev et al. (2023) have already advanced this field by developing a modified version of the PARODY code,

specifically tailored to analyze surface thermal patterns, light curves, and spectra of off-centered dipoles in middle-aged pulsars. Their enhanced code, named MAGPIES, is open-source and presents an opportunity for further development and application in studying similar cases.

Appendix

A&A 658, A95 (2022)
https://doi.org/10.1051/0004-6361/202141795

stronomy
strophysics

Toward an X-ray inventory of nearby neutron stars

A. Vahdat[1], B. Posselt[2,3], A. Santangelo[1], and G. G. Pavlov[3]

[1] Institut für Astronomie und Astrophysik, Universität Tübingen, Sand 1, 72076 Tübingen, Germany
e-mail: arminvahdat@astro.uni tuebingen.de
[2] Department of Astrophysics, University of Oxford, Denys Wilkinson Building, Keble Road, Oxford OX1 3RH, UK
[3] Department of Astronomy & Astrophysics, Pennsylvania State University, 525 Davey Lab, 16802 University Park, PA, USA

Received 14 July 2021 / Accepted 2 November 2021

BSTR CT

Context. The X-ray emission of neutron stars enables a probe of their temperatures, geometries and magnetospheric properties. The current number of X-ray emitting pulsars is insufficient to rule out observational biases that may arise from poorly known distance, age, or location of the neutron stars. One approach to overcome such biases is to create a distance-limited sample with sufficiently deep observations.
Aims. With the aim of better sampling of the nearby (2 kpc) population of neutron stars, we started an *XMM-Newton* survey of pulsars to measure their X-ray fluxes or derive respective constraining upper limits.
Methods. We investigated 14 nearby pulsars for potential X-ray counterparts using different energy bands and detectors. In addition to our new *XMM-Newton* data, we also considered archival data and catalogs. We discuss source properties and also check for alternative counterparts to the X-ray sources.
Results. In our new *XMM-Newton* data, we found two pulsar counterpart candidates with significance above 4σ and one candidate with 3.5σ by combining EPIC camera detection likelihoods. We also report the detection of potential X-ray counterparts to eight radio pulsars in the 4XMM-DR10 catalog which have not been reported in the literature.

Key words. stars: neutron – X-rays: general

1. Introduction

In solitary neutron stars (NSs), thermal X-rays are produced by the cooling of NS surfaces and from hot spots such as polar caps heated by particles accelerated in the magnetosphere. On the other hand, the accelerated particles generate non-thermal synchrotron and curvature radiation. Interaction of the pulsar wind with the interstellar medium (ISM) produces shocks that can contribute to the non-thermal X-ray emission. This can contaminate the observed pulsar spectrum considerably if the pulsar and pulsar wind nebula are not spatially resolved.

In young, energetic rotation-powered pulsars (RPPs), such as the Crab pulsar, the thermal radiation from the hot neutron star is outshined by non-thermal magnetospheric emission, and the X-ray spectra often have a power-law (PL) shape. As pulsars age, thermal emission becomes more prominent and the spectra can be described by the combination of thermal and non-thermal emission (an example is the Vela pulsar). There are also solitary pulsars that show predominantly thermal X-ray emission, such as central compact objects (CCOs) or the group of stars known as the Magnificent Seven (e.g., Haberl 2007; Gotthelf et al. 2013). Lastly, the millisecond pulsars (ms-pulsars) that are assumed to be spun up through accretion from a companion (Alpar et al. 1982) usually show both thermal and non-thermal emission components in their X-ray spectra. The small emission radii obtained by spectral fits imply the origin of thermal radiation to be one or two heated polar caps, whereas the non-thermal emission is presumed to have a magnetospheric origin (e.g., Zavlin & Pavlov 1998; Forestell et al. 2014).

X-ray emitting NSs have been identified in surveys such as the ROSAT All Sky Survey (0.1–2.4 keV energy; Voges et al. 1999), complemented by X-ray observations with *XMM-Newton* and *Chandra* (e.g., Becker 2009). Neutron stars that were not already known as radio or γ-ray pulsars were noticed in X-rays, either due to signatures of ongoing accretion or simply because they were nearby, young and powerful, or hot. Other NSs were discovered by their variability (outbursts) or activity in other wavelengths, (e.g., soft gamma-ray repeaters). Many X-ray emitting NSs were found in targeted (deeper) searches based on their radio and γ-ray properties. A few pulsars falling in the field of view (FOV) of pointed observations by X-ray satellites have also been discovered (e.g., Pires et al. 2009; Prinz & Becker 2015). However, many NSs were not covered by sufficiently deep X-ray exposures. A selection effect cannot be excluded and may lead to a biased view of the known X-ray emitting NS population, which could result in a biased interpretation of their general X-ray properties such as temperature, spectral index of non-thermal emission, and X-ray efficiency. To date, roughly 5–7% of the known pulsar population has been detected in X-rays.

Pulsars lacking X-ray detection may simply be too faint for the previous surveys, for example because they are too far away or too absorbed, or they may indeed be "X-ray quiet". X-ray monitoring with all-sky surveys such as the ongoing eROSITA will provide an important contribution to obtain a flux-limited population of X-ray emitting NSs in the Galaxy. A complementary approach that aims for an unbiased coverage of the NS population is to restrict the analyzed sample to a certain distance and increase the number of observed sources in that distance range. In this study, we present the first results of an *XMM-Newton* survey aimed at a better sampling of the nearby (2 kpc) NS population.

Although thermal and non-thermal emission can coexist during the lifespan of a NS, the dominant type of emission depends

Table 1. Properties of the ordinary and millisecond pulsars investigated with *XMM-Newton* in this study.

Pulsar	ObsID	t_{PN} (ks)	t_{M1} (ks)	t_{M2} (ks)	b_{PN} (c/s)	b_{M1} (c/s)	b_{M2} (c/s)	P (ms)	D_1 (kpc)	D_2 (kpc)	log $\dot{E}$ (ergs s^{-1})	$N_{H,21}$
J0711–6830	0823030601	11.9 (6.1)	13.8 (9.8)	13.8 (9.2)	2.5 (TN)	0.35 (M)	0.35 (M)	5	0.11	0.86	33.6	0.6
J0745–5353	0823031401	18.9 (13.5)	20.8 (18.4)	20.8 (16.1)	0.4 (TN)	0.2 (TN)	0.2 (TN)	215	0.57	0.25	34.0	3.8
J0942–5552	0823031301	18.7 (13.5)	20.6 (20.2)	20.6 (20.2)	0.5 (TN)	0.35 (TN)	0.35 (TN)	664	0.30	3.8	33.5	5.6
J0945–4833	0823031101	17.7 (11.2)	19.6 (17.5)	19.6 (17.2)	0.5 (TN)	0.2 (TN)	0.25 (TN)	331	0.35	1.51	33.7	3.0
J0954–5430	0823030401	14.7 (4.7)	16.6 (6.9)	16.6 (6.0)	2.0 (M)	0.35 (M)	0.35 (M)	473	0.43	3.96	34.2	6.2
J0957–5432	0823031001	15.7 (5.6)	17.6 (17.2)	17.6 (17.3)	0.8 (M)	0.35 (M)	0.35 (M)	203	0.45	4.33	34.0	7.0
J1000–5149	0823030301	7.0 (5.8)	8.9 (6.2)	8.9 (8.7)	0.4 (TN)	0.35 (M)	0.35 (M)	255	0.13	1.93	33.4	2.2
J1003–4747	0823030201	14.7 (9.3)	16.6 (16.4)	16.6 (16.3)	1.0 (TN)	0.35 (M)	0.35 (M)	307	0.37	2.94	34.5	3.0
J1017–7156 $^{(B)}$	0823030701	10 (5.3)	11.9 (10.7)	11.9 (10.0)	0.6 (TN)	0.2 (M)	0.25 (M)	2	0.26	2.98	33.8	2.9
J1125–5825 $^{(B)}$	0823031601	18.7 (5.7)	20.6 (16.9)	20.6 (16.9)	0.7 (TN)	0.35 (M)	0.35 (M)	3	1.74	2.62	34.9	3.9
J1543–5149 $^{(B)}$	0823030901	6.5 (5.3)	8.4 (8.3)	8.4 (8.2)	0.4 (TN)	0.35 (TN)	0.35 (TN)	2	1.15	2.42	34.9	1.6
J1725–0732	0823031501	15.1 (12.3)	17.0 (16.7)	17.0 (16.7)	0.4 (TN)	0.35 (M)	0.35 (M)	240	0.20	1.90	33.1	1.8
J1740–3015	0823030101	4.7 (1.7)	6.6 (6.0)	6.6 (5.7)	1.0 (TN)	0.35 (M)	0.35 (M)	607	0.40	2.94	34.9	4.7
J1755–0903	0823030501	4.7 (3.9)	6.6 (6.5)	6.6 (6.5)	0.4 (TN)	0.35 (M)	0.35 (M)	191	0.23	1.79	33.6	2.0

Notes. Pulsar names and their *XMM-Newton* obsid's are given in the first and second column. The pulsars in binary systems are marked with $^{(B)}$. The following six column displays EPIC-pn and EPIC-MOS total and GTI-filtered exposure times (given in parentheses) and the GTI filter for the background light curve and the corresponding filters for each EPIC detector. "TN" is thin filter and "M" is medium filter. Source properties are noted in the last five columns. P is the spin period in seconds, D_1 is the best estimate of the pulsar distance in kpc according to ATNF pulsar catalog which uses the *YMW 17* DM-based distance as default, D_2 is the distance in kpc based on the NE2001 model, log $\dot{E}$ is the common logarithm of the spin-down energy loss rate in ergs s^{-1} and N_H is the hydrogen column density in unit of 10^{21} cm^{-2} estimated from the DM as outlined in Sect. 2.4.

on its physical properties such as age and overall energy budget. One key question at the origin of X-ray emission from pulsars is to figure out how much of the available energy budget is converted into X-rays, and how this changes over the NS lifespan.

There is a general correlation between the X-ray luminosity (L_X) from non-thermal and thermal emission (from polar caps) and spin-down luminosity ($\dot{E}$) of NSs, but the X-ray efficiency ($\eta_X = L_X/\dot{E}$) shows a large variation ($\eta_X \sim 10^{-6}$–10^{-2}). The reported spread of η_X can be related to the choice of energy range, spectral model, and consideration of extended emission (Becker & Truemper 1997; Possenti et al. 2002; Li et al. 2008; Kargaltsev et al. 2012). For example, the fluxes in the soft X-ray range are more sensitive to the uncertainties due to the interstellar absorption which may cause a biased view toward the population of thermally dominated NSs.

Furthermore, it has been pointed out by several authors that the X-ray emission becomes more efficient at $\dot{E}$ 10^{34}–10^{35} erg s^{-1}. This could support polar cap and pair cascade model predictions indicating an increase in electron-positron pair heating luminosity (Harding & Muslimov 2011, 2001) or it could reflect the presence of the dominant non-dipole magnetic field (Kisaka & Tanaka 2017). However, there are too few pulsars with $\dot{E}$ 10^{34} ergs s^{-1} to constrain theoretical models. Different sample selections may lead to different X-ray efficiencies. For instance, in middle-aged pulsars the X-ray efficiencies, $\eta_X \sim 10^{-3}$–10^{-2}, seem to be higher than in younger ones, $\eta_X \sim 10^{-5}$–10^{-3} (Kargaltsev et al. 2012; Posselt et al. 2012).

The number of X-ray detected nearby pulsars is currently insufficient to exclude selection biases towards their observational properties. We approach this problem by conducting a survey of the nearby (2 kpc) NS population. In Sect. 2 we describe our source selection strategy and data analysis steps for our survey, including the consideration of nearby multiwavelength sources as alternative X-ray counterparts. In Sect. 3 we present the initial results of the survey, where we provide the significance and upper limits for the observed sources. Section 4 covers the details of our additional serendipitous archival candidates study. Finally, Sect. 5 discusses the X-ray efficiency of sources, the effect of different distance estimates, and the implications.

2. Observations and analyses

2.1. Source selection and observations

We used the ATNF catalog (Manchester et al. 2005, V1.57) to select all known nearby (2 kpc) NSs that had no X-ray coverage in the field of view of archived *XMM-Newton* pointing (search radius 13′ around pulsar position) and *Chandra* pointing (search radius 10′) observations. We chose 2 kpc as a cutoff threshold for the distance of the pulsars. Above this value, the absorption effects become much more problematic for thermal emission, making it harder to detect NS where this type of emission dominates (e.g., the Magnificent Seven, Haberl et al. 2004).

We used distance estimates from the ATNF, which are typically based on the dispersion measure (DM) from radio timing observations, and the electron density model by Yao et al. (2017) (*YMW 17*). Some of these estimates may differ up by to an order of magnitude from the results based on the electron density model by Cordes & Lazio (2002) (*NE2001*). We also list these distances for completeness in Table 1 and discuss distance differences of these estimates in Sect. 5.1. Using the pulsar's spin-down luminosity ($\dot{E}$), distance (D), and average expected hydrogen column density (N_H) calculated from the DM, we assumed a preliminary X-ray efficiency of 10^{-4} to estimate expected absorbed X-ray fluxes. We started our survey with those pulsars for which a detection seemed most likely in a short exposure time. Fourteen pulsars were observed with the *XMM-Newton* EPIC instrument in 2018, with 5–20 ks exposures (Program ID: 082303) with the *Thin* and *Medium* filters. Here we present the results of the first year of the survey. The survey sources observed to date, their exposure times, and their selected observational properties are presented in Table 1.

2.2. Source detection optimization

To optimize the choice of our energy bands for source detection, we analyzed the detection likelihoods of known X-ray-detected pulsars in 4XMM-DR10. We found that the energy bands 0.3–2.0 keV and 1.0–4.5 keV have the highest number of detections based on their maximum likelihood (ML) distributions compared to other bands at soft and mid-X-ray energies. We then analyzed a few pulsars with known X-ray detections using the archival data to test these values and also checked for other broader and narrower bands. We decided to add the following energy ranges for our analyses: 0.3–1.2 keV, 0.3–1.5 keV, and 0.3–4.5 keV. These ranges provided the highest detection significance defined as:

$$S = \frac{N_s}{\hat{\sigma}(N_s)} = \frac{N_T - \alpha N_{bgr}}{\sqrt{N_T + \alpha^2 N_{bgr}}} \quad (1)$$

where N_s is the number of background-subtracted source counts, N_T and N_{bgr} are total counts within the source and background regions, and α is ratio of source to background region[1].

2.3. Data reduction and analyses

All data were reduced with *XMM-Newton* Science Analysis Software (SAS, V18.0.0.) applying standard tasks. We filtered with `FLAG==0` to avoid CCD gaps and bad pixels. We performed a good time interval (GTI) screening to identify and remove flares caused by energetic protons. Since our short observations were impacted by many background flares, standard background flare screening would have often removed more than half of the exposure time. Therefore, we allowed a stronger background contribution in some observations to maximize potential photon numbers from our target. The full list of GTI rates used for observations are presented in Table 1. We tested several GTI filters derived from 100 s binned light curves of events with energies above 10 keV. For each GTI-filtered event file, we generated images and exposure maps in five energy bands as specified above. We then employed the SAS-tool `eregionanalyse` to optimize the aperture that maximizes the source to background count ratio. The range of the optimal extraction radii provided by the routine varied between 10″–15″. We allowed `eregionanalyse` to center on the position that is up to 3σ from the radio pulsar position[2]. We also applied a proper motion correction in our 3σ position uncertainty circle (if available). Only one source (PSR J0745−5353) in our survey has a noticeable proper motion ($\mu_\alpha = -60 \pm 10$ mas year^{-1}, $\mu_\delta = 50 \pm 10$ mas year^{-1}, Parthasarathy et al. 2019). We obtained the background-subtracted source count rates as well as the 3σ statistical upper limits for each X-ray NS candidate covered by the individual EPIC instruments.

In order to obtain combined EPIC count rates and significance, we used the `emldetect` task, and performed simultaneous ML point spread function (PSF) fits to the source count distributions of the EPIC-pn and EPIC-MOS events. The respective values and upper limit values are given in Table 2. The `emldetect` task also provided the statistical positional error for X-ray sources in our survey, and by combining it with the systematic error of 1.5″ (Webb et al. 2020) we obtained the total positional uncertainties to search for multiwavelength sources in the proximity of X-ray NS candidates.

For sources with a combined net count number above 100 in the EPIC instrument, we also performed a spectral fit. PSR J1831–0952 was the only source in our list that satisfied this criterion. For this source we generated source and background spectra from the extraction region provided by `eregionanalyse`. We produced redistribution matrices and effective area files using the usual SAS tasks `rmfgen` and `arfgen`. We then used the SAS task `specgroup` to group the source counts of each spectrum with $\geqslant$15 per bin. We repeated the procedure with 5 cts binning and *cstat* test statistics and obtained similar results, and therefore we only report the former. We provide the spectral fit results in Sect. 4.2.

2.4. Flux estimates

Since there are typically not enough counts to produce meaningful spectral fits for our sources, we had to assume a spectrum to convert the photon flux to energy flux. Ordinary and ms-pulsars can have both thermal and non-thermal emission components. Aiming to represent two extremes, we decided to convert count rates to fluxes assuming two different spectral models, namely a power law (PL) with a photon index of 1.7 (e.g., Becker 2009) and a blackbody (BB) with $kT = 300$ eV (e.g., Forestell et al. 2014). We used `PIMMS v4.11` for this conversion. To account for absorption, we estimated the N_H values using the formula N_H (10^{20} cm^{-2}) = $0.30^{+0.13}_{-0.09}$ DM from He et al. (2013).

For the BB (0.3–2.0 keV) and PL (1.0–4.5 keV) models we converted EPIC-pn count rates to absorbed and unabsorbed fluxes. For the PL model, we chose an output energy range of 1–10 keV for easier comparison with the literature. Since no good parallax or alternative distance estimates were available for our pulsars, we used the DM-based distances (Yao et al. 2017) to convert unabsorbed fluxes and upper limits to isotropic X-ray luminosities $L_{1-10\,keV} = 4\pi D^2 F^{unabs}$.

2.5. Are there alternatives to explain the X ray sources?

We used the 3σ position uncertainty radius to check for nearby optical or infrared sources that could be the origin of the observed X-ray emission or could contribute to it. We used the *Gaia*-EDR3 catalog (Riello et al. 2021), 2MASS (Skrutskie et al. 2006), WISE (Wright et al. 2010), NOMAD (Zacharias et al. 2004) and TESS Input Catalog (Stassun et al. 2018). To test the hypothesis of a different counterpart, we assumed that all the X-ray flux could come from an optical source, and investigated the resulting X-ray to optical flux ratios, and optical to NIR color-color and color-magnitude diagrams, and proper motions and distances if known. We used this information to classify each optical source based on the studies by Maccacaro et al. (1988), Covey et al. (2007), and Bailer-Jones et al. (2019).

We obtained visual magnitudes (m_V) by converting the *Gaia*-EDR3 passbands and colors using Landolt standard stars observed with *Gaia* (Riello et al. 2021). We interpret the obtained ratios of X-ray to optical flux by using the classification scheme by Maccacaro et al. (1988) to determine whether the optical source has a high likelihood of being an AGN or a main sequence star. Objects such as galaxies, and AGNs might not follow the *Gaia* photometry conversion relations (Riello et al. 2021). However, we also used astrometric properties such as distances and proper

[1] Although we list the conservative S (Eq. (1)), an alternate significance definition by Li & Ma (1983),
$S = \sqrt{2}\left\{N_T \ln\left[\frac{\alpha+1}{\alpha}\frac{N_T}{N_T+N_{bgr}}\right] + N_{bgr}\ln\left[(\alpha+1)\frac{N_{bgr}}{N_T+N_{bgr}}\right]\right\}^{1/2}$ would result in a significance higher by a factor of ∼1.2–1.4.

[2] For positions, proper motions, and parallaxes we used the values listed in the ATNF catalog V1.64

Table 2. Properties of the selected ordinary and millisecond pulsars investigated in this study.

Pulsar	ObsID	Δ_{X-R}	PN $_{0.3-2\,keV}$			MOS1 $_{0.3-2\,keV}$			MOS2 $_{0.3-2\,keV}$			Combined EPIC		
			N_s	S	UL	N_s	S	UL	N_s	S	UL	N_s	S	ML
		(arcsec)	(counts)	(σ)	(c/s)	(counts)	(σ)	(c/s)	(counts)	(σ)	(c/s)	(counts	(σ)	
J0711–6830	0823030601	1.7	23.5 ± 13.0	1.8	0.0080	–	–	0.0005	11.3 ± 4.7	2.4	0.0018	54.8 ± 15.7	3.5	14.9
J0745–5353	0823031401	1.5	27.2 ± 7.6	3.6	–	6.2 ± 4.0	1.6	0.0006	8.1 ± 4.3	1.9	0.0007	39.6 ± 9.2	4.3	16.2
J0942–5552	0823031301	9.7	31.7 ± 10.3	3.1	–	–	–	0.0004	–	–	0.0006	–	–	–
J0945–4833	0823031101	2.3	14.8 ± 7.2	2.2	0.0021	3.3 ± 5.1	–	0.0007	–	–	0.0004	–	–	–
J0954–5430	0823030401	1.2	4.4 ± 4.2	1.1	0.0021	1.7 ± 3.2	–	0.0009	2.5 ± 2.9	–	0.0012	–	–	–
J0957–5432	0823031001	8.5	9.0 ± 5.8	1.6	0.0024	8.3 ± 5.6	1.5	0.0008	–	–	0.0003	–	–	–
J1000–5149	0823030301	2.7	–	–	0.0007	–	–	0.0005	–	–	0.0010	–	–	–
J1003–4747	0823030201	2.1	10.5 ± 8.4	1.3	0.0019	3.4 ± 3.8	–	0.0005	–	–	0.0002	–	–	–
J1017–7156	0823030701	5.3	1.6 ± 3.9	–	0.0015	–	–	0.0002	–	–	0.0003	–	–	
J1125–5825	0823031601	0.6	18.8 ± 6.7	2.8	0.0038	17.4 ± 6.3	2.8	0.0012	10.3 ± 5.2	2.0	0.0009	47.4 ± 10.2	4.7	20.9
J1543–5149	0823030901	1.2	4.0 ± 4.0	1.0	0.0018	3.8 ± 3.6	1.2	0.0011	–	–	0.0007	–	–	–
J1725–0732	0823031501	4.4	3.3 ± 3.8	–	0.0006	1.6 ± 2.7	–	0.0004	–	–	0.0003	–	–	–
J1740–3015	0823030101	7.8	6.4 ± 3.5	1.8	0.0064	–	–	0.0008	–	–	0.0008	–	–	–
J1755–0903	0823030501	0.3	6.2 ± 4.1	1.5	0.0031	–	–	0.0006	–	–	0.0009	–	–	–

Notes. The Δ_{X-R} column displays angular separation in arcseconds between the pulsar's radio timing position and the centroid of the nearest X-ray source. Background-subtracted counts N_s at the optimized X-ray source position and their corresponding significance S according to Eq. (1) are listed for each detector, as well as the ML for the detections considering all EPIC instruments together. The 3σ upper limits (UL) for individual instruments are Bayesian upper limits according to Kraft et al. (1991). The ML values are given in 0.3–2.0 keV for PSRs J0745–5353 and J1125–5825 and in 0.3–4.5 keV for PSR J0711–6830.

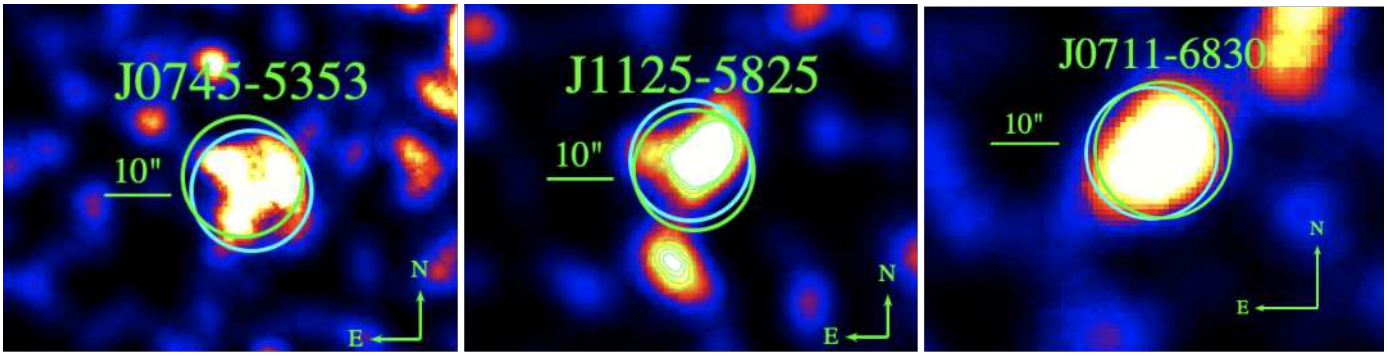

ig. 1. X-ray counterpart candidates in 0.3–2.0 keV as observed with the EPIC-pn and EPIC-MOS2 (PSR J0711-6830). The green circles are centered at the radio timing position of the pulsars, the cyan circles are centered at the position where the X-ray source has the highest significance. The images have pixel scales of 0.4″, and are smoothed with Gaussian length scales σ = 3.4″ (for PSR J1125–5825), and σ = 2.4″ (for PSRs J0745–5353 and J0711–6830). The angular separations between X-ray and radio positions are given in Table 2.

motions from *Gaia*-EDR3 to verify a stellar origin. In the absence of 2MASS counterparts, we converted *Gaia* colors to SDSS colors (Riello et al. 2021) for classifications shown in Table 3 of Covey et al. (2007). Bailer-Jones et al. (2019) did an empirical classification of *Gaia*-DR2 objects (with $G \geqslant 14.5$ mag) using only *Gaia*-DR2 data. They used a probabilistic classifier to catalogue sources as stars, quasars or galaxies based on their *Gaia* colors, magnitudes, and astrometric features such as parallax and proper motion. We took their results into account to classify the potential multiwavelength counterparts in our list.

Finally, we considered the classification into point sources (stars) and extended sources (e.g., galaxies) provided by the TESS Input Catalog. We found ten potential optical counterparts within the 3σ position uncertainty regions of six of our X-ray candidates (including five archival X-ray sources, see section Sect. 4). In order to determine whether these optical sources can be excluded as counterparts of the X-ray emission, we evaluated the respective results of the studies (Table 7).

3. Results

Among the five energy bands mentioned in Sect. 2.2, 0.3−2.0 keV provided the highest overall detection significance in the EPIC instruments for our survey sources. We therefore present the results for this band. We note that the sensitivity loss due to background flaring events (up to 65% exposure time loss) was higher than anticipated for our sources.

In the framework of our program we detected three X-ray point sources with at least 3.5σ sufficiently close to the radio positions of pulsars J0711–6830, J0745–5353, and J1125–5825 to investigate a possible association. The exposure times, used distances, and source properties are listed in Table 1. The angular separation between radio and X-ray position of these pulsars and their EPIC-pn and EPIC-MOS significance are given in Table 2. The corresponding EPIC images of the X-ray counterpart candidates to the three pulsars are displayed in Fig. 1. Their estimated flux and luminosity values are given in Table 5.

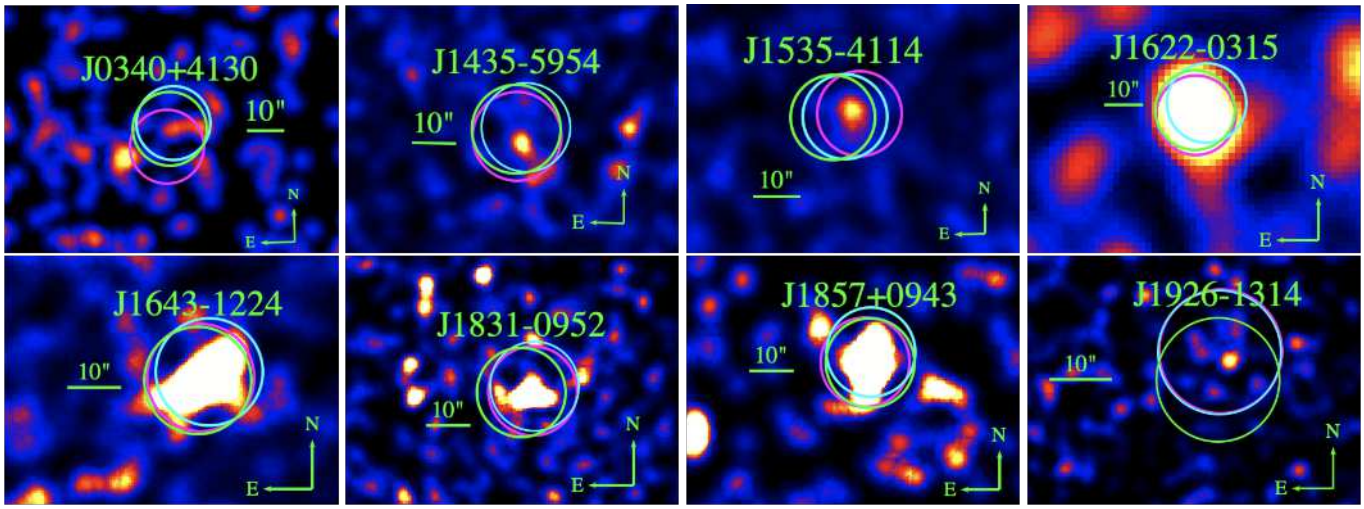

ig. 2. X-ray counterpart candidates in 0.3–2.0 keV as seen with the EPIC-pn (except for J1831 and J1535, which are displayed in EPIC-MOS1). The green circles are centered at the radio timing position of the pulsars, whereas the blue circles are centered at the X-ray source with the highest significance. The magenta circles show the 4XMM-DR10 positions close to these pulsars. The images have pixel scales of 0.4″ and are smoothed with Gaussian length scales $\sigma = 2.2''$ (except for PSRs J1535–4115 and J1926–1314, with $\sigma = 1.4''$). The angular separations between X-ray and radio positions are given in Table 4.

3.1. PSR J0711–6830

The X-ray counterpart candidate is detected 1.7″ away from the radio position of the pulsar. The source may be an example of strong non-thermal emission as the inclusion of higher energies resulted in a detection in contrast to the narrower soft energy band that did not have enough counts. However, detailed inspection of the data revealed an irregular shape of the count distribution in EPIC-MOS2, a noise-like appearance in EPIC-pn, and the absence of the source in EPIC-MOS1, raising doubts about the reality of the detection of this source.

3.2. PSR J0942–5552

For this X-ray source, the location with the highest significance according to `eregionanalyse`, is 9.7″ away from the radio pulsar position. However, the lack of detection in EPIC-MOS1/MOS2 and the high angular separation between the X-ray and radio position prevents us from claiming a match. We also noticed a nearby (unknown) extended X-ray source, but the angular separation of ≈25″ between its emission peak and the radio pulsar position indicates that an association with the pulsar is unlikely. Thus, we conclude that in the sample of 14 pulsars only 2 pulsars, J0745–5353 and J1125–5825, are likely detected (see Fig. 2).

4. dditional archival X-ray counterpart candidates of pulsars

While using archival X-ray source catalogs to optimize our detection energy range, we noticed some potential pulsar counterparts, which to our best knowledge, have not been reported. To identify them, we first matched the radio position of pulsars in the latest ATNF catalog (Manchester et al. 2005, V1.64) with the *XMM-Newton* (4XMM DR10, Webb et al. 2020) and *Chandra* (CSC v2, Evans et al. 2010) catalogs, and selected all the pulsars that fall within the search radius of 10″ (4XMM DR10) and 5″ (CSC v2), respectively. We selected 340 X-ray sources. Assuming an upper limit of 2 kpc on pulsar distance, the number of candidates is reduced to 101. Finally, we excluded all pulsars with known X-ray counterparts using archives such as SIMBAD and ADS. As a result, we identified new potential X-ray counterparts for three nearby pulsars in the 4XMM-DR10 catalog not reported in the literature.

Furthermore, we used the same catalogs to also look for new significant detections of pulsars for which upper limits were reported in X-ray surveys such as carried out by Prinz & Becker (2015) and Lee et al. (2018). Typically, new detections are due to additional data or improved SAS/CIAO processing routines. We found five additional *XMM-Newton* catalog sources within a 10″ search radius of the radio pulsar positions. We did not find any unpublished X-ray emitting pulsar candidates in CSC v2. For consistency, for all the archival sources, we performed the same analyses as we did for our survey pulsars. This allowed a direct comparison in terms of energy bands and fluxes. The source properties and analysis results are provided in Tables 3 and 4. The fluxes are given in 0.3–2.0 keV for the BB model and 1–10 keV for the PL model in Table 5. The total positional uncertainty of archival sources are obtained from the 4XMM-DR10 catalog. We use the `POSERR` at the 3σ confidence level. We note that two of our archival sources have a distance >2 kpc based on the *YMW 17* model, but we decided to include them due to their interesting X-ray characteristics.

4.1. PSR J1622–0315

The redback millisecond pulsar was observed in 2017 in a 22 ks exposure with EPIC and reported to be fitted well with a PL ($= 2.0 \pm 0.3$) in the PhD thesis by Gentile (2018). The X-ray counterpart candidate is located 0.8″ away from the radio pulsar position.

Considering a total position uncertainty of 3.3″ (3σ), we found one *Gaia* source 0.9″ away from the X-ray source which can be excluded as the sole counterpart to the X-ray source (Table 7). The *Gaia* source is reported as the companion counterpart of the pulsar (Strader et al. 2019), but the X-ray emission is expected to come from the pulsar and possibly from an intra-binary shock (e.g., Romani & Sanchez 2016). We can also exclude this source as the main X-ray counterpart of the pulsar based on the contradiction between the expected temperature

Table 3. Properties of the ordinary and millisecond pulsars that are investigated in this study.

Pulsar	ObsID	t_{PN} (ks)	t_{M1} (ks)	t_{M2} (ks)	b_{PN} (c/s)	b_{M1} (c/s)	b_{M2} (c/s)	P (ms)	D_1 (kpc)	D_2 (kpc)	log $\dot{E}$ (erg s^{-1})	$N_{H,21}$
J0340+4130	0605470101	19.5 (6.3)	20.7 (14.8)	20.6 (15.0)	0.4 (TN)	0.35 (TN)	0.35 (M)	3	1.60$^{(*)}$	1.73	33.9	1.5
J1435−5954	0692050101	130.1 (90.0)	–	–	0.4 (M)	–	–	473	1.06	1.18	32.7	1.3
J1535−4114	0652610201	101.4 (63.2)	102.4 (84.6)	102.4 (83.9)	0.4 (TK)	0.35 (TK)	0.35 (TK)	432	2.77	1.95	33.3	1.99
J1622−0315 $^{(B)}$	0784770401	19.0 (4.8)	20.6 (16.5)	20.6 (16.1)	0.4 (M)	0.30 (M)	0.35 (M)	4	1.14	1.11	33.9	0.6
J1643−1224 $^{(B)}$	0742520101	21.8 (9.3)	23.4 (13.8)	23.4 (11.1)	0.4 (M)	0.35 (M)	0.35 (M)	5	0.74$^{(*)}$	2.40	33.8	1.87
J1831−0952	0822330101	–	66.6 (6.2)	66.6 (8.7)	–	0.35 (M)	0.35 (M)	67	3.68	4.05	36.0	7.41
J1857+0943 $^{(B)}$	0742520201	10.0 (5.3)	11.6 (6.3)	11.6 (8.8)	0.4 (M)	0.25 (M)	0.25 (M)	5	1.20$^{(*)}$	1.17	33.6	0.40
J1926−1314	0742620101	75.0 (56.6)	76.6 (54.4)	76.6 (74.7)	0.4 (TN)	0.35 (TN)	0.35 (TN)	4864	1.53	1.48	31.1	1.22

Notes. Pulsar names and their *XMM-Newton* obsid's are given in the first and second column. The pulsars in binary systems are marked with $^{(B)}$. The following six column displays EPIC-pn and EPIC-MOS total and GTI-filtered exposure times (given in parentheses) and the GTI filter for the background light curve and the corresponding filters for each EPIC detector. "TN" is thin filter, "TK" is thick filter and "M" is medium filter. Source properties are noted in the last five columns. P is the spin period in seconds, D_1 is the best estimate of the pulsar distance in kpc according to the ATNF pulsar catalog which uses the *YMW 17* DM-based distance as default, log $\dot{E}$ is the common logarithm of the spin-down energy loss rate in erg s^{-1} and N_H is the hydrogen column density in unit of 10^{21} cm^{-2} estimated from the DM as outlined in Sect. 2.4. Sources with parallactic distance are marked with $^{(*)}$.

Table 4. Properties of ordinary and ms-pulsars with possible counterparts in the 4XMM-DR10 catalog for which we could not find a respective note in the literature or that were previously marked as upper limits.

Pulsar	ObsID	Δ_{X-R}		IAU name	ML	PN$_{0.3-2\,keV}$		MOS1$_{0.3-2\,keV}$		MOS2$_{0.3-2\,keV}$	
		(arcsec)	(arcmin)			N_s (counts)	S (σ)	N_s (counts)	S (σ)	N_s (counts)	S (σ)
J0340+4130	0605470101	4.74	7.8	4XMM J034023.3+413040	12.0	11.4 ± 5.4	2.1	13.9 ± 5.6	2.5	13.6 ± 4.3	3.1
J1435−5954	0692050101	2.59	16.9	4XMM J143500.1–595452	11.3	66.8 ± 17.9	3.7	–	–	–	–
J1622−0315	0784770401	0.84	1.7	4XMM J162259.6–031538	63.5	33.9 ± 7.8	4.3	24.1 ± 6.8	3.5	20.1 ± 6.9	2.9
J1535−4114	0652610201	5.6	4.3	4XMM J153516.5–411402	12.7	72.5 ± 16.5	4.4	21.0 ± 9.8	2.1	19.8 ± 8.5	2.3
J1643−1224	0742520101	1.5	1.1	4XMM J164338.0–122458	112.7	66.8 ± 11.3	5.9	24.4 ± 6.4	3.8	22.3 ± 6.3	3.5
J1831−0952	0822330101	2.2	2.3	4XMM J183134.1–095201	96.9	–	–	28.9 ± 9.6	3.0	29.0 ± 9.7	3.0
J1857+0943	0742520201	1.3	1.2	4XMM J185736.4+094317	38.3	27.9 ± 6.8	4.1	7.1 ± 4.5	1.6	13.8 ± 4.7	2.9
J1926−1314	0742620101	5.5	1.1	4XMM J192653.7–131358	6.9	59.6 ± 16.7	3.5	13.5 ± 8.2	1.6	27.6 ± 9.6	2.8

Notes. Δ_{X-R} column displays angular separation in $''$ between the pulsar's radio timing position and the centroid of the nearest X-ray source according to 4XMM-DR10. is the EPIC-pn off-axis angle. ML is the reported 4XMM-DR10 maximum likelihood in the energy band 0.2–12.0 keV. Background-corrected counts N_s at the optimized X-ray source position and their corresponding significance are displayed for EPIC-pn and EPIC-MOS1/MOS2. PSR J1831–0952 has a ~6σ significance in 0.3–4.5 keV with Epic-MOS cameras. The off-axis angle is given for Epic-MOS1.

of an M star (~3200 K; Rajpurohit et al. 2013) and the reported temperature T_{eff} = 6108 K according to Stassun et al. (2019). There is also one WISE source (ID: J162259.63–031536.9) with an angular separation of 1.2$''$, and due to the lack of WISE colors we are not able to classify the nature of this source.

4.2. PSR J1831–0952

Since the X-ray counterpart candidate has 155 ± 40 combined net counts in the energy range 0.3–10 keV, we performed a spectral fit. *XMM-Newton* only covered the source with EPIC-MOS. For the fit we combined EPIC-MOS1 and EPIC-MOS2 spectra in the 0.3–10 keV energy range. We fitted the spectra with a single PL by first fixing N_H to DM-derived 7.4 × 10^{21} atoms cm^{-2} and then freeing it. In both cases, the photon index is <1.3, consistent with emission from a pulsar (Table 6). Since the N_H value is unconstrained, we only list the latter case. We also carried out BB fits. The temperature we obtained from the fit is ~1.2 keV, which is relatively high. Using the spectral fit, we estimated an unabsorbed flux f, $f_{-14} = f/10^{-14}$ erg s^{-1} = 4.3 ± 0.4 in 1–10 keV for the PL and N_H from Table 3. The reported errors are estimated for the 90% confidence level using the steppar command. Abichandani et al. (2019) briefly reported the *Chandra* detection of a possibly extended source which is coincident with the *XMM-Newton* source (XGPS-I J183134–095155). We also investigated the corresponding *Chandra* observation. The source was observed in VFAINT mode with ACIS-I for 29 ks. We obtained 30.6 net counts in 0.3–8.0 keV. The *Chandra* image of the source is shown in Fig. 3. The image indicates that the source is more extended than a typical point source with the extension of ~10$''$. Most of these counts (~60%) of this extended emission are detected in the energy range 2.4–8.0 keV. Considering this is likely an extended emission, the PWN could be the main contributor of the non-thermal emission.

4.3. PSR J1926−1314

The solitary (τ = 2 Myr) pulsar J1926–1314 was discovered by Rosen et al. (2013) with a relatively high inferred magnetic

Table 5. X-ray fluxes and luminosities of the investigated sources.

Pulsar	Blackbody ($kT = 0.3$ keV)		Power-law (= 1.7)	
	$F^{\rm unabs}_{0.3-2\,\rm keV}$ (10^{-14} erg s^{-1} cm^{-2})	$L^{\rm BB}_{0.3-2\,\rm keV}$ (10^{29} erg s^{-1})	$F^{\rm unabs}_{1-10\,\rm keV}$ (10^{-14} erg s^{-1} cm^{-2})	$L^{\rm PL}_{1-10\,\rm keV}$ (10^{29} erg s^{-1})
J0340+4130	0.46 ± 0.23	14.1 ± 7.1	1.07 ± 0.58	33.4 ± 18.1
J0711–6830	0.58 ± 0.32	0.10 ± 0.06	2.75 ± 1.22	0.44 ± 0.21
J0745–5353	0.80 ± 0.23	3.15 ± 0.90	0.92 ± 0.33	3.58 ± 1.21
J0942–5552	1.38 ± 0.43	1.48 ± 0.52	0.25 ± 0.30	0.23 ± 0.40
J1125–5825	1.36 ± 0.48	49.3 ± 17.5	2.45 ± 1.44	88.9 ± 51.2
J1435–5954	0.45 ± 0.14	6.05 ± 1.3	0.59 ± 0.23	7.93 ± 3.12
J1535–4114	0.31 ± 0.10	28.5 ± 6.4	0.34 ± 0.10	31.2 ± 10.1
J1622–0315	0.85 ± 0.24	13.2 ± 2.9	1.30 ± 0.42	20.2 ± 6.5
J1643–1224	1.58 ± 0.27	10.4 ± 1.8	2.23 ± 0.51	14.6 ± 3.2
J1831–0952	0.41 ± 0.14	66.4 ± 22.7	2.36 ± 0.40	371 ± 60
J1857+0943	0.84 ± 0.23	13.8 ± 3.4	0.54 ± 0.22	9.4 ± 4.9
J1926–1314	0.20 ± 0.05	5.8 ± 1.4	0.15 ± 0.11	4.3 ± 3.1
J0942–5552	<1.21	<1.30	<2.69	<2.90
J0945–4833	<0.79	<1.16	<1.74	<2.55
J0954–5430	<1.22	<2.70	<2.65	<5.86
J0957–5432	<1.57	<3.80	<3.38	<8.19
J1000–5149	<0.19	<0.03	<0.42	<0.08
J1003–4747	<0.63	<1.03	<1.39	<2.28
J1017–7156	<0.49	<0.40	<1.07	<0.87
J1543–5149	<0.42	<6.65	<0.90	<14.2
J1725–0732	<0.15	<0.07	<0.32	<0.15
J1740–3015	<2.96	<5.67	<6.50	<12.4
J1755–0903	<0.81	<0.51	<1.75	<1.11

Notes. The flux values are based on the EPIC-pn count rates (or limits) and two spectral model assumptions. $F^{\rm unabs}$ represents the unabsorbed X-ray flux whereas $L^{\rm BB}$ and $L^{\rm PL}$ columns represent the X-ray BB and PL luminosities respectively. For the luminosity calculation, distances based on the Yao et al. (2017) electron density model are used. The distance uncertainty is not taken into account for error estimation. For PSR J1831–0952, spectral parameters have been obtained (see Table 6) but here we list the flux derived from typical model parameters for consistency.

Table 6. Spectral fit parameters for PSR J1831–0952 obtained from combined MOS data.

Model	/kT / (keV)	$N_{\rm H,21}$	$F^{\rm unabs}_{-14}$	$F^{\rm abs}_{-14}$	χ^2/d.o.f.
PL	0.9 ± 0.3	7.4	4.3 ± 0.4	4.0 ± 0.7	17.8/15
BB	1.2 ± 0.2	7.4	0.4 ± 0.1	0.2 ± 0.04	12.3/15

Notes. Absorbed and unabsorbed fluxed are calculated in 1–10 keV for PL model and in 0.3–2 keV for BB model. Errors are estimated with a 90% confidence interval.

dipole field of $B_{\rm surf} = 1.4 \times 10^{13}$ G. A faint soft X-ray source is detected 5.4″ from the pulsar.

If this X-ray source is indeed the counterpart of the pulsar J1926–1314, and its DM distance estimate (1.5 kpc) is correct, then the estimated X-ray efficiency (above 0.01 for the chosen spectral model parameters, see Fig. 4) is unusually high. Considering the inferred magnetic dipole strength of 10^{13} G, this is interesting with respect to the suggested hypothesis that the magnetic field affects the observed thermal properties of pulsars (e.g., Olausen et al. 2013; Pons et al. 2009).

However, there are three *Gaia* TESS sources within 5″ of the X-ray source (Table 7), and we cannot exclude that any of them is the actual (stellar) counterpart of the X-ray source or contributes to the X-ray flux. Detecting pulsations of the X-ray source would confirm the pulsar counterpart. For this, however, more X-ray counts (i.e., a longer observation) would be required.

5. Discussion

The X-ray analyses of our radio pulsars revealed a few important aspects that explain the low detection rate in the sample. First, more observation time than anticipated was lost due to background flaring events, leading to much shorter scientifically useful exposures. For instance, for four pulsars in our list (J0954–5430, J0957–5432, J1125–5825, and J1740–3015) we lost nearly 65% of the exposure time in the most sensitive detector.

Second, our assumptions for estimating expected fluxes could be too optimistic. We assumed certain spectral models to compute the expected fluxes of ordinary and ms-pulsars. We also assumed an isotropic emission from the compact object for flux-luminosity conversion which may be substantially different in reality. There is another important but rather uncertain parameter that has a substantial impact on the calculated fluxes: distance.

5.1. Distance

Since none of our survey sources had a reliable parallax measurement, we used distances that are based on the DM and the *YMW 17* electron density model. *YMW 17* noted that for high-latitude pulsars, the model benefited considerably from recent parallax measurements of VLBI and pulsar timing array projects,

Table 7. *Gaia*-EDR3 sources that fall within a 3σ positional uncertainty radius of the X-ray sources.

Gaia-EDR3	Associated PSR	μ_α (mas y^{-1})	μ_δ (mas y^{-1})	D (kpc)	$T_{\rm eff}$ (K)	V (mag)	log ($f_{\rm x}/f_{\rm v}$)	Macc88	CV07 (Spectral type)	BJ19	Excluded (S)	Excluded (GXY)
237123598225544064	J0340+4130 (4.64″)	−0.5 ± 0.4	−2.6 ± 0.4	2.0 ± 1.1	4154 ± 182	20.6 ± 0.7	−0.5	AGN	–	S, QSR	Y	Y
5339616527672093056	J1125–5825 (1.27″)	−4.8 ± 0.1	1.1 ± 0.1	4.0 ± 2.0	–	18.7 ± 0.4	−0.85	M, AGN, GXY	M1, M5, M2	S, QSR	N	Y
5339616527704864768	J1125–5825 (3.85″)	−6.8 ± 0.1	1.0 ± 0.1	1.7 ± 0.1	5488 ± 393	16.4 ± 0.3	−1.7	M, K, GXY	G8	S, GXY	N	Y
5878785517750906240	J1435–5954 (4.35″)	−9.5 ± 0.1	−2.4 ± 0.1	2.2 ± 1.1	6635 ± 180	19.1 ± 0.4	−1.3	M, GXY	M6, M7, M8	S, GXY	N	Y
5878785517754291968	J1435–5954 (6.83″)	−6.5 ± 0.2	−2.6 ± 0.1	2.3 ± 1.1	5456 ± 212	19.9 ± 0.5	−0.9	M, AGN, GXY	M5, M6, K7	S, GXY, QSR	N	Y
4358428942492430336	J1622–0315 (0.89″)	−13.2 ± 0.3	2.3 ± 0.2	2.7 ± 1.9	6108 ± 254	19.6 ± 0.4	−0.7	M, GXY, AGN	– – –	S	Y	Y
4310888159960965632	J1857+0943 (2.71″)	−1.9 ± 0.6	−4.1 ± 0.6	1.5 ± 0.8	–	21.5 ± 0.5	−0.2	AGN	– – –	S, GXY, QSR	Y	Y
4186460380401976448	J1926–1314 (0.96″)	–	–	–	–	18.2 ± 0.5	−2.1	M,K	–	S, QSR	N	Y
4186460380401976576	J1926–1314 (1.96″)	5.6 ± 0.9	−4.9 ± 0.5	4.2 ± 2.3	–	14.7 ± 0.4	−1.8	M,K	–	S, QSR	N	Y
4186460380410768640	J1926–1314 (2.97″)	2.4 ± 0.1	−5.4 ± 0.1	1.5 ± 0.1	5861 ± 123	18.4 ± 0.5	−3.5	B-F,G,K	M3, M4, F-8	S, GXY	N	Y

Notes. The respective pulsars are listed in the second column, followed by the angular distance to the *Gaia*-EDR3 source in parentheses. The next columns show the proper motions, distances and effective temperatures obtained from TESS Input Catalog – v8.0 (Stassun et al. 2019). The V-band magnitude (Vega) was estimated from the *Gaia* magnitudes using Johnson-Cousins relationships of Landolt standard stars that were observed with *Gaia* according to Evans et al. (2018). log ($f_{\rm x}/f_{\rm v}$) is the X-ray to optical flux ratio. The Macc88, CV07 and BJ19 columns represent classifications according to Maccacaro et al. (1988) Covey et al. (2007) and Bailer-Jones et al. (2019) respectively. S, GXY, QSR and AGN represents star, Galaxy, Quasar and active galactic nucleus, respectively. For all investigated optical/NIR sources, Stassun et al. (2019) reported a star classification in the TESS input catalog.

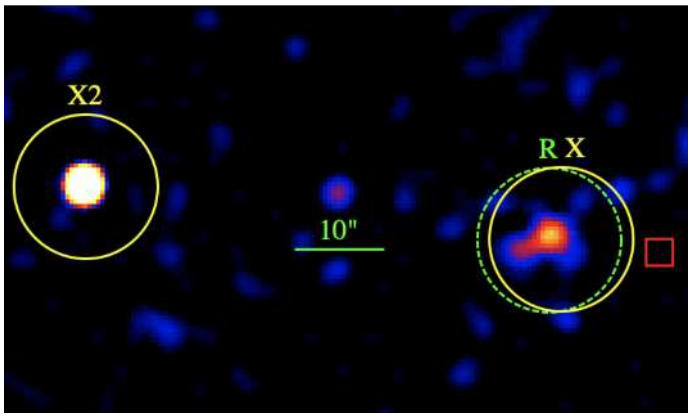

ig. 3. *Chandra* image of PSR J1831–0952 and X2, a point source in the field of view. The green circle is centered at the radio timing position of the pulsar, whereas the yellow circles are centered at the positions of *Chandra* X-ray sources (with off-axis angle of 12.2″ for the extended source, X, and 1.1′ for X2) with the highest significance in *Chandra* observations. The image has a pixel scale of 0.49″ and was smoothed with a Gaussian length scale of $\sigma = 1.25''$. The red square shows the position of the *Chandra* optical axis. Altough the X-ray counterpart of the pulsar is much closer to the optical axis, only X2 has a point-like shape, not showing a tail as the pulsar.

resulting in smaller distance errors compared to *NE2001*-based distance.

In our sample, for ∼70% of the sources, the distances differ by more than a factor of ∼2 between the two models with the *NE2001* model mostly resulting in the larger distance estimates. Interestingly, 57% of our target list would not have satisfied the 2 kpc criterion if we had have had used the *NE2001* model for the distances. Among our detected sources, for J0745–5353 and J1125–5825, the distances provided by the two models differ by a factor of 2 whereas for J0711–6830 the *NE2001*-based distance is ∼8 times higher.

Based on our detection rates, we conclude that we may have underestimated distances in our initial assessments. An improved approach would be to compare different estimates and only observe targets that have parallax measurements, have small distance deviations (less than a factor of 2) for different DM models, or are detectable for the largest listed distance.

5.2. X ray efficiency

Assuming temporarily that the X-ray fluxes of our candidates are solely attributed to pulsars and that the distance estimates are close to reality, we show in Fig. 4 the L_X versus $\dot{E}$ plot for the survey and archival sources for both thermal and non-thermal emission. Many sources in our sample cluster around an efficiency $\eta \sim 10^{-4}$. Only three pulsars from our list of archival X-ray observations have parallactic distances (in yellow in Fig. 4), which are reasonably firm flux estimates. Except for J0711–6830, the two DM distance estimates agree within a factor of 2 for the rest of the pulsars.

The solitary ms-pulsar J0711–6830 has an X-ray efficiency that is 1–1.5 orders of magnitude lower than the typical value. However, if the distance uncertainty is taken into account, this X-ray efficiency is very uncertain. The source does not have a parallax measurement and there is factor of 8 difference between the two DM-based distances ($(D_2/D_1)^2 = 61.1$). If we assume the pulsar is located at 0.86 kpc based on the *NE2001* model, we obtain a luminosity of $L_{0.3-2\ \rm keV} = 5.2 \times 10^{29}$ ergs s^{-1} for the BB model and $L_{1-10\ \rm keV} = 2.5 \times 10^{30}$ ergs s^{-1} for the PL model which places the source at the typical 10^{-4} range in the X-ray efficiency diagram.

Another outlier in Fig. 4 is the middle-aged pulsar J1926–1314 with an X-ray efficiency of $\eta_{\rm X} \sim 10^{-1.5}$. We note that the X-ray efficiency only marginally changes if the *NE2001*-based distance is used. As mentioned in Sect. 4, this source is thought to have a dipole magnetic field that is stronger by a factor 10 than that of a typical middle-aged pulsar. If the X-ray source is indeed the pulsar counterpart and the DM distances are correct, this could indicate a case of magnetothermal heating (see Sect. 4.3).

As can be seen from Fig. 4, our X-ray efficiency values do not vary much for different spectra and energy bands. One reason is that we converted a fixed number of counts in the same energy band to fluxes for both spectral models. Therefore, a large flux variation is not expected. More reliable X-ray efficiencies can be obtained in future works if pulsars have better distance estimates and their thermal versus non-thermal components

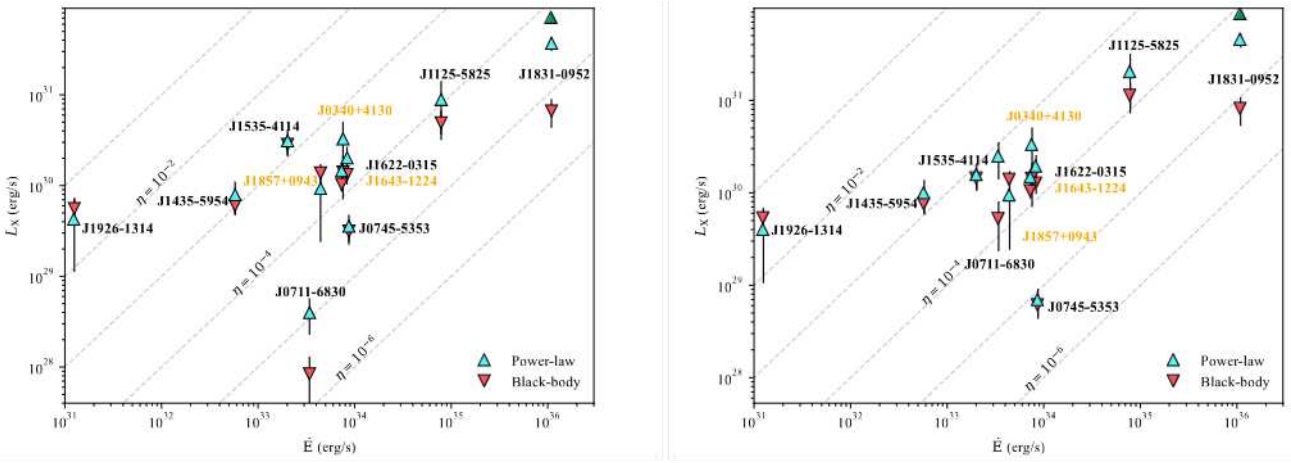

ig. 4. X-ray luminosity of ordinary and millisecond pulsars investigated in this study versus their spindown powers $\dot{E}$ calculated with *YMW 17*-based distances (*left*) and *NE2001*-based distances (*right*). Sources with parallax measurements are displayed with yellow. The up-pointing triangles show the 1–10 keV non-thermal luminosities obtained via the PL assumption (with = 1.7) for the underlying spectra, and the down-pointing triangles show the 0.3–2.0 keV thermal luminosities obtained via the BB assumption (with kT = 300 eV) (see discussion in Sect. 2.4). The spectrum-derived PL flux for J1831–0952 is shown as a green triangle. $\dot{E}$ values are corrected for the Shklovskii effect where relevant (Shklovskii 1970).

are resolved with follow-up observations, as illustrated by PSR J1831–0952.

6. Summary and conclusion

In this study, we reported the first result of our *XMM-Newton* survey aimed at a better sampling of the nearby NS population. We also checked archival catalogues for new X-ray counterpart candidates of pulsars. Our work can be summarized as follows:

1. We searched for X-ray counterparts for 14 nearby pulsars as part of our *XMM-Newton* survey. We analyzed data in all EPIC cameras and obtained background-subtracted source counts and 3σ upper limits for non-detections.
2. We detected two X-ray counterpart candidates at the pulsar positions with over $\sim 4.3\sigma$ significance and one candidate with $\sim 3.5\sigma$ significance.
3. We report on eight X-ray counterpart candidates in the 4XMM-DR10 catalogue for which we could not find a respective note on the X-ray detection of the pulsar in the literature.
4. We suspect that some of our initially chosen distance values may have been underestimated. For the optimized continuation of our survey, a more promising approach is to compare different distance models and choose only pulsars with good parallactic distances or small differences of DM-based distances.
5. Assuming that the X-ray sources are indeed the pulsar counterparts, we calculated the X-ray fluxes, X-ray luminosities, and X-ray efficiencies of these pulsars with two stand-in model spectra, and provided upper limits for our undetected pulsars.
6. We assessed the possibility of an alternative MW counterpart of the reported X-ray sources using their 3σ position uncertainties in combination with the *Gaia*-EDR3, 2MASS, and TESS source catalogs.
7. We argued the possibility of extended emission in PSR J1831–0952 by examining both *XMM-Newton* and *Chandra* data.
8. We speculated that the high X-ray efficiency of PSR J1926–1314 could be attributed to the magneto-thermal heating if the distance is correct and the three stellar sources are excluded as counterparts of or contributors to the X-ray source in the pulsar vicinity.

We obtained X-ray constraints for 22 pulsars, increasing in particular the sample of X-ray investigated pulsars with $\dot{E} < 10^{34}$ erg s^{-1}. Nearby stars might contribute to the X-ray fluxes of some of our pulsar counterpart candidates. For clarification, the candidates could be probed with follow-up X-ray observations aiming for higher position accuracy or pulsation detections.

cknowledgements. We thank the anonymous referee for constructive comments that helped to improve the manuscript. This work was supported by the Bundesministerium für Wirtschaft und Energie through Deutsches Zentrum für Luft-und Raumfahrt (DLR) under the grant number 50 OR 1917. BP acknowledges funding from the UK Science and Technology Facilities Council (STFC) Grant Code ST/R505006/1. GGP acknowledges support from the ACIS Instrument Team contract SV4-74018 issued by the *Chandra* X-ray Observatory Center, which is operated by the Smithsonian Astrophysical Observatory for and on behalf of NASA under contract NAS8-03060. This research has made use of the VizieR catalogue access tool, CDS, Strasbourg, France (DOI : 10.26093/cds/vizier). The original description of the VizieR service was published in 2000, A&AS 143, 23. Software: `Astropy` (Astropy Collaboration 2018), `NumPy` (Harris et al. 2020), `Matplotlib` (Hunter 2007), `Seaborn` (Waskom 2021)

References

Abichandani, R., Mathur, M. B., Drake, J. J., et al. 2019, ATel., 12463, 1
Alpar, M., Cheng, A., Ruderman, M., & Shaham, J. 1982, Nature, 300, 728
Astropy Collaboration (Price-Whelan, A. M., et al.) 2018, AJ, 156, 123
Bailer-Jones, C. A. L., Fouesneau, M., & Andrae, R. 2019, MNRAS, 490, 5615
Becker, W. 2009, in Neutron Stars and Pulsars (Springer), 91
Becker, W., & Truemper, J. 1997, A&A, 326, 682
Cordes, J. M., & Lazio, T. J. W. 2002, ArXiv e-prints [arXiv:astro ph/0207156]
Covey, K. R., Ivezić, Ž., Schlegel, D., et al. 2007, AJ, 134, 2398
Evans, D. W., Riello, M., De Angeli, F., et al. 2018, A&A, 616, A4
Evans, I. N., Primini, F. A., Glotfelty, K. J., et al. 2010, ApJS, 189, 37
Forestell, L. M., Heinke, C. O., Cohn, H. N., et al. 2014, MNRAS, 441, 757
Gentile, P. A. 2018, Ph.D. Thesis, West Virginia University, USA
Gotthelf, E. V., Halpern, J. P., & Alford, J. 2013, ApJ, 765, 58
Haberl, F. 2007, Ap&SS, 308, 181
Haberl, F., Motch, C., Zavlin, V. E., et al. 2004, A&A, 424, 635
Harding, A. K., & Muslimov, A. G. 2001, ApJ, 556, 987
Harding, A. K., & Muslimov, A. G. 2011, ApJ, 743, 181
Harris, C. R., Millman, K. J., van der Walt, S. J., et al. 2020, Nature, 585, 357

He, C., Ng, C. Y., & Kaspi, V. M. 2013, ApJ, 768, 64
Hunter, J. D. 2007, Comput. Sci. Eng., 9, 90
Kargaltsev, O., Durant, M., Pavlov, G. G., & Garmire, G. 2012, ApJS, 201, 37
Kisaka, S., & Tanaka, S. J. 2017, ApJ, 837, 76
Kraft, R. P., Burrows, D. N., & Nousek, J. A. 1991, ApJ, 374, 344
Lee, J., Hui, C. Y., Takata, J., et al. 2018, ApJ, 864, 23
Li, T. P., & Ma, Y. Q. 1983, ApJ, 272, 317
Li, X.-H., Lu, F.-J., & Li, Z. 2008, ApJ, 682, 1166
Maccacaro, T., Gioia, I. M., Wolter, A., Zamorani, G., & Stocke, J. T. 1988, ApJ, 326, 680
Manchester, R. N., Hobbs, G. B., Teoh, A., & Hobbs, M. 2005, AJ, 129, 1993
Olausen, S. A., Zhu, W. W., Vogel, J. K., et al. 2013, ApJ, 764, 1
Parthasarathy, A., Shannon, R., Johnston, S., et al. 2019, MNRAS, 489, 3810
Pires, A. M., Motch, C., & Janot-Pacheco, E. 2009, A&A, 504, 185
Pons, J. A., Miralles, J. A., & Geppert, U. 2009, A&A, 496, 207
Posselt, B., Pavlov, G., Manchester, R., Kargaltsev, O., & Garmire, G. 2012, ApJ, 749, 146
Possenti, A., Cerutti, R., Colpi, M., & Mereghetti, S. 2002, A&A, 387, 993
Prinz, T., & Becker, W. 2015, ArXiv e-prints [arXiv:1511.07713]
Rajpurohit, A. S., Reylé, C., Allard, F., et al. 2013, A&A, 556, A15
Riello, M., De Angeli, F., Evans, D. W., et al. 2021, A&A, 649, A3
Romani, R. W., & Sanchez, N. 2016, ApJ, 828, 7
Rosen, R., Swiggum, J., McLaughlin, M. A., et al. 2013, ApJ, 768, 85
Shklovskii, I. S. 1970, Sov. Ast., 13, 562
Skrutskie, M. F., Cutri, R. M., Stiening, R., et al. 2006, AJ, 131, 1163
Stassun, K. G., Oelkers, R. J., Pepper, J., et al. 2018, AJ, 156, 102
Stassun, K. G., Oelkers, R. J., Paegert, M., et al. 2019, AJ, 158, 138
Strader, J., Swihart, S., Chomiuk, L., et al. 2019, ApJ, 872, 42
Voges, W., Aschenbach, B., Boller, T., et al. 1999, A&A, 349, 389
Waskom, M. L. 2021, J. Open Source Softw., 6, 3021
Webb, N. A., Coriat, M., Traulsen, I., et al. 2020, A&A, 641, A136
Wright, E. L., Eisenhardt, P. R. M., Mainzer, A. K., et al. 2010, AJ, 140, 1868
Yao, J. M., Manchester, R. N., & Wang, N. 2017, ApJ, 835, 29
Zacharias, N., Monet, D. G., Levine, S. E., et al. 2004, Am. Astron. Soc. Meeting Abstracts, 205, 48.15
Zavlin, V. E., & Pavlov, G. G. 1998, A&A, 329, 583

The Astrophysical Journal 963:138 15pp), 2024 March 10 https: doi.org 10.3847 1538-4357 ad20ca

Multiwavelength Pulsations and Surface Temperature Distribution in the Middle aged Pulsar B1055 52

Armin Vahdat[1], B. Posselt[2], G. G. Pavlov[3], P. Weltevrede[4], A. Santangelo[1], and S. Johnston[5]
[1] Institut für Astronomie und Astrophysik, Universität Tübingen, Sand 1, D-72076 Tübingen, Germany; mv.armin@gmail.com
[2] Department of Astrophysics, University of Oxford, Denys Wilkinson Building, Keble Road, Oxford OX1 3RH, UK
[3] Department of Astronomy & Astrophysics, Pennsylvania State University, 525 Davey Lab, University Park, PA 16802, USA
[4] Jodrell Bank Centre for Astrophysics, Department of Physics and Astronomy, University of Manchester, Manchester M13 9PL, UK
[5] CSIRO Astronomy and Space Science, Australia Telescope National Facility, P.O. Box 76, Epping, NSW 1710, Australia
Received 2023 November 26; revised 2024 January 18; accepted 2024 January 19; published 2024 March 7

Abstract

We present a detailed study of the X-ray emission from PSR B1055–52 using XMM-Newton observations from 2019 and 2000. The phase-integrated X-ray emission from this pulsar is poorly described by existing models of neutron star atmospheres. Instead, we con rm that, similar to other middle-aged pulsars, the best- tting spectral model consists of two blackbody components, with substantially different temperatures and emitting areas, and a nonthermal component characterized by a power law. Our phase-resolved X-ray spectral analysis using this three-component model reveals variations in the thermal emission parameters with the pulsar s rotational phase. These variations suggest a nonuniform temperature distribution across the neutron star s surface, including the cold thermal component and probable hot spot s). Such a temperature distribution can be caused by external and internal heating processes, likely a combination thereof. We observe very high pulse fractions, 60%–80% in the 0.7–1.5 keV range, dominated by the hot blackbody component. This could be related to temperature nonuniformity and potential beaming effects in an atmosphere. We nd indication of a second hot spot that appears at lower energies 0.15–0.3 keV) than the rst hot spot 0.5–1.5 keV) in the X-ray light curves and is offset by about half a rotation period. This nding aligns with the nearly orthogonal rotator geometry suggested by radio observations of this interpulse pulsar. If the hot spots are associated with polar caps, a possible explanation for their temperature asymmetry could be an offset magnetic dipole and or an additional toroidal magnetic eld component in the neutron star crust.

Uni ed Astronomy Thesaurus concepts: Neutron stars 1108); Pulsars 1306); Compact objects 288); X-ray astronomy 1810); High energy astrophysics 739)

1. Introduction

PSR B1055–52 B1055 hereafter, also known as PSR J1057–5226) is a middle-aged isolated neutron star NS) sharing common observational properties with Geminga and PSR B0656+14. These three pulsars were dubbed the "Three Musketeers" by Becker & Truemper 1997) due to having similar spin-down energy loss rates, inferred surface dipole magnetic elds, distances, -ray emission, and X-ray spectral properties. The X-ray emission of these pulsars includes thermal and nonthermal components. It is commonly accepted that most of the thermal radiation emanating from the bulk surface of these pulsars results from the heat transfer from the NS interior, hot spots are caused by either anisotropic heat transfer or returning currents from the magnetosphere or both, while the nonthermal emission is due to synchrotron radiation in the magnetosphere e.g., Harding & Muslimov 1998; Pavlov et al. 2002).

The spin frequency and the frequency derivative of B1055 at the reference epoch MJD 57600 are $\nu = 5.07318862008$ 2) Hz and $\dot{\nu} = -150.272(1) \times 10^{-15}$ s^{-2} where 1σ uncertainty of the last signi cant digit is provided in parentheses Jankowski et al. 2019). This corresponds to the characteristic age $\tau = 535$ kyr, rotational energy loss rate $\dot{E} = 3.0 \times 10^{34}$ erg s^{-1}, and surface dipole magnetic eld strength $B = 1.1 \times 10^{12}$ G.

The source was discovered as a radio pulsar by Vaughan & Large 1972). The X-ray emission was discovered with the Einstein observatory Cheng & Helfand 1983). The X-ray pulsations were detected with ROSAT by Oegelman & Finley 1993), who suggested that the X-ray spectrum consists of two components, including soft thermal emission from the NS surface. The results were con rmed with ASCA observations Becker & Truemper 1997, and references therein).

Chandra observations of B1055 revealed that its X-ray spectrum, like those of the two other Musketeers, is best described by a three-component model, comprising cold and hot blackbodies as well as a power-law component Pavlov et al. 2002). XMM-Newton observations of the Three Musketeers allowed for a phase-resolved, low-resolution X-ray spectroscopy, which highlighted some differences between the Three Musketeers in surface temperature distribution and orientations of the rotation and magnetic axes De Luca et al. 2005). There are also differences regarding the X-ray detection of pulsar wind nebulae PWNe) around these close 500 pc) NSs. B1055 and PSR B0656+14 have surprisingly faint PWNe while the three-tail Geminga s PWN is relatively bright e.g., Caraveo et al. 2003; De Luca et al. 2006; Posselt et al. 2015, 2017; Bîrzan et al. 2016).

In the radio region, B1055 exhibits a unique emission pro le, featuring a main pulse MP) and an interpulse IP) separated by approximately 160° in pulse longitude Weltevrede & Wright 2009). These components likely originate from distinct

Table 1
XMM-Newton EPIC Observations of B1055 Used in This Study

Obs. ID	Start Time MJD)	Net Exposure Time ks)			Modes and Filters			Total Count Rate Net Source Count Fraction, %)		
		pn	MOS1	MOS2	pn	MOS1	MOS2	pn	MOS1	MOS2
0113050101	51892	19.3	21.0	21.0	Ti-ME	FF-ME	FF-ME	444.7 ± 6.2 83)	141.7 ± 2.6 98)	147.7 ± 2.7 99)
0113050201	51893	51.1	53.4	53.4	Ti-ME	FF-ME	FF-ME	435.8 ± 3.8 82)	147.5 ± 1.7 99)	148.9 ± 1.7 98)
0842820101	58654	51.7	75.5	75.0	SW-TN	FF-ME	FF-ME	764.2 ± 3.9 97)	124.7 ± 1.3 96)	114.4 ± 1.3 96)
0842820201	58673	54.4	77.7	77.7	SW-TN	FF-ME	FF-ME	738.2 ± 3.7 97)	120.4 ± 1.3 96)	121.3 ± 1.3 96)

Note. Ti-ME: timing mode with medium lter, SW-TN: small window with thin lter, FF-ME: full frame with medium lter. Total count rate counts ks ^{1}) in 0.3–10 keV for 2019 observations and in 0.4–10 keV for 2000 observations.

magnetic poles. The MP–IP separation remains consistent across different radio frequencies, suggesting a highly inclined magnetic axis relative to the pulsar s rotation axis Weltevrede & Wright 2009, and references therein).

In the -ray regime, B1055 exhibits an unusual pro le, as emphasized in the Third Fermi-LAT pulsar catalog 3PC; Smith et al. 2023). It has three overlapping principal peaks with indications of two small peaks preceding and following the outer steep wing of the principal -ray emission components. Only two of the 150 young pulsars in the 3PC show such a complex pro le, and the origin of these pro les is not understood.

The distance to B1055 is still a matter of debate. The ATNF Pulsar Catalogue ver. 1.68) reports 0.093 kpc, based on the DM-based value dispersion measure, DM = 29.69 ± 0.01, Petroff et al. 2013) and the electron density model of Yao et al. 2017), while a distance of 0.714 kpc is derived using the NE2001 model Cordes & Lazio 2002). Mignani et al. 2010) suggested a much smaller distance of 0.2–0.5 kpc by investigating the contributions of the individual thermal components to the multiwavelength spectrum. This distance can also explain the unusually high -ray ef ciency of the pulsar, which has been previously obtained assuming a distance of 750 pc Abdo et al. 2010). Throughout this paper, we will scale the distance to 0.35 kpc to calculate the luminosity and other related quantities.

In this paper we report the results of two new XMM-Newton observations of B1055 carried out in 2019 PI B. Posselt). Posselt et al. 2023a) analyzed the phase-integrated data for a long-term flux variability, but did not nd signi cant differences between these new data and the 2000 XMM-Newton data. However, the new data allow for a better characterization of the spectral and timing properties of the source and tighter constraints on the geometry of the pulsar.

The paper is structured as follows. In Section 2, we describe the data and our data reduction procedure. Section 3 is dedicated to phase-integrated spectroscopy, for which we combine the previous 2000 XMM-Newton data with our new observations to better constrain temperatures and test various atmosphere models. Results of timing analysis are reported in Section 4, where we discuss the pulse pro le and its properties such as pulsed fraction and phase–energy map. In Section 5 we focus on phase-resolved spectroscopy of B1055. Lastly, in Section 6 we discuss our results.

2. Observations and Data Reduction

2.1. X Ray Data

The XMM-Newton observatory observed B1055 on 2019 June 21 for 85 ks and on 2019 July 9 for 81 ks Table 1). During both observations, the European Photon Imaging Camera EPIC, Strüder et al. 2001) was operated in small-window SW) mode for EPIC-pn time resolution 5.7 ms), while EPIC-MOS1 and EPIC-MOS2 cameras Turner et al. 2001) were operated in full-frame FF) mode time resolution 2.6 s). To better constrain the phase-integrated spectral t parameters Section 3), we also reanalyzed the previous XMM-Newton observations of B1055 taken on on 2000 December 14 and 15 for 24 ks and 57 ks, respectively De Luca et al. 2005).

Unfortunately, due to the the collapse of data along the CCD columns, the EPIC-pn data of 2000 obtained in timing mode, are faced with signi cantly higher background contamination, resulting in a lower signal-to-noise ratio S N) above a few keV compared to the 2019 observations.

The data processing of the four EPIC observations was done with the XMM-Newton Science Analysis System SAS) ver. 20.0.0 Gabriel et al. 2004) applying standard tasks. The dead-time-corrected net exposure times, corresponding camera modes and lters, and count rates are given in Table 1.

2.2. Radio Data

We obtained radio pulsar data simultaneously with the XMM-Newton observations. Two 34 ks observations program ID P1010) were carried out on MJD 58655 and MJD 58673 with the CSIRO Parkes 64 m radio telescope also known as Murriyang). We used the UWL receiver 0.7–4.0 GHz) and the MEDUSA backend e.g., Hobbs et al. 2020). The observations were excised of radio-frequency interference RFI) and calibrated using standard `PSRCHIVE` tools Hotan et al. 2004; van Straten et al. 2012). From the averaged pulse pro le, we produced a smoothed, high-S N template. By cross-correlating this template in the Fourier domain Taylor 1992), we generated pulse times of arrival ToAs) for 57 subintegrations for each Parkes observation.

We also obtained simultaneous and contemporaneous data on B1055 from the MeerTime Thousand Pulsar Array TPA) program Johnston et al. 2020). The observations were carried out with the 64-dish SARAO MeerKAT radio telescope. The TPA used the L-band receiver centered at a frequency of 1284 MHz) and a total bandwidth of 775 MHz. Details of the data reduction and RFI removal can be found in Lazarus et al. 2016) and Parthasarathy et al. 2021); details of the TPA procedures such as template production) are reported by Posselt et al. 2023b). We used three observing epochs: MJD 58655.65 simultaneous with XMM-Newton, 5.4 ks), MJD 58678.68 202 s), and MJD 58689.72 202 s) to generate ToAs with the appropriate MeerKAT-based template.

2.3. Ray Data

We used the Fermi Large Area Telescope LAT) -ray data set for this pulsar that was provided with 3PC Smith et al. 2023). The data set consists of photons detected between MJD 54682 and 58791, including the epochs of our X-ray and radio observations, with energies between 50 MeV and 300 GeV.

3. Phase integrated Spectral Analysis

3.1. Spectral Extraction

XMM-Newton observations of 2000 December 14–15 were carried out in timing mode for pn and FF imaging) mode for MOS1 and MOS2. Following the works of Posselt et al. 2015, 2023a), we extracted pn spectra covering energies higher than 0.4 keV since soft background noise can impact the extracted spectra below this energy. We used 33 RAWX pixel 39 to extract the source spectra of both observations 101 and 201 hereafter) whereas 5 RAWX 7 and 4 RAWX 6 were used for background regions of 101 and 201, respectively.

The 2000 EPIC-MOS1 2 data were extracted in the same way as described in Posselt et al. 2015; e.g., circular apertures of 45 and 60 radii for source and background regions).

The EPIC data of 2019 June 20 and July 19 were collected in imaging modes see Table 1). For EPIC-pn the source region is a circle with a radius of 30 . We utilized the SAS tool `eregionanalyse` to ne-tune the position and the aperture that maximize the source-to-background count ratio. For EPIC-MOS1 2 we used the circular aperture of 45 radius, similar to the data of 2000, to extract the phase-integrated spectra. As shown in Figure 1, we have selected the background regions with a circular aperture of 60 radius, suf ciently close to the pulsar to get an accurate estimate of the nearby background contribution but far enough away to avoid contamination from the point-spread function of the source.

3.2. Spectral Fitting

We started our analysis by comparing the two observations of 2019 101N and 201N hereafter) with each other. We have checked and con rmed the consistency of the two data sets in terms of source and background count ratio and distribution and spectral t parameters.

We restricted our energy range to 0.3–8 keV. Above 8 keV, not only does the background contribution exceed the source flux but also the accuracy of our t parameters did not improve further on increasing the upper energy bound.

For X-ray spectral tting, we made use of PyXspec ver. 2.1.0 Python interface with XSPEC ver. 12.12.0 Arnaud 1996; Gordon & Arnaud 2021).

We used the Tübingen–Boulder model through its XSPEC implementation `tbabs` to t the interstellar absorption by setting the abundance table to `wilm` Wilms et al. 2000) and photoelectric cross-section table to `vern` Verner et al. 1996).

We rst tted the high-energy part 2.3–8 keV) of the spectra with an absorbed power-law PL) model `powerlaw` in XSPEC). Although the absorbing hydrogen column density, $N_{\rm H}$, generally does not affect the spectrum at high energies, we xed $N_{\rm H}$ and varied $N_{\rm H}$ at different values and checked the con dence contours of PL-index Γ)-normalization for the two epochs and found an agreement within 1σ in each case.

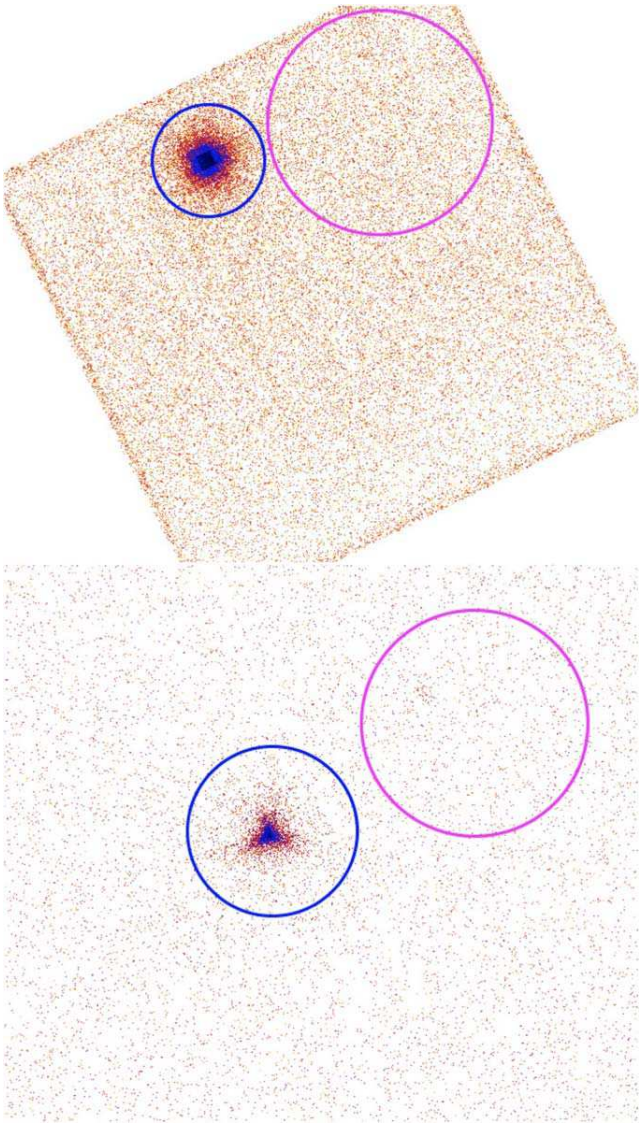

Figure 1. Count map of the eld in the direction of B1055 for the rst observation. The source extraction regions of radii 30 EPIC-pn, top) and 45 EPIC-MOS2, bottom) are displayed in blue whereas the background region of radius 60 is shown in magenta. The images are smoothed with a Gaussian kernel with $\sigma = 1\farcs25$.

In the next step, we t the 0.3–8 keV broadband spectra using a three-component model. This model comprises two blackbody BB) models `bbodyrad` in XSPEC) and a PL model with a best- t value of $\Gamma = 1.8$, determined from the PL-only t. We also allowed $N_{\rm H}$ to vary freely. For the two observations of 2019, we compared the con dence contours of temperature–normalization for the hot and cold BB components and found that their values agreed within a 3σ range Figure 3).

After establishing consistency, we combined the two data sets of 2019 and compared the combined data with the data of 2000 by repeating the same checks. While we obtained a similar consistency level between the 2000 and 2019 data as before, the count statistic and background noise level were different, which was most noticeable at high energies.

Finally we combined the 12 spectra and carried out a 2BB +PL t. We obtained the best t $\chi^2_\upsilon = 1.09$, where $\upsilon = 822$ is the number of degrees of freedom) with BB temperatures

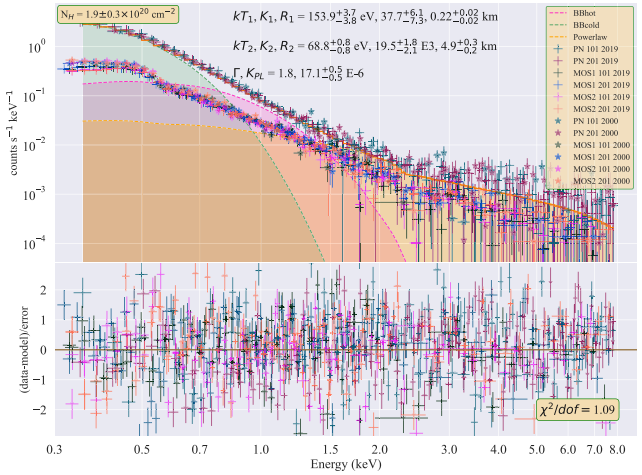

Figure 2. 0.3–8 keV phase-integrated spectral t to the combined 2000 and 2019) data set of 12 spectra with the 2BB+PL model Table 2). Hot BB, cold BB, and PL components are displayed in red, green, and yellow. The t parameters with a margin of 1σ error are also shown at the top of the gure.

$kT_1 = 153.9 \pm 3.7$ eV, $kT_2 = 68.6 \pm 0.8$ eV, and $N_{\rm H} = 1.9 \pm 0.3) \times 10^{20}$ cm ^{2} Figure 2 and Table 2).

We also tested several NS atmosphere models available in XSPEC and applicable to atmospheres with magnetic elds of about 10^{12} G: NSATMOS Heinke et al. 2006), NSA Pavlov et al. 1995; Zavlin et al. 1996), and NSMAXG Mori & Ho 2007; Ho et al. 2008). Fitting with single-component and two-component atmosphere models resulted in large systematic residuals at higher energies $\chi^2_\nu \gtrsim 8$) whereas two-component and three-component models by adding a PL or BB) also produced unacceptable ts as a consequence of large systematic residuals at low energies, 1.5 keV.

4. Timing Analysis

4.1. Radio Timing Solutions

We applied the pulsar-timing code `tempo` Hobbs et al. 2006) for our ToAs to determine the timing solutions for either the two Parkes or the three MeerKAT observations. For this, we used reference epoch MJD 58664.376 near the middle of the two X-ray observations of 2019, see Section 4.3), a contemporaneous MJD 58602) Hubble position and the proper motion from Posselt et al. 2023a). From the `tempo` ts, we obtain the frequency, ν, and its time derivative, $\dot{\nu}$; see Table 3. The difference in ν is 0.13 nHz between the Parkes and MeerKAT timing solutions. This difference is 1.9σ of the MeerKAT timing solution; the difference in $\dot{\nu}$ has a similarly low signi cance level 1.3σ). Hence, the two independent radio timing solutions agree with each other. For comparison with the X-ray data, we will use the Parkes radio timing solution in the following.

4.2. Relative Ray Timing Solution

We folded these Fermi-LAT data for this pulsar using the 3PC ephemeris Smith et al. 2023), which was developed from 12 years of monitoring with Parkes. We replaced the "TZRMJD" and "TZRFRQ" parameters with those from our own radio timing ephemeris to phase-align the -ray pulse pro le with our own radio pro le, and found a radio -ray alignment very similar to that found in 3PC.

Table 2
Parameters for the 2BB+PL Fit of the Phase-integrated Spectrum in the 0.3–8 keV Band for the Combined 12 Data Sets

Parameter Units)	Best- t Results
$N_{\rm H}$ 10^{20} cm ^{2})	1.9 ± 0.3
$kT_{\rm BB,c}$ eV)	68.6 ± 0.8
$K_{\rm BB,c}$ 10^3 $R^2_{\rm km}$ D^2_{10})	19.5 ± 1.9
$R_{\rm BB,c}$ km)	4.94 ± 0.1
$kT_{\rm BB,h}$ eV)	153.9 ± 3.7
$K_{\rm BB,h}$ $R^2_{\rm km}$ D^2_{10})	37.7 ± 6.5
$R_{\rm BB,h}$ km)	0.22 ± 0.02
Γ	1.8
$K_{\rm PL}$ 10 ^{6} photons keV ^{1} cm ^{2} s ^{1} at 1 keV)	17.1 ± 0.5
χ^2 dof	899 822
$F^{\rm abs}_{0.3-8\ \rm keV}$ 10 ^{12} erg cm ^{2} s ^{1})	1.50 ± 0.02
$L^{350\ \rm pc}_{0.3-8\ \rm keV}$ 10^{31} erg s ^{1})	2.80 ± 0.12

Note. Errors are reported at the 1σ con dence level. $K_{\rm PL}$, $K_{\rm BB,c}$, and $K_{\rm BB,h}$ are `powerlaw`, cold, and hot `bbodyrad` normalization parameters.

Table 3
The Radio Timing Properties of B1055

Parameter	Value
R.A. J2000)	10:57:59.0123
Decl. J2000)	52:26:56.509
Position epoch MJD)	58602
Radio timing epoch MJD)	58664.376
Dispersion measure DM)	29.69 cm ^{3} pc
Parkes MJD time span	58655.096–58673.441
Parkes frequency ν)	5.073174809812 17) Hz
Parkes frequency derivative $\dot{\nu}$)	1478 16) $\times$ 10 ^{16} s ^{2}
Parkes tempo2 rms residual	17.6 μs
MeerKAT MJD time span	58655.651–58689.720
MeerKAT frequency ν)	5.073174809686 70) Hz
MeerKAT frequency derivative $\dot{\nu}$)	1500 1) $\times$ 10 ^{16} s ^{2}
MeerKAT tempo2 rms residual	95.1 μs

4.3. X Ray Timing Solutions

Since the time resolution of the MOS detectors in FF mode is as large as 2.6 s, they are not suitable for the timing analysis of B1055. Therefore, we only use the 101N and 201N pn observations, which have a nominal frame time of 5.7 ms in SW mode. We corrected all event times in our data sets to the solar system barycenter using the standard SAS task `barycen`.

The rst event in 101N observation was detected at MJD 58654.849534 barycentric dynamical time, TDB or $t_1 =$ 677,449,468.950103 s in XMM-Newton mission reference time, MRT). For the second observation, the rst event was detected at MJD 58673.018533 TBD or $t_2 =$ 679,019, 270.421713 s in MRT).

The times elapsed between the rst and last detected events for 101N and 201N data sets were $T_{\rm span1} = 79{,}988.797120$ s $\approx$0.9258 days) and $T_{\rm span2} = 79{,}135.1205240$ s $\approx$0.9159 days), respectively.

We used the Z^2_n statistic Buccheri et al. 1983) to study X-ray pulsations in the vicinity of the frequency expected from the radio timing solution. We optimized good time intervals GTI) screenings, energy regions, and extraction apertures to ensure high-S N extraction and large $Z^2_{n,\rm max}$ values.

Table 4
Maximum Values of $Z_n^2(\nu, \dot{\nu})$ for Different Energy Ranges and Numbers of Harmonics n)

Energies keV)	N %bkg)	Z_1^2	Z_2^2	Z_3^2	Z_4^2	χ_v^2
		Combined Z_n^2 values				
0.15–0.3	81,103 6.6)	300	422	440	450	1.2
0.3–0.45	47,549 2.6)	833	983	1002	1004	0.9
0.45–0.6	20,866 1.7)	1209	1260	1291	1294	1.0
0.6–0.8	9181 2.5)	1817	1922	1932	1939	0.9
0.8–1.2	4304 7.5)	1109	1197	1210	1214	1.0
1.2–2.0	1740 27.2)	186	223	242	246	1.5
2.0–5.0	1542 61.5)	20	26	39	33	1.9
0.3–7.0	86,097 4.7)	3739	4082	4155	4159	1.0
	101N top) and 201N bottom) individual Z_n^2 values					
0.3–7.0	44,113 4.6)	1925	2092	2123	2125	1.0
0.3–7.0	41,984 4.7)	1802	1985	2029	2031	1.0

Note. N and %bgd are the total number of counts and the percentage of the average background counts in the source aperture of the combined and individual 101N and 201N) data. χ_v^2 characterizes the agreement between the binned histograms and the harmonic description of the phase-folded light curve in each band.

Prior to the ν and $\dot{\nu}$ search in our X-ray data, we subtracted $t_1 + T_{\rm span2} + t_2$) 2 from the event times of 101N and 201N to minimize the correlation between ν and $\dot{\nu}$, so that the measured ephemeris corresponds to the middle of the two observations i.e., $T_{\rm ref} =$ MJD 58664.376681).

We rst performed the Z_n^2 test separately for the two data sets at xed $\dot{\nu} = -1.478 \times 10^{-13}$ Hz s ^{1} the Parkes frequency derivative; see Table 3), using the `stingray` Python package Huppenkothen et al. 2019). For 101N 201N), we extracted 44,113 41,984) events from GTI- ltered 0.3–7 keV data using the extraction region of 30 radius, which provided the largest $Z_{n,\rm max}^2$ values. From the H-test de Jager et al. 1989) we found that the H-statistic reaches a maximum for three harmonics $n = 3$) for each of the data sets. We obtained $Z_{1,\rm max}^2 =$ 1925 1802) and $Z_{3,\rm max}^2 =$ 2123 2029) for 101N 201N) data at the frequency $\nu =$ 5.07317468 13) Hz 5.07317498 14) Hz). The numbers in brackets indicate the 1σ uncertainties calculated as

$$Z_1^2(\nu_0 \pm \sigma_\nu) = Z_{1,\rm max}^2 - 1 \quad (1)$$

where $Z_1^2(\nu_0) = Z_{1,\rm max}^2$.

The frequencies obtained from the two individual X-ray observations agree with each other within 2σ, and within 5σ with the frequency measured by the Parkes telescope.

In the next step, we combined the two EPIC-pn data sets 86,097 events in the 0.3–7 keV band) and chose the middle of our two observations as the reference time MJD 58664.376681). For the total time span $T_{\rm span\ 1+2)} \approx 19.085$ days, the combined observation should allow one to measure not only frequency, but also frequency derivative. Therefore, we calculated Z_n^2 on a ν–$\dot{\nu}$ grid and found $Z_{1,\rm max}^2 =$ 3739 $Z_{3,\rm max}^2 =$ 4155) at $\nu(Z_{1\rm max}^2) =$ 5.073174881(4) Hz and $\dot{\nu}(Z_{1,\rm max}^2) = +7 \times 10^{-14}$ Hz s ^{1} see Figure 4).

The $Z_{1,\rm max}^2$ and $Z_{3,\rm max}^2$ values in the summed data are very close to the sums of $Z_{1,\rm max}^2$ and $Z_{3,\rm max}^2$ in separate data sets see Table 4), indicating that we reached a good phase connection between the two data sets and obtained a coherent timing solution. However, the difference of 72 nHz between the frequencies measured in the X-ray and Parkes radio data exceeds the formal statistical uncertainty of 4 nHz by a factor of 18. The positive value of $\dot{\nu}(Z_{1,\rm max}^2)$ is in conflict with the well constrained, negative radio timing value, likely indicating an issue with the accuracy of the X-ray timing solution. Since the two independent radio timing solutions agree with each other, we explored technical reasons for the deviating XMM-Newton results and possibilities for correction. First, we checked possible time jumps in our two X-ray time series. Time jumps can occur due to the known effect of temperature on the frame time of the EPIC-pn detector as well as "reset" errors of the counter clock Kirsch et al. 2004). In 101N no real-time jumps have been recognized by SAS, and in 201N they were successfully corrected we set the SAS environment parameter `SAS_JUMP_TOLERANCE` to a value of 44).[6]

The second observation lacks some internal house-keeping data that would allow a detailed monitoring of the detector temperature. Without these additional data, SAS relies on approximations for correcting the temperature-based clock drifts, which, however, usually work very well. Because of the lack of these additional data, we have investigated in particular whether the second observation may cause faulty results. Unrecognized time jumps could in principle occur in ground station switches. Gotthelf & Halpern 2020) had an XMM-Newton observation in the same instrument mode immediately after our second observation. Their results do not indicate any unusual timing offset or timing problems. Instead of the three ground stations in our observation, the data of Gotthelf & Halpern 2020) use only two. We excluded in our observation those times of the additional ground station, suspecting that it may introduce some problem. However, this did not change the X-ray-determined ν which was different by only 2 nHz from the solution with the full X-ray data). Thus, ground station switches in the second observation are unlikely to have introduced any timing error.

Comparing radio- and X-ray-determined pulsation periods of different pulsars in different XMM-Newton instrument modes, Martin-Carrillo et al. 2012) reported a relative timing accuracy, $\Delta P\ P_{\rm radio}$, of better than 10 ^{8}, where ΔP is the difference between the measured period. For our B1055 observations, the relative error is $\Delta P\ P_{\rm radio} = 1.4 \times 10$ ^{8}. This value seems to be reasonably close to expectation. Together with our checks for any possible time jumps, we therefore conclude that we have to add a systematic uncertainty of the order of 60 nHz to our statistical uncertainty of the X-ray-determined frequency.

Similarly, $\dot{\nu}_X$ has a larger uncertainty. Although the timing solution derived from X-rays is less accurate than the one obtained from radio, using this speci c X-ray timing solution maximizes the pulsed X-ray signal. Since the resulting errors in the photon phases are small see Section 4.4), we employed the derived values of ν_X and $\dot{\nu}_X$ in the subsequent X-ray analyses to maximize statistical robustness and consistency in X-rays.

4.4. Timing Properties

We studied the harmonic behavior of the X-ray pulse pro le using the Fourier coef cients. For comparison, we also obtained the folded light curve in the form of a histogram at 0.3–7 keV with the timing solution determined above. The

[6] For more information on the SAS environment parameter, please refer to SAS documentation.

phase-folded light curve and contributions from each harmonic are displayed in Figure 5. The appropriate number of harmonics can be different in different energy bands. We used a chi-square test from the Python library SciPy Virtanen et al. 2020) to compare the sum of three harmonics with the 20-bin histogram of the folded light curve.

The two descriptions of the pulse pro le are in very good agreement. This result implies that binning is not necessary to examine the pulse pro le in such a case of smooth pulsations, and additional uncertainties associated with the binning procedure can be avoided using the Fourier analysis.

The normalized X-ray pulse pro le $\mathcal{F}(\phi)$ see Equation A1) in Hare et al. 2021 for its de nition), in the 0.3–7 keV range, is plotted over the Parkes radio pro le at 2.4 GHz, and the Fermi-LAT -ray light curve from 50 MeV to 300 GeV is shown in Figure 6. Figure 7 highlights the pulse pro les and their 3σ uncertainties in four energy bands together with Parkes radio and Fermi-LAT -ray light curves.

In order to estimate the intrinsic uncertainty in the alignment of the radio and X-ray pro les, we calculated the maximum phase shift, $\Delta\phi_{\max}$, between the X-ray timing solution ν_X, $\dot{\nu}_X$) and the Parkes radio timing solution ν_R, $\dot{\nu}_R$) as follows.

For a given timing solution, the change in phase between times t_1 and t_2 the rst event in the rst observation and the last event in the second observation) is

$$\Delta\phi = \left[\nu + \dot{\nu}\left(\frac{t_1 + t_2}{2} - T_{\rm ref}\right)\right]\Delta t, \tag{2}$$

where $\Delta t = t_2 \quad t_1$ and $T_{\rm ref}$ is the reference time. The difference in phase changes between the radio solution and X-ray solution is

$$\begin{aligned}\Delta\phi_X - \Delta\phi_R = {} & (\nu_X - \nu_R)\Delta t \\ & + (\dot{\nu}_X - \dot{\nu}_R)\frac{t_1 + t_2}{2}\Delta t \\ & - (\dot{\nu}_X T_{\rm ref,X} - \dot{\nu}_R T_{\rm ref,R})\Delta t. \end{aligned} \tag{3}$$

We estimated $\Delta\phi_{\max} = 0.12$, considering the midpoint of each observation as the reference time for the respective solution, and $\Delta\phi_{\max} = 0.13$, considering the beginning of observation 1 and the end of observation 2 as the reference times.

The pulsed fraction PF) is one of the important properties of a folded light curve and depends primarily on the phases and amplitudes of Fourier harmonics and their dependence on energy. We estimated PFs for three different PF de nitions, namely, the amplitude PF $p_{\rm amp}$, sometimes referred to as "peak-to-peak" or "max-to-min" PF), the area PF $p_{\rm area}$), and the rms PF $p_{\rm rms}$; see Appendix C in Hare et al. 2021 for exact de nitions). The energy dependence of the PFs is shown in Figure 8. Both the amplitude and area PFs increase with the photon energy, saturate at ~70%–75% above 1 keV, and show a hint of a decrease toward 5 keV. Similarly, $p_{\rm rms}$ increases with energy in the 0.15 to ~1.2 keV range, and then decreases at higher energies.

While the pulse pro les presented in Figure 7 do not explicitly show all the energy ranges discussed below, it is important to note that the analysis includes a broader range of energy bands to explore the pulsar s emission behavior comprehensively.

In accordance with Figure 7, the pulse pro le at the lower energies, E 0.4 keV, displays the lowest maxima and minima.

The energy range 0.6–0.8 keV, where the transition between the cold and hot BB components takes place see Figure 2), exhibits the highest maxima and deepest minima. Similarly, the range 1.2–2 keV corresponds to the transition region between the hot BB and PL components, with the maxima aligned in phase, but the minimum at 1.2–2 keV occurring approximately 0.2 phases earlier.

A signi cant phase difference of about 0.5 is observed between the maxima and minima in the 0.45–0.6 keV cold BB), 0.6–0.8 keV transition from cold to hot BB), and 0.8–1.2 keV hot BB) ranges. This suggests the presence of a hotter region on the NS s surface once per period, with the closest approach to the line of sight occurring at phases of 0.15–0.2.

Lastly, in the 2–5 keV range PL), the light curve seemingly exhibits two maxima and two minima per period. These maxima occur at phases around 0.2 and 0.7.

There is a noticeable difference in the shape and amplitude of the light curve between 0.15 and 0.3 keV red color with a maximum amplitude at $\mathcal{F}(\phi)\sim$ 1.15) and other bands. It is noteworthy that about half $N = 81{,}103$) of the total events $N = 167{,}600$) are con ned in 0.15–0.3 keV.

We also investigated the pulsation behavior through two different representations of the 2D phase–energy space of the X-ray events. Following the work of Arumugasamy et al. 2018), we calculated the deviations of the counts, N_{ij}, in each phase–energy bin from the phase-averaged value. These deviations from the phase-averaged values are then represented by the signi cance map with pixel values:

$$\Delta\chi_{ij} = \frac{N_{ij} - \overline{N_i}}{\sqrt{N_{ij}}}, \tag{4}$$

where i and j enumerate the energy and phase intervals, respectively, and $\overline{N_i} = J^{-1}\sum_{j=1}^{J} N_{i,j}$ is the phase-averaged counts in the ith energy bin, and J is the number of phase bins. Here we have binned the events in the phase–energy space, using $J = 10$ equal-sized phase bins and choosing variable-size energy bins to maintain $\gtrsim$40 counts per phase–energy bin. Note that this phase–energy deviation map is restricted to the 0.15–7.0 keV energy range, where we have enough source counts Figure 9, left).

Using alternatively a normalization method by Tiengo et al. 2013), the numbers of counts in phase–energy bins, $N_{i,j}$, are divided rst by the phase-averaged counts in the ith energy bin, $\overline{N_i}$, and then by the energy-averaged for the 0.15–7.0 keV energy band) counts in the jth phase bin, $\overline{N_j} = I^{-1}\sum_{i=1}^{I} N_{ij}$, where I is the number of energy channels. The resulting normalized phase–energy map has the following pixel values:

$$I_{ij} = \frac{N_{ij}}{\overline{N_i}\,\overline{N_j}} \tag{5}$$

These results are displayed in Figure 9 right).

Upon examining the right panel the normalized phase–energy map according to Tiengo et al. 2013), we can classify the counts in the map into four distinct regions based on energy. In the rst region 0.15–0.3 keV), a minimum pulsation between phases 0.1 and 0.4 is observed, followed by a faint peak between phases 0.7 and 0.9.

The second region 0.3–0.5 keV) shows a minimal to negligible pulsation across all phases. Interestingly, this contrasts with both the left panel the phase–energy deviation

map) and the pulse pro le in Figure 7, where continuous pulsation is more evident throughout the soft to mid X-ray range.

In the fourth region 0.5–1.5 keV), a pronounced pulsation maximum is present between phases = 0.1 and 0.4, and a pulse minimum between phases = 0.6 and 1, both of which are corroborated by Figure 7.

The count distribution in the last region 2–5 keV) appears dispersed in both the right and left panels, posing a challenge in determining the nature of the observed pulsation. However, it is worth noting that a pulsation minimum and maximum are observed between 2 and 3 keV.

5. Phase resolved Spectral Analysis

We de ned ve equal-sized phase bins and extracted spectra in each bin using the same extraction radius, ltering, and binning criteria as those in the phase-integrated analysis Section 3). We veri ed that these bins contained enough at least 15,000) counts to suf ciently constrain the spectrum. Building on the phase-integrated best 2BB+PL t, we carry out spectral ts, freezing the absorbing hydrogen column and photon index to their best- t values, $N_{\rm H} = 2 \times 10^{20}$ cm ^{2} and $\Gamma = 1.8$. Each spectrum, its best- t model parameters, and χ^2_ν values are shown in Figure 10. In contrast to the approach by De Luca et al. 2005), where the temperatures were xed due to a low S N, our analysis bene ts from a higher S N, which allowed us to vary both the temperatures and their corresponding normalizations in our spectral t. For each bin, a good t was obtained, constraining the parameters of the three spectral components throughout all phases. However, in the fourth bin = 0.6–0.8), the `ftest` indicated that the inclusion of the hot BB component is statistically not required. Variations of hot and cold thermal components with rotational phase are demonstrated by the temperature–normalization con dence contours for ve phase bins Figure 11), as well as the phase dependences of temperature, radius, and unabsorbed flux Figure 12).

For the cold BB component, the phase-integrated spectrum yields the best- t temperature $kT_{\rm BB,c} = 69$ eV and an equivalent emitting sphere radius of $R_{\rm BB,c} = 0.035 K^{1/2}_{\rm BB,c} d_{350} \sim 5$ km. We see that the best- t temperature varies from 75 eV in Bin 1 to approximately 65 eV in Bins 2 and 3, subsequently returning to a value of 70 eV in Bin 5. The apparent radius exhibits variations anticorrelated with temperature, increasing from 4.4 km in Bin 1 to around 7 km in Bin 2 and then decreasing to 4.8 km in Bin 5. Although the temperature–normalization contours move almost in the direction of their maximal stretch, caused by the anticorrelation between the temperature and radius, the variation is likely real as demonstrated by the parameter uncertainties in Figure 12. In addition, the 99% con dence contours of Bin 1 and Bin 5 are clearly separated from the respective contours of the other bins in Figure 11.

The variability in the variations of unabsorbed 0.3–8 keV flux $F^{\rm unab}_{\rm BB,c}$ varies approximately in phase with $kT_{\rm BB,c}$ perhaps with a slight phase shift) because the flux in the Wien tail of a thermal spectrum is particularly sensitive to temperature variations. However, the relative variations of the flux are small, within ∼10% of its average value, because the effect of temperature variations is partly compensated by antiphase variations of emitting area, $\propto R^2$.

The hot BB component exhibits more pronounced phase variations. Its temperature oscillates with phase, with minimum in Bin 2 and maximum in Bin 5, in concert with the cold BB temperature. The variations in radius and emitting area) are anticorrelated with the temperature variations, similar to the cold BB. In contrast to the cold BB component, the unabsorbed flux associated with the hot BB component $F^{\rm unab}_{\rm BB,h}$) varies in phase with $R_{\rm BB,h}$ hence with the projected area of the hot region), and in antiphase with hot and cold temperatures and the cold BB flux. Such behavior is consistent with the phase shift between the low-energy and mid-energy light curves Figure 7). The hot BB flux is substantially lower by a factor of about 6, on average) than the cold BB flux, and it shows much stronger variations, with a minimum value close to zero, and relative amplitude of about 50%.

We also checked whether allowing Γ to vary would change the variations in thermal parameters. The results are also plotted in Figure 12, showing no signi cant differences between the cases of free and xed Γ. For both xed and free Γ, the PL normalization varies in antiphase with the emitting area of the hot BB component Figure 13).

6. Discussion

6.1. Discrepancy between X Ray and Radio Timing Solutions of B1055 52

As described in Section 4.3, we nd a relative difference between the measured X-ray and radio periods of ΔP $P_{\rm radio} = 1.4 \times 10$ ^{8}. Although this is in agreement with the relative timing accuracy in different XMM-Newton instrument modes Martin-Carrillo et al. 2012), the high statistical signi cance of this difference prompted us to also consider a pulsar glitch as a potential nontechnical explanation.

However, the simultaneous radio observations from Parkes, which are sensitive to frequency variations, show no indication of a glitch during the observed period. There is also no indication of a glitch from the three considered epochs of MeerKAT data. Moreover B1055 is not known to exhibit glitching behavior. From a monthly monitoring program with Parkes since the beginning of 2007, Lower et al. 2021) reported only a 90% upper limit on the size of undetected glitches of $\Delta\nu_g^{90\%}/\nu < 3.4 \times 10^{-9}$ for B1055. This glitch limit is below our X-ray radio discrepancy. For these reasons, we regard it as highly unlikely that B1055 experienced an undetected glitch between the X-ray observations or after the simultaneous Parkes coverage ended in the second XMM-Newton observation.

6.2. The Phase resolved Thermal X Ray Spectra

One or two BB components are commonly used to describe the thermal spectra of middle-aged pulsars e.g., Caraveo et al. 2004; De Luca et al. 2005 for the Three Musketeers; Schwope et al. 2022 for PSR B0656+14; Rigoselli et al. 2022 for PSR 1740+1000). However, our phase-resolved spectral analysis shows that such a two-temperature model is not a fully consistent description of the data because both the hot and cold BB components show signi cant variations with phase. Hence, the temperature is not uniformly distributed, neither in the hot spot nor on the bulk NS surface. Arumugasamy et al. 2018) showed similar phase variations of the cold and possibly the hot BB temperatures for PSR B0656+14 their Figure 13), although without providing 2D con dence contours for normalization and temperature.

Based on the phase-resolved spectra of B1055 Figure 10) and the respective parameter evolution over phase left panels of Figures 11 and 12), the behavior of the hot spot BB "S1") can be summarized as follows.

Starting from Bin 1, which includes the maximum of the 0.5–1.5 keV light curve where the hot BB component dominates; see Figure 7), the temperature of the hot BB component decreases with increasing phase and reaches a minimum near the boundary between Bin 2 and Bin 3, i.e., on the descending part of the light curve. While the light curve reaches its minimum near the boundary between Bin 3 and Bin 4, the temperature rises to its maximum at Bin 5, at the ascending part of the light curve. The phase shift between the temperature and the 0.5–1.5 keV flux oscillations is caused by the normalization projected area) varying in the opposite direction to the temperature variation. In particular, the increase in temperature between Bin 3 and Bin 5 is partly compensated by the decrease in normalization between Bin 2 and Bin 5, so that the increase in the flux is substantially smaller than it would be at a constant normalization.

The cold BB component exhibits similar behavior to the hot BB component between Bin 1 and Bin 2, where the temperature starts to decrease and the normalization radius) begins to increase right panels of Figures 11 and 12). However, during the transition from Bin 2 to Bin 4, both kT and the normalization remain nearly constant, within a 1σ range. The cold BB component shows antiphase variations of the temperature and radius, similar to the hot BB component.

The observed behavior of the temperature and visible area is incompatible with the assumption of a uniform temperature in the hot and cold BB components. With this assumption the kT–normalization con dence contours would be shifting along the normalization axis, in contrast to the actual observations Figure 11, left).

Evidence for at least one other thermal component is also provided by the phase–energy maps. They indicate the presence of another, secondary spot "S2"), best visible in the right panel of Figure 9, at phases ~ 0.2–0.5 and energies E 0.3 keV. For a centered dipole, one would expect two similar hot spots. For a nearly orthogonal rotator, these two hot spots should correspond to two maxima in the light curves. In principle, the location of the second hot spot could be such that only a portion of it is visible during a rotational cycle. B1055 is likely a nearly orthogonal rotator, as indicated by the radio pulse pro le with two pulses per period Figure 7). Therefore, second hot spots would be the natural explanation for the pulsar s S2 emissions. However, S2 s apparent lower temperature lower energy in the phase–energy map) is puzzling. S2 is also noticeable in the light curves. In the softer energy band, ∼0.3–0.5 keV, a second smaller hump, which might be associated with S2, appears. It is aligned perhaps coincidentally) with the radio interpulse. In addition, the phase-dependent cold BB temperature Figure 12) shows a flattening around the minimum $= 0.2$–0.8), possibly due to the contribution from the warm second spot S2.

Taking into account bending of photon trajectories by the NS gravitational eld and assuming locally isotropic BB emission emerging from the surface, Turolla & Nobili 2013) calculated light curves and the pulsed fraction, $\mathrm{PF}_{\mathrm{amp}}$, as a function of the viewing angle and hot spot position for one and two spots with various angular radii. In particular, they found that for two antipodal spots of equal temperatures and sizes on the surface of a NS with mass $M = 1.4\ M$ and radius $R = 15$ km, the maximum pulsed fraction, $\mathrm{PF}_{\mathrm{amp}} \approx 29\%$ for energy-integrated flux, is reached for an orthogonal rotator. The measured PF in the 0.8–1.2 keV range for B1055, corresponding to the hot spot emission, is signi cantly higher, reaching approximately 65%–70%. But Turolla & Nobili 2013) also showed that much higher PFs up to 100%) can be obtained if there is only one spot, or two rather different non-antipodal spots. However, this nding alone does not allow us to conclude that B1055 has very different or non-antipodal hot spots because another reason for high PFs can be the presence of a light-element H or He) NS atmosphere. Emission from such an atmosphere is beamed along the magnetic eld Pavlov et al. 1994), and we can expect a higher PF if the hot spot is associated with the magnetic pole, where the magnetic eld is normal to the emitting surface. We note that the badly tting) atmosphere models mentioned in Section 3.2 are not applicable to phase-resolved spectra.

Hot spots could be formed by two different mechanisms. First, they could be due to anisotropic internal heating, i.e., anisotropic heat transfer from the very hot NS interiors to colder surface layers in the presence of a nonuniform magnetic eld. Even a moderately strong dipole magnetic eld, such as B1055 s $B \sim 10^{12}$ G, can lead to noticeable temperature nonuniformity, with a colder equatorial belt and a hotter area of the rest of the surface, slowly increasing toward the magnetic poles of a centered dipole e.g., Yakovlev 2021). However, although the spectrum of such an NS can be tted with a BB +BB model, the ratios of hot and cold temperatures and radii are very different from the observed ones, for B1055 and other middle-aged pulsars Figure 14).

If, in addition to the dipolar magnetic eld, there is a toroidal eld component in the NS crust, then the two hot spots around the poles of the dipolar component can have different temperatures and sizes Geppert et al. 2006). The toroidal component leads to the blanketing effect, channeling heat flow along the polar axis and creating an extended cold equatorial belt with an asymmetric temperature distribution that covers most of the stellar surface.

Any scenario that involves hot spot s) should explain the observed high PFs. Geppert et al. 2006) estimated PFs for various surface temperature distributions involving two warm spots, assuming semi-isotropic BB emission. They obtained a maximum pulsed fraction of $\mathrm{PF}_{\mathrm{amp}} = 33\%$ for an orthogonal rotator, which remains much below the observed values for B1055 65%–70% in the 0.8–1.2 keV energy range and even 38% for energies 0.5 keV).

Perna et al. 2013) considered coupled thermal and magnetic evolution of an NS and computed surface temperature and magnetic eld distributions at different ages for a variety of initial magnetic eld con gurations. Assuming local BB spectra, they considered not only the semi-)isotropic angular distribution of emitted radiation but also radiation moderately beamed along the local magnetic eld direction, mimicking emission from a light-element atmosphere. Interestingly, addition of a large-scale toroidal magnetic component disrupts the north–south symmetry of the temperature distribution due to the Hall effect, resulting in single-peaked light curves and notably heightened PFs. For speci c models, these PFs exceed 50%, within the 0.5–2 keV energy band. Overall, the presence of a dominant large-scale toroidal magnetic component and or atmospheric beaming effects could explain high PFs.

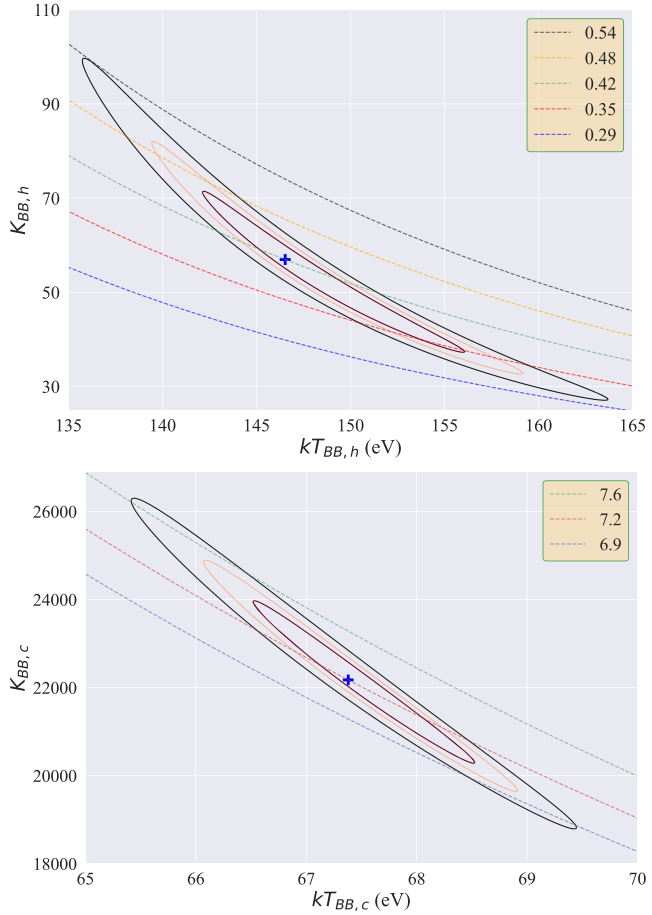

Figure 3. Hot BB top) and cold BB bottom) con dence contours for phase-integrated spectra using 101N and 201N pn data. Blue plus signs correspond to minimum values of χ^2. Contours of constant bolometric luminosity of an equivalent sphere, $L_{\rm BB} = 4\pi R_{\rm BB}^2 \sigma T_{\rm BB}^4$, in units of 10^{31} erg s ^{1} are overplotted in the $kT_{\rm BB}$–$K_{\rm BB}$ planes. The red, orange, and black contours correspond to con dence levels of 68.3%, 90%, and 99%, respectively.

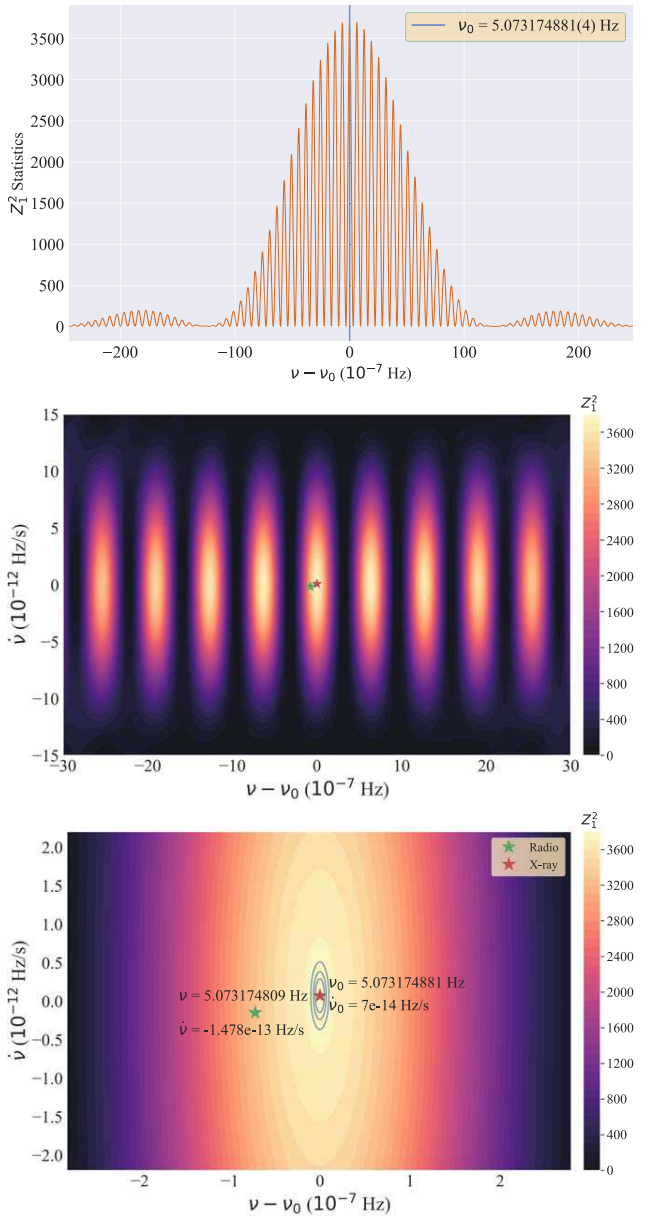

Figure 4. Top: Z_1^2 statistics with a xed $\dot{\nu} = 7 \times 10^{-14}$ Hz s ^{1} obtained for 0.3–7 keV events extracted from the EPIC-pn source region. Middle and bottom: maps of $Z_1^2(\nu, \dot{\nu})$ in the vicinity of the pulsar s expected frequency green star) and its derivative from the Parkes radio timing solution for the energy range 0.3–7 keV. The red star indicates the location of the highest $Z_1^2(\nu, \dot{\nu})$ value $Z^2_{1,\rm max} = 3739$). The 1σ, 2σ, and 3σ statistical error contours for $Z_1^2(\nu, \dot{\nu})$ are displayed with blue ellipses.

Conversely, multipolar con gurations yield intricate temperature pro les with relatively smaller PFs Perna et al. 2013).

For B1055, a 50% PF is still too low. Only in combination with atmospheric effects could internal heating in the presence of a toroidal magnetic eld component) explain the large observed PFs.

Hot spots could be also due to external heating by relativistic particles accelerated in the pulsar s magnetosphere, which subsequently precipitate onto the NS polar caps PCs) and heat them Ruderman & Sutherland 1975). This mechanism is responsible for thermal X-ray emission from hot spots in old pulsars, including millisecond pulsars, whose bulk surface is too cold to emit X-rays, but it can also contribute to the hot thermal components in middle-aged pulsars e.g., Pavlov et al. 2002). The range of bolometric luminosities, $L_{\rm BB,h}$, associated with B1055 s hot BB con dence contours is ~ 3–$5) \times 10^{30}$ erg s ^{1} Figure 3). Harding & Muslimov 2001), who considered the PC heating in the space charge-limited flow acceleration model, predicted a polar cap luminosity $L_{\rm PC} \sim 2 \times 10^{-4}\, \dot{E} = 6 \times 10^{30}$ erg s ^{1} for a pulsar with a characteristic age $\tau \sim 500$ kyr and a spin period $P \sim 0.2$ s, consistent with our estimates of the hot BB luminosity. This suggests that the hot spots, associated with the hot thermal component in B1055 s X-ray emission, could be polar caps heated by relativistic particles precipitating from the pulsar s magnetosphere.

Furthermore, the conventional polar cap radius of B1055, calculated based on a simple "centered" dipole magnetic eld geometry, $R_{\rm pc} = (2\pi R_{\rm NS}^3/cP)^{1/2} \approx 900$ m assuming a standard NS radius of 13 km), is consistent with the maximum radius from the phase-resolved analysis Figure 12).

Yet, in this scenario, we still lack a clear explanation for the differences in heating between the two magnetic poles. One plausible explanation for the anisotropy in external heating could be associated with off-centered dipole magnetic eld

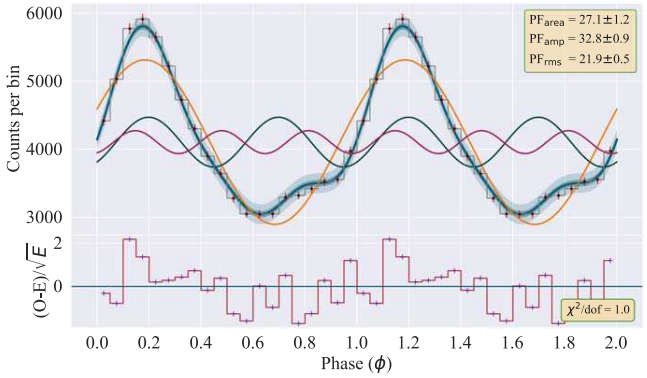

Figure 5. The 0.3–7 keV phase-folded light curve X-ray pulse pro le) plotted as a histogram with 20 phase bins and as the sum of three harmonics, $(N/20)\mathcal{F}(\phi)$, where $\mathcal{F}(\phi)$ is the normalized pulse pro le and $N = 86{,}097$ is the total number of events in the chosen energy range. The $\pm 3\sigma$ uncertainty of the X-ray pulse pro le is shown with transparent blue color. The orange, green, and red sine waves correspond to the rst, second, and third harmonics, respectively. Area, amplitude, and rms pulse fractions, with their 1σ uncertainties, are displayed as percentages in the top right corner.

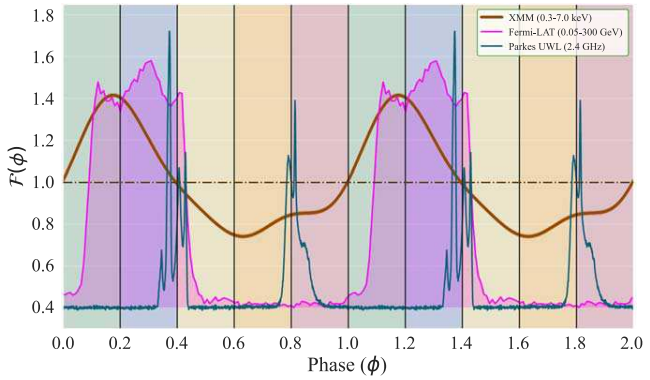

Figure 6. Normalized X-ray pulse pro le, $\mathcal{F}(\phi)$, at 0.3–7 keV. Phase bins are displayed with different transparent colors. The Parkes radio light curve at 2.4 GHz) and Fermi-LAT -ray light curve 0.05–300 GeV) are overplotted in blue and magenta, respectively.

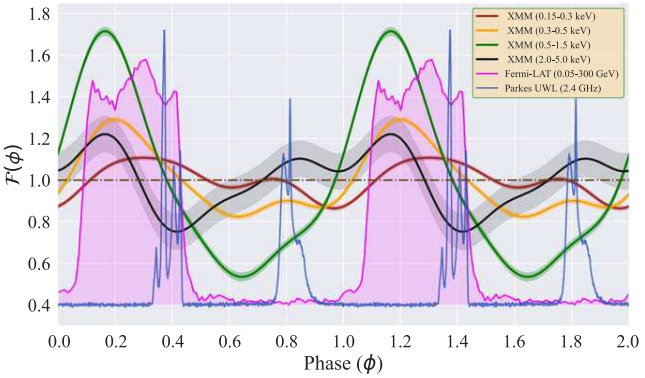

Figure 7. Normalized pulse pro les, $\mathcal{F}(\phi)$, are displayed for four energy bands. The X-ray pulse pro les 1σ uncertainties are depicted with transparent colors. The Parkes radio light curve at 2.4 GHz) and Fermi-LAT -ray light curve 0.05–300 GeV) are overplotted in blue and magenta, respectively.

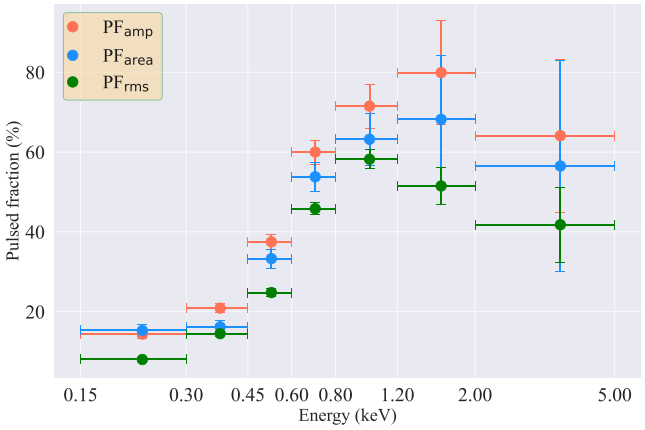

Figure 8. Energy dependence of three background-corrected pulse fractions plotted with 90% con dence level errors for the energy ranges de ned in Table 4. The orange, blue, and green dots correspond to amplitude, area, and rms pulse fractions.

con gurations e.g., Harrison & Tademaru 1975). A displacement of the dipole center from the NS center may lead to differences for internal and external heating, and thus different pole temperatures.

The effect of an off-centered dipole magnetic eld in the case of internal heating was recently studied by Igoshev et al. 2023). They investigated how these con gurations affect the temperature patterns on the surface, the light curves, and the spectra of middle-aged pulsars.

For an off-centered dipole eld with $B = 10^{13}$ G, Igoshev et al. 2023) reported $kT_{\rm BB,h}$ $kT_{\rm BB,c} \approx 1.1$ and $R_{\rm BB,h}$ $R_{\rm BB,c} \approx 2$. These values are notably different from the typical phase-integrated values of $kT_{\rm BB,h}$ $kT_{\rm BB,c} \approx 2$ and $R_{\rm BB,h}$ $R_{\rm BB,c} \approx 0.1$ for middle-aged pulsars Figure 14).

In summary, both the internal and external heating mechanisms can contribute to the formation of the observed hot spots on B1055 s surface. Detailed atmosphere modeling, with account for beamed emissions, is needed for full understanding of the emission properties of middle-aged pulsars like B1055. However, such modeling is beyond the scope of this paper and is planned for future research.

6.3. Nonthermal Emission and Multiwavelength Pulse Pro le of B1055

The phase shifts between the peaks in multiwavelength pulse pro les see Figures 6 and 7) can be attributed to different emission mechanisms operating in distinct emission regions that are located at different heights and azimuthal angles. For example, thermal X-ray emission comes directly from the NS surface while radio emission is thought to come from different heights above the magnetic poles. The relative shifts and shapes of the multiwavelength pulse pro les are governed by the location of the magnetic poles with respect to the rotation axis and the line of sight, in short the pulsar geometry.

6.3.1. Nonthermal X Ray Emission

In our spectral ts with the BB$_c$+BB$_h$+PL model, the nonthermal PL) component dominates at $E \gtrsim 2$ keV Figures 2 and 10). Its phase-integrated photon index, $\Gamma_X \approx 1.8$, substantially exceeds $\Gamma \approx 0.9$ in the GeV -ray range Posselt et al. 2023a). The X-ray photon index might show some variations with phase see Figure 13), but they are not statistically signi cant even in our relatively deep observation.

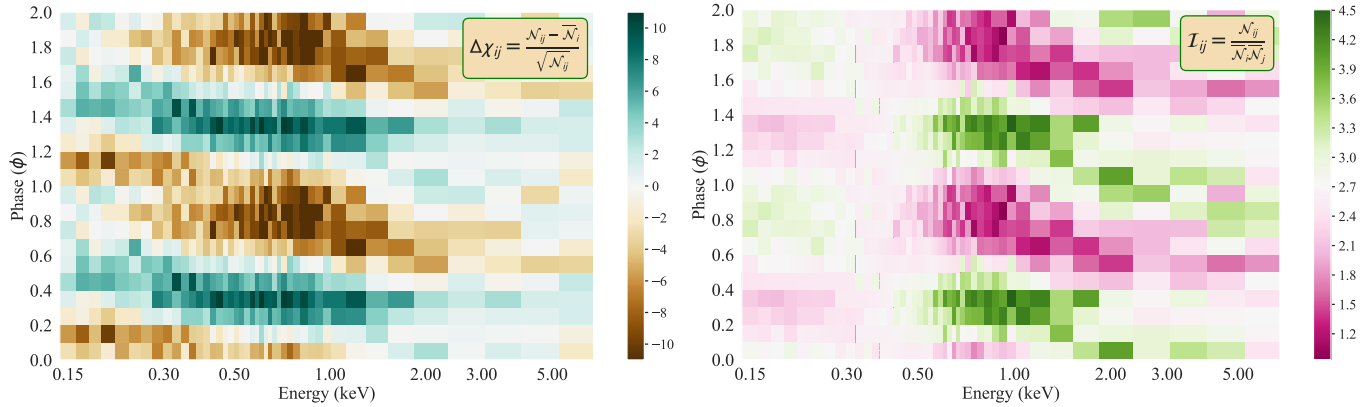

Figure 9. Different representations of the EPIC-pn X-ray events of B1055 in phase–energy space. The right panel shows a phase–energy map where only the normalization is applied, while the left panel shows deviations from the phase-averaged values in each phase–energy bin—see Equations 4) and 5).

The 2–5 keV light curve shows one clear peak with a maximum at ≈0.1, i.e., within the broad -ray pulse Figure 7). The maximum of the phase dependence of the PL flux, $F_{\rm PL}$), is seen at about the same phase Figure 13). The X-ray maximum slightly lags the leading edge of the -ray pulse, but it is ahead of the mean phase of the -ray pulse as well as of the radio MP. This X-ray peak is also seen in the energy–phase map Figure 9, right panel).

The 2–5 keV light curve also shows a hint of a second peak at ≈0.8, near the radio IP. This peak, however, is not seen in the $F_{\rm PL}$) curve, which suggests that it is due to an admixture of the thermal hot component rather than to the nonthermal emission.

Thus, we cannot exclude the possibility that the nonthermal X-ray emission is connected with the -ray emission and perhaps with the radio MP. Unfortunately, the small number of detected nonthermal X-ray photons does not allow us to investigate this connection in more detail.

6.3.2. Constraints on Pulsar Geometry from the Radio and Ray Light Curves

Similar to other radio pulsars with an IP, separated from the MP by about half a period, B1055 is usually interpreted as a nearly orthogonal rotator, i.e., the magnetic inclination α the angle between the rotation and magnetic axes) and the viewing angle ζ between the rotation axis and the line of sight) are not strongly different from 90°. Although Manchester & Lyne 1977) noted that such pulsars could also be interpreted as nearly aligned hollow-cone rotators, B1055 is typically interpreted as a nearly orthogonal rotator see, e.g., Weltevrede & Wright 2009, and references therein), even though the lag of the IP behind the MP is Δ = 0.44 peak to peak) rather than 0.5. Based on analysis of swings of linear polarization angle in both the MP and IP and assuming a dipole magnetic eld, Weltevrede & Wright 2009) estimate $\alpha \approx 75°$, $\zeta \approx 111°$ for the MP. They also suggest that the IP arises from emission formed on open eld lines close to the magnetic axis at a height ∼700 km above the magnetic pole, while the MP originates from eld lines lying well outside the polar cap boundary beyond the null surface, and farther away from the magnetic axis, at about the same height.

Additional constraints on the origin of nonthermal emission can be obtained from the analysis of -ray light light curves. Pierbattista et al. 2015) computed emission patterns for Fermi-LAT pulsars, including B1055, for four -ray emission models: Polar Cap, Slot Gap, Outer Gap and One Pole Caustic, for the core-plus-cone model of radio emission. For each of these models, they generated -ray and radio light curves across a parameter space de ned by α and ζ. However, none of these models provided a satisfactory explanation for both the -ray and radio light curves of B1055. Exceptionally for -ray pulsars, B1055 s -ray pulse can be explained by the Polar Cap model but this model does not work for the radio light curve. The Outer Gap model offered the most reasonable, although far from perfect, description of the general characteristics of both the -ray and radio light curves, with values of $\alpha \sim 77°$ and $\zeta \sim 87°$. Overall, it seems that those models cannot provide an accurate description of both the -ray and radio pulsations.

These models, as well as new models explaining pulsar -ray emission, are currently being further developed, and light-curve tting is used to constrain them, for instance for the Vela pulsar e.g., Venter et al. 2017; Barnard et al. 2022, and references therein). However, we are not aware of a recent work focusing on the unusual radio and -ray light curves of B1055.

6.3.3. Pulsar Geometry with Account for X Ray Pulsations

Over the past two decades, X-ray observations of B1055 have consistently shown a single peak at energies corresponding to the hot BB component, i.e., one hot spot. However, if this pulsar is indeed an orthogonal rotator, as suggested by the radio data, one might expect to observe two peaks in the folded light curve, corresponding to two magnetic poles of a centered magnetic dipole.

In our XMM-Newton data we see not only the peak from the dominating hot spot S1, centered at ≈0.3–0.4, but also a hint of a secondary thermal X-ray peak, possibly associated with another hot spot S2), which lags the main peak by approximately Δ ≈0.4–0.5 Figure 9, right panel). The S2 hot spot also appears as a hump at ≈0.8 near the phase of the radio interpulse) in the 0.3–0.5 keV light curve Figure 7).

Thus, the thermal X-ray light curves of B1055 are consistent with two observed magnetic poles, and hence a orthogonal

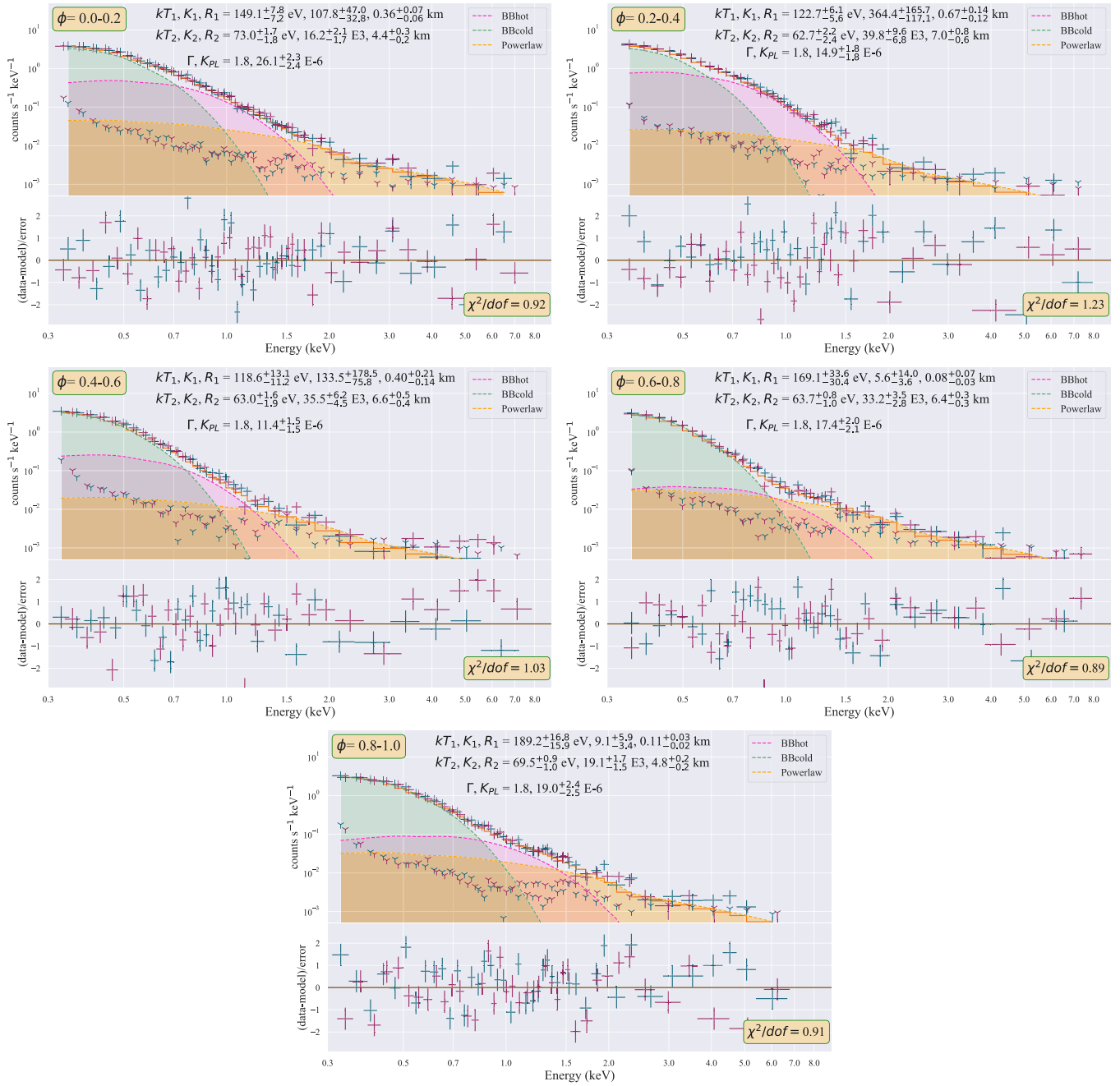

Figure 10. Fits to phase-resolved spectra for ve equal-sized phase bins of the 2019 EPIC-pn data. Hot BB, cold BB, and PL components are displayed in red, green, and yellow. The t parameters with a margin of 1σ error are shown at the top of each panel.

rotator geometry, but the poles show an asymmetry in their temperatures.

The radio IP and MP are separated by approximately $\sim$159° Δ = 0.44, Weltevrede & Wright 2009). As illustrated in Figure 5, the peak of the MP exhibits a phase lag of 0.22[7] with respect to the X-ray peak in the 0.3–7 keV region, while the IP aligns with the smaller hump = 0.7–0.8) of the X-ray pro le.

Based on the observed radio pulse pro les and phase dependence of the polarization angles, Weltevrede & Wright 2009) estimated emission heights and plotted a map of the polar cap showing sites of the production of radio emission projected onto the NS surface see their Figure 7). In their cartographic representation, the IP emerges from directly above the polar region while the site of MP generation is offset from the central polar region. This spatial arrangement could potentially explain the time delay between the observed thermal X-ray pulse and the MP, as well as the alignment between the IP and S2. Qualitatively, the lags between the X-ray and radio pulses are also consistent with the two-pole interpretation and further support the notion of B1055 being an orthogonal rotator.

[7] Our 0.22 ± 0.02 phase shift between the MP at 0.67 GHz) and X-ray is consistent with earlier results by De Luca et al. 2005; 0.2 ± 0.05).

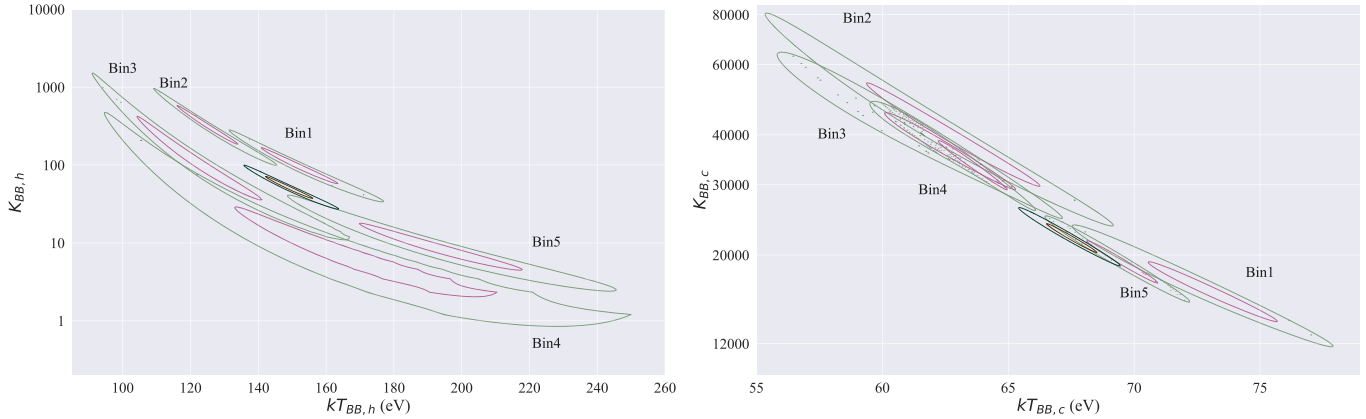

Figure 11. Variations of hot BB left) and cold BB right) with phase in the temperature–normalization plane. Red and green contours correspond to con dence levels of 68.3% and 99% respectively. Additionally, we depict the con dence contours of phase-integrated spectra using brown 68.3%) and black 99%). Errors are estimated for two parameters of interest. Small dots in some contour plots are small contours themselves, representing local minima and indicating a complicated shape of the χ^2 surface.

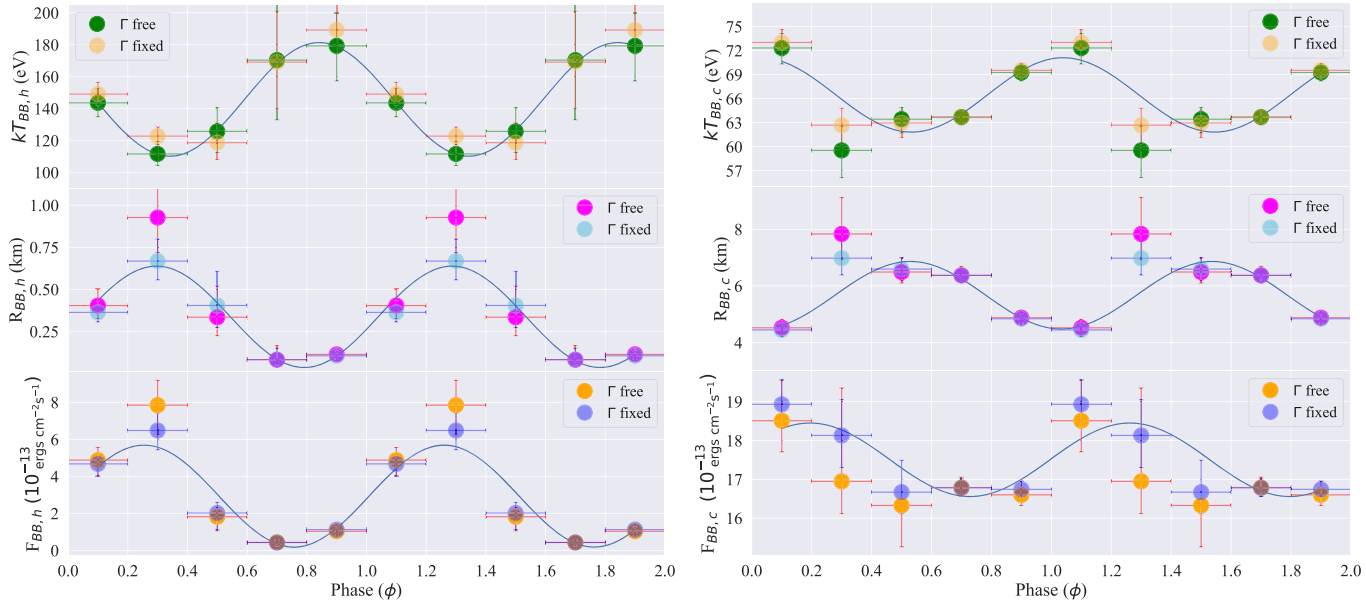

Figure 12. Phase dependences of the temperatures top), radii of equivalent emitting sphere middle), and unabsorbed fluxes in the 0.3–8.0 keV band bottom) for hot BB left) and cold BB right) components. The vertical error bars show 1σ uncertainties of the tting parameters. Blue lines represent sine function ts to the data for visualization purposes.

The maximum of the 2–5 keV light curve closely aligns with that of the 0.5–1.5 keV light curve see Figure 7), a phenomenon that may be attributed to a peculiar coincidence or to a region emitting nonthermal X-rays being close to the hot polar region. Conversely, the 2–5 keV maximum falls within the broader -ray pulse, which may indicate similar origin sites for the high-energy nonthermal emission.

The phase–energy map above 1.5 keV seems to show a slight trend of the maxima minima smoothly shifting to smaller phases with increasing energy. For the respective magnetospheric X-ray-emitting particles, this trend may indicate different emission heights or a different angular separation from the magnetic pole. Figure 7 also shows a statistically insigni cant indication of a second hump in proximity to the location of S2 and the IP. This observation is in agreement with the interpretation of S2 as a second magnetic pole. Puzzlingly, the -ray light curve shows a minimum at the respective rotation phase.

6.4. Absorption Lines in Middle aged Pulsars

Absorption features or hints of them were reported in the phase-resolved X-ray spectra of the two other Musketeers, B0656+14 Arumugasamy et al. 2018; Schwope et al. 2022) and Geminga Jackson & Halpern 2005), as well as in PSR J1740+1000, another interesting middle-aged pulsar Kargaltsev et al. 2008). However, in later XMM-Newton observations, Rigoselli et al. 2022) found no evidence of spectral lines in the phase-averaged and phase-resolved spectra of this pulsar, suggesting a time variation in the spectrum.

An explanation for phase-dependent absorption features could be provided by multipolar magnetic eld arcs that trap electrons in close proximity to the NS surface. Through the

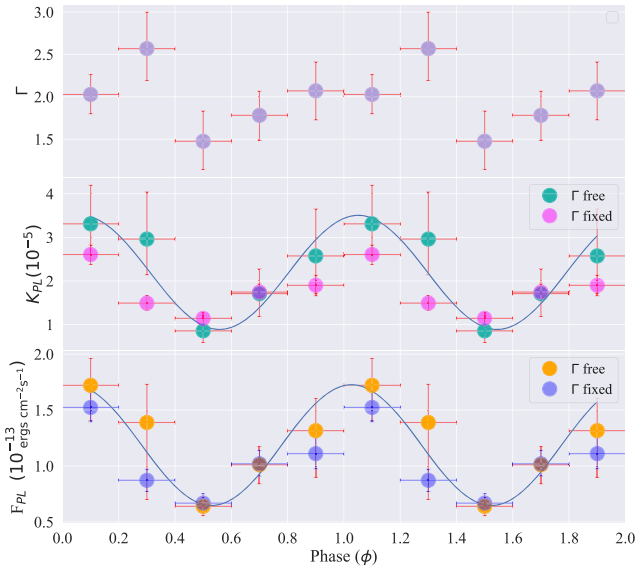

Figure 13. Phase dependence of the photon index Γ top), normalization $K_{\rm PL}$ middle), and unabsorbed fluxes in the 0.3–8.0 keV band bottom) for the PL component. The vertical error bars show 1σ uncertainties of the tting parameters. Blue lines represent sine function ts to the data for visualization purposes.

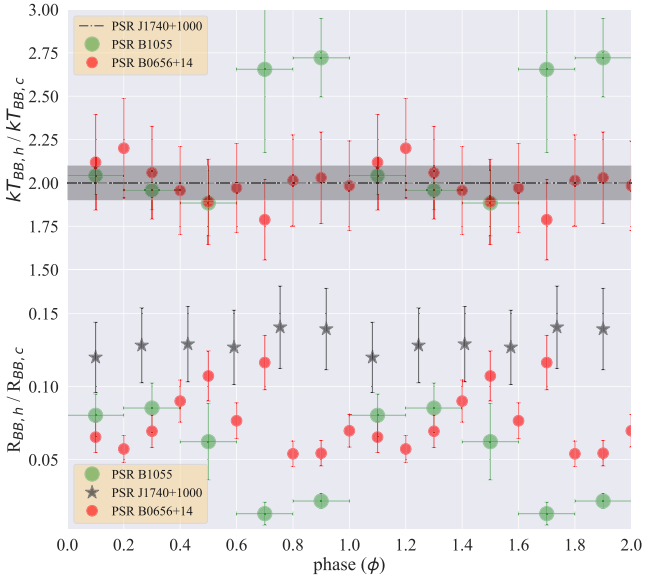

Figure 14. Phase dependences of the temperature and radius ratios derived from 2BB ts for B1055 this work), PSR J1740+1000 Rigoselli et al. 2022), and PSR B0656+14 Arumugasamy et al. 2018). The black horizontal line in the top panel represents the phase-integrated value for PSR J1740+1000.

process of cyclotron resonance scattering, this may lead to the formation of phase-dependent absorption lines in the X-ray spectra e.g., Arumugasamy et al. 2018). Such absorption lines can be alternatively explained by proton cyclotron lines if the local magnetic elds are high e.g., Tiengo et al. 2013). Viganò et al. 2014) showed that small-scale temperature variations can also mimic absorption lines.

Our analysis of the phase-resolved spectrum of B1055 did not show any evidence for absorption features, similar to the earlier study by De Luca et al. 2005). However, B1055 is notably fainter than the two other Musketeers. Considering this faintness and the variability seen for J1740+1000, the current nondetection for B1055 does not exclude the possibility of detecting phase-dependent spectral features with deeper X-ray observations achievable with more sensitive telescopes such as the upcoming Athena X-ray Observatory.

7. Conclusion

Using the most comprehensive X-ray data set to date, we nd that, in agreement with the ndings by De Luca et al. 2005), the spectrum of B1055 is best described by a tripartite model consisting of two blackbody components, presumably emitted from the bulk of the NS surface and small hot spots, and a power-law component, emitted from the pulsar s magnetosphere.

A phase-resolved spectral analysis shows periodic variations in the temperature of both the hot and cold blackbody components. These variations, in tandem with periodic changes in the projected emission areas, suggest nonuniform temperature distributions both over the bulk NS surface and within the alleged hot spot s). Previously published results on X-ray pulsations of the thermal components showed only one peak per period, likely associated with one visible hot spot, which did not agree with the nearly orthogonal rotator geometry of B1055 that is implied by the detailed radio studies of B1055 s main pulse and interpulse. In the new X-ray data, we nd indications for a second hot spot. However, it appears to be cooler than the one already known.

We explore two potential mechanisms to explain the thermal X-ray emission patterns of B1055: external heating by relativistic particles accelerated in the pulsar s magnetosphere, and internal heating resulting from anisotropic heat transfer due to an offset of the dipole magnetic eld and or the presence of an additional toroidal magnetic eld component within the NS s crust. Both mechanisms can, in principle, explain the observed high pulse fractions and phase dependence of the spectral parameters, particularly if beaming effects due to an atmosphere above the hot spots are additionally considered. The faintness and lower temperature of the putative second hot spot could perhaps be explained by an offset dipole, but more detailed modeling is needed.

The complexity of B1055 s spectral and temporal characteristics underscores the need for further investigations, including detailed atmosphere modeling and considerations of beamed emissions.

Acknowledgments

We express our gratitude to Colin J. Clark for his help with the Fermi-LAT data, Michael Freyberg for his assistance with EPIC-pn calibration issues, Prakash Arumugasamy for his support in resolving software-related challenges, as well as to Andrei Igoshev for useful discussions. This work was supported by the Bundesministerium für Wirtschaft und Energie through Deutsches Zentrum für Luft- und Raumfahrt DLR) under the grant No. 50 OR 1917. Support for this work was also provided by the National Aeronautics and Space Administration through the XMM-Newton award No. 80NSSC20K0806. B.P. acknowledges funding from the STFC consolidated grant to Oxford Astrophysics, code ST 000488. A.V. thanks the LSSTC Data Science Fellowship Program, which is funded by LSSTC, NSF Cybertraining Grant #1829740, the Brinson Foundation, and the Moore Foundation; his participation in the program has bene ted this work.

Facility: XMM, Parkes, MeerKAT, Fermi-LAT

Software: HEAsoft v6.29 c, Nasa High Energy Astrophysics Science Archive Research Center Heasarc), 2014), XMM-SAS v20.0.0, Gabriel et al. 2004) XSPEC v12.12.0, Arnaud 1996), PyXspec v2.1.0, Gordon & Arnaud 2021), Astropy v5.2.1, Astropy Collaboration et al. 2018), NumPy v1.23.5, Harris et al. 2020), SciPy v1.10.0, Virtanen et al. 2020), Matplotlib v3.6.3, Hunter 2007), Pandas v1.5.3, Pandas Development Team 2020), Seaborn v0.12.2, Waskom 2021), Stingray v1.1.1, Huppenkothen et al. 2019).

ORCID iDs

Armin Vahdat https: orcid.org 0000-0002-4026-5885
B. Posselt https: orcid.org 0000-0003-2317-9747
G. G. Pavlov https: orcid.org 0000-0002-7481-5259
P. Weltevrede https: orcid.org 0000-0003-2122-4540
A. Santangelo https: orcid.org 0000-0003-4187-9560
S. Johnston https: orcid.org 0000-0002-7122-4963

References

Abdo, A. A., Ackermann, M., Ajello, M., et al. 2010, ApJS, 187, 460
Arnaud, K. A. 1996, in ASP Conf. Ser. 101, Astronomical Data Analysis Software and Systems V, ed. G. H. Jacoby & J. Barnes San Francisco, CA: ASP), 17
Arumugasamy, P., Kargaltsev, O., Posselt, B., Pavlov, G. G., & Hare, J. 2018, ApJ, 869, 97
Astropy Collaboration, Price-Whelan, A. M., Sip cz, B. M., et al. 2018, AJ, 156, 123
Barnard, M., Venter, C., Harding, A. K., Kalapotharakos, C., & Johnson, T. J. 2022, ApJ, 925, 184
Becker, W., & Truemper, J. 1997, A&A, 326, 682
Bîrzan, L., Pavlov, G. G., & Kargaltsev, O. 2016, ApJ, 817, 129
Buccheri, R., Bennett, K., Bignami, G. F., et al. 1983, A&A, 128, 245
Caraveo, P., Bignami, G., DeLuca, A., et al. 2003, Sci, 301, 1345
Caraveo, P., De Luca, A., Mereghetti, S., Pellizzoni, A., & Bignami, G. F. 2004, Sci, 305, 376
Cheng, A. F., & Helfand, D. J. 1983, ApJ, 271, 271
Cordes, J. M., & Lazio, T. J. W. 2002, arXiv:astro-ph 0207156
de Jager, O. C., Raubenheimer, B., & Swanepoel, J. W. H. 1989, A&A, 221, 180
De Luca, A., Caraveo, P., Mattana, F., Pellizzoni, A., & Bignami, G. F. 2006, A&A, 445, L9
De Luca, A., Caraveo, P. A., Mereghetti, S., Negroni, M., & Bignami, G. F. 2005, ApJ, 623, 1051
Gabriel, C., Denby, M., Fyfe, D. J., et al. 2004, in ASP Conf. Ser. 314, Astronomical Data Analysis Software and Systems ADASS) XIII, ed. F. Ochsenbein, M. G. Allen, & D. Egret San Francisco, CA: ASP), 759
Geppert, U., Küker, M., & Page, D. 2006, A&A, 457, 937
Gordon, C., & Arnaud, K., 2021 PyXspec: Python interface to XSPEC spectral- tting program, Astrophysics Source Code Library, ascl:2101.014
Gotthelf, E. V., & Halpern, J. P. 2020, ApJ, 900, 159
Harding, A. K., & Muslimov, A. G. 1998, ApJ, 508, 328
Harding, A. K., & Muslimov, A. G. 2001, ApJ, 556, 987
Hare, J., Volkov, I., Pavlov, G. G., Kargaltsev, O., & Johnston, S. 2021, ApJ, 923, 249
Harris, C. R., Millman, K. J., van der Walt, S. J., et al. 2020, Natur, 585, 357
Harrison, E., & Tademaru, E. 1975, ApJ, 201, 447
Heinke, C. O., Rybicki, G. B., Narayan, R., & Grindlay, J. E. 2006, ApJ, 644, 1090
Ho, W. C. G., Potekhin, A. Y., & Chabrier, G. 2008, ApJS, 178, 102
Hobbs, G., Manchester, R. N., Dunning, A., et al. 2020, PASA, 37, e012
Hobbs, G. B., Edwards, R. T., & Manchester, R. N. 2006, MNRAS, 369, 655
Hotan, A. W., van Straten, W., & Manchester, R. N. 2004, PASA, 21, 302
Hunter, J. D. 2007, CSE, 9, 90
Huppenkothen, D., Bachetti, M., Stevens, A. L., et al. 2019, ApJ, 881, 39
Igoshev, A. P., Hollerbach, R., & Wood, T. 2023, MNRAS, 525, 3354
Jackson, M. S., & Halpern, J. P. 2005, ApJ, 633, 1114
Jankowski, F., Bailes, M., van Straten, W., et al. 2019, MNRAS, 484, 3691
Johnston, S., Karastergiou, A., Keith, M. J., et al. 2020, MNRAS, 493, 3608
Kargaltsev, O., Misanovic, Z., Pavlov, G. G., Wong, J. A., & Garmire, G. P. 2008, ApJ, 684, 542
Kirsch, M. G. F., Becker, W., Larsson, S., et al. 2004, in Proc. of the 5th INTEGRAL Workshop on the INTEGRAL Universe ESA SP-552), ed. V. Schoenfelder, G. Lichti, & C. Winkler Paris: European Space Agency), 863
Lazarus, P., Karuppusamy, R., Graikou, E., et al. 2016, MNRAS, 458, 868
Lower, M. E., Johnston, S., Dunn, L., et al. 2021, MNRAS, 508, 3251
Manchester, R., & Lyne, A. 1977, MNRAS, 181, 761
Martin-Carrillo, A., Kirsch, M. G. F., Caballero, I., et al. 2012, A&A, 545, A126
Mignani, R. P., Pavlov, G. G., & Kargaltsev, O. 2010, ApJ, 720, 1635
Mori, K., & Ho, W. C. G. 2007, MNRAS, 377, 905
Nasa High Energy Astrophysics Science Archive Research Center Heasarc), 2014 HEAsoft: Uni ed Release of FTOOLS and XANADU, Astrophysics Source Code Library, ascl:1408.004
Oegelman, H., & Finley, J. P. 1993, ApJL, 413, L31
Pandas Development Team 2020, pandas-dev pandas: Pandas, latest, Zenodo, doi:10.5281 zenodo.3509134
Parthasarathy, A., Bailes, M., Shannon, R. M., et al. 2021, MNRAS, 502, 407
Pavlov, G., Shibanov, Y. A., Ventura, J., & Zavlin, V. 1994, A&A, 289, 837
Pavlov, G. G., Shibanov, Y. A., Zavlin, V. E., & Meyer, R. D. 1995, in NATO ASI Ser. C 450, The Lives of the Neutron Stars, ed. M. A. Alpar, U. Kiziloglu, & J. van Paradijs Dordrecht: Kluwer), 71
Pavlov, G. G., Zavlin, V. E., & Sanwal, D. 2002, in Proc. of the 270, WE-Heraeus Seminar on Neutron Stars, Pulsars, and Supernova Remnant,. MPE Report 278, ed. W. Becker, H. Lesch, & J. Trümper Garching bei München: Max-Plank-Institut für extraterrestrische Physik), 273
Perna, R., Viganò, D., Pons, J. A., & Rea, N. 2013, MNRAS, 434, 2362
Petroff, E., Keith, M. J., Johnston, S., van Straten, W., & Shannon, R. M. 2013, MNRAS, 435, 1610
Pierbattista, M., Harding, A. K., Grenier, I. A., et al. 2015, A&A, 575, A3
Posselt, B., Pavlov, G. G., Kargaltsev, O., & Hare, J. 2023a, ApJ, 952, 134
Posselt, B., Karastergiou, A., Johnston, S., et al. 2023b, MNRAS, 520, 4582
Posselt, B., Pavlov, G. G., Slane, P. O., et al. 2017, ApJ, 835, 66
Posselt, B., Spence, G., & Pavlov, G. G. 2015, ApJ, 811, 96
Rigoselli, M., Mereghetti, S., Anzuinelli, S., et al. 2022, MNRAS, 513, 3113
Ruderman, M. A., & Sutherland, P. G. 1975, ApJ, 196, 51
Schwope, A., Pires, A. M., Kurpas, J., et al. 2022, A&A, 661, A41
Smith, D. A., Bruel, P., Clark, C. J., et al. 2023, ApJ, 958, 191
Strüder, L., Briel, U., Dennerl, K., et al. 2001, A&A, 365, L18
Taylor, J. H. 1992, RSPTA, 341, 117
Tiengo, A., Esposito, P., Mereghetti, S., et al. 2013, Natur, 500, 312
Turner, M. J. L., Abbey, A., Arnaud, M., et al. 2001, A&A, 365, L27
Turolla, R., & Nobili, L. 2013, ApJ, 768, 147
van Straten, W., Demorest, P., & Oslowski, S. 2012, AR&T, 9, 237
Vaughan, A. E., & Large, M. I. 1972, MNRAS, 156, 27P
Venter, C., Harding, A. K., & Grenier, I. 2017, in XII Multifrequency Behaviour of High Energy Cosmic Sources Workshop MULTIF2017), 38
Verner, D. A., Ferland, G. J., Korista, K. T., & Yakovlev, D. G. 1996, ApJ, 465, 487
Viganò, D., Perna, R., Rea, N., & Pons, J. A. 2014, MNRAS, 443, 31
Virtanen, P., Gommers, R., Oliphant, T. E., et al. 2020, NatMe, 17, 261
Waskom, M. L. 2021, JOSS, 6, 3021
Weltevrede, P., & Wright, G. 2009, MNRAS, 395, 2117
Wilms, J., Allen, A., & McCray, R. 2000, ApJ, 542, 914
Yakovlev, D. 2021, MNRAS, 506, 4593
Yao, J. M., Manchester, R. N., & Wang, N. 2017, ApJ, 835, 29
Zavlin, V. E., Pavlov, G. G., & Shibanov, Y. A. 1996, A&A, 315, 141

Symbols

Δ Delta, difference between two quantity

Γ Gamma, Powerlaw Photon index

Ω Omega, angular frequency

Θ Theta, inclination in nsmaxg XSPEC model

α Alpha, inclination angle

χ Chi, used in statistical contexts

δ Delta, indicating change or variation

$\dot{\nu}$ Nudot, frequency derivative

ϵ Epsilon, a small quantity

η Eta, representing efficiency in here

γ gamma, representing high energy γ-rays

∇ gradient

ν Nu, frequency

$\odot$ denotes the Sun, solar nit

ϕ Phi, representing the phase angle

π Pi

ρ Rho, representing density in physics

σ Sigma, standard deviation in statistics

τ Tau, representing characteristic age

θ theta, representing an angle in here

υ Upsilon, used in for degree of freedom

ξ Xi, used in various mathematical contexts

Acronyms

ACIS	Advanced CCD Imaging Spectrometer
ADS	Astrophysics Data System
AGN	Active Galactic Nuclei
ATNF	Australia Telescope National Facility
AXP	Anomalous X-ray Pulsar
BB	BlackBody
DM	Dispersion Measure
EPIC	The European Photon Imaging Camera
FF	Full Frame
FWHM	Full Width at Half Maximum
GTI	Good Time Intervals
HE	High Energy
HETG	High-Energy Transmission Grating
HRC	High Resolution Camera
IAU	International Astronomical Union
IR	Infrared
ISM	Interstellar medium
LAT	Large Area Telescope
MJD	Modified Julian Date
ML	Maximum likelihood

MOS	Metal Oxide Semi-conductor
MSP	Millisecond Pulsar
MW	Multiwavelength
NASA	National Aeronautics and Space Administration
NH	Galactic Hydrogen Column Density
NIR	Near Infrared
NOMAD	Naval Observatory Merged Astrometric Dataset
NPL	Powerlaw Normalization
NS	Neutron Star
NSA	Neutron Star Atmosphere
NSATMOS	NS Hydrogen Atmosphere with electron conduction and self-irradiation
NSMAXG	Neutron Star with a Magnetic Atmosphere
OM	Optical/UV Monitor Telescope
PF	Pulsed Fraction
PL	Powerlaw
PSF	Point Spread Function
PSR	Pulsar
PWN	Pulsar Wind Nebula
QSR	Quasar
RGS	Reflection Grating Spectrometer
ROSAT	Röntgensatellit
RPP	Rotation-Powered Pulsars
RRAT	Rotating Radio Transient
SARAO	South African Radio Astronomy Observatory
SAS	Science Analysis Software

SDSS	Sloan Digital Sky Survey
SGR	Soft Gamma Repeater
SIMBAD	SIMBAD Astronomical Database
SK	Full form not found
SW	Small Window
TDB	Barycentric Dynamical Time
TESS	Transiting Exoplanet Survey Satellite
TPA	Thousand Pulsar Array
ULX	Ultraluminous X-ray source
UV	Ultraviolet
UWL	Ultra Wide-bandwidth Low
VLBI	Very Long Baseline Interferometry
WD	White Dwarf
WISE	Wide-field Infrared Survey Explorer
XGPS	XMM–Newton Galactic Plane Survey
XMM	XMM–Newton
YMW	Yao Manchester Wang Electron Density Model

Index

Bibliography

Abdo, A. A., Ackermann, M., Ajello, M., Atwood, W. B., Axelsson, M., Baldini, L., Ballet, J., Barbiellini, G., Baring, M. G., Bastieri, D., Baughman, B. M., Bechtol, K., Bellazzini, R., Berenji, B., Blandford, R. D., Bloom, E. D., Bonamente, E., Borgland, A. W., Bregeon, J., Brez, A., Brigida, M., Bruel, P., Burnett, T. H., Buson, S., Caliandro, G. A., Cameron, R. A., Camilo, F., Caraveo, P. A., Casandjian, J. M., Cecchi, C., Çelik, Ö., Charles, E., Chekhtman, A., Cheung, C. C., Chiang, J., Ciprini, S., Claus, R., Cognard, I., Cohen-Tanugi, J., Cominsky, L. R., Conrad, J., Corbet, R., Cutini, S., den Hartog, P. R., Dermer, C. D., de Angelis, A., de Luca, A., de Palma, F., Digel, S. W., Dormody, M., Silva, E. d. C. e., Drell, P. S., Dubois, R., Dumora, D., Espinoza, C., Farnier, C., Favuzzi, C., Fegan, S. J., Ferrara, E. C., Focke, W. B., Fortin, P., Frailis, M., Freire, P. C. C., Fukazawa, Y., Funk, S., Fusco, P., Gargano, F., Gasparrini, D., Gehrels, N., Germani, S., Giavitto, G., Giebels, B., Giglietto, N., Giommi, P., Giordano, F., Glanzman, T., Godfrey, G., Gotthelf, E. V., Grenier, I. A., Grondin, M. H., Grove, J. E., Guillemot, L., Guiriec, S., Gwon, C., Hanabata, Y., Harding, A. K., Hayashida, M., Hays, E., Hughes, R. E., Jackson, M. S., Jóhannesson, G., Johnson,

A. S., Johnson, R. P., Johnson, T. J., Johnson, W. N., Johnston, S., Kamae, T., Kanbach, G., Kaspi, V. M., Katagiri, H., Kataoka, J., Kawai, N., Kerr, M., Knödlseder, J., Kocian, M. L., Kramer, M., Kuss, M., Lande, J., Latronico, L., Lemoine-Goumard, M., Livingstone, M., Longo, F., Loparco, F., Lott, B., Lovellette, M. N., Lubrano, P., Lyne, A. G., Madejski, G. M., Makeev, A., Manchester, R. N., Marelli, M., Mazziotta, M. N., McConville, W., McEnery, J. E., McGlynn, S., Meurer, C., Michelson, P. F., Mineo, T., Mitthumsiri, W., Mizuno, T., Moiseev, A. A., Monte, C., Monzani, M. E., Morselli, A., Moskalenko, I. V., Murgia, S., Nakamori, T., Nolan, P. L., Norris, J. P., Noutsos, A., Nuss, E., Ohsugi, T., Omodei, N., Orlando, E., Ormes, J. F., Ozaki, M., Paneque, D., Panetta, J. H., Parent, D., Pelassa, V., Pepe, M., Pesce-Rollins, M., Piron, F., Porter, T. A., Rainò, S., Rando, R., Ransom, S. M., Ray, P. S., Razzano, M., Rea, N., Reimer, A., Reimer, O., Reposeur, T., Ritz, S., Rodriguez, A. Y., Romani, R. W., Roth, M., Ryde, F., Sadrozinski, H. F. W., Sanchez, D., Sander, A., Saz Parkinson, P. M., Scargle, J. D., Schalk, T. L., Sellerholm, A., Sgrò, C., Siskind, E. J., Smith, D. A., Smith, P. D., Spandre, G., Spinelli, P., Stappers, B. W., Starck, J. L., Striani, E., Strickman, M. S., Strong, A. W., Suson, D. J., Tajima, H., Takahashi, H., Takahashi, T., Tanaka, T., Thayer, J. B., Thayer, J. G., Theureau, G., Thompson, D. J., Thorsett, S. E., Tibaldo, L., Tibolla, O., Torres, D. F., Tosti, G., Tramacere, A., Uchiyama, Y., Usher, T. L., Van Etten, A., Vasileiou, V., Venter, C., Vilchez, N., Vitale, V., Waite, A. P., Wang, P., Wang, N., Watters, K., Weltevrede, P., Winer, B. L., Wood, K. S., Ylinen, T., and Ziegler, M.

(2010). The First Fermi Large Area Telescope Catalog of Gamma-ray Pulsars. *The Astrophysical Journal Supplement Series*, 187(2):460–494.

Alpar, M., Cheng, A., Ruderman, M., and Shaham, J. (1982). A new class of radio pulsars. *Nature*, 300(5894):728–730.

Arnaud, K. A. (1996). XSPEC: The First Ten Years. In Jacoby, G. H. and Barnes, J., editors, *Astronomical Data Analysis Software and Systems V*, volume 101 of *Astronomical Society of the Pacific Conference Series*, page 17.

Arumugasamy, P., Kargaltsev, O., Posselt, B., Pavlov, G. G., and Hare, J. (2018). Possible Phase-dependent Absorption Feature in the X-Ray Spectrum of the Middle-aged PSR J0659+1414. *The Astrophysical Journal*, 869(2):97.

Baade, W. and Zwicky, F. (1934). Remarks on Super-Novae and Cosmic Rays. *Physical Review*, 46(1):76–77.

Bailer-Jones, C. A. L., Fouesneau, M., and Andrae, R. (2019). Quasar and galaxy classification in Gaia Data Release 2. *MNRAS*, 490(4):5615–5633.

Becker, W. and Truemper, J. (1997). The X-ray luminosity of rotation-powered neutron stars. *AA*, 326:682–691.

Bhattacharya, D. and van den Heuvel, E. P. J. (1991). Formation and evolution of binary and millisecond radio pulsars. *Physics Reports*, 203(1-2):1–124.

Bhattacharyya, B., Lyne, A., Stappers, B., Weltevrede, P., Keane, E., McLaughlin, M., Kramer, M., Jordan, C., and Bassa, C. (2018). A long-term study of three rotating radio transients. *Monthly Notices of the Royal Astronomical Society*, 477(3):4090–4103.

Bildsten, L., Chakrabarty, D., Chiu, J., Finger, M. H., Koh, D. T., Nelson, R. W., Prince, T. A., Rubin, B. C., Scott, D. M., Stollberg, M., et al. (1997). Observations of accreting pulsars. *The Astrophysical Journal Supplement Series*, 113(2):367.

Bogdanov, S., Grindlay, J. E., Heinke, C. O., Camilo, F., Freire, P. C. C., and Becker, W. (2006). Chandra X-Ray Observations of 19 Millisecond Pulsars in the Globular Cluster 47 Tucanae. *The Astrophysical Journal*, 646(2):1104–1115.

Buccheri, R., Bennett, K., Bignami, G. F., Bloemen, J. B. G. M., Boriakoff, V., Caraveo, P. A., Hermsen, W., Kanbach, G., Manchester, R. N., Masnou, J. L., Mayer-Hasselwander, H. A., Özel, M. E., Paul, J. A., Sacco, B., Scarsi, L., and Strong, A. W. (1983). Search for pulsed γ-ray emission from radio pulsars in the COS-B data. *Astronomy & Astrophysics*, 128:245–251.

Buchner, J. and Boorman, P. (2023). Statistical Aspects of X-ray Spectral Analysis. *arXiv e-prints*, page arXiv:2309.05705.

Bühler, R. and Blandford, R. (2014). The surprising crab pulsar and its nebula: a review. *Reports on Progress in Physics*, 77(6):066901.

Caleb, M., Heywood, I., Rajwade, K., Malenta, M., Willem Stappers, B., Barr, E., Chen, W., Morello, V., Sanidas, S., Van Den Eijnden, J., et al. (2022). Discovery of a radio-emitting neutron star

with an ultra-long spin period of 76 s. *Nature Astronomy*, 6(7):828–836.

Camilo, F., Ransom, S. M., Halpern, J. P., Reynolds, J., Helfand, D. J., Zimmerman, N., and Sarkissian, J. (2006). Transient pulsed radio emission from a magnetar. *Nature*, 442(7105):892–895.

Caraveo, P. A. (2014). Gamma-ray pulsar revolution. *Annual Review of Astronomy and Astrophysics*, 52:211–250.

Cerutti, B. (2019). Gamma-ray pulsars: what have we learned from ab initio kinetic simulations? *Rendiconti Lincei. Scienze Fisiche e Naturali*, 30:89–92.

Cocke, W., Ferguson, D., and Muncaster, G. (1973). Optical polarization of the crab nebula pulsar. il observational results and fits by the relativistic vector model. *Astrophysical Journal, Vol. 183, pp. 987-996 (1973)*, 183:987–996.

Contopoulos, I. (2016). The equatorial current sheet and other interesting features of the pulsar magnetosphere. *Journal of Plasma Physics*, 82(3):635820303.

Contopoulos, I., Kalapotharakos, C., and Kazanas, D. (2014). A new standard pulsar magnetosphere. *The Astrophysical Journal*, 781(1):46.

Contopoulos, I., Ntotsikas, D., and Gourgouliatos, K. (2024). On the pulsar y-point. *Monthly Notices of the Royal Astronomical Society: Letters*, 527(1):L127–L131.

Cordes, J. M. and Lazio, T. J. W. (2002). Ne2001. i. a new model for the galactic distribution of free electrons and its fluctuations. *arXiv preprint astro-ph/0207156*.

Cordes, J. M. and Lazio, T. J. W. (2002). NE2001.I. A New Model for the Galactic Distribution of Free Electrons and its Fluctuations. *arXiv e-prints*, pages astro–ph/0207156.

Covey, K. R., Ivezić, Ž., Schlegel, D., Finkbeiner, D., Padmanabhan, N., Lupton, R. H., Agüeros, M. A., Bochanski, J. J., Hawley, S. L., West, A. A., Seth, A., Kimball, A., Gogarten, S. M., Claire, M., Haggard, D., Kaib, N., Schneider, D. P., and Sesar, B. (2007). Stellar SEDs from 0.3 to 2.5 μm: Tracing the Stellar Locus and Searching for Color Outliers in the SDSS and 2MASS. *The Astronomical Journal*, 134(6):2398–2417.

de Jager, O. C., Raubenheimer, B., and Swanepoel, J. W. H. (1989). A powerful test for weak periodic signals with unknown light curve shape in sparse data. *Astronomy &Astrophysics*, 221:180–190.

De Luca, A. (2017). Central compact objects in supernova remnants. In *Journal of Physics: Conference Series*, volume 932, page 012006. IOP Publishing.

De Luca, A., Caraveo, P. A., Mereghetti, S., Negroni, M., and Bignami, G. F. (2005). On the Polar Caps of the Three Musketeers. *The Astrophysical Journal*, 623(2):1051–1069.

Demorest, P. B., Pennucci, T., Ransom, S., Roberts, M., and Hessels, J. (2010). A two-solar-mass neutron star measured using shapiro delay. *nature*, 467(7319):1081–1083.

Dessert, C., Foster, J. W., and Safdi, B. R. (2020). Hard x-ray excess from the magnificent seven neutron stars. *The Astrophysical Journal*, 904(1):42.

Deutsch, A. J. (1955). The electromagnetic field of an idealized star in rigid rotation in vacuo. *Annales d'Astrophysique, Vol. 18, p. 1*, 18:1.

Ducci, L. and Malacaria, C. (2023). Modeling and Simulating X-ray Spectra. *arXiv e-prints*, page arXiv:2309.07577.

Duncan, R. C. and Thompson, C. (1992). Formation of very strongly magnetized neutron stars-implications for gamma-ray bursts. *Astrophysical Journal, Part 2-Letters (ISSN 0004-637X), vol. 392, no. 1, June 10, 1992, p. L9-L13. Research supported by NSERC.*, 392:L9–L13.

Ekşi, K. Y., Andaç, I., Çıkıntoğlu, S., Gügercinoğlu, E., Motlagh, A. V., and Kızıltan, B. (2016). The inclination angle and evolution of the braking index of pulsars with plasma-filled magnetosphere: Application to the high braking index of psr j1640–4631. *The Astrophysical Journal*, 823(1):34.

Evans, D. W., Riello, M., De Angeli, F., Carrasco, J. M., Montegriffo, P., Fabricius, C., Jordi, C., Palaversa, L., Diener, C., Busso, G., Cacciari, C., van Leeuwen, F., Burgess, P. W., Davidson, M., Harrison, D. L., Hodgkin, S. T., Pancino, E., Richards, P. J., Altavilla, G., Balaguer-Núñez, L., Barstow, M. A., Bellazzini, M., Brown, A. G. A., Castellani, M., Cocozza, G., De Luise, F., Delgado, A., Ducourant, C., Galleti, S., Gilmore, G., Giuffrida, G., Holl, B., Kewley, A., Koposov, S. E., Marinoni, S., Mar-

rese, P. M., Osborne, P. J., Piersimoni, A., Portell, J., Pulone, L., Ragaini, S., Sanna, N., Terrett, D., Walton, N. A., Wevers, T., and Wyrzykowski, Ł. (2018). Gaia Data Release 2. Photometric content and validation. *AA*, 616:A4.

Fortin, M., Raduta, A. R., Avancini, S., and Providência, C. (2020). Relativistic hypernuclear compact stars with calibrated equations of state. *Physical Review D*, 101(3):034017.

Foster III, R. S. (1990). *Constructing a pulsar timing array*. University of California, Berkeley.

Freire, P. C., Wolszczan, A., van den Berg, M., and Hessels, J. W. (2008). A massive neutron star in the globular cluster m5. *The Astrophysical Journal*, 679(2):1433.

Garmire, G. P., Bautz, M. W., Ford, P. G., Nousek, J. A., and Ricker Jr, G. R. (2003). Advanced ccd imaging spectrometer (acis) instrument on the chandra x-ray observatory. In *X-Ray and Gamma-Ray Telescopes and Instruments for Astronomy*, volume 4851, pages 28–44. SPIE.

Gold, T. (1968). Rotating neutron stars as the origin of the pulsating radio sources. *Nature*, 218(5143):731–732.

Goldreich, P. and Julian, W. H. (1969). Pulsar electrodynamics. *Astrophysical Journal, vol. 157, p. 869*, 157:869.

Guillot, S. and Rutledge, R. E. (2014). Rejecting proposed dense matter equations of state with quiescent low-mass x-ray binaries. *The Astrophysical Journal Letters*, 796(1):L3.

Haberl, F. (2007). The magnificent seven: magnetic fields and surface temperature distributions. *ASS*, 308(1-4):181–190.

Haberl, F., Motch, C., Zavlin, V. E., Reinsch, K., Gänsicke, B. T., Cropper, M., Schwope, A. D., Turolla, R., and Zane, S. (2004). The isolated neutron star X-ray pulsars <ASTROBJ>RX J0420.0-5022</ASTROBJ> and <ASTROBJ>RX J0806.4-4123</ASTROBJ>: New X-ray and optical observations. *AA*, 424:635–645.

Harding, A. K. and Muslimov, A. G. (2011). Pulsar pair cascades in magnetic fields with offset polar caps. *Astrophysical Journal*, 743(2):181.

Hare, J., Volkov, I., Pavlov, G. G., Kargaltsev, O., and Johnston, S. (2021). Precise Timing and Phase-resolved Spectroscopy of the Young Pulsar J1617-5055 with NuSTAR. *The Astrophysical Journal*, 923(2):249.

He, C., Ng, C.-Y., and Kaspi, V. (2013). The correlation between dispersion measure and x-ray column density from radio pulsars. *The Astrophysical Journal*, 768(1):64.

Heger, A., Fryer, C. L., Woosley, S. E., Langer, N., and Hartmann, D. H. (2003). How massive single stars end their life. *The Astrophysical Journal*, 591(1):288.

Heinke, C. O., Rybicki, G. B., Narayan, R., and Grindlay, J. E. (2006). A Hydrogen Atmosphere Spectral Model Applied to the Neutron Star X7 in the Globular Cluster 47 Tucanae. *The Astrophysical Journal*, 644(2):1090–1103.

Hewish, A., Bell, S. J., Pilkington, J. D., Frederick Scott, P., and Collins, R. A. (1979). Observation of a rapidly pulsating radio source. In *A Source Book in Astronomy and Astrophysics, 1900–1975*, pages 498–504. Harvard University Press.

Hirotani, K. (2013). Luminosity evolution of gamma-ray pulsars. *The Astrophysical Journal*, 766(2):98.

Ho, W. C. and Lai, D. (2003). Atmospheres and spectra of strongly magnetized neutron stars—ii. the effect of vacuum polarization. *Monthly Notices of the Royal Astronomical Society*, 338(1):233–252.

Ho, W. C. G., Potekhin, A. Y., and Chabrier, G. (2008). Model X-Ray Spectra of Magnetic Neutron Stars with Hydrogen Atmospheres. *The Astrophysical Journal Supplement Series*, 178(1):102–109.

Hui, C. Y., Wu, K., Han, Q., Kong, A. K. H., and Tam, P. H. T. (2018). On the Orbital Properties of Millisecond Pulsar Binaries. *Astrophysical Journal*, 864(1):30.

Huppenkothen, D., Bachetti, M., Stevens, A. L., Migliari, S., Balm, P., Hammad, O., Khan, U. M., Mishra, H., Rashid, H., Sharma, S., Martinez Ribeiro, E., and Valles Blanco, R. (2019). Stingray: A Modern Python Library for Spectral Timing. *The Astrophysical Journal*, 881(1):39.

Hurley-Walker, N., Zhang, X., Bahramian, A., McSweeney, S., O'Doherty, T., Hancock, P., Morgan, J., Anderson, G., Heald, G., and Galvin, T. (2022). A radio transient with unusually slow periodic emission. *Nature*, 601(7894):526–530.

Igoshev, A. P., Hollerbach, R., and Wood, T. (2023). Three-dimensional magnetothermal evolution of off-centred dipole magnetic field configurations in neutron stars. *Monthly Notices of the Royal Astronomical Society*, 525(3):3354–3375.

Igoshev, A. P., Popov, S. B., and Hollerbach, R. (2021). Evolution of Neutron Star Magnetic Fields. *Universe*, 7(9):351.

Kargaltsev, O., Durant, M., Pavlov, G. G., and Garmire, G. (2012). Chandra pulsar survey (chaps). *Astrophysical Journals*, 201(2):37.

Kargaltsev, O., Misanovic, Z., Pavlov, G. G., Wong, J. A., and Garmire, G. P. (2008). X-Ray Observations of Parsec-scale Tails behind Two Middle-Aged Pulsars. *The Astrophysical Journal*, 684(1):542–557.

Kaspi, V. M. and Beloborodov, A. M. (2017). Magnetars. *Annual Review of Astronomy and Astrophysics*, 55:261–301.

Keane, E. and McLaughlin, M. (2011). Rotating radio transients. *arXiv preprint arXiv:1109.6896*.

Keith, M. J., Jameson, A., van Straten, W., Bailes, M., Johnston, S., Kramer, M., Possenti, A., Bates, S. D., Bhat, N. D. R., Burgay, M., Burke-Spolaor, S., D'Amico, N., Levin, L., McMahon, P. L., Milia, S., and Stappers, B. W. (2010). The High Time Resolution Universe Pulsar Survey - I. System configuration and initial discoveries. *MNRAS*, 409(2):619–627.

Kisaka, S. and Tanaka, S. J. (2017). Efficiency of synchrotron radiation from rotation-powered pulsars. *Astrophysical Journal*, 837(1):76.

Kraft, R. P., Burrows, D. N., and Nousek, J. A. (1991). Determination of Confidence Limits for Experiments with Low Numbers of Counts. *Astrophysical Journal*, 374:344.

Large, M., Vaughan, A., and Mills, B. (1968). A pulsar supernova association? *Nature*, 220(5165):340–341.

Lattimer, J. and Prakash, M. (2001). Neutron star structure and the equation of state. *The Astrophysical Journal*, 550(1):426.

Leahy, D. A. (1987). Searches for pulsed emission - Improved determination of period and amplitude from epoch folding for sinusoidal signals. *Astronomy & Astrophysics*, 180(1-2):275–277.

Leahy, D. A., Darbro, W., Elsner, R. F., Weisskopf, M. C., Sutherland, P. G., Kahn, S., and Grindlay, J. E. (1983). On searches for pulsed emission with application to four globular cluster X-ray sources : NGC 1851, 6441, 6624 and 6712. *The Astrophysical Journal*, 266:160–170.

Lee, J., Hui, C. Y., Takata, J., Kong, A. K. H., Tam, P. H. T., and Cheng, K. S. (2018). X-Ray Census of Millisecond Pulsars in the Galactic Field. *Astrophysical Journal*, 864(1):23.

Li, X.-H., Lu, F.-J., and Li, Z. (2008). Nonthermal X-Ray Properties of Rotation-powered Pulsars and Their Wind Nebulae. *Astrophysical Journal*, 682(2):1166–1176.

Lin, Z., Caplan, M. E., Horowitz, C. J., and Lunardini, C. (2020). Fast neutrino cooling of nuclear pasta in neutron stars: Molecular dynamics simulations. *Physical Review C*, 102(4):045801.

Lopez, M., Otte, N., Rissi, M., Schweizer, T., Shayduk, M., and Klepser, S. (2009). Detection of the crab pulsar with MAGIC. *arXiv e-prints*, page arXiv:0907.0832.

Lorimer, D. R. and Kramer, M. (2005). *Handbook of pulsar astronomy*, volume 4. Cambridge university press.

Lower, M. E., Johnston, S., Dunn, L., Shannon, R. M., Bailes, M., Dai, S., Kerr, M., Manchester, R. N., Melatos, A., Oswald, L. S., et al. (2021). The impact of glitches on young pulsar rotational evolution. *Monthly Notices of the Royal Astronomical Society*, 508(3):3251–3274.

Lyne, A. and Graham-Smith, F. (2012). *Pulsar astronomy*. Number 48. Cambridge University Press.

Maccacaro, T., Gioia, I. M., Wolter, A., Zamorani, G., and Stocke, J. T. (1988). The X-Ray Spectra of the Extragalactic Sources in the Einstein Extended Medium-Sensitivity Survey. *Astrophysical Journal*, 326:680.

Manchester, R., Hobbs, G., Bailes, M., Coles, W., Van Straten, W., Keith, M., Shannon, R., Bhat, N., Brown, A., Burke-Spolaor, S., et al. (2013). The parkes pulsar timing array project. *Publications of the Astronomical Society of Australia*, 30:e017.

Manchester, R. and Lyne, A. (1977). Pulsar interpulses–two poles or one? *Monthly Notices of the Royal Astronomical Society*, 181(4):761–767.

Manchester, R. N., Hobbs, G. B., Teoh, A., and Hobbs, M. (2005). The australia telescope national facility pulsar catalogue. *The Astronomical Journal*, 129(4):1993.

Manchester, R. N., Lyne, A. G., Camilo, F., Bell, J. F., Kaspi, V., D'Amico, N., McKay, N., Crawford, F., Stairs, I., Possenti, A., et al. (2001). The parkes multi-beam pulsar survey–i. observing and data analysis systems, discovery and timing of 100 pulsars. *Monthly Notices of the Royal Astronomical Society*, 328(1):17–35.

Manchester, R. N., Lyne, A. G., Taylor, J. H., Durdin, J. M., Large, M. I., and Little, A. G. (1978). The second Molonglo pulsar survey - discovery of 155 pulsars. *MNRAS*, 185:409–421.

Mardia, K. V. (1975). Statistics of directional data. *Journal of the Royal Statistical Society Series B: Statistical Methodology*, 37(3):349–371.

Mereghetti, S., Pons, J. A., and Melatos, A. (2015). Magnetars: properties, origin and evolution. *Space Science Reviews*, 191:315–338.

Michel, F. C. (1991). *Theory of neutron star magnetospheres*. University of Chicago Press.

Mignani, R. P. (2011). Optical, ultraviolet, and infrared observations of isolated neutron stars. *Advances in Space Research*, 47(8):1281–1293.

Mori, K. and Ho, W. C. G. (2007). Modelling mid-Z element atmospheres for strongly magnetized neutron stars. *Monthly Notices of the Royal Astronomical Society*, 377(2):905–919.

Murray, S. S., Austin, G. K., Chappell, J. H., Gomes, J. J., Kenter, A. T., Kraft, R. P., Meehan, G. R., Zombeck, M. V., Fraser, G. W., and Serio, S. (2000). In-flight performance of the chandra high-resolution camera. In *X-Ray Optics, Instruments, and Missions III*, volume 4012, pages 68–80. SPIE.

Nather, R., Warner, B., and Macfarlane, M. (1969). Optical pulsations in the crab nebula pulsar. *Nature*, 221(5180):527–529.

Ostriker, J. and Gunn, J. (1969). On the nature of pulsars. i. theory. *Astrophysical Journal, vol. 157, p. 1395*, 157:1395.

Özel, F. and Freire, P. (2016). Masses, radii, and the equation of state of neutron stars. *Annual Review of Astronomy and Astrophysics*, 54:401–440.

Pacini, F. (1968). Rotating neutron stars, pulsars and supernova remnants. *Nature*, 219(5150):145–146.

Parthasarathy, A., Shannon, R. M., Johnston, S., Lentati, L., Bailes, M., Dai, S., Kerr, M., Manchester, R. N., Osłowski, S., Sobey, C., van Straten, W., and Weltevrede, P. (2019). Timing of young radio pulsars - I. Timing noise, periodic modulation, and

proper motion. *Monthly Notices of the Royal Astronomical Society*, 489(3):3810–3826.

Pavlov, G., Shibanov, Y. A., Ventura, J., and Zavlin, V. (1994). Model atmospheres and radiation of magnetic neutron stars: Anisotropic thermal emission. *Astronomy and Astrophysics (ISSN 0004-6361), vol. 289, no. 3, p. 837-845*, 289:837–845.

Pavlov, G. G., Shibanov, Y. A., Zavlin, V. E., and Meyer, R. D. (1995). Neutron Star Atmospheres. In Alpar, M. A., Kiziloglu, U., and van Paradijs, J., editors, *The Lives of the Neutron Stars*, volume 450 of *NATO Advanced Study Institute (ASI) Series C*, page 71.

Pavlov, G. G., Zavlin, V. E., and Sanwal, D. (2002). Thermal Radiation from Neutron Stars: Chandra Results. In Becker, W., Lesch, H., and Trümper, J., editors, *Neutron Stars, Pulsars, and Supernova Remnants*, page 273.

Percival, J. W., Biggs, J., Dolan, J., Robinson, E., Taylor, M., Bless, R., Elliot, J., Nelson, M., Ramseyer, T., Van Citters, G., et al. (1993). The crab pulsar in the visible and ultraviolet with 20 microsecond effective time resolution. *Astrophysical Journal, Part 1 (ISSN 0004-637X), vol. 407, no. 1, p. 276-283.*, 407:276–283.

Pethick, C. (1992). Cooling of neutron stars. *Reviews of modern physics*, 64(4):1133.

Philippov, A., Tchekhovskoy, A., and Li, J. G. (2014). Time evolution of pulsar obliquity angle from 3d simulations of magnetospheres. *Monthly Notices of the Royal Astronomical Society*, 441(3):1879–1887.

Pierbattista, M., Harding, A. K., Grenier, I. A., Johnson, T. J., Caraveo, P. A., Kerr, M., and Gonthier, P. L. (2015). Light-curve modelling constraints on the obliquities and aspect angles of the young Fermi pulsars. *Astronomy &Astrophysics*, 575:A3.

Pons, J., Reddy, S., Prakash, M., Lattimer, J., and Miralles, J. (1999). Evolution of proto-neutron stars. *The Astrophysical Journal*, 513(2):780.

Posselt, B., Pavlov, G., Manchester, R., Kargaltsev, O., and Garmire, G. (2012). Chandra observations of the old pulsar psr b1451−68. *Astrophysical Journal*, 749(2):146.

Posselt, B., Pavlov, G. G., Kargaltsev, O., and Hare, J. (2023). X-ray and near-infrared observations of the middle-aged pulsar B1055-52, its multiwavelength spectrum, and proper motion. *arXiv e-prints*, page arXiv:2306.00185.

Possenti, A., Cerutti, R., Colpi, M., and Mereghetti, S. (2002). Re-examining the x-ray versus spin-down luminosity correlation of rotation powered pulsars. *AA*, 387(3):993−1002.

Potekhin, A. Y. (2014). Atmospheres and radiating surfaces of neutron stars. *Physics-Uspekhi*, 57(8):735.

Prinz, T. and Becker, W. (2015). A Search for X-ray Counterparts of Radio Pulsars. *arXiv e-prints*, page arXiv:1511.07713.

Raaijmakers, G., Greif, S., Hebeler, K., Hinderer, T., Nissanke, a., Schwenk, A., Riley, T., Watts, A., Lattimer, J., and Ho, W. (2021). Constraints on the dense matter equation of state and neutron

star properties from nicer's mass–radius estimate of psr j0740+6620 and multimessenger observations. *The Astrophysical Journal Letters*, 918(2):L29.

Sales, T., Lourenço, O., Dutra, M., and Negreiros, R. (2020). Revisiting the thermal relaxation of neutron stars. *Astronomy & Astrophysics*, 642:A42.

Saslaw, W. C., FAULKNER, J., and STRITTMATTER, P. A. (1968). Rapidly pulsing radio sources. *Nature*, 217(5135):1222–1227.

Shapiro, S. L., Teukolsky, S. A., Holes, B., Dwarfs, W., and Stars, N. (1983). The physics of compact objects. *Wiley, New York*, 19832:119–123.

Shibanov, I. A., Zavlin, V. E., Pavlov, G. G., and Ventura, J. (1992). Model atmospheres and radiation of magnetic neutron stars. I - The fully ionized case. *Astronomy & Astrophysics*, 266(1):313–320.

Shibanov, Y. A., Koptsevich, A., Sollerman, J., and Lundqvist, P. (2003). The vela pulsar in the near-infrared. *arXiv preprint astro-ph/0305273*.

Staelin, D. H. and Reifenstein III, E. C. (1968). Pulsating radio sources near the crab nebula. *Science*, 162(3861):1481–1483.

Stassun, K. G., Oelkers, R. J., Paegert, M., Torres, G., Pepper, J., De Lee, N., Collins, K., Latham, D. W., Muirhead, P. S., Chittidi, J., Rojas-Ayala, B., Fleming, S. W., Rose, M. E., Tenenbaum, P., Ting, E. B., Kane, S. R., Barclay, T., Bean, J. L., Brassuer, C. E., Charbonneau, D., Ge, J., Lissauer, J. J., Mann, A. W., McLean, B.,

Mullally, S., Narita, N., Plavchan, P., Ricker, G. R., Sasselov, D., Seager, S., Sharma, S., Shiao, B., Sozzetti, A., Stello, D., Vanderspek, R., Wallace, G., and Winn, J. N. (2019). The Revised TESS Input Catalog and Candidate Target List. *The Astronomical Journal*, 158(4):138.

Strüder, L., Briel, U., Dennerl, K., Hartmann, R., Kendziorra, E., Meidinger, N., Pfeffermann, E., Reppin, C., Aschenbach, B., Bornemann, W., Bräuninger, H., Burkert, W., Elender, M., Freyberg, M., Haberl, F., Hartner, G., Heuschmann, F., Hippmann, H., Kastelic, E., Kemmer, S., Kettenring, G., Kink, W., Krause, N., Müller, S., Oppitz, A., Pietsch, W., Popp, M., Predehl, P., Read, A., Stephan, K. H., Stötter, D., Trümper, J., Holl, P., Kemmer, J., Soltau, H., Stötter, R., Weber, U., Weichert, U., von Zanthier, C., Carathanassis, D., Lutz, G., Richter, R. H., Solc, P., Böttcher, H., Kuster, M., Staubert, R., Abbey, A., Holland, A., Turner, M., Balasini, M., Bignami, G. F., La Palombara, N., Villa, G., Buttler, W., Gianini, F., Lainé, R., Lumb, D., and Dhez, P. (2001). The European Photon Imaging Camera on XMM-Newton: The pn-CCD camera. *Astronomy & Astrophysics*, 365:L18–L26.

Taylor, J. H. and Cordes, J. (1993). Pulsar distances and the galactic distribution of free electrons. *Astrophysical Journal-Part 1 (ISSN 0004-637X), vol. 411, no. 2, p. 674-684.*, 411:674–684.

Thorne, K. S. and Ipser, J. R. (1968). White-Dwarf and Neutron-Star Interpretations of Pulsating Radio Sources. *APJL*, 152:L71.

Tiengo, A., Esposito, P., Mereghetti, S., Turolla, R., Nobili, L., Gastaldello, F., Götz, D., Israel, G. L., Rea, N., Stella, L., Zane, S., and Bignami, G. F. (2013). A variable absorption feature in the X-ray spectrum of a magnetar. *Nature*, 500(7462):312–314.

Townsley, L., Broos, P., Chartas, G., Moskalenko, E., Nousek, J., and Pavlov, G. (2002). Simulating ccds for the chandra advanced ccd imaging spectrometer. *Nuclear Instruments and Methods in Physics Research Section A: Accelerators, Spectrometers, Detectors and Associated Equipment*, 486(3):716–750.

Tsuruta, S. and Cameron, A. (1966). Cooling and detectability of neutron stars. *Canadian Journal of Physics*, 44(8):1863–1894.

Turner, M. J. L., Abbey, A., Arnaud, M., Balasini, M., Barbera, M., Belsole, E., Bennie, P. J., Bernard, J. P., Bignami, G. F., Boer, M., Briel, U., Butler, I., Cara, C., Chabaud, C., Cole, R., Collura, A., Conte, M., Cros, A., Denby, M., Dhez, P., Di Coco, G., Dowson, J., Ferrando, P., Ghizzardi, S., Gianotti, F., Goodall, C. V., Gretton, L., Griffiths, R. G., Hainaut, O., Hochedez, J. F., Holland, A. D., Jourdain, E., Kendziorra, E., Lagostina, A., Laine, R., La Palombara, N., Lortholary, M., Lumb, D., Marty, P., Molendi, S., Pigot, C., Poindron, E., Pounds, K. A., Reeves, J. N., Reppin, C., Rothenflug, R., Salvetat, P., Sauvageot, J. L., Schmitt, D., Sembay, S., Short, A. D. T., Spragg, J., Stephen, J., Strüder, L., Tiengo, A., Trifoglio, M., Trümper, J., Vercellone, S., Vigroux, L., Villa, G., Ward, M. J., Whitehead, S., and Zonca, E. (2001). The European Photon Imaging Camera on XMM-Newton: The MOS cameras. *Astronomy & Astrophysics*, 365:L27–L35.

Vahdat, A., Kalemci, E., and Maccarone, T. J. (2019). Investigating state transition luminosities of Galactic black hole transients in the outburst decay. *Monthly Notices of the Royal Astronomical Society*, 485(2):2744–2758.

Vahdat, A., Posselt, B., Pavlov, G. G., Weltevrede, P., Santangelo, A., and Johnston, S. (2024). Multiwavelength Pulsations and Surface Temperature Distribution in the Middle-aged Pulsar B1055–52. *The Astrophysical Journal*, 963(2):138.

Vahdat, A., Posselt, B., Santangelo, A., and Pavlov, G. G. (2022). Toward an X-ray inventory of nearby neutron stars. *Astronomy & Astrophysics*, 658:A95.

Verbiest, J., Osłowski, S., and Burke-Spolaor, S. (2022). Pulsar timing array experiments. In *Handbook of Gravitational Wave Astronomy*, pages 157–198. Springer.

Viganò, D. and Pons, J. A. (2012). Central compact objects and the hidden magnetic field scenario. *Monthly Notices of the Royal Astronomical Society*, 425(4):2487–2492.

Viganò, D., Rea, N., Pons, J. A., Perna, R., Aguilera, D. N., and Miralles, J. A. (2013). Unifying the observational diversity of isolated neutron stars via magneto-thermal evolution models. *Monthly Notices of the Royal Astronomical Society*, 434(1):123–141.

Webb, N. A., Coriat, M., Traulsen, I., Ballet, J., Motch, C., Carrera, F. J., Koliopanos, F., Authier, J., de la Calle, I., Ceballos, M. T., Colomo, E., Chuard, D., Freyberg, M., Garcia, T., Kolehmainen, M., Lamer, G., Lin, D., Maggi, P., Michel, L., Page, C. G., Page,

M. J., Perea-Calderon, J. V., Pineau, F. X., Rodriguez, P., Rosen, S. R., Santos Lleo, M., Saxton, R. D., Schwope, A., Tomás, L., Watson, M. G., and Zakardjian, A. (2020). The XMM-Newton serendipitous survey IX. The fourth XMM-Newton serendipitous source catalogue. *arXiv e-prints*, page arXiv:2007.02899.

Weltevrede, P. and Wright, G. (2009). Mapping the magnetosphere of PSR B1055-52. *Monthly Notices of the Royal Astronomical Society*, 395(4):2117–2126.

Wilms, J., Allen, A., and McCray, R. (2000). On the Absorption of X-Rays in the Interstellar Medium. *The Astrophysical Journal*, 542(2):914–924.

Woosley, S. E., Heger, A., and Weaver, T. A. (2002). The evolution and explosion of massive stars. *Reviews of modern physics*, 74(4):1015.

Yakovlev, D. (2021). Two-blackbody portraits of radiation from magnetized neutron stars. *Monthly Notices of the Royal Astronomical Society*, 506(3):4593–4602.

Yakovlev, D. G., Levenfish, K. P., and Shibanov, Y. A. (1999). Cooling of neutron stars and superfluidity in their cores. *Physics-Uspekhi*, 42(8):737.

Yakovlev, D. G. and Pethick, C. J. (2004). Neutron Star Cooling. *Annual Review of Astronomy and Astrophysics*, 42(1):169–210.

Yao, J., Manchester, R., and Wang, N. (2017). A new electron-density model for estimation of pulsar and frb distances. *The Astrophysical Journal*, 835(1):29.

Yao, J. M., Manchester, R. N., and Wang, N. (2017). A New Electron-density Model for Estimation of Pulsar and FRB Distances. *Astrophysical Journal*, 835(1):29.

Zavlin, V. E. and Pavlov, G. (2002). Modeling neutron star atmospheres. *Arxiv preprint astro-ph/0206025*.

Zavlin, V. E., Pavlov, G. G., and Shibanov, Y. A. (1996). Model neutron star atmospheres with low magnetic fields. I. Atmospheres in radiative equilibrium. *Astronomy & Astrophysics*, 315:141–152.

Zhang, L. and Jiang, Z. (2006). Non-thermal pulsed x-ray emission from rotation-powered pulsars. *Astronomy & Astrophysics*, 454(2):537–542.

Acknowledgments

This thesis marks the formal conclusion of my twenty-four years as a student – two and a half decades replete with cherished memories, many of which are intricately tied to the remarkable individuals who have been part of my journey.

When I penned my bachelor thesis in Electronics Engineering back in 2015, the list of those I needed to thank was relatively short. A brief and formal acknowledgment extended to my supervisor and my family felt sufficient at the time. It was a moment tinged with nostalgia and boundless excitement for what the future held.

Around two years later, as I defended my master's thesis in Physics, I realized that the circle of people who had a hand in shaping my path had grown significantly. In this period, I underwent remarkable personal and career growth, and I endeavored to reflect this transformative journey within the pages of my thesis.

Now, after another six years, tradition calls for me once again to commence this thesis by expressing my gratitude to those who played a profound role in its realization. However, no tradition adequately captures the depth of my appreciation for their contributions. Their significance goes far beyond the confines of words.

My passion for Astronomy ignited in primary school with the awe-inspiring experience of a solar eclipse. This interest blossomed in college while exploring high-energy astrophysics, especially Pulsars. Despite the challenging nature of my Engineering studies, I enthusiastically attended extra astrophysics classes in my free time. Ingeniously, I secured a position at the TUBITAK National Observatory (TUG) in Antalya, Turkey, ostensibly for a 'mandatory' engineering internship. My real aim, though, was to observe stars and galaxies at night. This dual commitment meant working day shifts from 8 AM to 5 PM and then dedicating my nights from 9 PM to 4 AM to astronomy. Observing the Milky Way every night and witnessing spectacular sunrises above the clouds was surreal. Although it was an intense period, looking back, it was worth every moment, and I am now ready to bring this chapter to a close.

I would like to start by thanking my advisor, Bettina Posselt, for her exceptional guidance throughout this journey. Bettina, you have been an incredible day-to-day advisor, consistently available whenever I had a question. Your support, guidance, and uplifting words during moments of uncertainty were invaluable. You have not only been an ever-caring and thoughtful advisor but also a delightful person to work with, profoundly impacting my experience. Your endless patience, keen insights, and wealth of innovative ideas have been a true blessing.

I would also like to express my appreciation to Andrea Santangelo for fostering such a welcoming and collaborative group dynamic. Your efforts in creating a friendly and productive working atmosphere have made a significant difference in my academic journey. Being part of this community, where science, camaraderie, and support harmoniously coexist, has been truly inspiring. Your ability to dedicate time to each of us, sharing anecdotes, wisdom, and motivation, has been especially cherished, particularly during the challenging times brought about by the Covid-19 pandemic.

I'd also like to express gratitude to Prof. Dr. Klaus Werner for serving as an extra reviewer for my thesis. His comments and encouragement were greatly appreciated.

I want to acknowledge George Pavlov for his unwavering patience and guidance as we delved into the enigmatic world of pulsars. Though not my formal advisor, your support felt every bit as essential. The experience of working alongside you has been a joy and a privilege. Your expertise and camaraderie have made this academic journey all the more rewarding.

I extend my gratitude to the XMM instrument team, including the talented individuals in Tübingen who were part of the design team, for their exceptional expertise and dedication in constructing a truly remarkable satellite.

I would like to express my deep appreciation for the city of Tübingen. Before moving there, I knew nothing about it, but it quickly revealed itself to be one of the most beautiful and welcoming places I've ever experienced. I remember walking through a deserted Central Park NYC at the onset of the pandemic pondering what my next adventure would be like and whether I could adapt to life in a 'small town'. Aboard the plane to Germany, a fellow passenger showed me a video of President Donald Trump announcing the suspension of all air traffic starting the next day.

The initial months in Tübingen were challenging. My interactions were limited, and precautions like N95 masks, gloves, and adherence to local night curfews were the norm. However, things began to shift when I established a local hiking group. This initiative allowed me to explore the state of Baden-Württemberg and form connections with new friends from around the globe, even amidst the pandemic. This experience transformed my time in Tübingen, turning it into a period of memorable adventures and personal growth.

I would like to express my thanks to my office mates, Emre and Youli, for all the memorable times and the countless amusing bets we've shared. Our morning tea sessions and 'yellow donkey' lunch breaks will be deeply missed. Emre, you are one of the few people with whom I've shared a mutual understanding and likemindedness, especially in humor and discussions on politics, history, and cultural norms. Youli, coming from a vastly different cultural background, blended seamlessly into our conversations, demon-

strating admirable personal growth.

Additionally, I extend my gratitude to my friends in Turkey: Oğuz, Aras, and Abdülhamid. Since our days as classmates during our bachelor's program, we have remained close. Each visit to Istanbul rekindles our bond as we catch up on each other's lives, reminisce about old times, enjoy our traditional meal at 'Hayri Usta', gossip about our former professors, and share hearty laughs.

I would like to thank two of my good friends, Ceren and Ali Nazim, for our great times in Texas. They were the 'Flowers in the Desert' to me. :)

Another thank you goes to my friend Gökce for being an awesome, independent person with a great sense of humor.

I would also like to express my gratitude to my friend Louise for being a kind-hearted and humble individual. Her presence makes the world a better place.

A heartfelt thank you to my friend Amalia for her incredible journey of personal growth. From her initial shyness to blossoming into a confident and inspiring individual, her transformation has been remarkable.

I extend my heartfelt thanks to two of my best friends, Julia and Nikos. Despite a relatively short period of 3 years and living in dif-

ferent countries, we have forged so many wonderful memories together. From extreme hikes to navigating challenging pandemic restrictions (and the occasional run-in with the police), to visiting beautiful countries together, it's been a wild ride. I look forward to many more adventures in the future.

My mom has always been there for me, no matter what. I could never have come this far without her affection and sacrifices. Thanks, Mom, I love you.

Last but not least, I would like to deeply thank my fiancée, Louise, for being an exceptional, loving, and caring partner during this period. After spending time in so many different places and meeting countless souls, I have come to understand how valuable it is to find someone who matches you on every level – from interests to commitment, to love, to a sense of humor. For this, I consider myself incredibly fortunate to be in her presence.

Just as Frodo said to Sam in the shadow of Mount Doom, *"I'm glad to be with you, here at the end of all things"*, I find myself deeply thankful to be in the company of such compassionate and remarkable people as I conclude this part of my life's journey.

"I am glad to be with you [all], here at the end of [this chapter]"...

All of this has happened before, and it will all happen again.
But this time it happened in [Tübingen]